

## AN ABSTRACT OF THE THESIS OF

Maren Scheidhauer for the degree of Master of Science in Geophysics presented on May 29, 1997. Title: Crustal Structure of the Queen Charlotte Transform Fault Zone from Multichannel Seismic Reflection and Gravity Data.

*Redacted for Privacy*

Abstract approved: \_\_\_\_\_

Anne M. Tréhu

The Queen Charlotte Fault system is a segment of the North America - Pacific plate boundary. From 45 Ma - 5 Ma, plate motion has been primarily translational. Since 5 Ma, transpression has been the dominant mode of interaction. The plate boundary west of the Queen Charlotte Islands is characterized by an approximately 30-km wide terrace, flanked to the west by a topographic trough and to the east by the seismically active Queen Charlotte Fault. At 53.4°N the fault bends eastward and the terrace becomes wider and discontinuous, forming triangular shaped highs and intervening lows.

Approximately 300 km of multichannel seismic reflection and gravity data along and across the Queen Charlotte Fault off Dixon Entrance were collected as part of the ACCRETE experiment in 1994. Structural interpretation of the five new profiles reveals the presence of faults and folds within the terrace, which form an angle of 20° to the strike of the Queen Charlotte Fault. The direction of these structures corresponds to the trend of the plate boundary south of the bend and west of the Queen Charlotte Islands, implying that through complex compression and shear, material must have been carried from south to north along the margin during oblique plate motion. Based on this observation and on forward gravity modeling, which places limits on the

possible plate configuration at depth, a four-dimensional model has been developed to explain the temporal and spatial evolution of structural styles in this region.

Considering the amount of shortening that must be accommodated within the past 5 Ma (a maximum of 100 km), a model of an underthrusting Pacific plate is preferred over one of pure upthrusting. About 5-6 Ma ago, when transpression began, oceanic crust was flexed and thrust upward at the plate boundary to eventually reach a steady-state configuration of a subducting slab. Fractured basement rock and consolidated, deformed sediments underlie the terrace and form its foundation. As a result of strain partitioning, the terrace is now decoupled and moves both parallel to the continent and perpendicular to the underthrusting Pacific plate. North of the bend in the Queen Charlotte Fault, underthrusting north of it occurs obliquely along preexisting fractures at the base of the terrace. The repetitive pattern of triangular terrace slivers is the result of continuing uplift and shear along these trends. Active tectonism influences sediment dispersal and creates traps.

A N-S trending fault was also identified in the trough segment and possibly involves oceanic basement. Its origin is thought to be due to distributed shear that was transmitted across the plate boundary. Sea-floor spreading magnetic anomalies trend north-south as well. Along these zones of weakness, synthetic strike-slip faults of a transpressional strain ellipse could have been initiated during early stages of subduction. Reactivation of such faults may occur when oceanic crust approaches the outer terrace boundary, as is the case in the study region.

Gravity modeling confirmed the existence of thin (24 km) continental crust and an increase in oceanic Moho dip beneath the terrace, which is topped by unconsolidated sediments and underlain by material of near-basement densities. It could not be determined using gravity modeling whether oceanic crust exists beneath the continent, but if it does, it must be welded to the North American plate in shallow subduction.

© Copyright by MAREN SCHEIDHAUER  
May 29, 1997  
All Rights Reserved

**Crustal Structure of the Queen Charlotte Transform Fault Zone from  
Multichannel Seismic Reflection and Gravity Data**

by

**Maren Scheidhauer**

**A THESIS**

submitted to

**Oregon State University**

in partial fulfillment of  
the requirements for the  
degree of

**Master of Science**

**Presented May 29, 1997  
Commencement June 1998**

Master of Science thesis of Maren Scheidhauer presented on May 29, 1997

APPROVED:

*Redacted for Privacy* \_\_\_\_\_

Major Professor, representing Geophysics

*Redacted for Privacy* \_\_\_\_\_

Dean of College of Oceanic and Atmospheric Sciences

*Redacted for Privacy* \_\_\_\_\_

Dean of Graduate School

I understand that my thesis will become part of the permanent collection of Oregon State University libraries. My signature below authorizes release of my thesis to any reader upon request.

*Redacted for Privacy* \_\_\_\_\_

MAREN SCHEIDHAUER, AUTHOR

## ACKNOWLEDGMENTS

First, I would like to thank my advisor, Anne M. Trehu, and Kristin M. M. Rohr for their help and advice during the research process and for making the writing of this thesis possible. I would like to extend my gratitude to my other committee members, Clayton Paulson and Albert Stetz. I also wish to thank Bob Lillie for the time he took to discuss my ideas, John Chen, Gary Egbert, Friedemann Wenzel, Shaul Levi, John Nabelek, and Blanka Sperner, and all professors and researchers at the College of Oceanic and Atmospheric Sciences, the O.S.U. Geoscience Department, and the Geophysical Institute of Karlsruhe University, who helped to extend my knowledge in the field. Thanks to Christof Lendl for his patience and support in computer questions, and to my fellow grad students in the Department of Geophysics, including Jochen Braunmiller, Axel Fabritius, Sean Fleming, Alexander Goertz, Albrecht Haeussermann, Michael Jordan, Beate Leitner, Xiao-Qing Li, Lisa McNeill, Bernd Schurr, Wolfgang Seher, Weerachai Siripunvaraporn and Thorsten Warneke.

A special thanks to my friends Carrie Hall, Barbara Barrett, Katie Busse, Kelly Chapin, Kathy Konicki, Lynne David, Emily Oatney, Julie Pullen, Hilary Stockton, as well as to my housemates Anna Bandick, Barbara Goetz, Andrew Longyear, and Bill McNaulty for their moral support and for keeping up my physical strength. Lastly, I would like to thank my mother, my sister, the rest of my family and all my friends in Germany, who were there for me even over this great distance.

This work was funded by the National Science Foundation through grants 9219870-EAR and 9527001-EAR.

## TABLE OF CONTENTS

	<u>Page</u>
1. INTRODUCTION .....	1
2. GEOLOGIC AND TECTONIC SETTING .....	3
2.1 LOCATION .....	3
2.2 TECTONIC HISTORY AND PLATE MOTION.....	3
2.3 STRUCTURE WEST OF THE QUEEN CHARLOTTE ISLANDS .....	7
2.4 STRUCTURE OFF DIXON ENTRANCE.....	10
2.5 STRUCTURE NORTH OF DIXON ENTRANCE.....	13
2.6 SEISMICITY .....	13
2.7 GRAVITY.....	17
2.8 PREVIOUS PLATE TECTONIC MODELS .....	19
3. ACQUISITION.....	26
3.1 THE SEISMIC DATA .....	26
3.2 THE GRAVITY DATA .....	30
4. SEISMIC DATA PROCESSING .....	32
4.1 GENERAL DESCRIPTION .....	32
4.2 THE SOFTWARE.....	35
4.3 PREPROCESSING.....	36
4.4 PROCESSING FLOWCHART .....	37
4.5 LINE 1262 .....	38
4.5.1 Common Shot Gather .....	38
4.5.1.1 GAIN.....	39
4.5.1.2 TRACE EDITING .....	43
4.5.1.3 TYPES OF ENERGY IN THE FIELD RECORD.....	43
4.5.1.4 MULTIPLES.....	45
4.5.1.5 FREQUENCIES AND FILTERING .....	47

**TABLE OF CONTENTS (CONTINUED)**

4.5.2 CMP Sorting .....	51
4.5.3 Velocity Analysis.....	54
4.5.3.1 NORMAL MOVEOUT (NMO) .....	54
4.5.3.2 VELOCITY PICKING.....	56
4.5.3.3 2-D VELOCITY DISTRIBUTION.....	60
4.5.4 CMP Stacking .....	70
4.5.5 Post-stack Processes .....	70
4.6 LINE 1250 .....	71
4.7 LINES 1264 AND 1265.....	70
4.8 MIGRATION.....	74
<b>5. GEOLOGIC INTERPRETATION AND DISCUSSION OF SEISMIC DATA.....</b>	<b>86</b>
5.1 GEOPHYSICAL ASSUMPTIONS AND DEFINITION OF UNITS.....	87
5.2 STRUCTURAL FEATURES .....	87
5.3 PROCEDURE .....	88
5.4 THE QUEEN CHARLOTTE TROUGH REGION .....	91
5.4.1 Basement.....	92
5.4.2 Sediments.....	105
5.4.3 Faults.....	114
5.5 THE QUEEN CHARLOTTE TERRACE .....	120
5.5.1 Structure at Depth .....	121
5.5.2 Stratified Units.....	127
5.5.3 Faults.....	131
5.6 THE CONTINENTAL SHELF REGION .....	133
5.7 SUMMARY.....	134

**TABLE OF CONTENTS (CONTINUED)**

6. GRAVITY MODELING .....	138
6.1 CONSTRAINTS ON GRAVITY MODELING .....	138
6.2 RESULTS .....	145
7. TECTONIC MODEL AND CONCLUSION .....	158
7.1 PRESENTATION OF A TECTONIC MODEL .....	158
7.2 CONCLUSIONS .....	170
7.3 SUGGESTED FUTURE INVESTIGATIONS .....	171
BIBLIOGRAPHY .....	172
APPENDICES .....	177

## LIST OF FIGURES

<u>Figure</u>	<u>Page</u>
2.1 Location map (adapted from Riddihough and Hyndman, 1991) showing the modern plate tectonic regime of the northeast Pacific _____	4
2.2 Bathymetry and location map of all reflection and refraction profiles _____	5
2.3 Present magnetic anomaly pattern formed by spreading between the Juan de Fuca and Pacific Plates (from Atwater, 1989) _____	6
2.4 A sample seismic reflection profile from Davis and Seemann (1981) across the trough and terrace _____	10
2.5 Free-air gravity anomaly in mGal _____	11
2.6 Bathymetry (in meters) of the study region _____	12
2.7 Generalized interpretation of the refraction work done by Horn et al. (1984)____	14
2.8 Simplified line drawings of multichannel seismic-reflection profiles across the southeast Alaska continental margin from Bruns and Carlson (1987) _____	15
2.9 Focal mechanisms of the two largest historical earthquakes in the study area (modified from Bérubé et al., 1989) _____	16
2.10 Two possible tectonic end-member models (from Mackie et al., 1989) _____	20
2.11 Final velocity model derived from airgun and explosion data (modified from Dehler and Clowes, 1988)_____	22
2.12 Block diagram showing how strike-slip and thrust faulting might be related at the Queen Charlotte Transform Fault region _____	24
3.1 Location map of the EW9412 -- "ACCRETE" ship cruise (from Diebold, 1994). _____	27
3.2 EW9412 - airgun configuration from Diebold (1994)_____	28
3.3 EW9412 - streamer configuration from Diebold (1994) _____	29
3.4 Ship track free air gravity anomaly (blue) and geosatellite gravity data _____	31

## **LIST OF FIGURES (CONTINUED)**

4.1 Common midpoint profiles (from Telford et al., 1994)_____	33
4.2 Common shot gather of shot 23000 of line 1262_____	40
4.3 Common shot gather of shot 23000 of line 1262_____	42
4.4 Common shot gather of shot 23000 of line 1262_____	44
4.5 Common shot gather of shot 23500 of line 1262_____	46
4.6 Waveform of primary, first, and second order multiple from CMP of line 1264 _____	49
4.7 Amplitude spectra of the fast Fourier transform of six traces from shot 23000 of line 1262 _____	50
4.8 Common shot gather of shot 23000 of line 1262_____	52
4.9 a) data acquisition in the shot-receiver (s, r) domain and b) recording in the midpoint-offset (m, o)_____	53
4.10 Common depth point gather of CMP 11100 in the trough segment of line_____	55
4.11 Two reflection hyperbolas before and after NMO correction _____	56
4.12 Semblance contour of CMP 11100 of line 1262 _____	58
4.13 Semblance contour plot of CMP 10500 of line 1262 _____	59
4.14 Final stacked section of profile 1262 _____	62
4.15 Final two-dimensional stacking velocity distribution of line_____	63
4.16 Two-dimensional interval velocity distribution of line 1262 _____	64
4.17 Simple velocity function of four velocity-time pairs _____	66
4.18 Stack of the trough portion of line 1262 from CMP 10700 through 11500 ____	68
4.19 Curves of depth below sea floor versus interval velocities _____	69

## LIST OF FIGURES (CONTINUED)

4.20	Final stacked section of profile 1250	72
4.21	Final two-dimensional stacking velocity distribution of line 1250	73
4.22	Two-dimensional interval velocity distribution of line 1250	74
4.23	Final stacked section of profile 1264	76
4.24	Final two-dimensional stacking velocity distribution of line 1264	77
4.25	Two-dimensional interval velocity distribution of line 1264	78
4.26	Final stacked section of profile	79
4.27	Final two-dimensional stacking velocity distribution of line	80
4.28	Two-dimensional interval velocity distribution of line 1265	81
4.29	Time-to-depth conversion of the migrated section of line 1262	85
5.1	The angular relations between structures that tend to form in right-lateral simple shear under ideal conditions (from Christie-Blick and Biddle, 1985)	89
5.2	Location map of all interpreted profiles of this study on bathymetry	90
5.3 a)	Finite-Difference Migration of line 1262	93
5.3 b)	Structural interpretation of line 1262	94
5.4 a)	Stack of the trough portion of line S.P. Lee 5	95
5.4 b)	Stack of the terrace portion of line S.P. Lee 5	96
5.5 a)	Finite-Difference Migration of line 1250	97
5.5 b)	Structural interpretation of line 1250	98
5.6	Stack of line S.P. Lee 3	99
5.7 a)	Finite-Difference Migration of line 1263	100
5.7 b)	Structural interpretation of line 1263	101

## **LIST OF FIGURES (CONTINUED)**

5.8	Stack of the trough portion of line S.P. Lee 1 _____	102
5.9	Stack of the trough portion of line S.P. Lee 2 _____	103
5.10	Graphs showing twtt versus depth below the sea floor for line 1262 in the Queen Charlotte _____	106
5.11	Graphs showing interval velocity versus depth below the sea floor for line 1250 _____	108
5.12	Map of contours of twtt to the unconformity between units D and E _____	109
5.13	Map of contours of twtt to the unconformity between units C and D _____	111
5.14	East-west trending single-channel reflection data in Dixon Entrance (from Rohr and Dietrich, 1992) _____	115
5.15	Schematics of a positive flower structure (after Harding, 1985) _____	116
5.16	Time-to-depth conversion of the western portion of line 1263 (processed by K.M.M. Rohr) _____	117
5.17	Map of contours of twtt to the top of the basement _____	120
5.18 a)	Finite-Difference Migration of line 1264 _____	122
5.18 b)	Structural interpretation of line 1264 _____	123
5.19	Line 1265 a) without and b) with structural interpretation _____	124
5.20	Map of contours of twtt to the top of unit F within the terrace _____	126
5.21	Compilation of structures interpreted within the Queen Charlotte Trough and Terrace _____	129
6.1	P-wave velocity-density relationships for different lithologies (from Telford et al., 1994) _____	144
6.2 a)	Gravity forward model of line 1262 _____	147
6.2 b)	Gravity forward model of line 1262 _____	148

**LIST OF FIGURES (CONTINUED)**

6.2 c) Gravity forward model of line 1262 _____	150
6.2 d) Gravity forward model of line 1262 _____	151
6.3 a) Gravity forward model of line 1250 _____	153
6.3 b) Gravity forward model of line 1250 _____	154
6.3 c) Gravity forward model of line 1250 _____	155
7.1 Block diagrams showing the beginning and development of the transpressional regime west of the Queen Charlotte Islands _____	161
7.2 Diagrams show orientations of fractures in a) a transpressional regime, b) a simple shear environment (adapted from Sanderson and Marchini, 1984) ____	162
7.3 Cartoon demonstrating the migration of plate boundary parallel fractures and thrusts of the base formation of the terrace _____	166
7.4 Block diagram to illustrate relative movements on the NS-fault and the Queen Charlotte Fault _____	169

## LIST OF TABLES

<u>Table</u>	<u>Page</u>
2.1 This table shows the azimuth and velocity of relative plate motion of the Pacific plate relative to the North American plate _____	8
2.1 (continued)_____	9
4.1 SIOSEIS shell script _____	35
4.2 List of shot point-numbers, corresponding CMPs, their average spacing and the maximum folds of the lines processed _____	37
4.3 Processing flowchart showing processing sequence used for line 1262 _____	37
4.4 Determination of sea floor reflection coefficient r_____	47
4.5 Typical reflectivity values for two different layer interfaces, adapted from Sheriff and Geldart (1985) _____	48
4.6 Data values corresponding to graph shown in figure 4.17_____	65
5.1 Properties of units and horizons within the Queen Charlotte Trough _____	136
5.1 (continued)_____	137
6.1 Compilation of interval velocities, unit thicknesses, and depths to interfaces between units at several selected CMPs of line 1262 _____	139
6.1 (continued)_____	140
6.2 Compilation of interval velocities, unit thicknesses and depths to interfaces between units at several selected CMPs of line 1250 _____	141
6.2 (continued)_____	142
6.2 (continued)_____	143
6.3 Calculation of isostasy at various sites along the profile 1262 _____	157

## LIST OF APPENDICES

	<u>Page</u>
APPENDIX A: Normal moveout _____	178
APPENDIX B _____	181
Semblance _____	181
Interval Velocity _____	182
APPENDIX C: Migration _____	183

## **DEDICATION**

**This thesis is dedicated to my father.**

# **Crustal Structure of the Queen Charlotte Transform Fault Zone from Multichannel Seismic Reflection and Gravity Data**

## **1. INTRODUCTION**

The Queen Charlotte fault system represents a major segment of the transpressive plate boundary between the North American and Pacific plates. Three structural domains are distinguished from west to east across the fault: the Queen Charlotte Trough, the 30-45-km-wide and elevated Queen Charlotte Terrace, and the shallow continental shelf. Sidescan and seismicity data place the currently active Queen Charlotte Fault on a vertical fault plane at the inner terrace boundary. The appearance of the terrace changes abruptly from a relatively linear narrow feature west of the Queen Charlotte Islands to discontinuous triangular shaped slivers north of 53.4°N, where the fault bends eastward.

This was the location of a piggy-back of the ACCRETE experiment in September 1994, during which 300 km of multichannel seismic reflection and gravity data were collected along and across the plate boundary off Dixon Entrance, near the US-Canada border. Five profiles (1250, 1262-1265) were processed as part of this thesis to provide the basis for a new four-dimensional structural and temporal interpretation of the evolution and tectonics of this region.

Stacked and migrated sections reveal the presence of a variety of faults and folds in the terrace that are oriented mainly NW-SE, about 20° oblique to the Queen Charlotte Fault off Dixon Entrance but parallel to the plate boundary south of the bend. The terrace has been uplifted, tilted and sheared along these faults, and active tectonics appears to have a strong influence on sediment dispersal. Another fault is found to

strike north-south, and to increase its surface expression where it approaches the trough-terrace boundary.

The discrepancy between the strike of the Queen Charlotte Fault and the relative plate motion vector decreases from  $26^\circ$ , west of the Queen Charlotte Islands, to  $13^\circ$ , off Dixon Entrance, and suggests that the predominant mode of plate interaction is right-lateral strike-slip. A key to understanding the complex structures and orientations observed off Dixon Entrance is to comprehend their formation and alteration during migration from south to north.

The first main part of this thesis gives an overview of the geology and plate tectonic setting of the Queen Charlotte fault system (chapter 2). Chapter 3 introduces the ACCRETE data acquisition and chapter 4 is mainly concerned with the processing of seismic lines 1250, 1262, 1264, and 1265. In the second part of this thesis, the focus turns toward geologic interpretation of the data. Chapter 5 presents a stratigraphic and structural interpretation of all ACCRETE profiles as well as of a set of additional seismic reflection data, which were collected on the R/V S.P. Lee in 1977 (Rohr et al., 1992). Chapter 6 uses the ship track gravity data and forward gravity modeling to constrain possible tectonic models. A discussion of the favored tectonic model and a summary of results conclude the work in chapter 7.

## **2. GEOLOGIC AND TECTONIC SETTING**

The Queen Charlotte Fault (QCF) offshore British Columbia and Alaska, accommodates the right-lateral strike-slip transform boundary between the Pacific and North American plates. A transform fault is a strike-slip fault along which two plates move past each other without lithosphere being formed or destroyed, and typically connects offset mid-ocean ridges or subduction zones.

### **2.1 LOCATION**

The Queen Charlotte Fault System links the Cascadia Subduction Zone and Juan de Fuca Ridge offshore Vancouver Island with the Aleutian Trench south of Alaska (Figure 2.1, Riddihough and Hyndman, 1991). The location of the Queen Charlotte Fault was deduced from GLORIA sidescan data (reference), which highlight a very linear feature parallel to the shelf break (figure 2.2). In the following text, characteristics of plate motion, crustal structure, seismicity and gravity patterns, as well as two tectonic models and a brief tectonic history for this region will be introduced to provide a better understanding of the overall tectonic setting.

### **2.2 TECTONIC HISTORY AND PLATE MOTION**

Stock and Molnar (1988) proposed that at more than 90 Ma ago a triple junction of spreading centers between the Kula, Farallon and Pacific plates was located in the deep northeastern Pacific ocean. At that time, the Kula-Farallon boundary could have intersected the west coast of North America at any point from Vancouver to Mexico. It is, therefore, uncertain as to which of these plates was subducting beneath western North America at this time. It can be assumed that part of the American

continent, producing the reversed sense of magnetic anomalies decreasing in age toward the Pacific/North America plate boundary (figure 2.3).

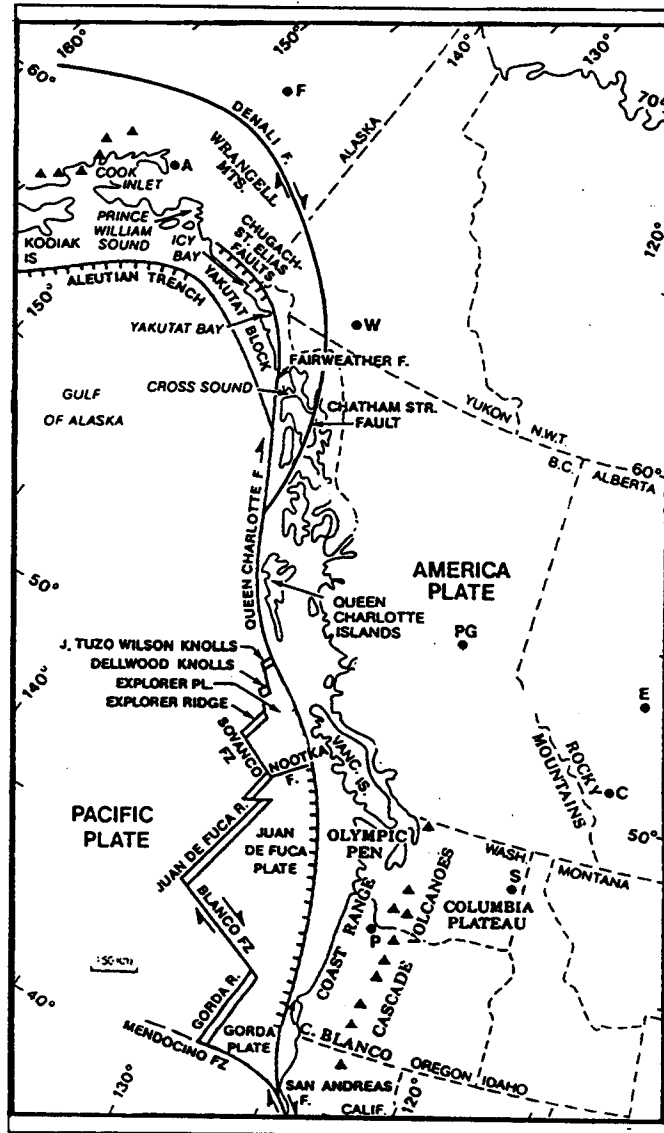


Figure 2.1 Location map (adapted from Riddiough and Hyndman, 1991) showing the modern plate tectonic regime of the northeast Pacific; A, Anchorage; F, Fairbanks; W, Whitehorse; PG, Prince George; V, Vancouver; P, Portland; S, Spokane; C, Calgary; E, Edmonton; triangles represent Miocene to Recent volcanic centers

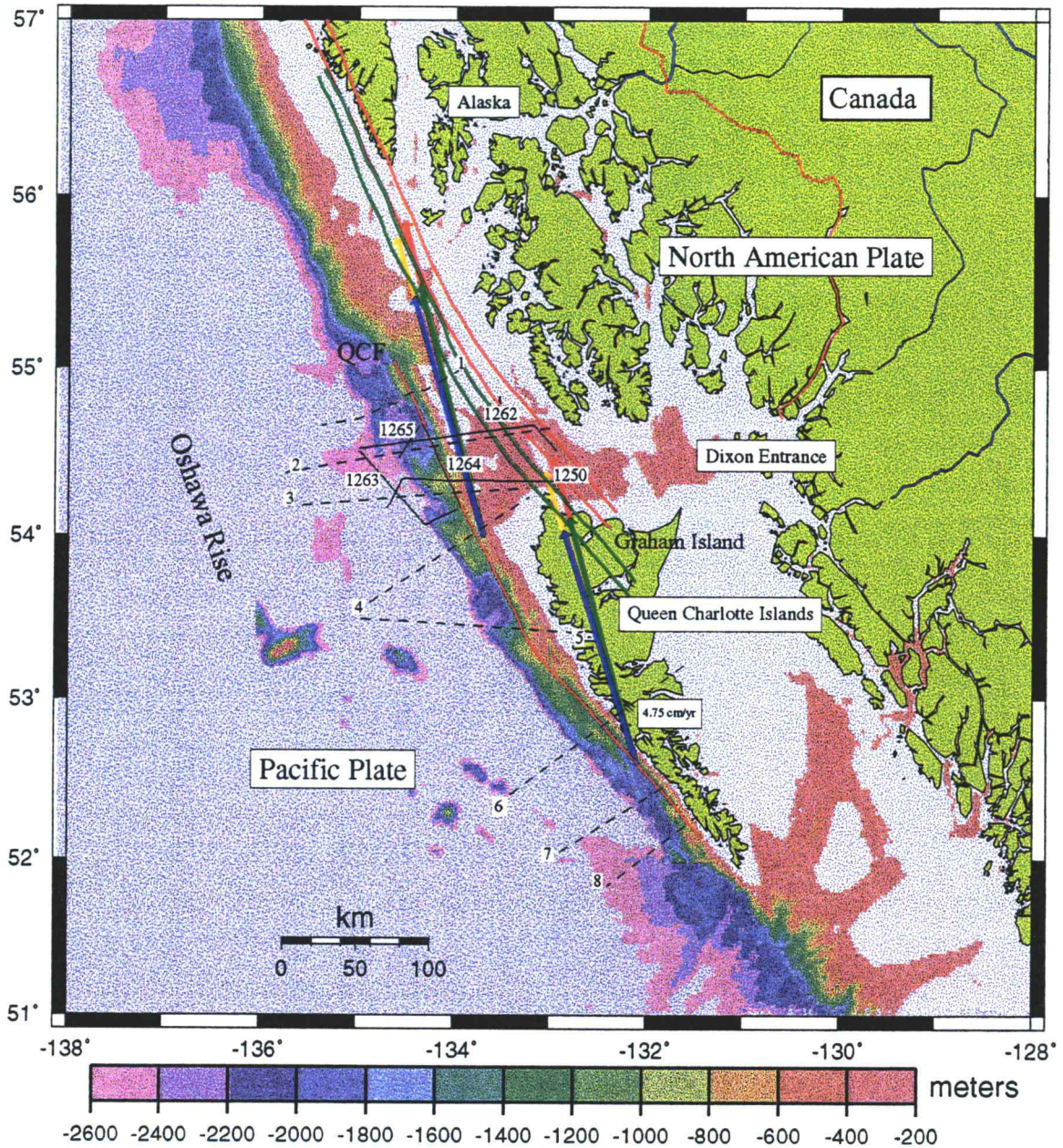


Figure 2.2 Bathymetry and location map of all reflection and refraction profiles mentioned in this work; profiles in solid are the ACCRETE lines; dashed lines, numbered from 1 to 8, refer to: (1) MCS line 951 from Bruns and Carlson (1987); (2)-(5) MCS lines SPLee 5,3,2,1 from Rohr et al. (1992); (6) refraction line from Dehler and Clowes (1988); (7) single channel seismic reflection profile from Davis and Seemann (1981); (8) refraction line from Horn et al. (1984); Queen Charlotte Fault (red); relative plate motion vector (table 2.1): red and yellow (maximum and minimum angle and distance after 5 Ma), green and blue (maximum and minimum angle and distance after 4 Ma); maximum possible extent of Pacific oceanic crust obliquely underthrusting beneath the western margin of the Queen Charlotte Islands within error limits (red: 5 Ma, green: 4 Ma)

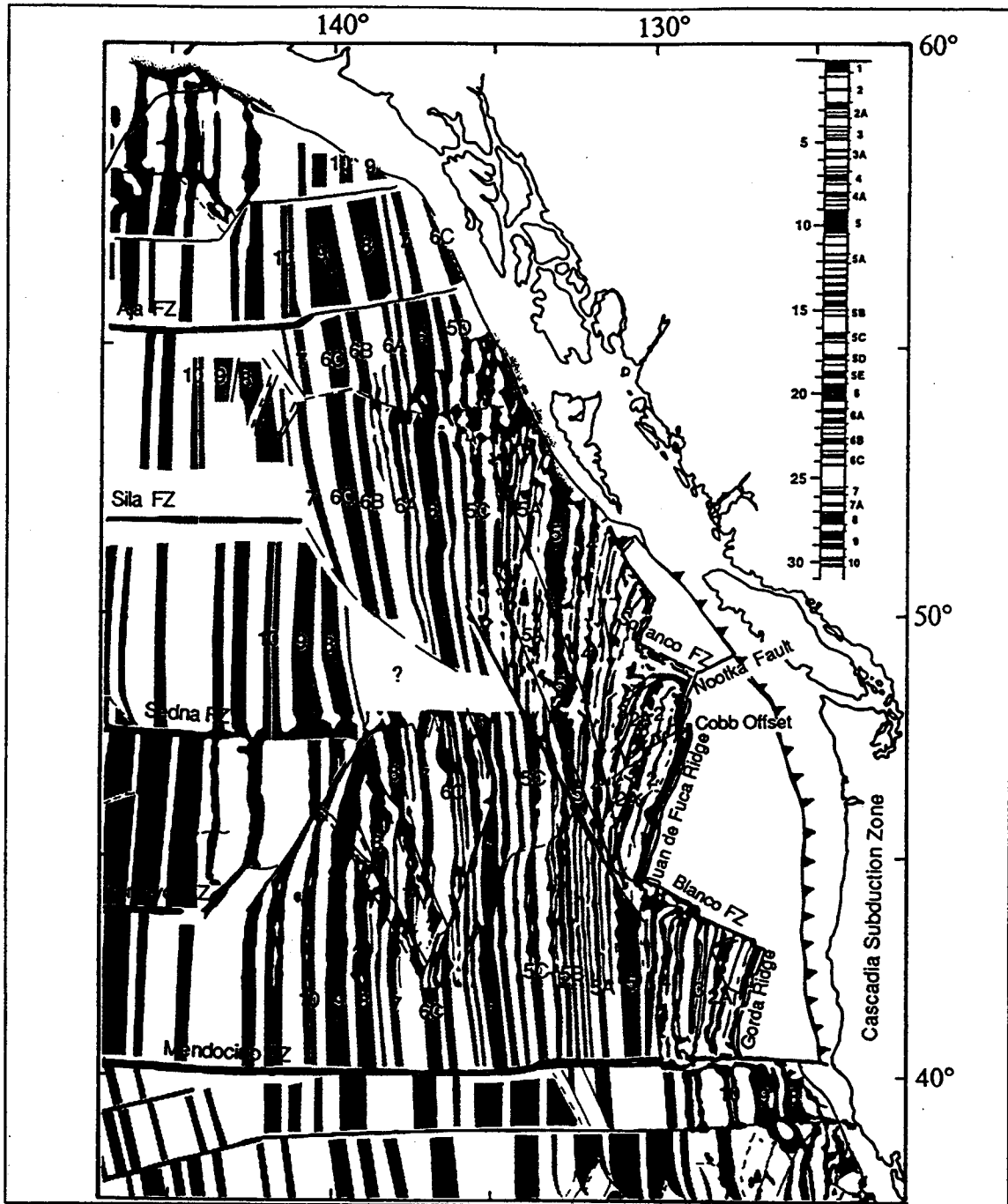


Figure 2.3 Present magnetic anomaly pattern formed by spreading between the Juan de Fuca and Pacific Plates (from Atwater, 1989)

Two major shifts took place in the Pacific-North America Tertiary plate tectonic record (Stock and Molnar, 1988; Norton, 1995). First, relative plate motions shifted from nearly orthogonal to right-lateral strike-slip at about 45 Ma (late Eocene), followed by small amounts of transpression and transtension. At approximately 5 Ma (early Pliocene) a transpressive regime was initiated and has since been the dominant mode of interaction, resulting in a component of convergence along the Queen Charlotte fault.

Close to the Queen Charlotte Islands, the discrepancy between the strike of the Queen Charlotte Fault ( $\approx 40^\circ$  west of north, figure 2.2) and the direction of relative motion between the Pacific and North American plates is found to be about  $26^\circ$  (table 2.1). Table 2.1 presents the directions and velocities of plate motion of the Pacific plate relative to North America, as well as the resulting discrepancies with the strike of the QCF at various locations along it. These values were calculated using the NUVEL-1 Euler vector (from DeMets, 1990; table 1), and the best-fitting Euler vector (from DeMets, 1990, table 4) to demonstrate the effect of small uncertainties in the location of the pole.

A different setting is encountered north of the Queen Charlotte Islands and opposite Dixon Entrance. There, the Queen Charlotte Fault system curves eastward to approach the direction of relative plate motion. The fault is thus divided into two segments, each representative of different average velocities and obliquity of the plate motion vector with the plate boundary. Average velocities are found to be about 4.8 and 4.7 cm/yr west of the Queen Charlotte Islands and off Dixon Entrance, respectively.

### **2.3 STRUCTURE WEST OF THE QUEEN CHARLOTTE ISLANDS**

Three structurally different domains can be distinguished here: (1) the Queen Charlotte Islands, (2) the Queen Charlotte Terrace, and (3) the Queen Charlotte Trough. The

Table 2.1 This table shows the **azimuth (column III)** and **velocity (column IV)** of relative plate motion of the Pacific plate relative to the North American plate at 15 locations (**latitude (column I) and longitude (column II)**) along the QCF, as well as **the difference in orientation between plate motion vector and trend of the fault (column V)**. The NUVEL-1 Euler vector (**N**) (48.709°N and 78.167°W from DeMets, 1990, table 1) and the best-fitting Euler vector (**B**) (49.6°N and 76.7°W from DeMets, 1990, table 4) were used for calculation. **Column VI and VII** present the average total lengths of the plate motion vector for a time span of **4 and 5 Ma** respectively, while **columns VIII and IX** contain the vector's average parallel and perpendicular components with the plate boundary for both times. The table is split into two portions, one for the fault segment off Dixon Entrance (north) and one for the region west of the Queen Charlotte Islands (south in gray). For each of the two portions average values (av.) of each column were found and used in subsequent discussion.

I	II	III	IV in cm/yr	V	VI in km	VII in km	VIII in km	IX in km
55.011	-134.6086	346.5	4.91	15.0	196.4	245.5		
54.804	-134.4010	346.3	4.90	14.8	196.0	245.0		
54.611	-134.2591	346.1	4.90	14.6	196.0	245.0		
54.403	-134.0878	345.9	4.89	14.4	195.6	244.5		
<b>N</b> 54.197	-133.9046	345.7	4.89	14.2	195.6	244.5		
54.007	-133.7290	345.6	4.88	14.1	195.2	244.0		
53.808	-133.5581	345.4	4.87	13.9	194.8	243.5		
53.598	-133.3732	345.2	4.87	13.7	194.8	243.5		
53.403	-133.2090	345.0	4.86	13.5	194.4	243.0		
53.195	-133.0102	344.8	4.85	13.3	194.0	242.5		
av.		345.65 ± 0.53	4.88 ± 0.02	14.15 ± 0.53	195.28 ± 0.73	244.1 ± 0.92	4 Ma: 189.36 5 Ma: 236.69	4 Ma: 47.74 5 Ma: 59.67
55.011	-134.5616	344.3	4.69	12.8	187.6	234.5		
54.804	-134.4010	344.1	4.69	12.6	187.6	234.5		
54.611	-134.2591	343.9	4.68	12.4	187.2	234.0		
54.403	-134.0878	343.7	4.68	12.2	187.2	234.0		
<b>B</b> 54.197	-133.9046	343.6	4.67	12.1	186.8	233.5		
54.007	-133.7290	343.4	4.67	11.9	186.8	233.5		
53.808	-133.5581	343.2	4.66	11.7	186.4	233.0		
53.598	-133.3732	343.0	4.66	11.5	186.4	233.0		
53.403	-133.2090	342.8	4.65	11.3	186.0	232.5		
53.195	-133.0102	342.7	4.65	11.2	186.0	232.5		
av.		343.47 ± 0.52	4.67 ± 0.01	11.97 ± 0.52	186.8 ± 0.57	233.5 ± 0.71	4 Ma: 182.74 5 Ma: 228.42	4 Ma: 38.74 5 Ma: 48.43
av.		344.56 ± 1.09	4.78 ± 0.11	13.06 ± 1.09	191.04 ± 4.24	238.8 ± 5.3	186.05 ± 3.31 232.56 ± 4.14	43.24 ± 4.5 54.05 ± 5.62

Table 2.1 (continued)

	52.981	-132.6625	344.7	4.83	27.1	193.2	241.5		
<b>N</b>	52.808	-132.4079	344.6	4.82	27.0	192.8	241.0		
	52.624	-132.1126	344.5	4.81	26.9	192.4	240.5		
	52.384	-131.7549	344.4	4.79	26.8	191.6	239.5		
	52.198	-131.5040	344.2	4.78	26.6	191.2	239.0		
<b>av.</b>			344.48	4.81	26.88	192.24	240.3	4 Ma:	4 Ma:
			$\pm 0.17$	$\pm 0.02$	$\pm 0.17$	$\pm 0.74$	$\pm 0.93$	171.47	86.92
								5 Ma:	5 Ma:
								214.34	108.65
	52.981	-132.6625	343.5	4.63	25.0	185.2	231.5		
	52.808	-132.4079	342.4	4.62	24.8	184.8	231.0		
<b>B</b>	52.624	-132.1126	342.3	4.61	24.7	184.4	230.5		
	52.384	-131.7549	342.2	4.59	24.6	183.6	229.5		
	52.198	-131.5040	342.0	4.58	24.4	183.2	229.0		
<b>av.</b>			343.2	4.61	24.7	184.24	230.3	4 Ma:	4 Ma:
			$\pm 0.17$	$\pm 0.02$	$\pm 0.2$	$\pm 0.74$	$\pm 0.93$	167.38	76.98
								5 Ma:	5 Ma:
								209.23	96.23
<b>av.</b>			343.84	4.71	25.79	188.24	235.3	169.43	81.96
			$\pm 0.64$	$\pm 0.1$	$\pm 1.09$	$\pm 4.0$	$\pm 5.0$	$\pm 2.05$	$\pm 4.97$
								211.79	102.44
								$\pm 2.56$	$\pm 6.21$

continental shelf is very narrow, and the terrace, 30 km wide and 1500 m deep, is bounded by two scarps (figure 2.4). The outer scarp of the terrace steps down to the 2500 to 3000 m deep Queen Charlotte Trough. Gravity contours (figure 2.5) are aligned roughly parallel to the QCF, and the terrace has a block-like appearance in bathymetry data (figure 2.6) with the outer scarp forming its rather linear western boundary (figure 2.4).

Magnetic anomalies of the Pacific Ocean floor (figure 2.3) terminate at this outer scarp, suggesting a structurally independent domain (Currie et al., 1983). The age of the oceanic crust along the outer scarp increases from 7 Ma at the southern end of the Queen Charlotte Islands to 15 Ma off northern Dixon Entrance (Riddihough and Hyndman, 1991).

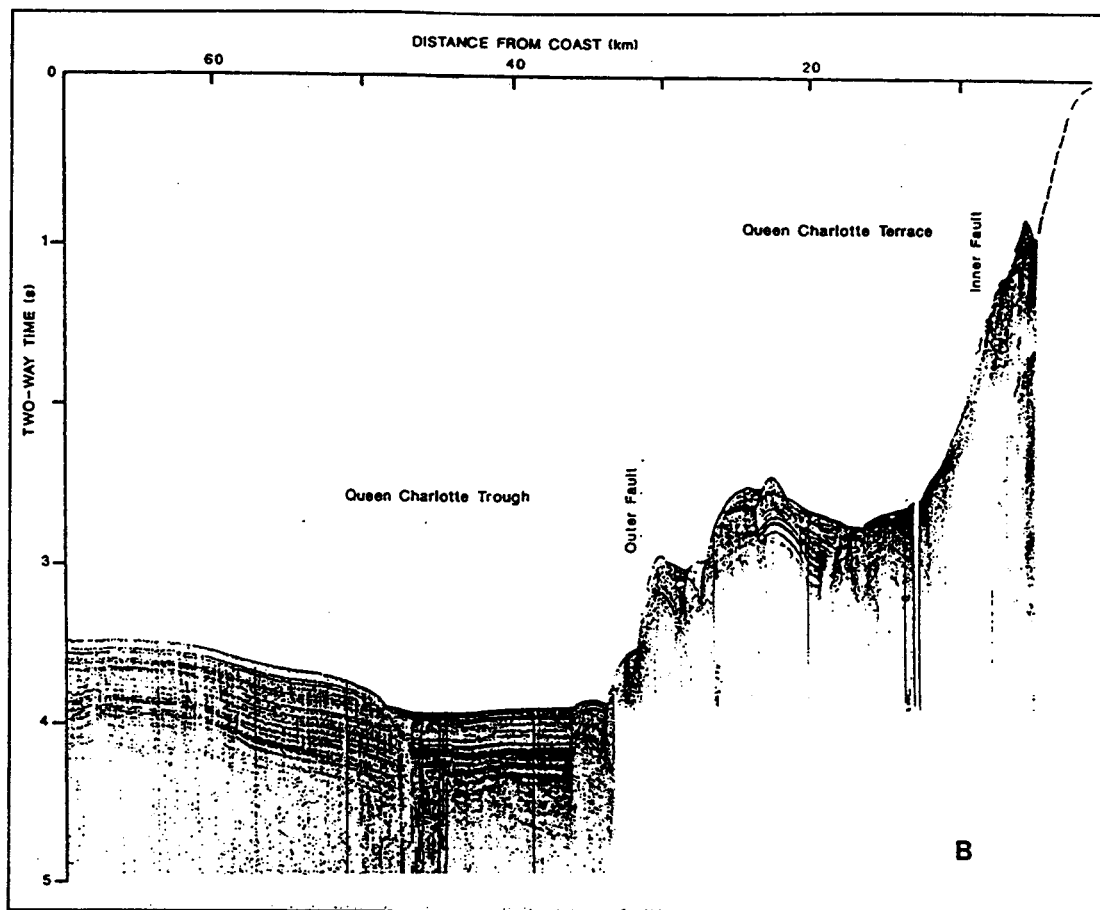


Figure 2.4 A sample seismic reflection profile from Davis and Seemann (1981) across the trough and terrace; location of profile is shown in Figure 2.2

#### 2.4 STRUCTURE OFF DIXON ENTRANCE

The main focus of this study is the region between  $54^{\circ}\text{N}$  and  $55^{\circ}\text{N}$ , off Dixon Entrance and just north of the Queen Charlotte Islands (figure 2.2). The linear pattern of the terrace west of the Queen Charlotte Islands seems to abruptly stop at  $53.4^{\circ}\text{N}$ , where the QCF bends to a more easterly trend. The Queen Charlotte Terrace becomes wider (45 km) and less linear, and a repetitive pattern of triangular shaped bathymetry (figure 2.6) and gravity highs (figure 2.5) result in a jagged western terrace boundary. Also visible in the gravity data is a more pronounced low and a much steeper gradient

## Gravity

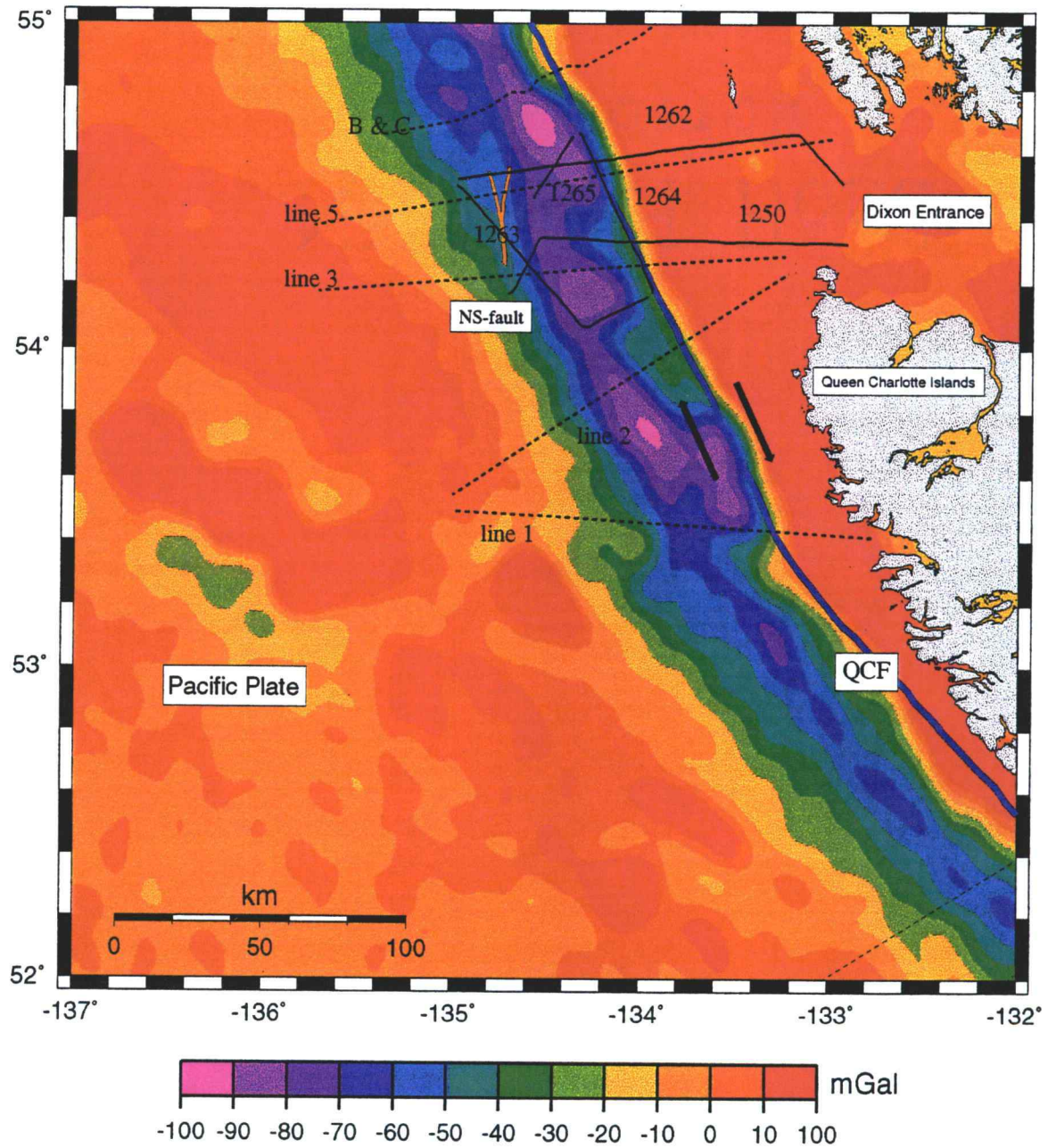


Figure 2.5 Free-air gravity anomaly in mGal, showing a more pronounced gravity low off Dixon Entrance than west of the Queen Charlotte Islands; superimposed are the locations of the Queen Charlotte Fault and of the N-S fault to demonstrate their influence on the regional gravity field, as described in later chapters

## Bathymetry

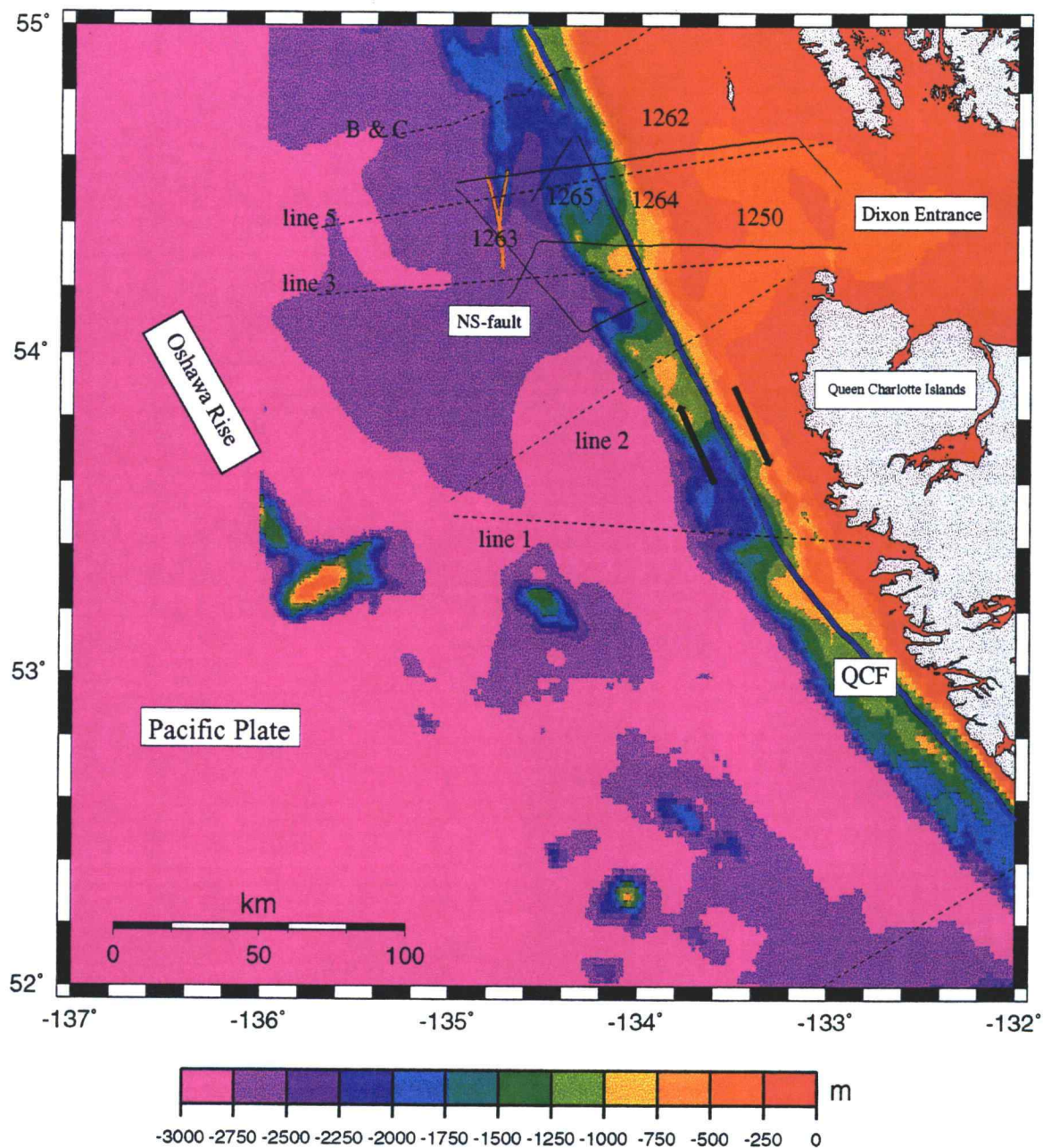


Figure 2.6 Bathymetry (in meters) of the study region, surrounding the Queen Charlotte Fault (black line); showing the well-resolved terrace segment with its triangular-shaped structure off Dixon Entrance and its more linear, block-like appearance west of the Queen Charlotte Islands

off Dixon Entrance relative to the south. This is an indicator of the much larger sedimentation rates in this area. The 5 km thick sediment layer at the foot of the terrace (this study) produces a stronger gravity low than the 1 km of sediments west of the Queen Charlotte Islands (figure 2.7) (Horn et al., 1984; Dehler and Clowes, 1988).

## 2.5 STRUCTURE NORTH OF DIXON ENTRANCE

Bruns and Carlson's (1987) single-channel and multichannel seismic-reflection data provide an image of the sedimentary basins and structure of the Fairweather-Queen Charlotte Fault zone farther north, between Dixon Entrance and the onshore Fairweather fault near Cross Sound (Figure 2.8, Bruns and Carlson, 1987). From Dixon Entrance to Chatham Strait, the sections show markedly deformed strata in two structural zones. In the outer structural zone (OSZ), folds and faults affect even the shallowest sedimentary strata. The inner structural zone (ISZ), in contrast, has in places a cover of as much as 0.5 km of undeformed strata (Bruns and Carlson, 1987). This indicates that structures of the ISZ are older than those of the OSZ.

## 2.6 SEISMICITY

The Queen Charlotte Fault system has been the site of numerous large earthquakes. Canada's largest earthquake in 1949 ( $M_s = 8.1$ ) (figure 2.9), northwest of Graham Island and about 100 km south of the ACCRETE profiles, showed mainly strike-slip motion with a very small component of thrust (Bérubé, 1989). Nishenko and Jacob (1990) found a rupture length of about 500 km (300 km north and 190 km south of the epicenter) with an average coseismic displacement of 4-7.5 meters. Since the azimuth of the fault-plane corresponds well with the strike of the Queen Charlotte Fault, the component of convergence (table 2.1) must not have been taken up by this event. In

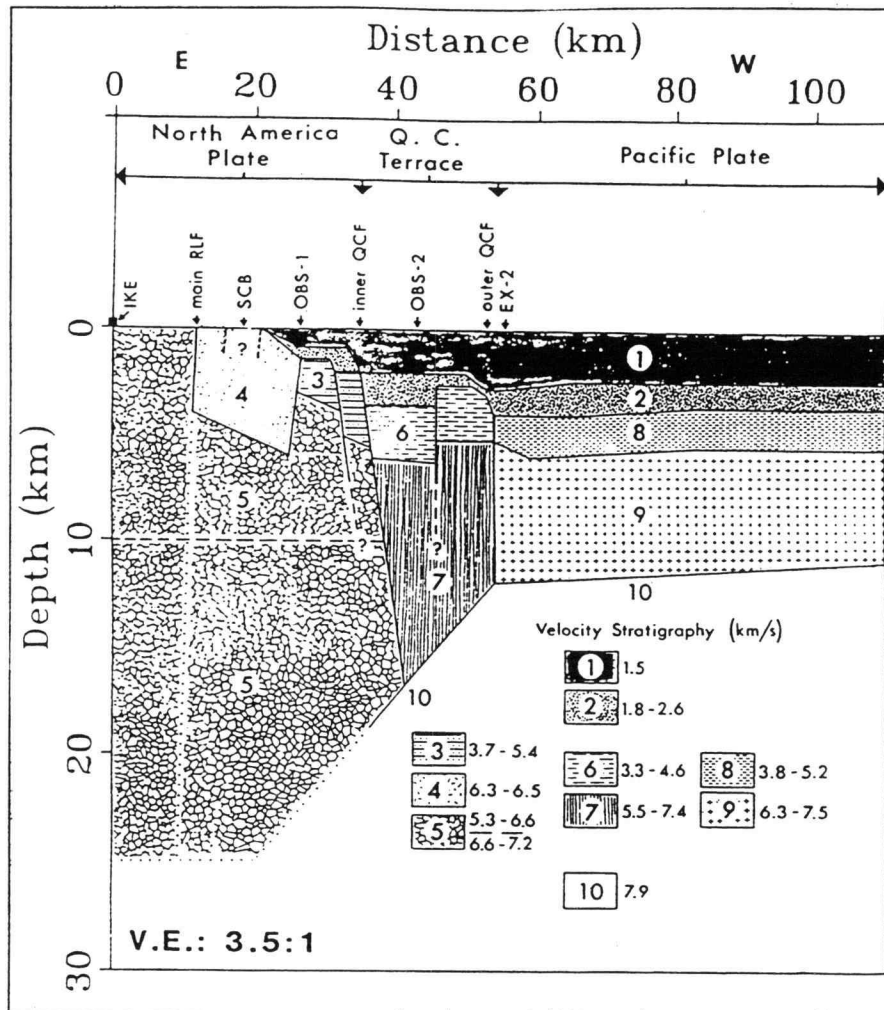


Figure 2.7 Generalized interpretation of the refraction work done by Horn et al. (1984), using seismic data recorded at OBS2, OBS1, and IKE from explosive charges detonated between 23 and 110 km distance; the first number in the velocity stratigraphy gives the velocity at the top of the unit, and the second number gives the velocity at the bottom of the same unit, a linear gradient being assumed. RLF, Louscoone Inlet fault; SCB, San Cristoval batholith; QCF, Queen Charlotte fault

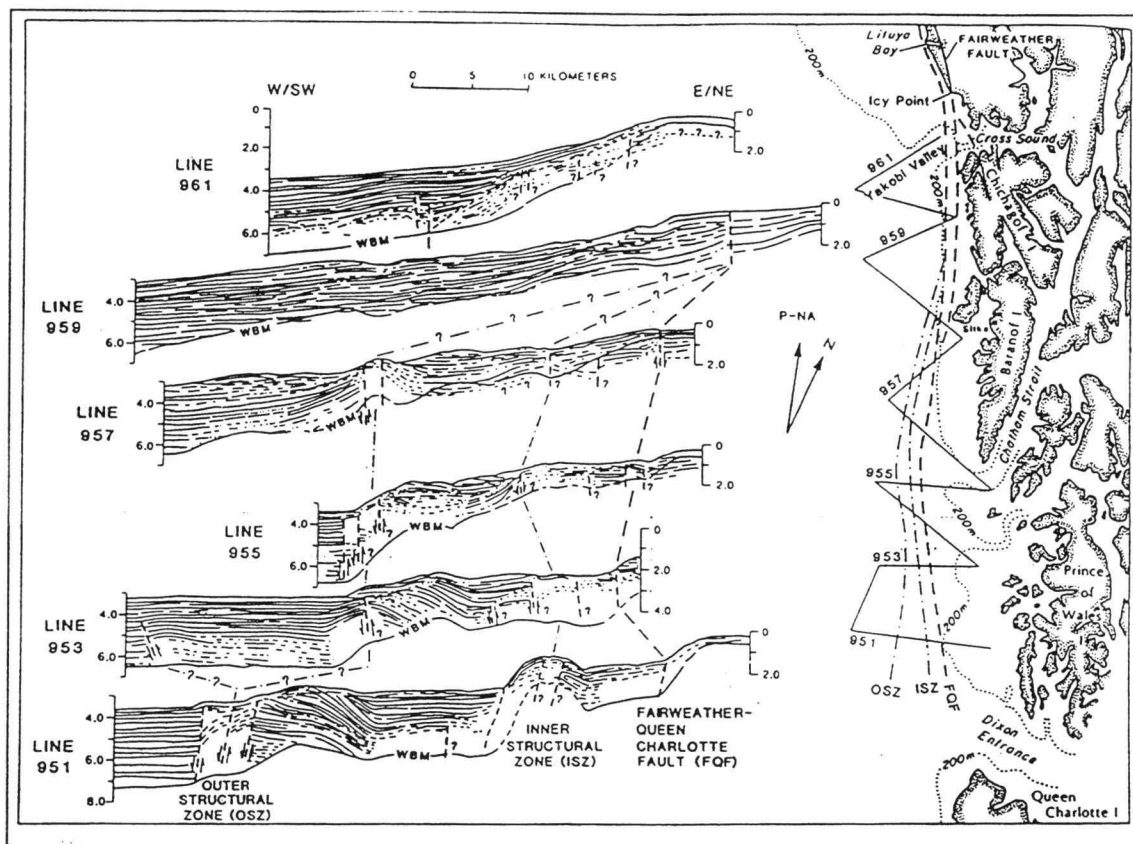


Figure 2.8 Simplified line drawings of multichannel seismic-reflection profiles across the southeast Alaska continental margin from Bruns and Carlson (1987), showing locations of principle structural trends; trends shown are the Fairweather-Queen Charlotte fault trace (FQF), and outer structural zone (OSZ), and an inner structural zone (ISZ); vertical scale on seismic-reflection lines is two-way time in seconds; WBM = water-bottom multiple; Pacific-North America (PNA) relative convergence direction (arrow) from Minter and Jordan (1978)

addition, microseismicity studies by Hyndman and Ellis (1981) propose that the main active Queen Charlotte Fault zone is nearly vertical and located under the landward edge of the terrace. Earthquakes are thought to predominantly occur as strike-slip between 9 and 21 km depth (with an accuracy of  $\pm 3$  km; Hyndman and Ellis, 1981; Bérubé, 1989), suggesting that the conditions required for seismic instability or brittle fracture must exist at least to this observed maximum depth. Composite fault plane

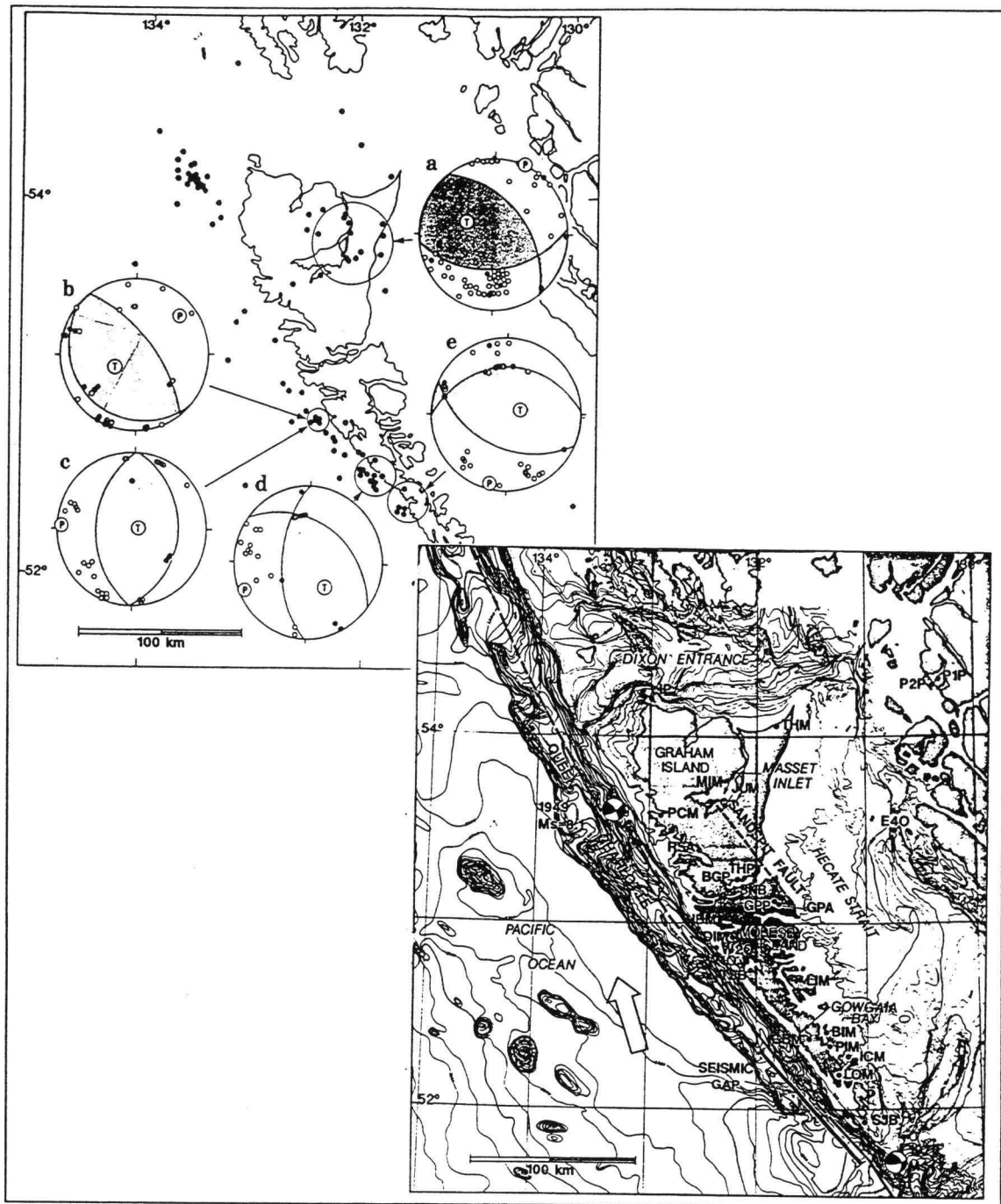


Figure 2.9 The Queen Charlotte Islands region showing bathymetry in meters, faults, locations, focal mechanisms of the two largest historical earthquakes, and equal-area, lower focal-hemisphere composite focal-mechanism solutions for five groupings of microearthquakes after Bérubé et al. (1989); solid circles indicate compressions, open circles, dilatations; P = pressure axis, T = tension axis (modified form Bérubé et al., 1989)

solutions west of Moresby Island presented in the more recent microseismicity analysis of Bérubé et al. (1989) (figure 2.9), however, have thrust mechanisms. Their northeast-southwest direction of near-horizontal maximum compressive stress could correspond to a contemporary regional stress field caused by right-lateral shear, which could be distributed over a currently locked Queen Charlotte Fault. Due to the significant difference between the apparent orientation of maximum compressive stress and the Pacific and North American plate motion vector, the thrusting can not simply be explained by a component of plate motion convergence. The 1970 ( $M_s = 7.4$ ) earthquake at the southern tip of Moresby Island (figure 2.9) has a mechanism of combined strike-slip and thrust motion, but with a larger thrust component than observed in the 1949 event (Bérubé et al., 1989). The horizontal motion is consistent with the theoretical plate-motion vector, which is an indicator of oblique convergence between the two plates in this region.

## 2.7 GRAVITY

Figure 2.5 shows the regional free-air gravity anomaly of the relevant area. The large gravity low over the terrace segment parallels the Queen Charlotte Fault, and the positive anomaly landward of the shelf break is very striking. Further west, where water depth decreases over the Oshawa rise (figure 2.2), gravity values reach the same level (about 50 mGal) measured at the edge of the continent. The Oshawa Rise is a 100 km wide gentle rise, which separates the trough from the deeper Pacific floor to the west, and which appears to be the southeast continuation of the Kodiak-Bowie Seamount Chain (Chase et al., 1975).

The positive/negative anomaly pair across the Queen Charlotte Fault resembles the edge effect typically found at continental margins. The edge effect results from the combined and opposite effects of abrupt changes in water depth and crustal thicknesses. If the lithosphere is in isostatic equilibrium, the edge-effect is confined to the vicinity of the plate boundary, with a maximum amplitude over the continent and a

minimum over the ocean, as the contributions due to the shallow and deep density contrasts have different gradients in their gravity signatures. By looking at figure 2.5 and assuming the location of the gravity high and low to be a result of the ocean-continent transition, the plate boundary is indeed expected (0 mGal-crossing) to be close to the shelf break and the Queen Charlotte Fault, where seismicity places the plate boundary. But instead of leveling out to zero fairly close to the boundary as would be expected for passive continental margins, anomalously high gravity values are seen east of the shelf break as well as to the west, over the Oshawa rise. The continental crust beneath the Queen Charlotte Islands was by no means found to be of normal (33 km) thickness, but remarkably thin and dipping eastward from 21-28 km (Spence and Asudeh, 1993). Thin continental crust is consistent with the observed gravity high above the Queen Charlotte Islands and further north. In addition, the islands are underlain by thick, dense mafic volcanics of the Karmutsen formation, and might have undergone tremendous uplift (up to 5 km) over the past 5-6 Ma (Sutherland Brown, 1968), which would enhance a positive anomaly.

The gravity high above the Oshawa Rise could be an indication of underthrusting if the Rise is interpreted to be the bulge formed by flexural bending of the oceanic lithosphere. Upwarping of the crust will produce a positive gravity anomaly due to the denser crust and elevated mantle relative to surrounding areas. Analogously, the Queen Charlotte trough gives rise to a relative gravity low, as a result of the extra sea water, an abundance of low-density sediments and the downwarping of the crust/mantle interface. Independent of flexure caused by possible subduction, higher sediment deposition close to the base of the continental slope will produce an excess load that would bend the crust. The terrace is an area where all these features interfere with the tectonic signature of an active plate boundary, superimposed on a simple edge-effect; the following section summarizes previously proposed plate tectonic models.

## 2.8 PREVIOUS PLATE TECTONIC MODELS

Two end-member models (Mackie et al., 1989), both consistent with the transpressional regime of the past 5-6 Ma, have been suggested to explain the tectonics that produced the structure of the Queen Charlotte Fault zone. The first one accounts for the shortening west of the Queen Charlotte Islands by flexure and underthrusting of the oceanic lithosphere beneath the continent. In the second, compression results in upthrusting and considerable deformation of the oceanic crust in the terrace region (figure 2.10).

The models of Hyndman and Ellis (1981), Hyndman et al. (1982), Yorath and Hyndman (1983), Dehler and Clowes (1988), and Mackie et al. (1989) all propose shallow subduction of the oceanic lithosphere, which began suddenly about 6 Ma ago and resulted in its downward bending. In all models, transcurrent motion occurs on a near vertical fault zone on the Queen Charlotte Fault (as suggested by the seismicity down to 21 km depth), which breaks through the subducting slab and progressively jumps seaward, and stays fixed with respect to the upper plate. Dehler and Clowes (1988) have the processes of subduction and upthrusting of sedimentary and upper crustal material occurring concurrently: after transcurrent motion cuts through the lithosphere, compression is accommodated by upthrusting and might eventually resume again in subduction that pushes the old fault down. Flexural modeling by Prims et al. (1996) predicts 5 km of plate rebound in the terrace region after failure of the Pacific plate and implies subsidence of the western margin of the Queen Charlotte Islands as its elastic foundation is lost. No evidence is found for either of these events, but the question remains as to whether simple flexural modeling based only on loading and excluding compressive stresses is capable of predicting the complex effects of the above model.

Several observations support the model of active oblique subduction, shown in figure 2.10 a). In this model, the terrace complex would contain deformed sedimentary

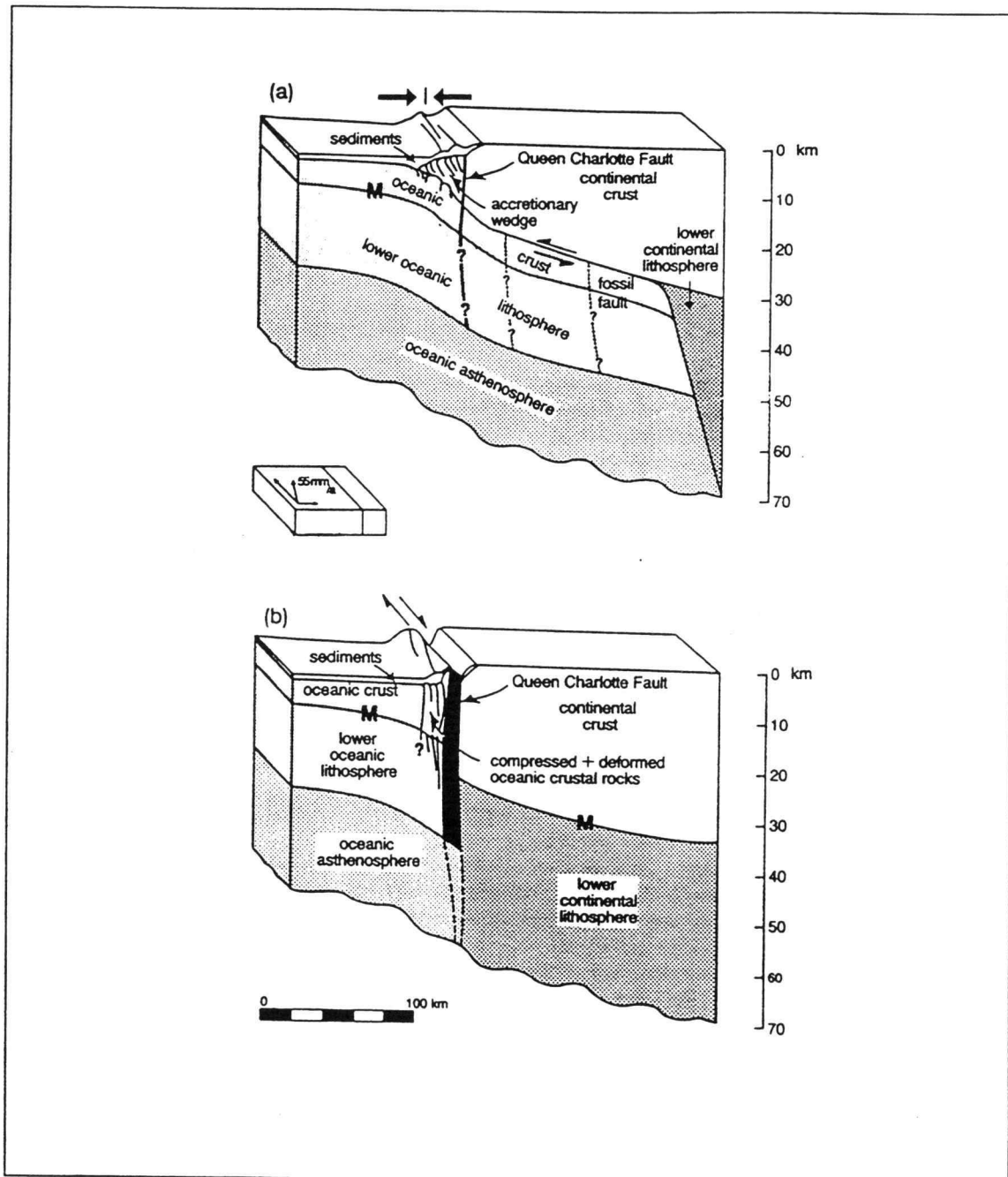


Figure 2.10 Two possible tectonic end-member models (a) oblique subduction of the Pacific plate beneath North America for the past 6 Ma and transform motion along the vertical Queen Charlotte Fault; fossil faults as suggested by Yorath and Hyndman (1983) result from the combination of strike-slip and convergent motion; (b) representation of a tectonic regime in which the Queen Charlotte Fault Zone is the boundary between oceanic and continental lithosphere and no oblique subduction has occurred; compression is taken up by pure upthrusting and deformation of the oceanic crust (from Mackie et al., 1989)

material that was scraped off from the subducting slab. Faults within the terrace should reflect underthrusting of sedimentary or upper oceanic crustal blocks, and should merge into a detachment fault that forms the suture between the two plates. Velocities within the terrace are anomalously low compared to those of normal oceanic crust (Dehler and Clowes, 1988) these were interpreted to correspond to extensively deformed and sheared gabbros and peridotites at depth, and deformed upper ocean crust basalts or compressed sediments in shallower areas (figure 2.11, Dehler and Clowes, 1988). Prims et al. (1997) suggest that the terrace is predominantly a sedimentary prism consisting of deformed marine sediments adjacent to the margin. Furthermore, Hyndman et al. (1982) found a systematic decrease in heat flow from west of the terrace to the Queen Charlotte Islands. While heat flow values in the trough are similar to values expected for oceanic crust of about 7 Ma, a sharp jump occurs to much lower, less scattered values over the terrace. Numerical modeling suggested that no reasonable steady state ocean-continent boundary would explain the observed heat flow pattern, and Hyndman et al (1982) proposed underthrusting beneath the Queen Charlotte Islands. A thick wedge of consolidated sediments, formed by underthrusting and compression, would tend to reduce temperatures and, therefore heat flow values measured at the surface of the terrace. The presence of the Queen Charlotte Trough and of a bathymetric high, the Oshawa Rise, some 100 km offshore also suggests flexural bending of an underthrust oceanic crust. This flexure would produce contemporary uplift of the overriding continental plate as indicated by Riddihough's (1982) study of sea-level and tidal records and geodetic levelling data in British Columbia (2 mm/yr), and is consistent with earlier uplift inferred from geologic mapping of the Queen Charlotte Islands (up to 5 km) by Sutherland Brown (1968). More recent work by Thompson and Thorkelson (1989), however, suggests that no preferred eastward dip of mapped structures exist. If underthrusting occurs, then a shallow angle would be more likely because of the relatively young and buoyant oceanic lithosphere (not older than 18 Ma). All previous refraction and gravity models

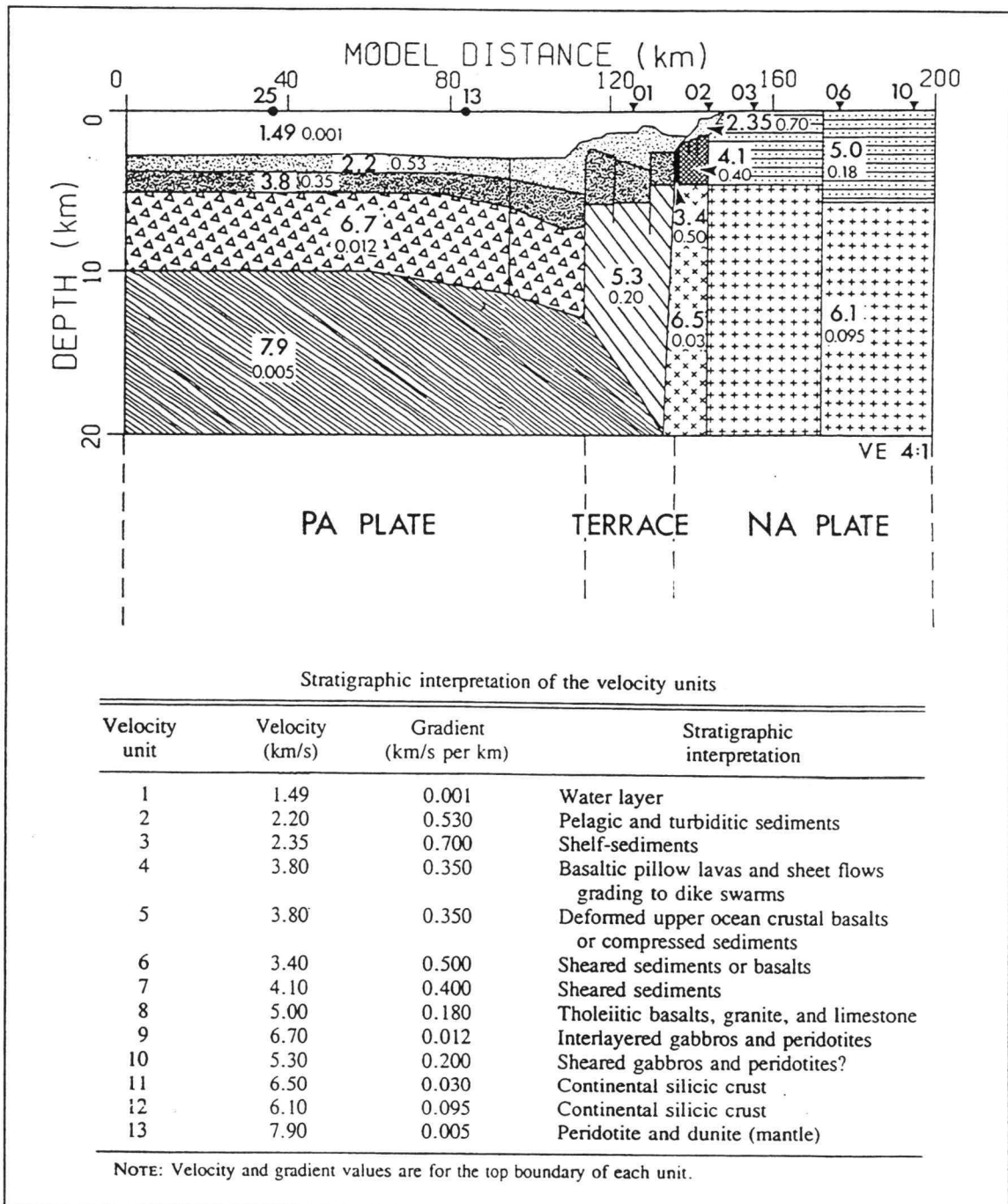


Figure 2.11 Final velocity model derived from airgun and explosion data modeling. Velocities are in kilometers per second; velocity gradients in kilometers per second follow in small print; below the interpretations of the velocity units (modified from Dehler and Clowes, 1988)

do not explicitly include underthrust oceanic crust, but a model including a subducted slab welded to the continent would still satisfy the gravity data. Horn et al. (1984) (figure 2.7), Spence and Asudeh (1993), Mackie et al. (1989), and Sweeney and Seemann (1991) suggest that the crust beneath the Queen Charlotte Islands is extremely thin (Moho dipping eastward from 21 to 28 km). Hence, continental crust at the plate boundary is not standard continental crust, and although a mountain range is present on the Queen Charlotte Islands, there is no root. Thickening through compression, as might be expected if stresses were transmitted across the fault and if no underthrusting were taking place, is not observed.

This is the second end-member model, which accommodates convergence only by thrusting up wedges of sedimentary rocks and oceanic basement along the transform margin (figure 2.10 b), juxtaposing continental against oceanic lithosphere across a narrow zone.

The existence of almost pure strike-slip events in spite of a component of convergence along the Queen Charlotte fault zone might suggest strain partitioning in a manner as was first proposed by Fitch (1972) for the Java trench of western Sunda as subsequently applied by Abers and McCaffrey (1988) and others, and as used as a basis for model (a) in figure 2.10. Figure 2.12 demonstrates a simplified block diagram of decoupled slip along a vertical strike-slip fault and an inclined detachment fault. The terrace block would be separated by these two faults and move parallel to the North American plate and perpendicular to the Pacific plate. Strike-slip mechanisms should be found on the vertical Queen Charlotte Fault, while thrust faulting is expected to occur on both sides of the inclined detachment fault between the terrace and oceanic crust to the west, and oceanic and continental crust to the east. Unfortunately, the current record of earthquakes (Bérubé et al., 1989, Hyndman and Ellis, 1981) does not reveal such Benioff-Wadati-type alignment of events, and continuing studies and location of earthquakes in this region is necessary. Besides, it is possible that the lack of subduction related seismicity is real, and that the slab descends aseismically or that the subduction zone is locked at present.

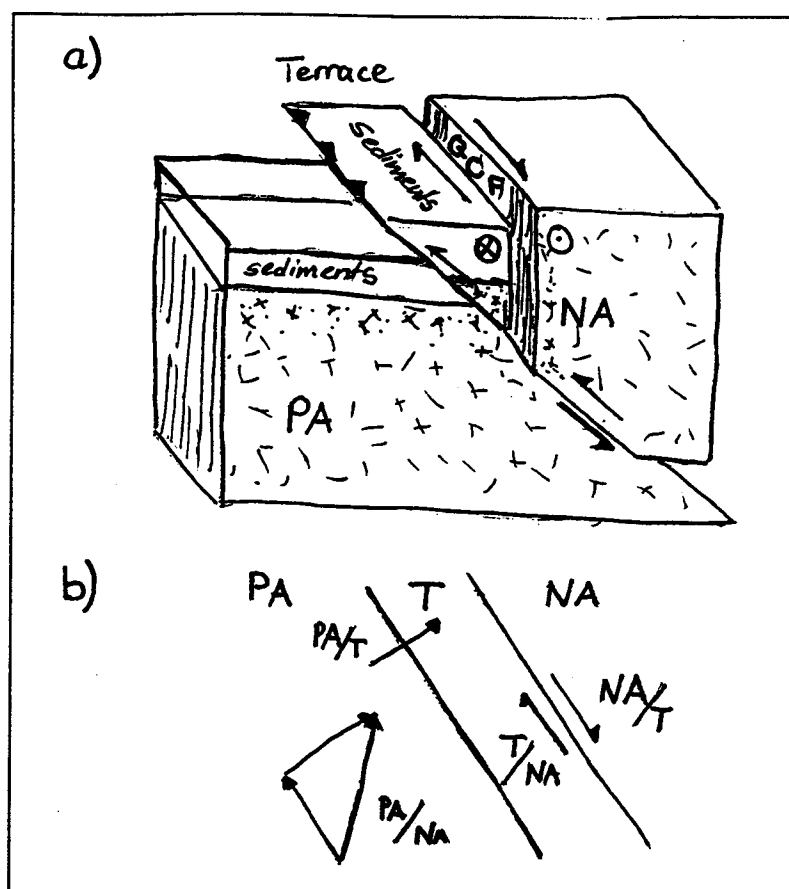


Figure 2.12. Block diagram showing how strike-slip and thrust faulting might be related at the Queen Charlotte Transform Fault region; the terrace block moves parallel relative to the North American plate and perpendicular relative to the Pacific plate; a) cross-section, NA = North American plate, PA = Pacific plate, T = terrace block consisting of off-scraped sediments and possibly fractures of upper oceanic crust, QCF = Queen Charlotte Fault; b) plan view with direction of relative plate motion, a/b = motion of plate or block 'a' relative to motion of plate or block 'b'

It is clearly difficult to produce a model that explains the tectonics of the whole Queen Charlotte fault zone based on data available prior to ACCRETE. In addition, data were almost exclusively collected west of the Queen Charlotte Islands, and few constraints exist in the region off Dixon Entrance. Seismicity data are the most essential tool for distinguishing between basic characteristics of the two end-member models, but they are sparse. Hyndman and Ellis (1981) determined location and magnitudes of eleven events, but deduced a strike-slip mechanism only from their position close to the

rupture zone of the main 1949 strike-slip event. Bérubé et al. (1989) located 84 earthquakes in the vicinity of the Queen Charlotte Fault (figure 2.9). However, only composite fault plane solutions were obtained for three sites along the fault west of Moresby Island, which indicate thrust mechanisms with a predominant NE-SW pressure axis orientation. Whether these few data are representative of the true seismicity pattern and provide a relative basis for a tectonic model remains questionable.

Could the Queen Charlotte Terrace off Dixon Entrance be formed by continuously compressed sediments off-scraped from the Pacific plate and transported to the north along the margin creating the en-echelon-type structures? This question will be addressed through interpretation of the new multichannel reflection and gravity data.

### **3. ACQUISITION**

This chapter describes the acquisition of 300 km of multichannel seismic reflection and gravity data along and across the Queen Charlotte fault system.

#### **3.1 THE SEISMIC DATA**

"The EW9412-cruise was the marine component of the "pilot" phase of ACCRETE, a highly integrated geophysical and geological study of continental accretion via processes of terrane docking" (Diebold, 1994). This work was done between 12 September and 22 September 1994 on the R/V EWING. The survey acquired gravity, magnetic and bathymetry profiles, shot and recorded multichannel seismic (MCS) data and provided the acoustic seismic source for an array of some seventy portable seismometers installed on land. It covered areas of the Queen Charlotte Fault, Dixon Entrance, Portland Inlet, Portland Canal and Clarence Strait (Figure 3.1, from Diebold, 1994). This thesis, however, is concerned exclusively with the Queen Charlotte Fault and the Dixon Entrance region, comprising MCS-lines 1250, 1262, 1263, 1264, and 1265 (Figure 2.2).

The marine component of the ACCRETE project was allowed 10 days of ship time. Line 1250 was the first line shot after deploying the streamer in deep water west of the Queen Charlotte Fault. After completing lines 1251 through 1261 in the Portland Canal and Clarence Strait, the EWING returned to record lines 1262-1265 to investigate the offshore transpressional zone of the Queen Charlotte Fault system west of Dixon Entrance.

A 20-airgun array with total volume of 8400 cu. in. served as a source. The gun towing configuration is shown in Figure 3.2. The lines were shot at a 20-second repetition rate to provide acquisition of common depth point (CDP) reflection data. A Digicon DMS-2000 seismic acquisition system was used for recording. Figure 3.3

shows the streamer configuration of 224-channels, a 12.5 m - group spacing and 2800 m active offset. A total trace length of 16.5 seconds was recorded.

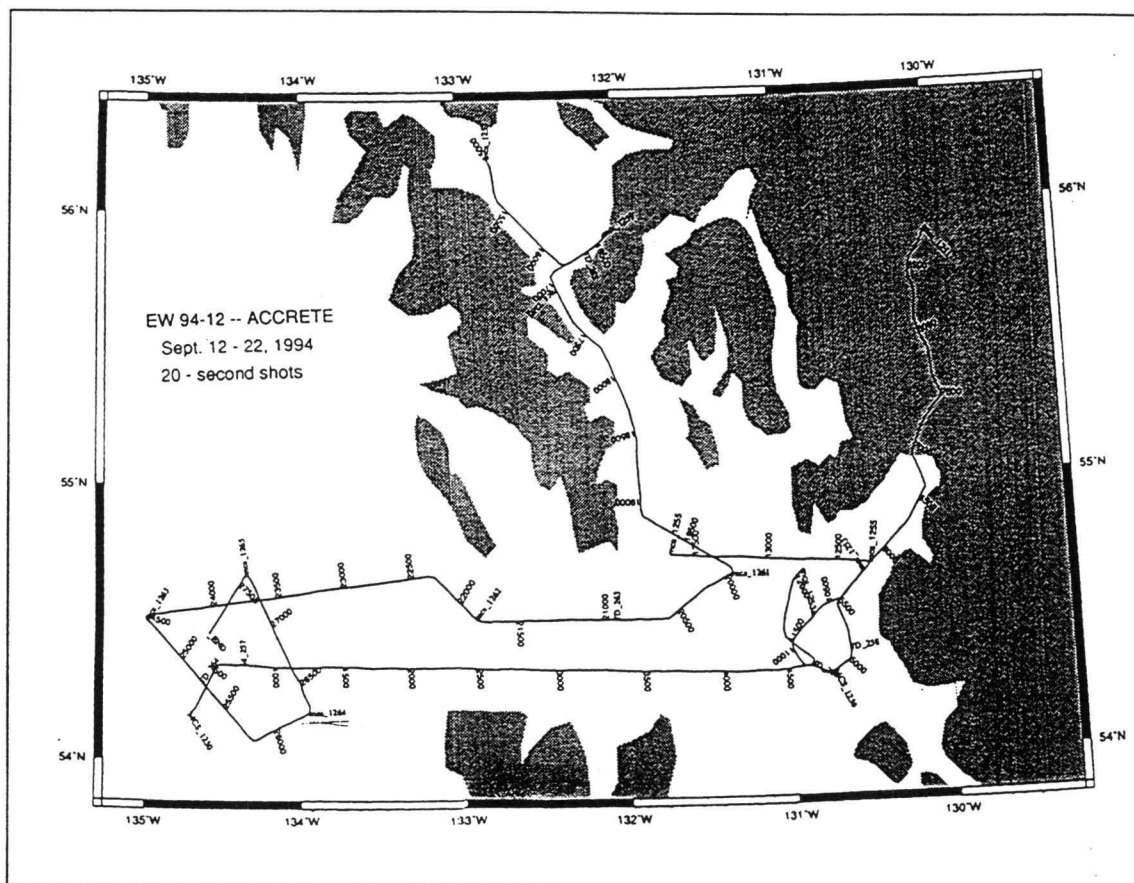


Figure 3.1 Location map of the EW9412 -- "ACCRETE" ship cruise, including tracks of MCS-lines 1250 through 1265 from Diebold (1994)

All lines were shot by time, rather than by distance, for several reasons (Diebold, 1994): (1) similarity of the source from shot to shot is best maintained with a regular shot time interval whereas distance shooting inevitably results in some shots being fired with partial air pressure, (2) maximum possible record length, and (3) accurate real-time navigation could be obtained.

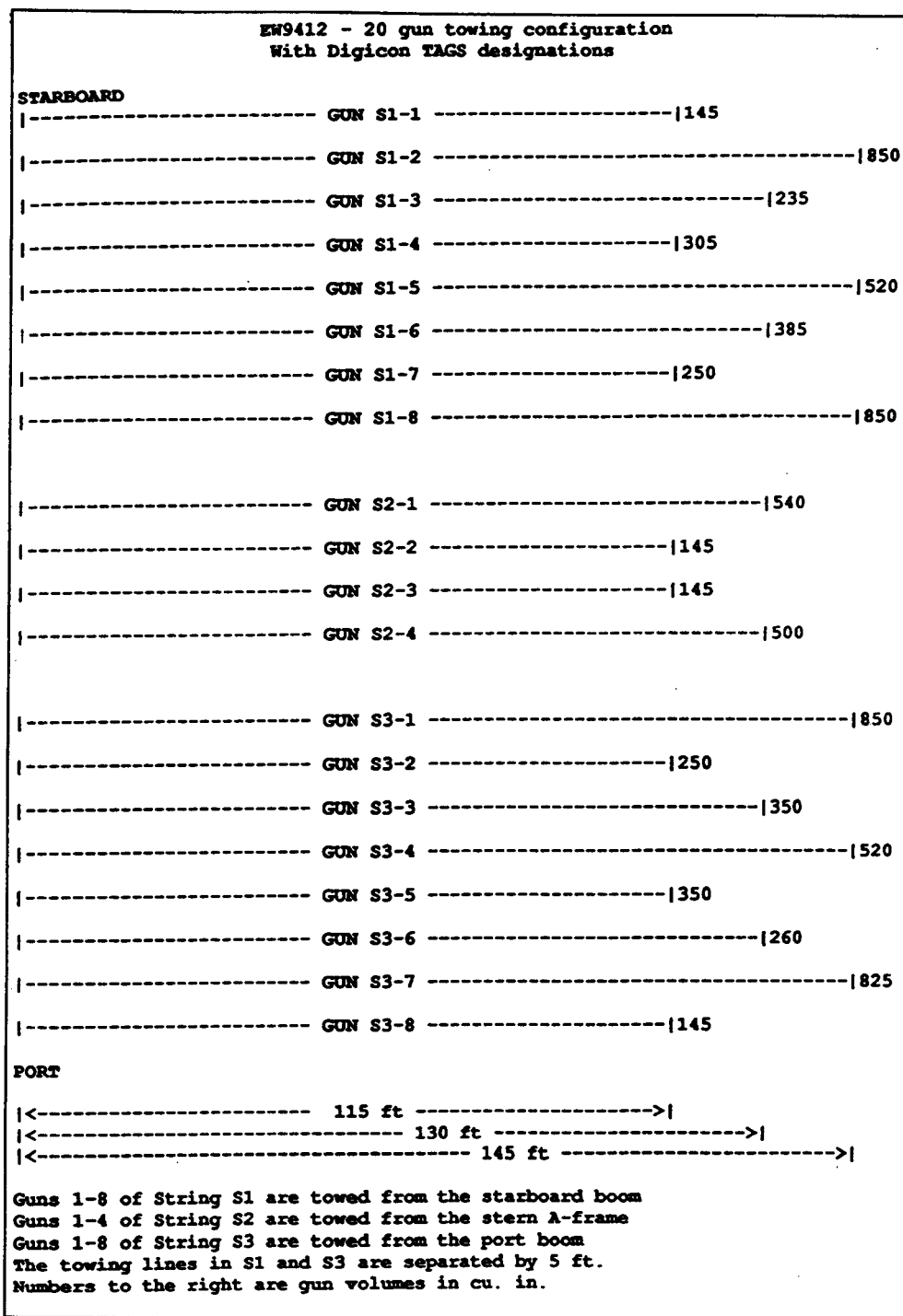


Figure 3.2 EW9412 - airgun configuration from Diebold (1994)

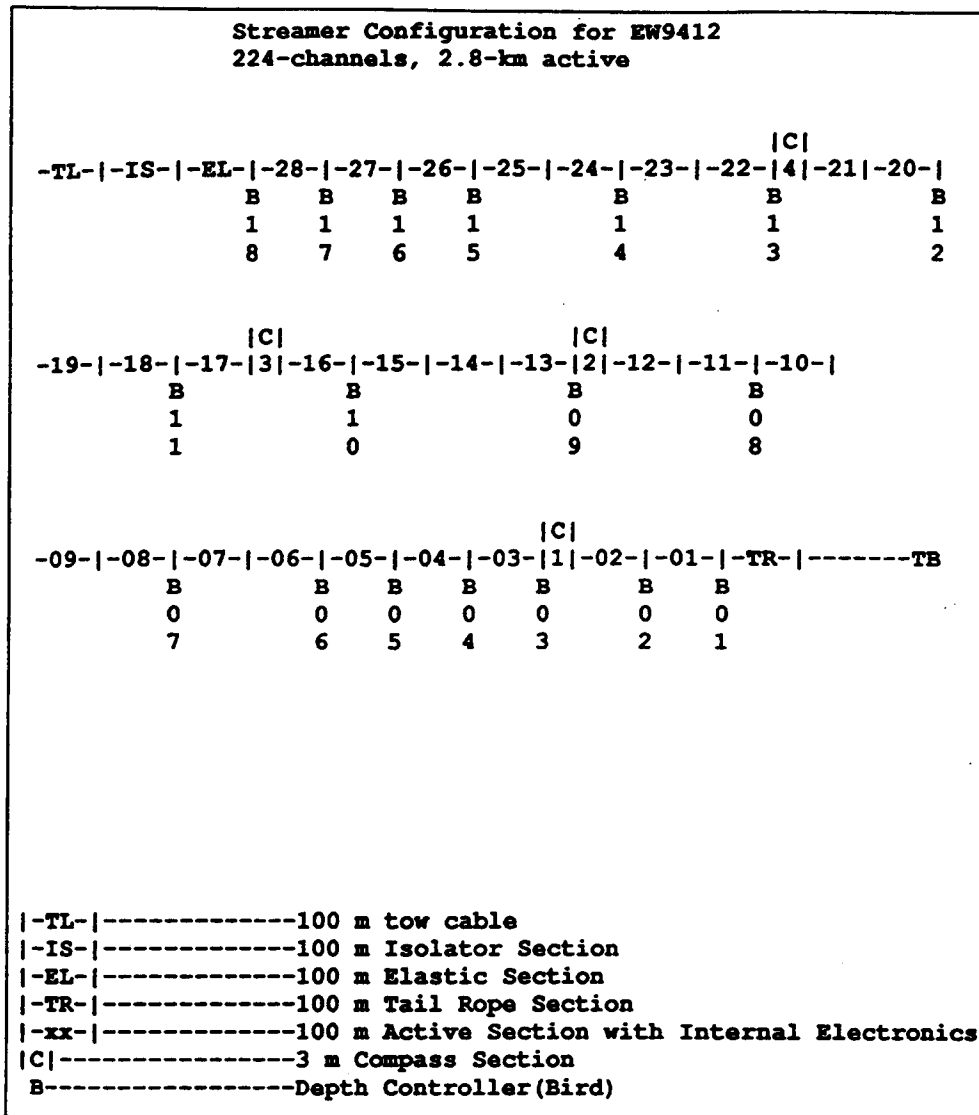


Figure 3.3 EW9412 - streamer configuration from Diebold (1994)

The ship's position at 1 - minute intervals was determined using GPS and Furuno (doppler speed log) sources. The speed data were smoothed by computing a mean value of all good values within the same minute. The Global Positioning System (GPS) receiver was logged at 10 second intervals and smoothed interpolated positions were determined at 00 and 30 seconds of each minute. These positions were compared to the Transit-Furuno navigation and resulted in the final smoothed navigation log.

"For all shots, a random time factor within the range -500 to +500 milliseconds was added, to eliminate the possibility of harmonic buildup of previous shot multiples" (Diebold, 1994).

### 3.2 THE GRAVITY DATA

A Bell Aerospace BGM-3 marine gravity meter and a Bodenseewerks KSS-30 marine gravimeter were used to collect gravity data. Logging was conducted at 1 second and 6 second intervals, respectively. The KSS-30 data were not used because of jumps of 4-8 mGals, which persisted for varying lengths of time.

A gravity value in mGal observed by the BGM-3 gravity meter was obtained by filtering the 1 second counts with a 360 second Gaussian filter, scaling the results, and adding a bias. This value was further smoothed by determining mean gravity values at 00 seconds of each minute from the mGal values at  $\pm 30$  seconds of this time. The free-air gravity anomaly was then computed every minute using the 1980 theoretical gravity formula and a DC-shift of 10.9 mGal obtained from the pre-cruise tie in Dutch Harbour, Alaska (see EW9412 R/V Maurice Ewing data report, Lamont-Doherty Geological Observation Columbia University).

Free-air gravity anomaly data are available along each of the seismic reflection lines. To get an idea of the trend of the gravity anomaly beyond the ship track, gravity profiles were extracted from the geosatellite database (Smith and Sandwell, 1995). Shown in figure 3.4 are the plots of the ship-track gravity in blue and the geosatellite gravity in red for line 1262 after application of a DC-shift (16.64 mGal) that was determined graphically. As expected, geosatellite data is smoother than the ship track data and does not properly represent short wavelength anomalies near the continent; however, the overall trend is similar. The ship-data were used for the forward gravity modeling described in chapter 6.

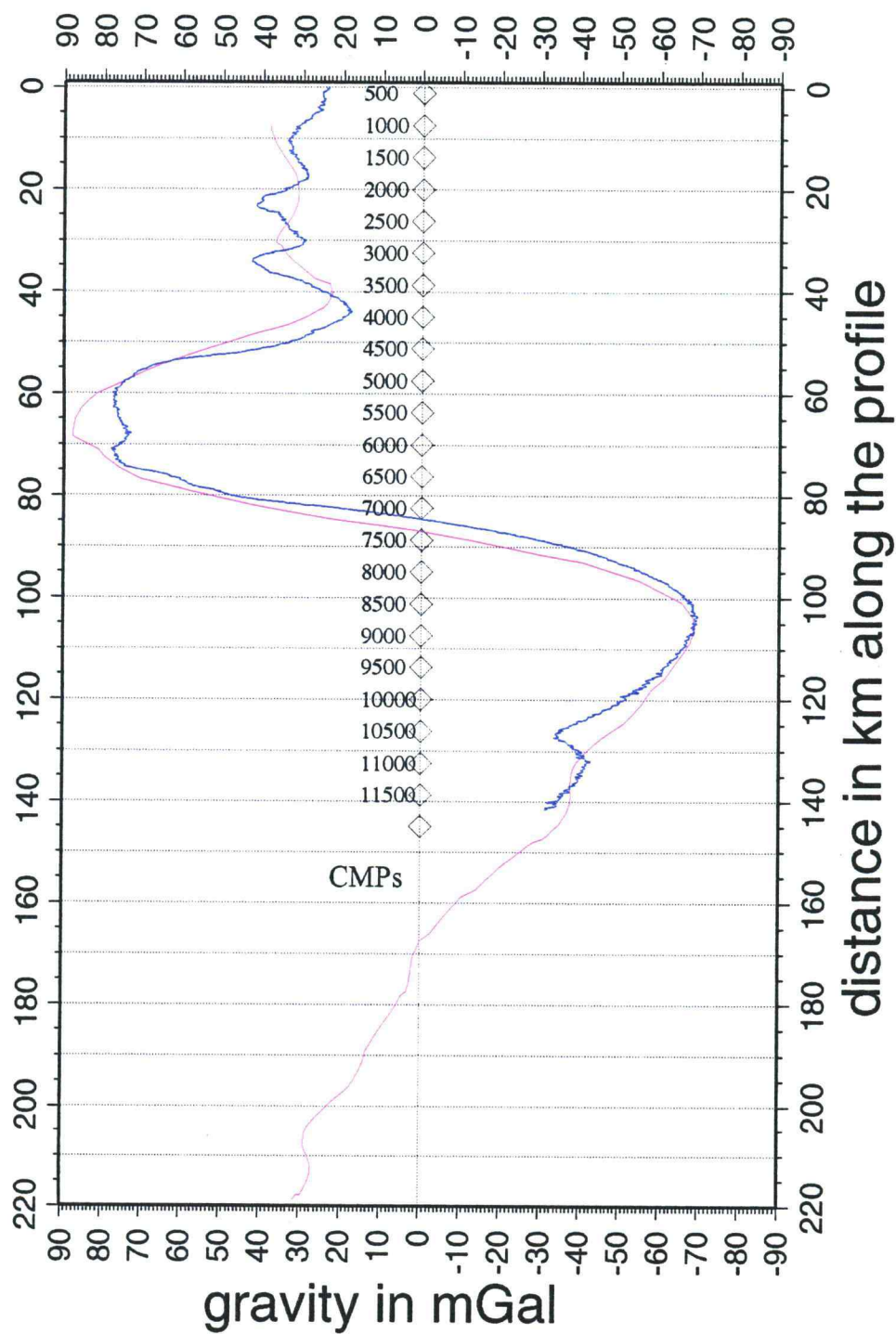


Figure 3.4 Ship track free-air gravity anomaly (blue) and geosatellite gravity data (red) of line 1262 - DC-shift of 16.64 mGal applied

## **4. SEISMIC DATA PROCESSING**

### **4.1 GENERAL DESCRIPTION**

The seismic method is one of the most important geophysical techniques because of its high resolution and great penetration. Exploration seismology consists of three main stages: acquisition, processing and interpretation.

For acquisition, controlled energy sources sample the earth's acoustic response along profile lines. The recording is based upon continuous subsurface coverage called profiling, and requires an arrangement of source points and receivers in a fashion as shown in figure 4.1. Single fold coverage samples each reflection point once, whereas the common midpoint (CMP) technique produces redundant reflection point coverage. This technique is common for marine recording and was used for the acquisition of the ACCRETE data.

Measuring the time required for the generated wave to travel from the source to a series of hydrophones allows reconstruction of the paths of specific seismic waves, which depend on the physical properties of the rocks and the orientation of acoustic interfaces. Two main categories of paths are distinguished: head or refracted waves have paths following the interface between two rock layers and are, therefore, nearly horizontal; reflected waves, which travel downward to be reflected back to the surface, can be considered as approximately vertical and are as a result characterized by relatively large apparent velocities.

Due to their nearly vertical incidence, focusing on reflected waves can limit data acquisition to relatively short offsets (~3000 m). Usable seismic reflection energy is confined to a passband which depends on the source as well as on attenuation by the Earth. The data are recorded digitally on magnetic tape.

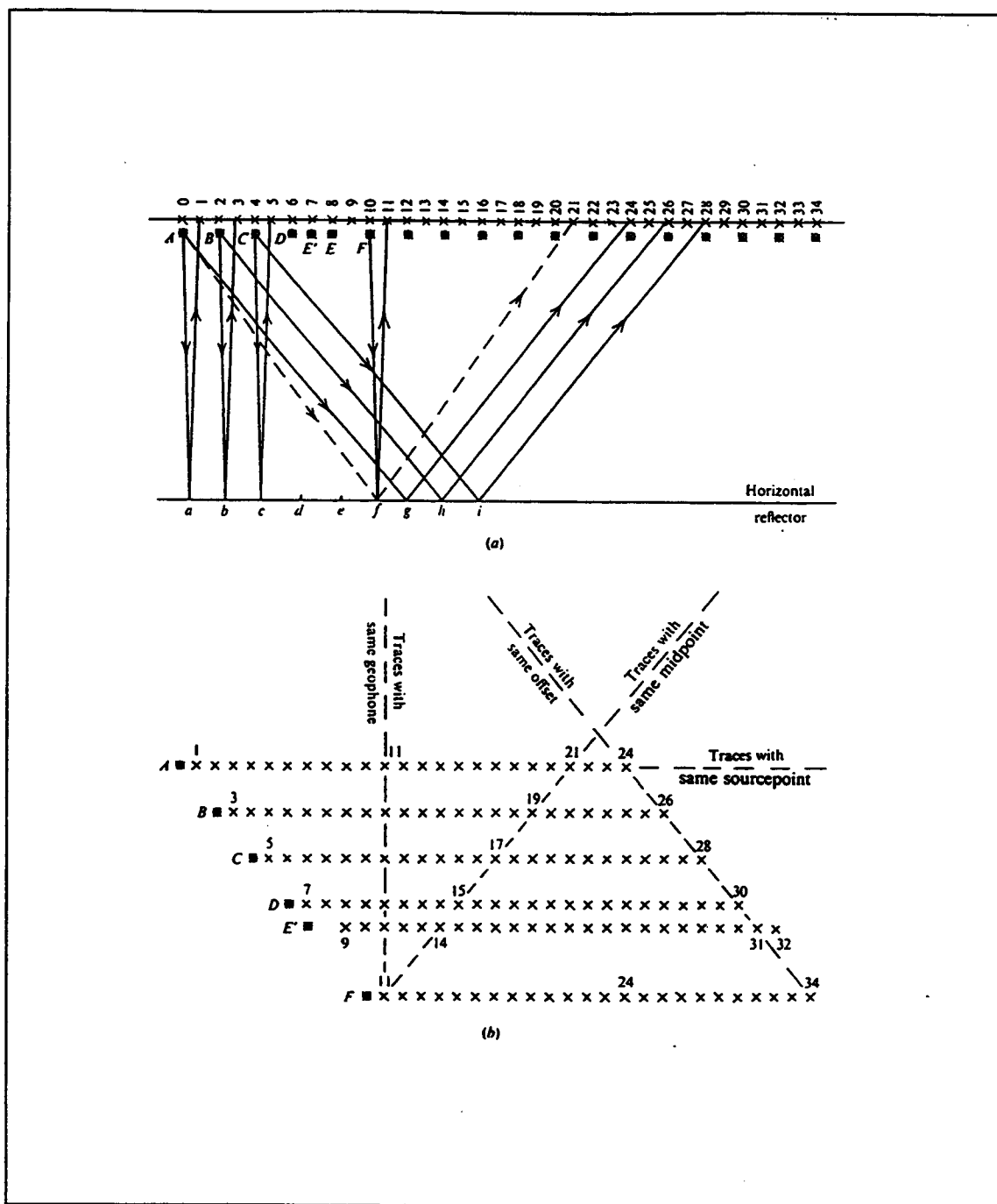


Figure 4.1 Common midpoint profiles; the symbols x and O represent geophone groups and source points, respectively; (a) vertical section illustrating common midpoint profiling; (b) stacking chart, (from Telford et al., 1994)

The main goal in processing seismic reflection data is to enhance the genuine reflection signal by suppressing unwanted energy in the form of coherent and random ambient noise. Coherent noise comprises energy from guided waves, side scattered noise, cable noise or multiples. Random noise could originate from wave or wind motion in the water or any transient movement in the vicinity of the recording cable.

The advantage of multi-fold data recording stems from a statistical concept. Random noise is uncorrelated. If several traces of random noise were added together, they will be out of phase and cause cancellation. Truly random, in the statistical sense, means that the sum of  $n$  random traces is proportional to  $\sqrt{n}$ . The sum of  $n$  in-phase signals, on the other hand, is proportional to  $n$ , assuming that the signal is identical in all traces. Thus, redundant recording and stacking (adding of redundant traces) improves the signal-to-noise (S/N) ratio by a factor of approximately  $\sqrt{n}$  (Sheriff and Geldart, 1985, p. 126).

At the beginning of seismic processing stands the task of selecting the proper sequence of processing steps for the field data of interest, which depends strongly on the field acquisition parameters. Standard seismic data processing comprises three principle steps: *deconvolution* attempts to improve temporal resolution by collapsing the seismic wavelet to approximately a spike; *CMP stacking* can significantly attenuate uncorrelated as well as portions of coherent noise and thereby increase the signal-to-noise (S/N) ratio, as described above; *migration* enhances the lateral resolution by collapsing diffractions, and moving dipping events closer to their true subsurface positions. Many other processes help increase the effectiveness of these principal ones.

At the end of seismic processing, the signal enhanced reflection data are displayed in a form resembling that of a geologic cross-section awaiting interpretation.

## 4.2 THE SOFTWARE

SIOSEIS, a computer system for enhancing and manipulating marine seismic reflection and refraction data, was used for processing purposes. It utilizes the

geophysical industry standard demultiplexed SEG-Y data format for tape and disk files. Processing variables are given by the user via free field named parameters.

Shell scripts read by SIOSEIS are organized into two parts. Part I contains the PROCS (processes) statement, listing all processing steps in the order that they will be applied to the data during that particular run. The list of processes must start with an "input" and terminate with an "output" process. Part II provides SIOSEIS with the necessary parameters for each processing step. The structure of a simple script is shown in table 4.1.

The next sections describe in detail the complete data processing sequence applied to line 1262 which, summarized in a processing flowchart, demonstrates the general processing approach used for all the ACCRETE profiles. Characteristics of the remaining lines will be presented, followed by a description of the migration process. These lead to the interpretable sections discussed in chapter 5.

Table 4.1 SIOSEIS shell script, showing the structure of a simple input/output process

<pre> SIOSEIS &lt;&lt; eof  PROCS process I process II END  process I   <i>parameter list</i> END END  process II   <i>parameter list</i> END END  END </pre>	<p>Part I: list of processes starting with an input and terminating with an output process</p> <p>Part II: the parameter list contains name and value of the filed named parameters</p>
---	---

### 4.3 PREPROCESSING

The field data were recorded in SEG-Y format (Society of Exploration Geophysicists) on the EWING and were put on tape.

A sampling rate of 4 milliseconds results in aliasing if the digitized signal contains energy above the Nyquist frequency of 125 Hz. A high-cut filter was applied in the field prior to analog-to-digital (A/D) conversion to attenuate frequencies above the Nyquist frequency. The total trace length was 16.5 seconds. 224 channels with a group spacing of 12.5 m were towed at a distance of 270 meters to the antenna. The first receiver (channel 224) was located 175 m from the airguns, followed by 2800 m of active streamer.

The recording geometry described above provided shot-receiver offsets, which were assigned to the trace header. For determining CMPs, the profile was divided into 12.5 m-bins equivalent to the group spacing. Thus, two traces of one shot were assigned the same CMP-number. In addition to the field geometry, latitude and longitude of each shot were used to calculate corresponding CMPs. Table 4.2 shows the shot point numbers and CMPs as well as the maximum fold of each of the processed lines.

Table 4.2 List of the shot point-numbers, corresponding CMPs, their average spacing in meters and the maximum folds of the lines processed; average shot spacing was determined from the 20-second shot rate and an average ship speed of 5 kt

	Shot point number	av. shot spacing in m	CMPs	CMP spacing	max. fold
Line 1250	101 to 1662	50	275 to 7000	12.5	68
Line 1262	22924 to 24489	50	4621 to 11626	12.5	68
Line 1263	24534 to 26230	50	275 to 7630	12.5	66
Line 1264	26260 to 27401	50	275 to 5191	12.5	62
Line 1265	27456 to 27920	50	275 to 2280	12.5	56

#### 4.4 PROCESSING FLOWCHART

A flowchart of data processing steps applied to line 1262 (table 4.3) summarizes the processing sequence described in this chapter and introduces the approach used for all remaining lines.

Table 4.3 Processing flowchart showing processing sequence used for line 1262

field tapes (sampled at 4 msec)	<u><i>CMP-domain processing</i></u>	<u><i>post-stack processing</i></u>
<b><u>1. preprocessing (4.3)</u></b>	<b><u>4. CMP sorting (4.5.2)</u></b>	<b><u>9. premigration processes</u></b>
	⇓	⇓
- reformatting to SEG-Y-format - setup of field geometry in trace headers	<b><u>5. velocity analysis (4.5.3)</u></b>	- bandpass filtering (10-60 Hz) (4.8)
⇓	CMP GATHERS	⇓
<b><u>shot-domain processing (4.5.1)</u></b>	- t <sup>2</sup> -gain (4.5.1.1)	- t <sup>2</sup> -gain (4.5.1.1)
SHOT GATHERS	- bandpass filtering for semblance (10-60 Hz) (4.5.1.5)	<b><u>10. finite-difference migration (4.8)</u></b>
⇓	⇓	⇓
- t <sup>2</sup> -gain (4.5.1.1) for display	<b><u>6. time-variant band-pass filtering (4.5.1.5)</u></b>	AGC (4.5.1.1) for display
⇓	⇓	⇓
- trace balancing (4.5.1.2) for display	<b><u>7. NMO-correction (4.5.3.1)</u></b>	<b><u>11. time-to-depth conversion (4.8)</u></b>
⇓	⇓	⇓
<b><u>2. trace editing (4.5.1.2)</u></b>	<b><u>8. stacking (4.5.4)</u></b>	-AGC (4.5.1.1) for display
⇓	⇓	⇓
<b><u>3. frequency analysis (Fourier transform) (4.5.1.5)</u></b>	-AGC (4.5.1.1) for display	
⇓	⇓	

## 4.5 LINE 1262

Line 1262 was shot over an approximate length of 90 km, from east to west across the continental shelf off Dixon Entrance, the shelf break, the assumed location of the Queen Charlotte Fault (QCF), the Queen Charlotte Terrace, and the Queen Charlotte Trough. The crossing of trough, terrace and shelf leads to rapid changes in water-bottom depth from very shallow at the shelf (300 m  $\cong$  0.4 s) over a steeply sloping terrace to the deep trough ( $\sim$ 2800 m  $\cong$  3.7 s). This results in time windows of different lengths undisturbed by water-bottom multiples.

### 4.5.1 Common Shot Gather

The common shot gather of shot 23000 is displayed in Figure 4.2, showing 224 data traces at different offsets from 0 - 8 seconds. At a first glance two features are striking: (1) gradual decay of signal amplitudes at later times (see 4.5.1.1), and (2) the gather contains bad traces (see 4.5.1.2).

#### 4.5.1.1 GAIN

A single shot is considered a point source that generates a spherical wave field. In a homogeneous medium, energy density decays proportionately to  $1/R^2$ , whereas wave amplitudes decay as  $1/R$  ( $R$  is the radius of the wave front). This phenomenon is called wave front divergence or geometrical spreading. Velocity usually increases with depth, resulting in more rapid divergence of the wave front and amplitudes that decay more quickly. Another effect the earth has on a propagating wave field is due to intrinsic attenuation in rocks. High frequencies are more rapidly absorbed than low frequencies, causing the frequency content of the source signal to change with time.

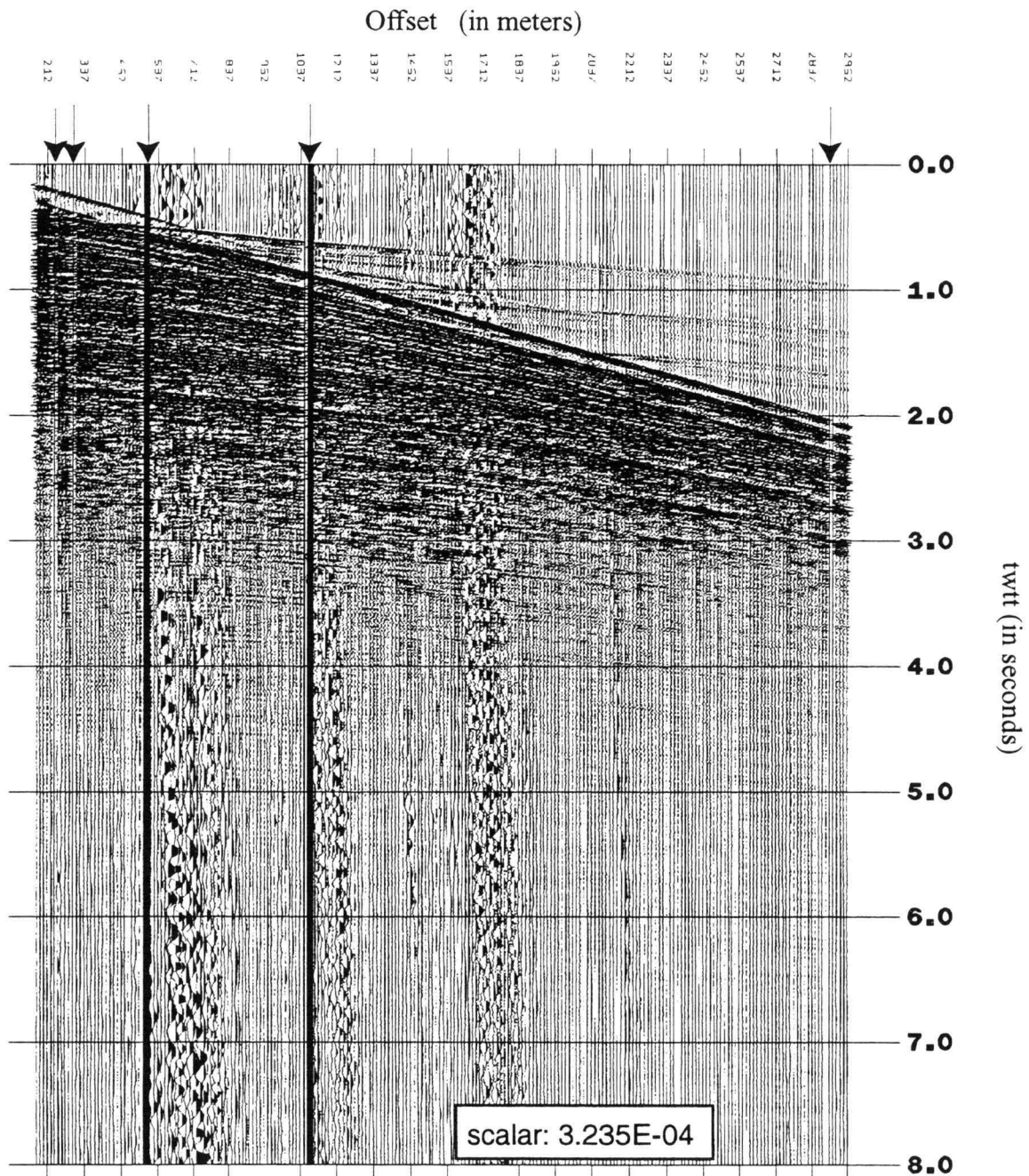


Figure 4.2 Common shot gather of shot 23000 of line 1262 demonstrates the gradual decay of signal amplitude with time; bad traces are marked by arrows

Because of the amplitude decay resulting from wave front divergence and attenuation, no signal is seen at late times in figure 4.2 and random noise is dominant. This earth effect must be removed to extract any signal that may be present at later parts of the record.

Gain is a time-variant scaling method. Since a gain function for geometric spreading correction is not directly implemented in SIOSEIS, the following function, which amplifies weak late reflections without destroying the amplitude relationship from trace to trace was applied:

$$g(t) = t^2.$$

Figure 4.3 shows the same common shot gather of figure 4.2, trace balanced (equalizes a group of traces to the same amplitude level) and with the  $t^2$ -function applied. Signal strength as well as noise are amplified in the later part of the record and all traces seem to have equal peak amplitudes.

Gain is often used simply for the display of data. AGC-type gain functions, for example, are applied to bring up weak signals and were used later for the final display of stacked or migrated sections.

Instantaneous AGC was calculated as follows. The mean absolute value of trace amplitudes within a specified time gate was computed by squaring each sample in this gate, then taking the mean and the square root. The resulting value of the gain function at the  $n$ th sample is the ratio of the desired rms (root mean square) level to this mean value. Then, the time gate was moved one sample down and the value of the gain function for the  $(n+1)$ th time sample was calculated, and so forth. If too small a time gate is chosen, significant loss of signal character can result from boosting zones with small amplitudes.

An undesired side effect is that gain corrections amplify random noise as well as the signal. Therefore, a significant part of the random noise was suppressed by filtering and CMP stacking before gain application.

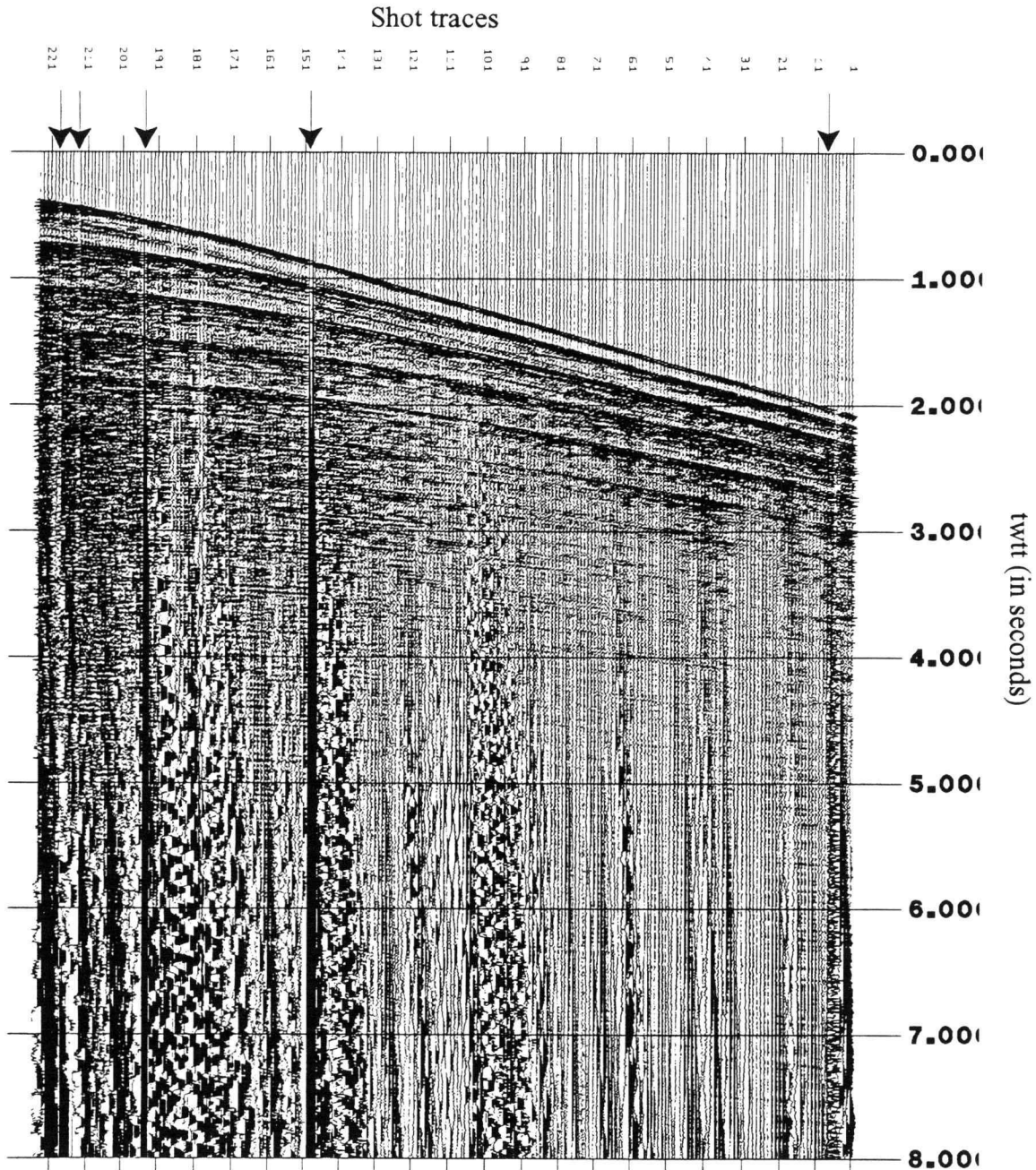


Figure 4.3 Common shot gather of shot 23000 of line 1262; trace balanced and t2-gain corrected; signal at later parts of the record is boosted up and all traces have the same peak amplitude; traces indicated by arrows contain either only noise (trace 5, 6, 214, and 219) or no data were recorded (dead trace) (traces 149, 150, and 195)

#### 4.5.1.2 TRACE EDITING

Sometimes traces appeared to be only noise (traces 5, 214 and 219 of figure 4.3), some have monofrequency signals, polarity reversals or constant amplitudes (=dead trace, no data recorded), (traces 149, 150 and 195 of figure 4.3). These needed to be deleted. Figure 4.4 shows figure 4.2 after trace editing and balancing, and application of the  $t^2$ -gain correction.

#### 4.5.1.3 TYPES OF ENERGY IN THE FIELD RECORD

Field records typically contain three types of energy: **(1) reflections**, **(2) coherent noise** and **(3) ambient noise**. Processing techniques attempted to enhance the reflection energy over noise.

**(1)** Reflection events are recognized by their hyperbolic travel times. The reflection hyperbola is centered at zero offset for a horizontal reflector, whereas its apex is shifted in the updip direction for a dipping interface.

**(2)** Several wave types fall under the coherent noise category, such as guided waves, side scattered noise, cable noise and multiples.

Irregularities at the water bottom, where topography is not flat and smooth, act as point scatterers producing diffractions, which can be off or on the vertical plane. The steeply sloping terrace as well as a ridge at the western termination of the terrace both could be sources for *side* or *back scattering*. Diffractions were observed on shot-gathers confined to the mentioned sloping regions of rough surface. Figure 4.5 shows shot-gather 23500, located along the slope of the terrace, as an example of back scattered energy (marked S).

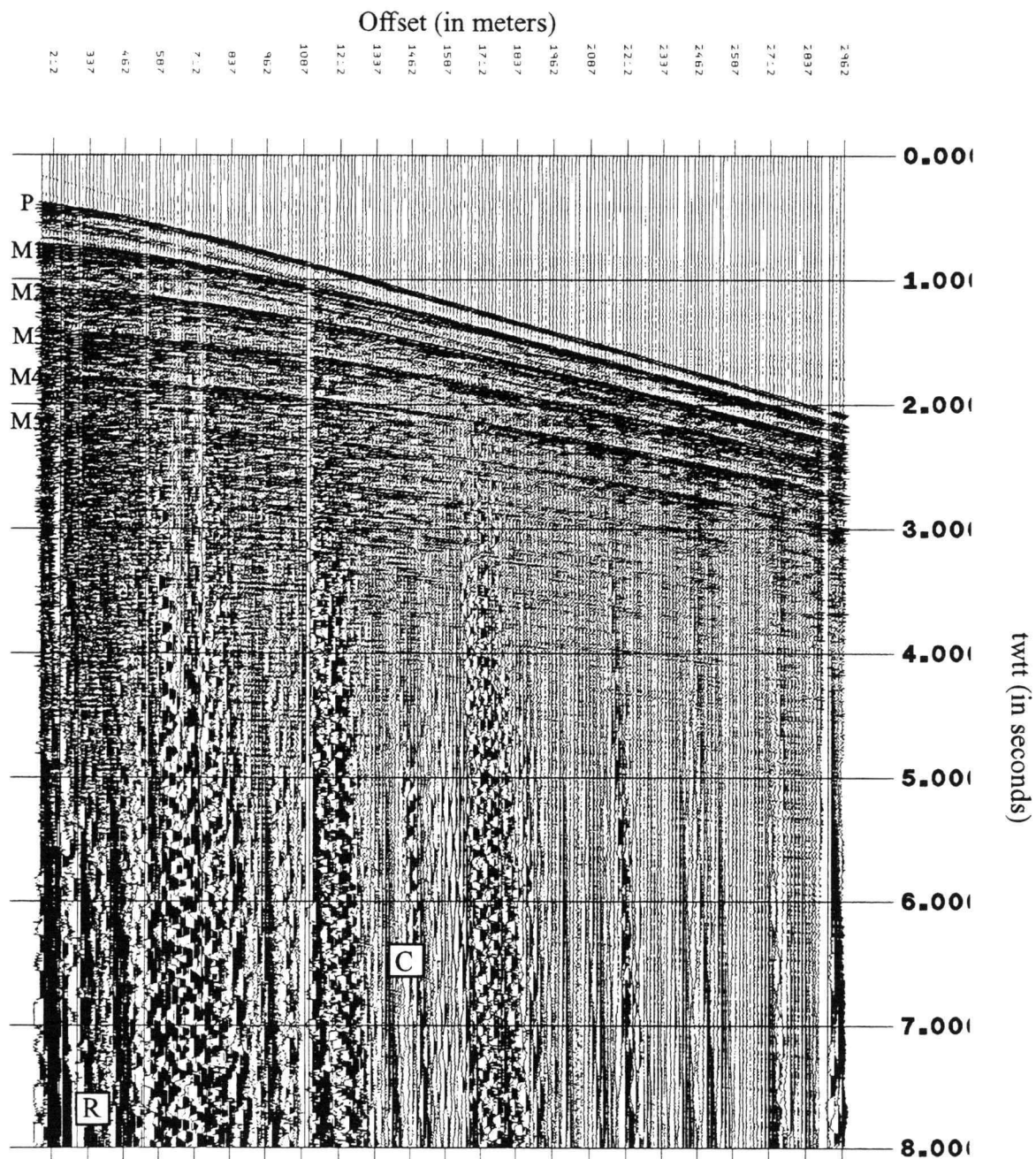


Figure 4.4 Common shot gather of shot 23000 of line 1262 after elimination of bad traces, trace balanced and  $t_2$ -gain corrected; C = cable noise, P, M1-M5 = primary, first, and higher order multiples, R = random low frequency noise

*Cable noise*, which is linear in  $t(x)$  space and low in amplitude, usually appears on shot records as late arrivals (Yilmaz, 1988) and could be present on some records, e.g. in figure 4.4 at the lower left corner (marked C).

*Multiples* were an important source of coherent noise. They are events that have undergone more than one reflection. Figure 4.4 as well as figure 4.5 show easily recognizable multiple reflections from the sea floor, characterized by their repetitiveness at equal time intervals at zero-offset. Due to shallow water depth, multiples in shot gather 23000 arrived early after the primary event and their energy is attenuated at about 3 seconds. Shot gather 23500 (figure 4.5), in contrast, shows multiples that are repeated only every 1.8 s and are therefore part of the record for longer times.

(3) *Ambient or random noise* in marine field data can have various sources: wind motion that indirectly affects the streamer, transient movements in the vicinity, wave motion in the water that causes vibration of the recording cable, or electrical noise from the recording instruments. This type of noise was randomly distributed throughout the shot gather and with frequencies usually found at the low end of the spectrum. Figure 4.4 contains a good deal of random low frequency noise, predominantly at near offsets and later times (marked R).

#### 4.5.1.4 MULTIPLES

Multiple energy as seen in the ACCRETE field data seemed to be extremely strong and suggests a high reflectivity of the sea floor. To determine the reflection coefficient of the water bottom, amplitudes of the primary reflection and of the first

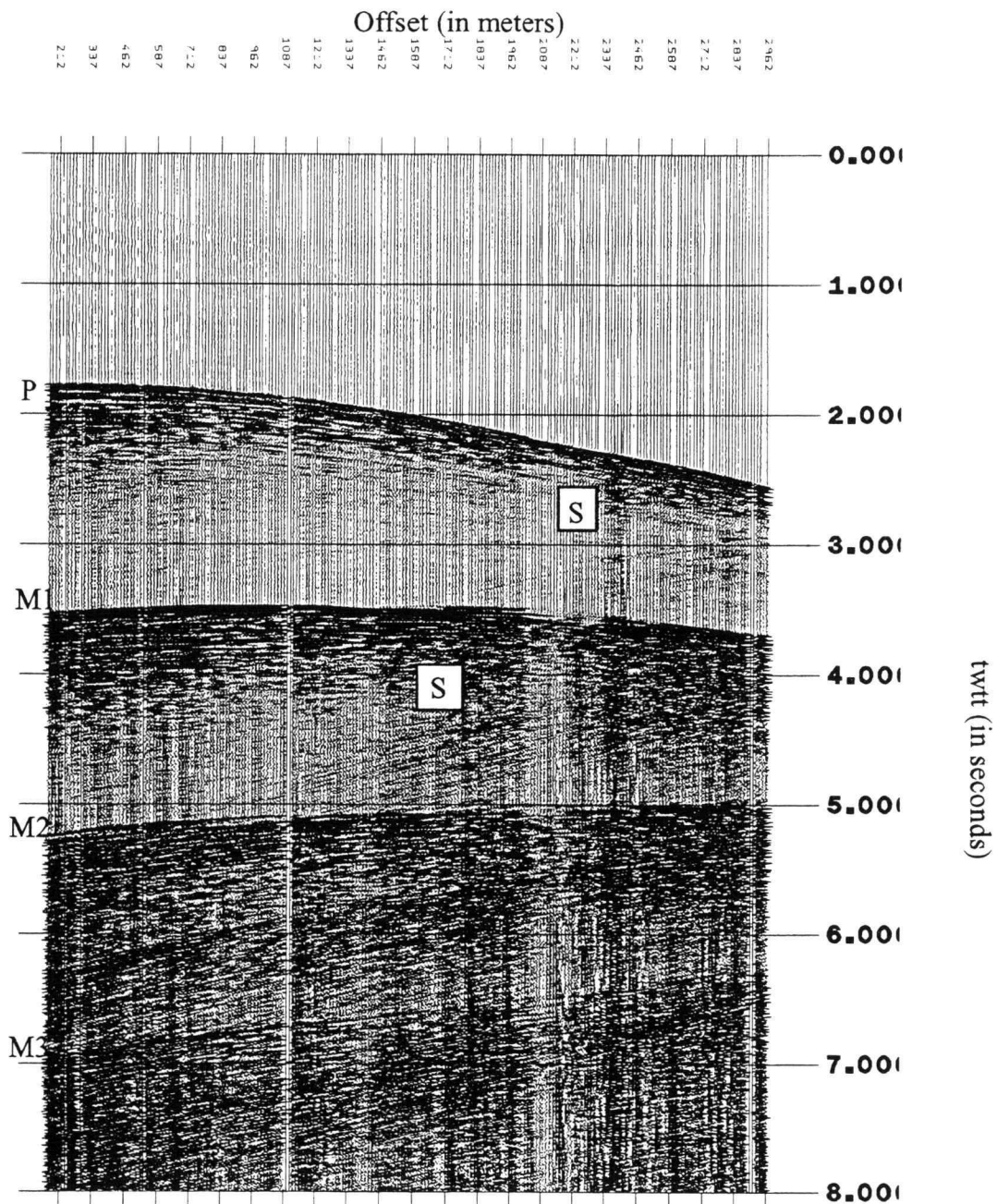


Figure 4.5 Common shot gather of shot 23500 on steeply sloping portion of the terrace segment of line 1262; back scattered energy is marked S; P, M1-M3 = primary, first, and higher order multiple

and second order multiples of one shot gather were considered. By measuring the amplitudes of the multiples at offsets that are twice and three times the offset at which the primary amplitude was determined, a geometrical divergence correction can be easily found. Assuming a homogeneous medium (here water), amplitude decreases linearly with distance  $R$ . Thus, geometrical divergence correction is proportional to the path length of the reflections,  $R$ ,  $2R$ , and  $3R$  for primary and multiples, respectively. Table 4.4 demonstrates the principle approach in defining the amplitudes of primary and two multiples used for the calculation of the reflection coefficient.

The reflection coefficients obtained from the primary and the two multiples differ considerably, which ideally should not be the case. These variations could be due to the fact that amplitude does not simply decay as  $1/R$  or the ground is heterogeneous in velocity, density or has a varying surface roughness. Also, it was not possible to find traces in the CMP gather that were at exactly 2 and 3 times the offset of the trace, where the amplitude of the primary was determined. The mean reflection coefficient was found to be 0.5. Looking at table 4.5, which gives typical reflection coefficients or reflectivity values for "soft" and "hard" ocean bottoms, the ocean floor at CMP 2500 of line 1264 is between soft and hard.

#### 4.5.1.5 FREQUENCIES AND FILTERING

To get a feel for the frequency content of the shot gathers, a fast Fourier transform of six traces from shot 23000 was conducted. Displayed in Figure 4.7 are only their amplitude spectra. The amplitude spectra of figure 4.7 display a frequency band between 0 and 125 Hertz (the Nyquist frequency). The usable frequency range of this shot gather lies between 10 and 90 Hz.

At the low end of the spectrum, especially at offset 1712 m, amplitudes peak around 6 Hz. This can be a typical frequency of random noise. A band pass filter that

Table 4.4 Determination of sea floor reflection coefficient  $r$ ; relative amplitude values are taken from CMP gather 2500, which is located in a relatively flat section of line 1264, measured in inches after use of the same scalar; the part of the waveform used to determine amplitudes is indicated in figure 4.6; length  $R$  is defined in the graph below

event	absolute amplitude equations	rel. amplitude in inches	determination of reflection coefficient $r$	$r$
primary	$A = A_i r / R$ measured at offset $X$	2.05	$A/A' = 2/r$ $\Rightarrow r = 2A'/A$	0.61
1. multiple	$A' = -A_i r^2 / 2R$ measured at offset $2X$	0.625	$A'/A' = -3/2r$ $\Rightarrow r = 3A''/A'$	0.4
2. multiple	$A'' = A_i r^3 / 3R$ measured at offset $3X$	0.167	$A''/A = r^2/3$ $\Rightarrow r = \sqrt{3A''/A}$	0.49

$A_i$  = amplitude of source signal  
 $A, A', A''$  = amplitudes of primary and multiple events

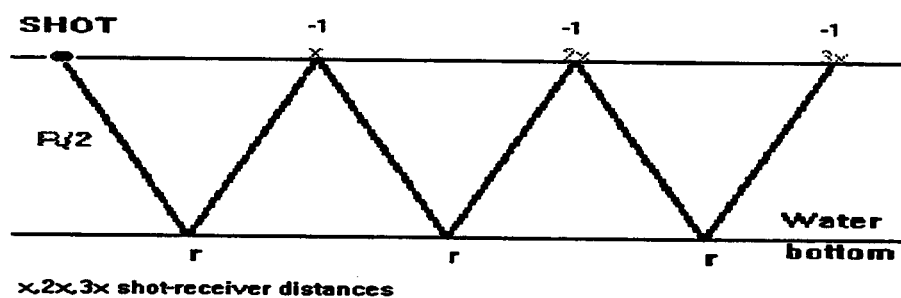


Table 4.5 Typical reflectivity values for two different layer interfaces, adapted from Sheriff and Geldart (1985, p. 67)

interface	velocity in km/s	density in g/cm	velocity in km/s	density g/cm <sup>3</sup>	reflectivity
"soft" ocean bottom	1.5	1.0	1.5	2.0	0.33
"hard" ocean bottom	1.5	1.0	3.0	2.5	0.67

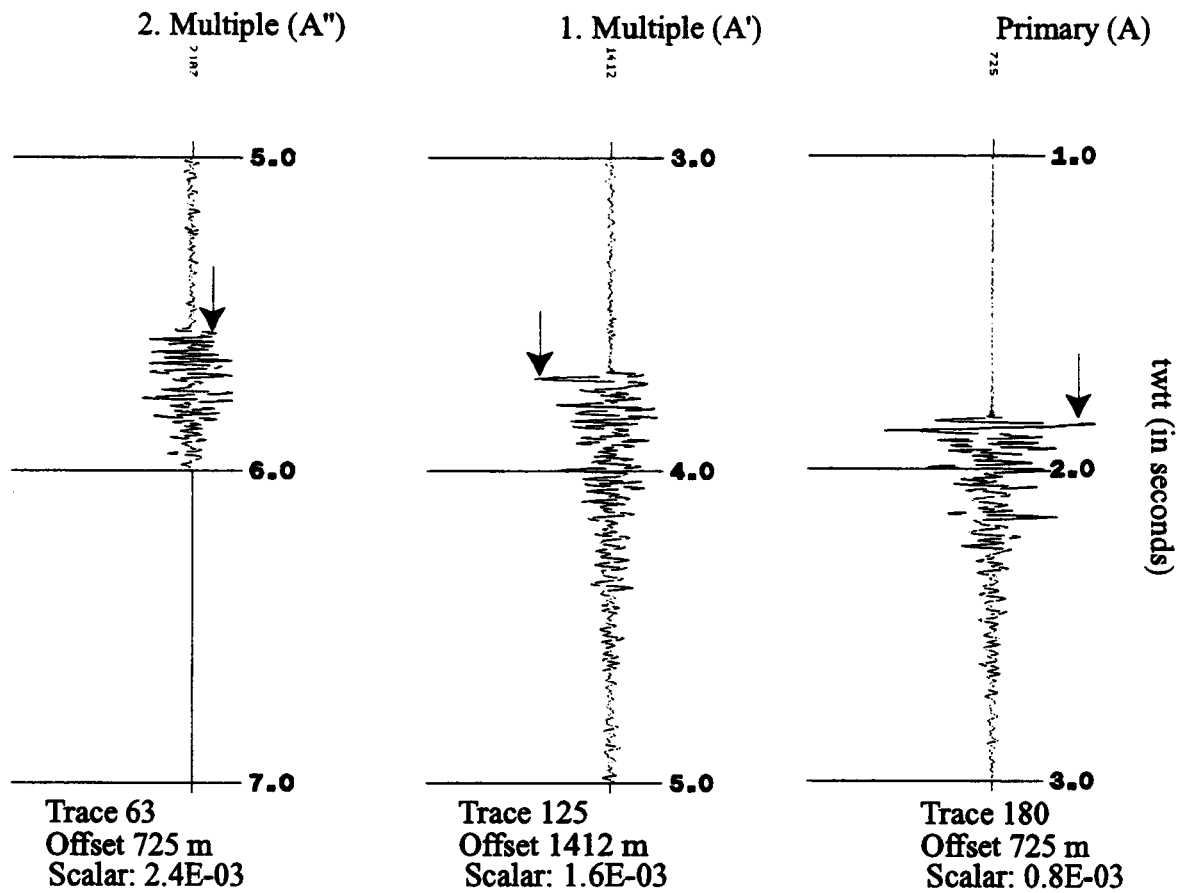


Figure 4.6 Waveform of primary, first and second order multiple from CMP 2500 of line 1264; indicated by arrows is the portion used for amplitude evaluation (after accounting for different scalars); first multiple is reversed as stated in table 4.4

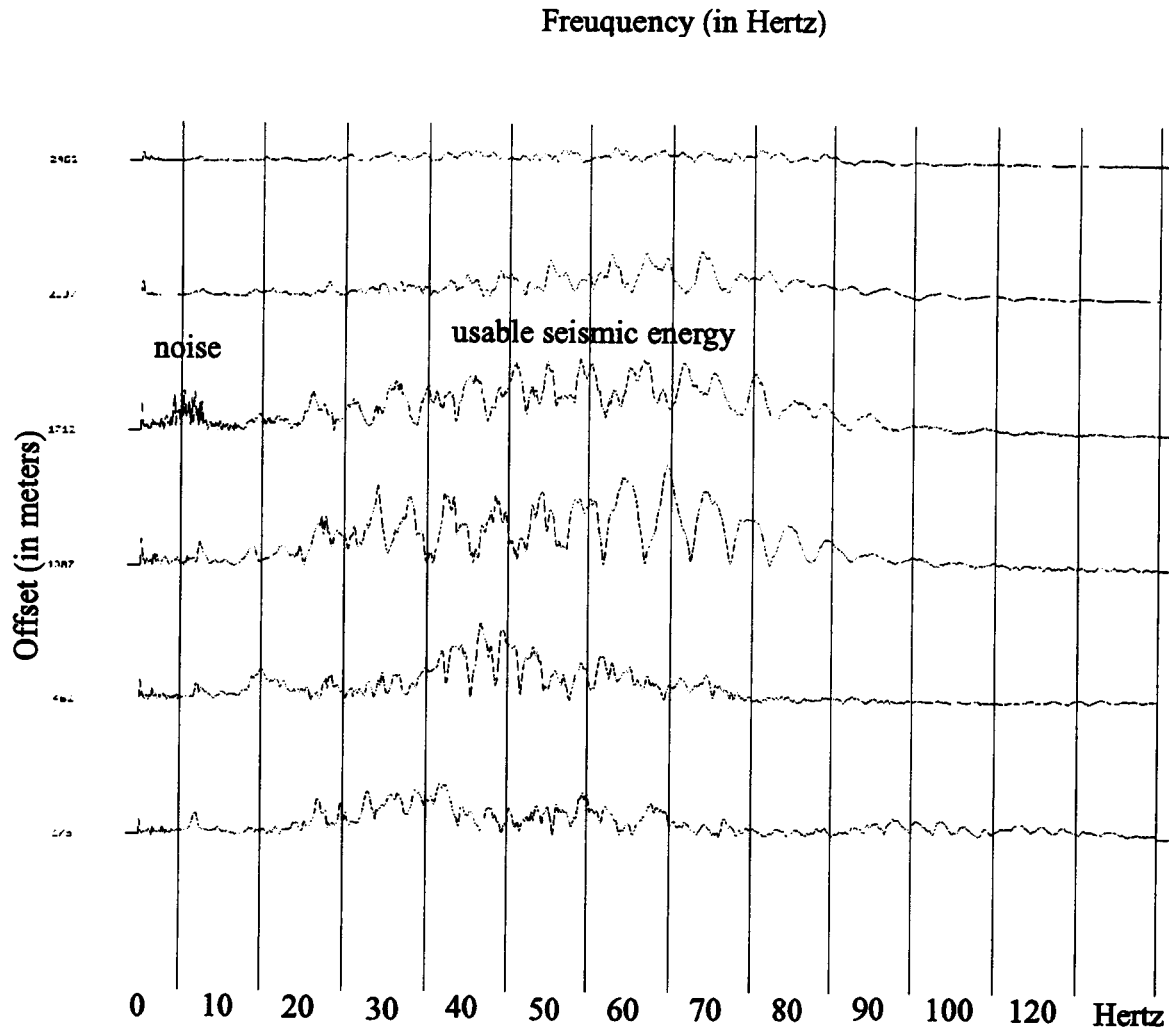


Figure 4.7 Amplitude spectra of the fast Fourier transform of six traces from shot 23000 of line 1262, showing that the usable seismic energy lies in a range between 10-90 Hz; low frequency random noise peaks about 6 Hz

passes the usable seismic reflection energy improved the signal-to-noise ratio of the data and was applied before boosting amplitudes with the aid of a gain function. Figure 4.8 demonstrates the effect of a 39-point time domain 10-100 Hz bandpass filter on shot gather 23000. Compared with Figure 4.4, the random low frequency noise level is decreased and the S/N ratio improved.

For prestack processing a convolutional zero phase time varying bandpass filter was chosen to deal with the varying S/N characteristics due to multiple energy. This filter is based upon the principle of constructing a zero-phase wavelet with an amplitude spectrum that contains the desired frequencies. This spectrum is then multiplied with the spectrum of the seismic data trace (equivalent to convolving the zero-phase wavelet with the trace), zeroing out the unwanted energy. A filter length set to 39 points (156 ms) and a passband that varied from 10-100 Hz above the multiple, and 10-40 below the multiple for the shelf area and 10-50 Hz below the multiple for the rest of the profile was found to produce good results. The small frequency band of 10-40/50 Hz helped to suppress multiples since genuine reflections at depth contain lower frequencies than sea floor multiples, which traveled only in water and were thus subjected to less attenuation. Some processing steps, such as calculation of semblance values for velocity analysis or special treatment of certain line segments with unusually high-frequency random noise, required different passbands. This will be mentioned as individual processes are described.

#### **4.5.2 CMP Sorting**

Multichannel seismic data were acquired in shot-receiver (s, r) coordinates (figure 4.9 a), determined from the field geometry, and stored in the trace headers. Data processing, on the other hand, deals with midpoint-offset (m, o) coordinates (figure 4.9 b).

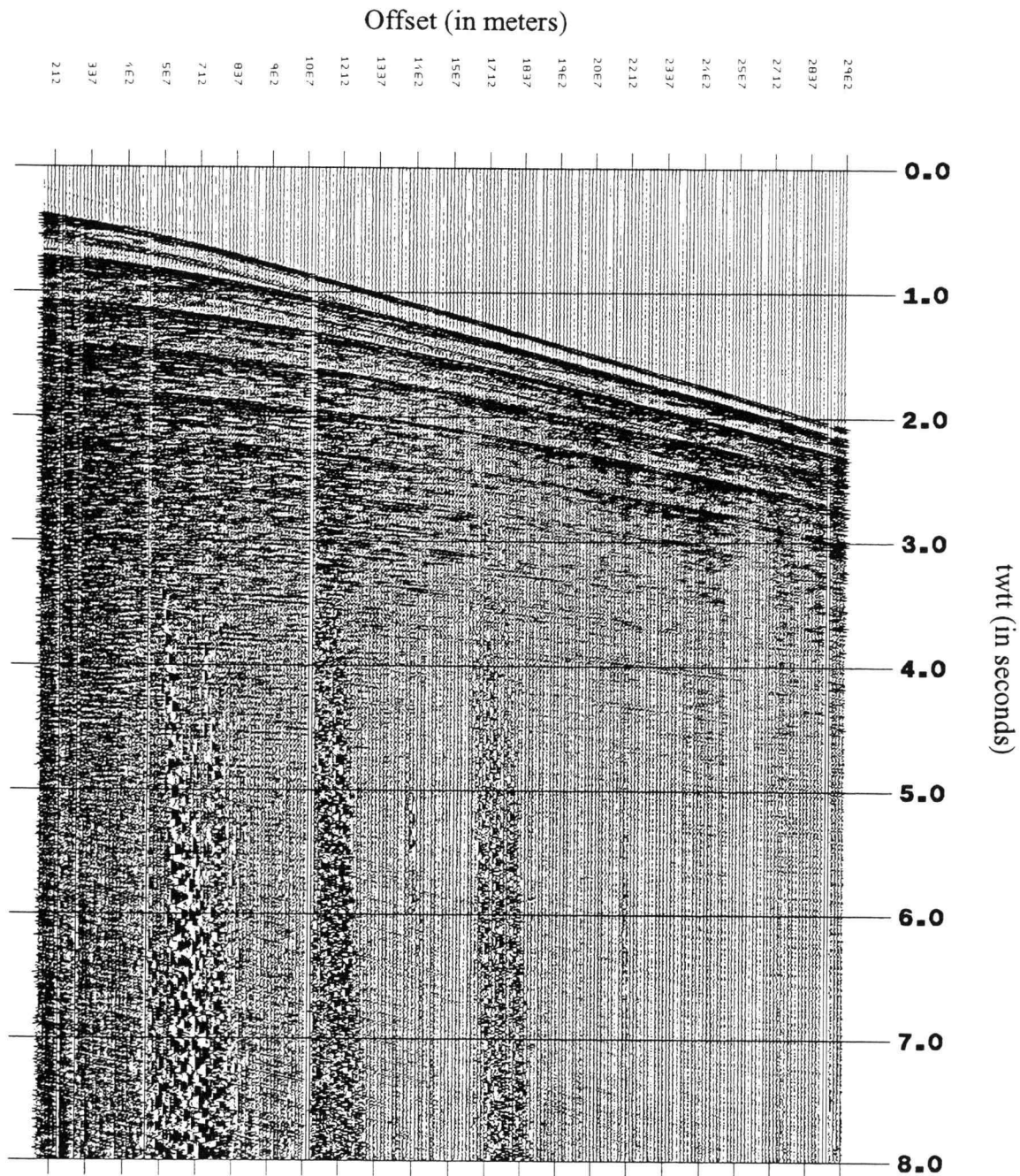


Figure 4.8 Common shot gather of shot 23000 of line 1262 after application of a 39-point time domain 10-100 Hz bandpass filter; compared with figure 4.4, random noise was significantly attenuated

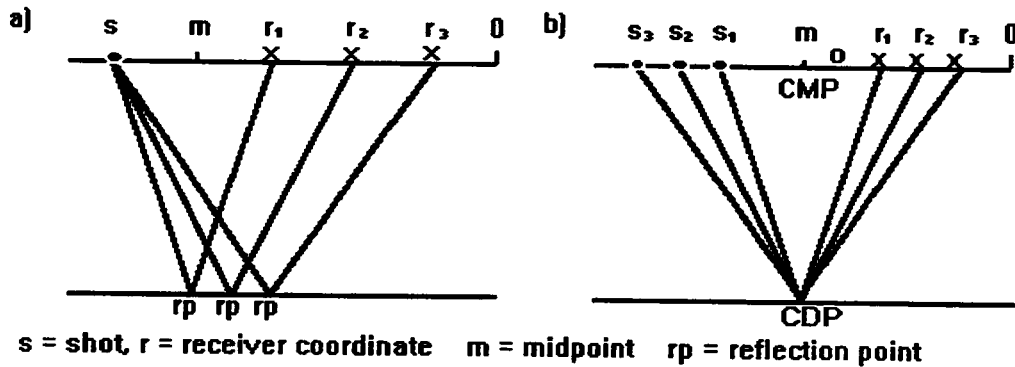


Figure 4.9 a) data acquisition in the shot-receiver (s, r) domain and b) recording in the midpoint-offset (m, o) domain; CMP = common midpoint; CDP = common depth point

Noteworthy is the fact that a common depth point (CDP) gather is equivalent to a CMP gather only when reflectors are horizontal and velocities do not vary laterally. As soon as dipping reflectors or heterogeneity occur, CMP and CDP (see figure 4.9 b) are no longer coincident, and reflection points corresponding to each source-receiver pair in a CMP gather do not fall on the same depth point over a dipping reflector. For this reason, the text refers exclusively to CMP.

The fold of line 1262 amounts to 68. One advantage of multi-fold data is the attenuation of multiples and guided waves. This is based on the fact that coherent noise usually possesses different stacking velocities than genuine reflections. Velocity analysis deals with finding the right stacking velocities and thereby constitutes a very significant portion of the data processing procedure.

### 4.5.3 Velocity Analysis

#### 4.5.3.1 NORMAL MOVEOUT (NMO)

Stacking velocity is the important criterion on which the success of multi-fold coverage with nonzero-offset recording is based. Nonzero-offset data are, in fact, required to estimate stacking velocities of the subsurface.

Figure 4.10 displays a 68-fold CMP gather of CMP 11100. Reflections are distinguishable by their hyperbolic shape. The small-spread approximation used to obtain the hyperbolic traveltime curve (Appendix A) does not strictly apply for sea floor and shallow sediments when the streamer is 3 km long, as is the case for the ACCRETE experiment. To account for this problem, far offset-traces were muted as described below.

A problem arises when NMO-correction (Appendix A) is applied. This is called NMO stretching and describes a frequency distortion that occurs particularly for shallow events and at large offsets. Figure 4.11 shows two reflection hyperbolae before (right) and after (left) NMO correction. Reflector b) is located at shallower depth and displays a greater NMO than reflector a). Due to this difference in NMOs, the distance between reflection hyperbola a) and b) at large offsets is stretched after NMO correction, causing the wave form with a dominant period  $T$  to be changed to a period  $T'$ , which is greater than  $T$ . Stretching is therefore a frequency distortion in which events are shifted to lower frequencies. Since significant NMO differences occur at small times, large offset stretching is confined to these times and stacking will cause shallow events to be severely damaged. This problem was solved by muting the stretched zones in the gather, which at the same time eliminates far offset traces that do not strictly apply to the small-spread approximation.

Automatic muting uses a preset stretch limit. If the S/N ratio is good, the stretch mute is acceptable to preserve the signal bandwidth. A poor S/N ratio requires

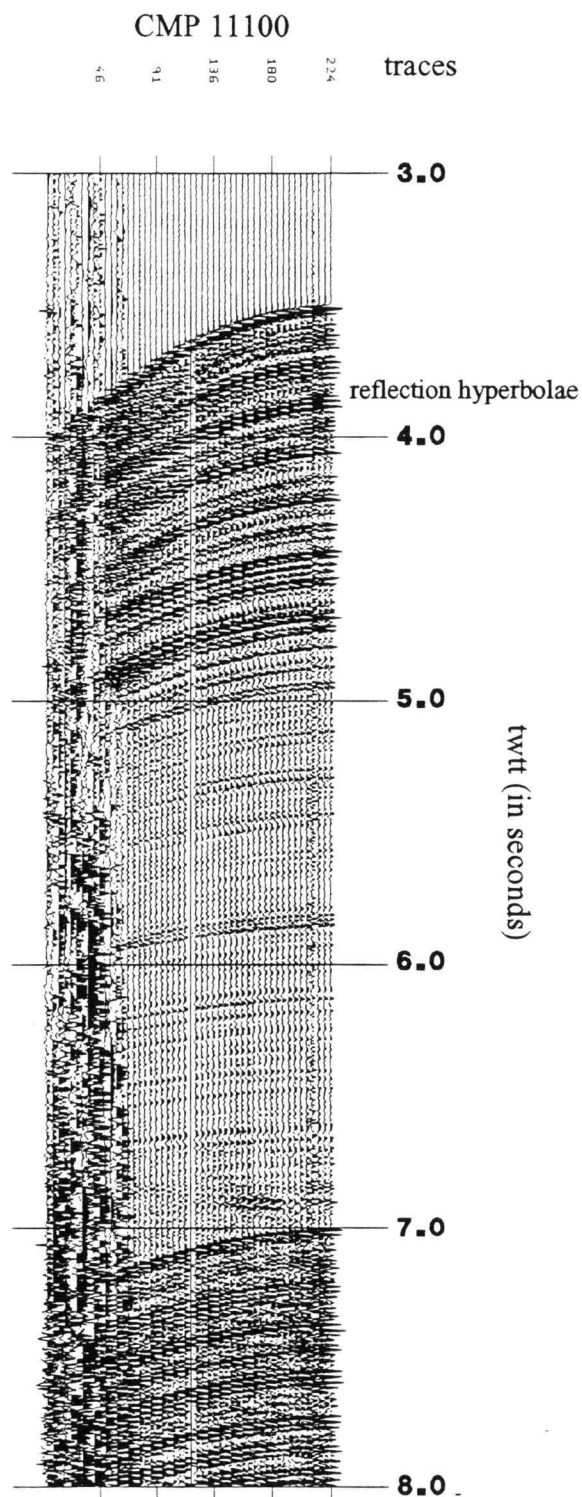


Figure 4.10 Common depth point gather of CMP 11100 in the trough segment of line 1262; a  $t_2$ -gain correction was applied as well as a time-domain bandpass filter with a passband of 10-125 Hz; far offset traces consist mainly of noise; reflections are distinguishable by their hyperbolic shape

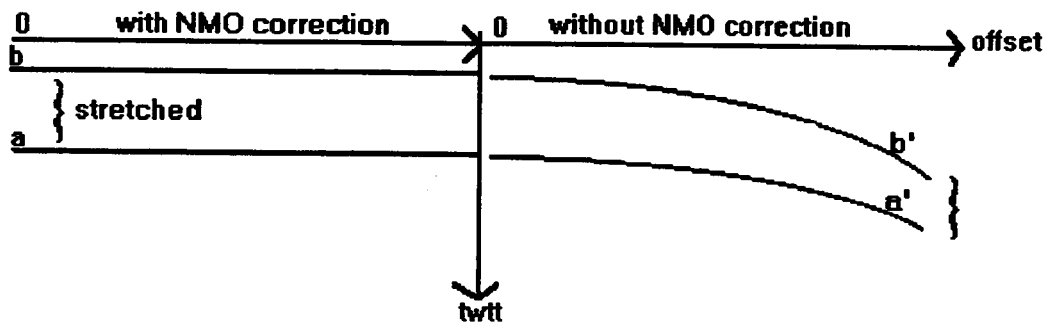


Figure 4.11 Two reflection hyperbolas before (right) and after (left) NMO correction; reflector (b) is located at shallower depths; the difference in length between reflectors (a) and (b) before and after NMO correction defines the stretch

more traces to boost the S/N and larger offsets should be included in the stack. Thus, it is necessary to evaluate the amount of muting to be applied. Stacking of all ACCRETE data was done with a stretch limit that allows 0.5 seconds total stretch.

#### 4.5.3.2 VELOCITY PICKING

Conventional velocity analysis is based upon the hyperbolic assumption and denotes the process of determining stacking velocities from the seismic data. A proper velocity function is in turn used to correct for NMO, so that reflections are aligned within one CMP gather and can be stacked. The fact that the moveout generally decreases with depth affects the resolution of velocity estimates.

Two different methods were used to conduct velocity analysis and details are discussed in Appendix B. The *constant velocity method* corrects normal moveout for a CMP gather using a range of constant velocities, and results for each velocity are displayed. Reflectors are overcorrected for too small and undercorrected for too high a velocity. The proper velocity for a given twtt is picked where the NMO is completely

removed and reflectors appear flat. This velocity analysis was used to determine velocity functions at specific locations of interest, e.g. in areas of complex structure or rapid lateral velocity changes. The *velocity spectrum method* generally displays coherency of the signal along a hyperbolic trajectory over the entire spread length of one CMP gather. Semblance (Appendix B) was chosen as display quantity to analyze the ACCRETE data.

Semblance contour plots were calculated for every 100th CMP (1.25 km) of each profile. Figure 4.12 shows such a semblance contour plot for CMP 11100 of line 1262, located on the Queen Charlotte Trough over oceanic crust. This is a good example of how semblance contour peaks are located at continuously greater stacking velocities as two-way traveltime (twtt) increases. Starting at 3.5 seconds water depth, the black line follows the velocity function picked for this CMP. A velocity function of one CMP consists of stacking velocity (in m/s) and two-way traveltime (in seconds) pairs. Semblance peaks of the water-bottom multiple (WBM) first appear at 7 s twtt and line up for consecutive depths along the water velocity of about 1500 m/s. Here, stacking velocities for primary and multiple differ as much as 1500 m/s. Unfortunately, the multiple energy is very strong, so that stacking of multiple energy from near traces with negligible moveout still overprints the faint energy from genuine reflections.

It was not always as simple a task as it seemed in figure 4.12 to pick velocity-time pairs. Figure 4.13, for example, shows a semblance contour plot of CMP 10500, where the signal-to-noise ratio is significantly reduced by diffracted energy due to a surface with topographic relief (ridge) and dipping events, which would require dip moveout instead of normal moveout. In this plot, strong semblance peaks are only visible above 3.7 seconds, and even there their appearance is more scattered than at comparable depths in figure 4.12. Velocity picking below this depth was very difficult. To help correlate strong reflections with semblance peaks, the corresponding CMP gather was plotted next to the semblance contour plot. The choice of a set of velocity picks started with the correlation to prominent reflections visible in the CMP gather.

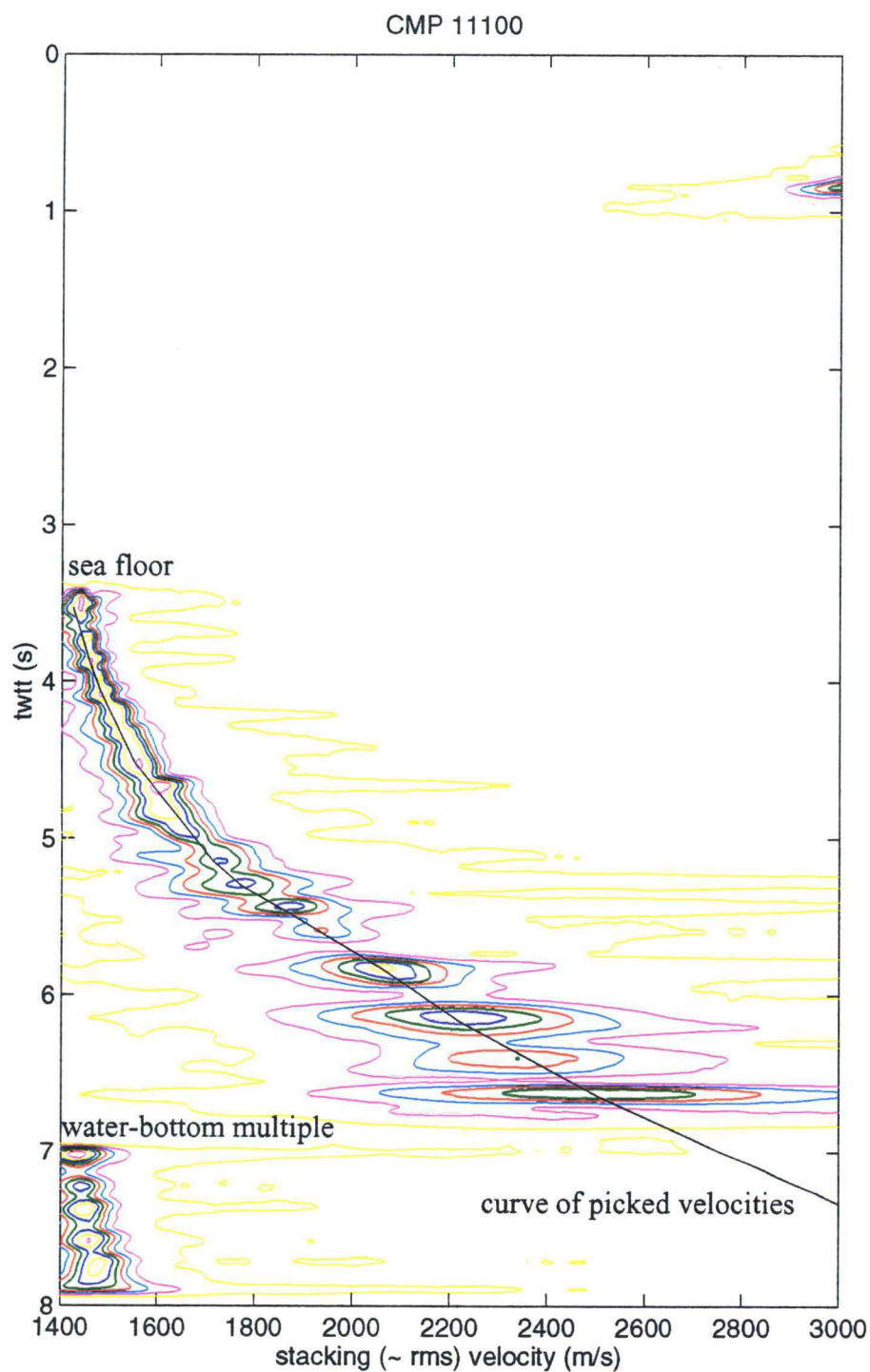


Figure 4.12 Semblance contour plot (calculated at a 100 ms time gate and a velocity increment of 20 m/s) of CMP 11100 of line 1262 located on the Queen Charlotte Trough segment, showing how semblance contour peaks group around continuously greater velocities as twtt increases; sea floor at 3.5 seconds twtt, water bottom multiple first appears at 7 seconds

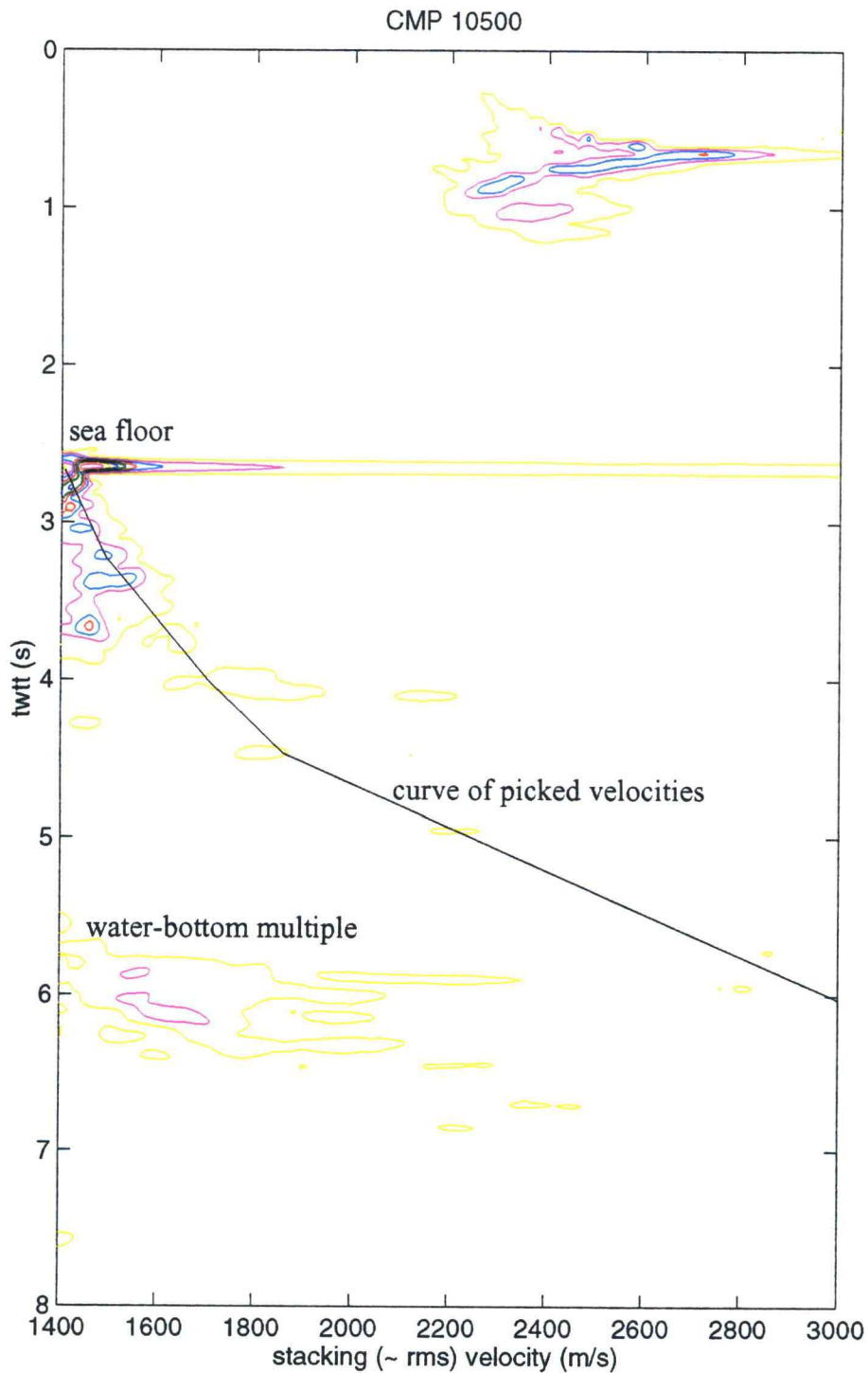


Figure 4.13 Semblance contour plot (calculated at a 100 ms time gate and a velocity increment of 20 m/s) of CMP 10500 of line 1262 located on rough surface of topographic relief and dipping events; S/N ratio is significantly reduced by diffraction energy; strong semblance peaks are visible only above 3.7 seconds and show a more scattered appearance than those at comparable depths in figure 4.12

This first choice was then continuously improved by stacking and using the newly gained information for repeated velocity picking. To better understand this procedure, factors that affect velocity estimates are discussed briefly.

The velocity spectrum was computed along hyperbolic search paths for a range of stacking velocities over a specific two-way time gate. More coarsely chosen gate lengths resulted in less temporal resolution. Gate lengths commonly range between one-half and one times the dominant period in the data (Yilmaz, 1988). A dominant frequency of about 30-40 Hz suggests a gate length of 25-33 ms. Semblance contour plots in this analysis, however, were computed with a 100 ms gate, which reduced computation time and still provided good results for velocity picking. The velocity range should span the stacking velocities that correspond to primary reflections present on the CMP gather. Semblance values were determined over a range from 1400 m/s to 3000 m/s in velocity increments of 20 m/s. Band-pass filtering and gain-corrections can sometimes improve velocity spectra, particularly in gathers with low S/N ratios. The CMP gathers used in this analysis were zero-phase bandpass filtered in the frequency domain with a passband of 10-60 Hz and a filter response slope of 48 db/octave. The  $t^2$ -gain function was applied to have evenly leveled amplitude values over all two-way traveltimes.

Another way to improve the quality of the velocity spectrum is to include more than just one CMP gather in the analysis. A requirement for this is that no dip should be present over the range of these gathers. Semblance contour plots were calculated over four adjacent CMPs (50 m).

#### 4.5.3.3 2-D VELOCITY DISTRIBUTION

To find the optimum velocity distribution for the whole profile, a set of velocity functions was determined located at every 100th CMP-control point. Stacking of CMP gathers at these control points gave a first insight of how well reflections stack in. Stacking of the whole profile or portions of it revealed the quality of the two-

dimensional velocity field, which can be seen in the continuity of reflectors. To verify velocities at specific CMPs, constant velocity panels were used to pick velocities and improve the stack.

Interval velocities are a good approximation to the actual velocity in subsurface layers. They might indicate unreasonably high or low stacking velocities at depth, where resolution of the seismic data is poor, and large variation in stacking velocity causes little change in moveout. Interval velocities for horizontal constant velocity layering ( $v_{stack} \approx v_{rms}$ ) were calculated by using the Dix formula (Appendix B).

The next three figures (figures 4.14, 4.15, and 4.16) present the results of the velocity analysis of line 1262. Figure 4.14 shows the final stacked section, illustrating the locations of CMPs relative to structure. Figures 4.15 and 4.16 then display the two-dimensional stacking and interval velocity distribution. To obtain velocity functions of CMPs between those obtained from velocity analysis every 100th CMPs, SIOSEIS was used to perform a spatial and temporal variation. Iso-velocity spatial variation traces iso-velocity contours through the subsurface and determines the time associated with each velocity. To produce a stacking velocity distribution plot such as the one in figure 4.15, SIOSEIS found velocity-time pairs by iso-velocity spatial variation for every 10th CMP and by linear temporal interpolation every 0.002 seconds. These values were read into MATLAB, and converted to a matrix. The grid-file was then plotted with use of a rainbow color palette and contoured in 0.25 km/s-intervals.

A similar procedure lead to the interval velocity distribution along 1262 (figure 4.16). Here, every column of the grid-file of stacking velocities from figure 4.15 was put value after value into the Dix formula (Appendix B) to compute interval velocities between adjacent elements. As a result, this matrix possesses one row less than the matrix of stacking velocities.

While the stacking velocity distribution looks very smooth, interval velocities calculated at very small time intervals show greater lateral and vertical variations. To show why, a simple velocity function at one CMP of four velocity-time pairs is shown

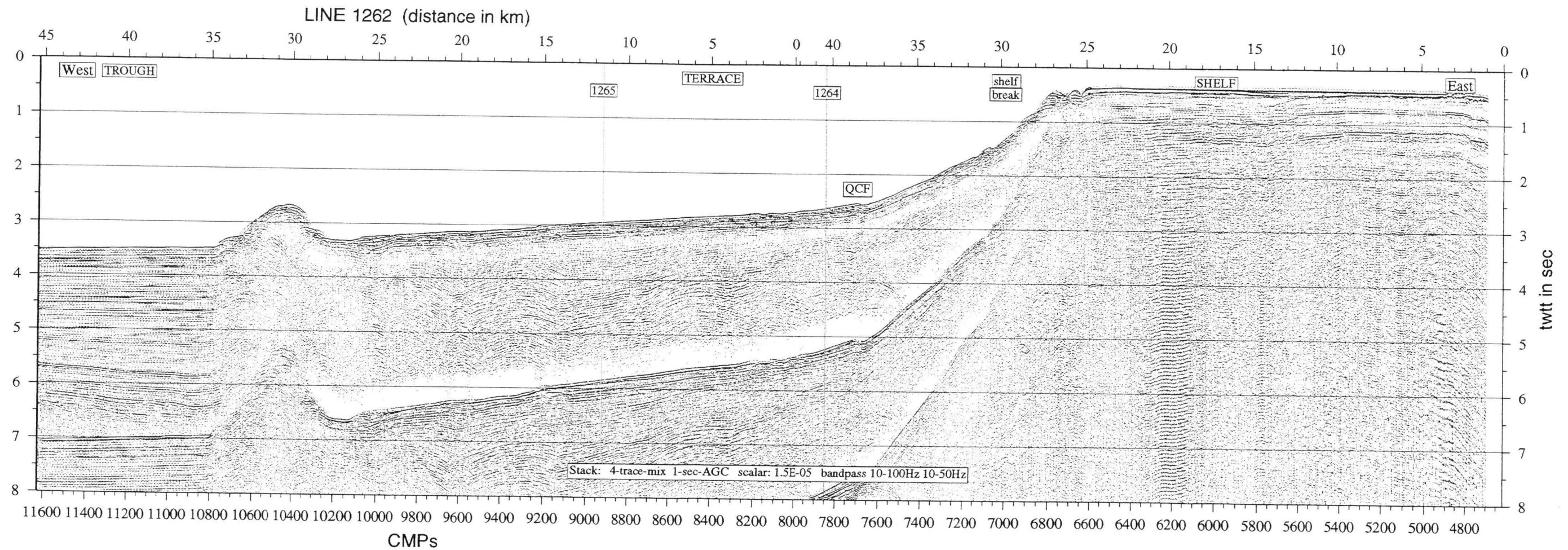


Figure 4.14 Final stacked section of profile 1262, using the stacking velocities as displayed in figure 4.15; marked are the three structural domains, the Queen Charlotte Trough, the Queen Charlotte Terrace, and the continental shelf, as well as the location of the Queen Charlotte Fault zone; the data are displayed after application of a 4-trace-mix, a prestack time-variant bandpass filter (passband 10-100 Hz above and 10-50 Hz below the first water-bottom multiple), and a 1-second AGC; vertical exaggeration: 2.19

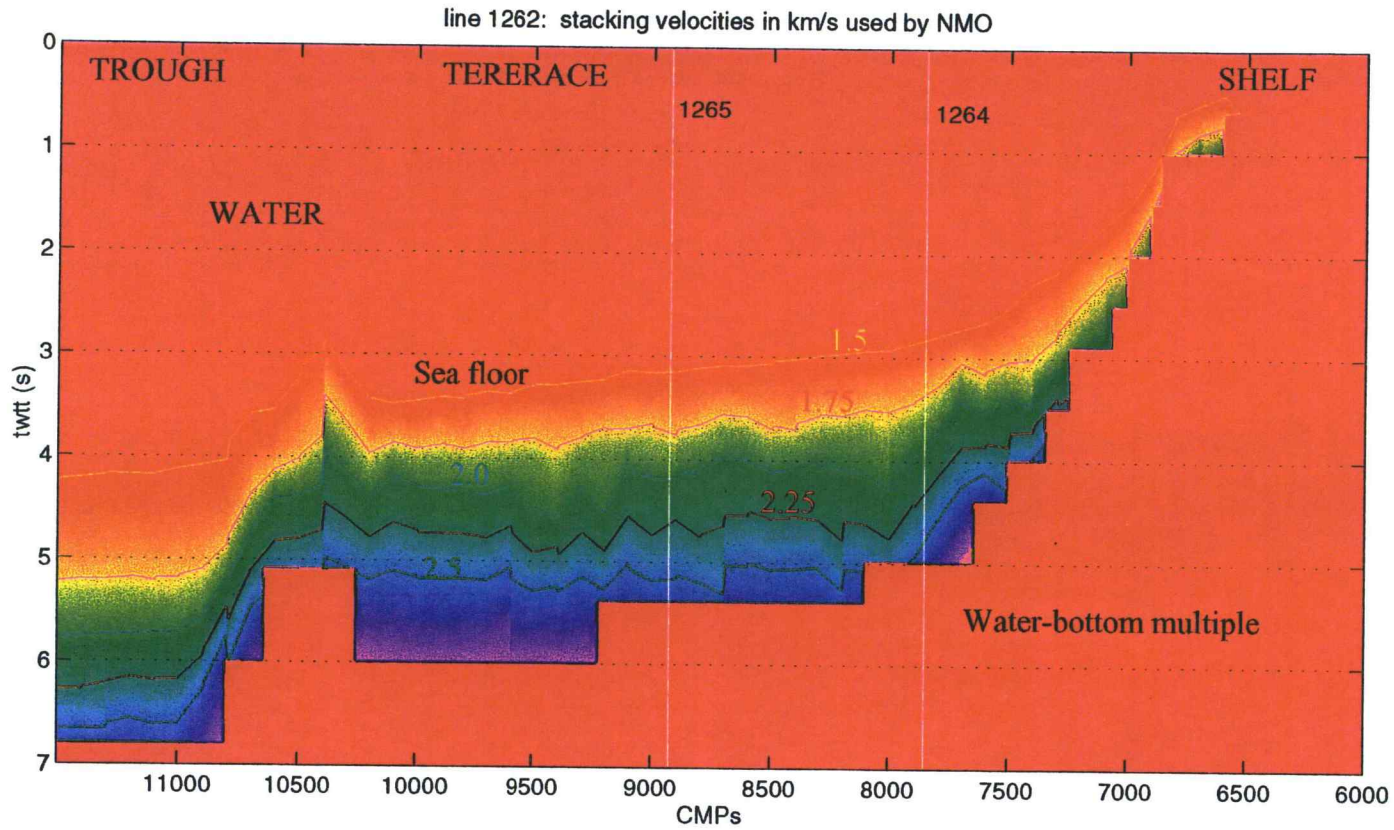


Figure 4.15 Final two-dimensional stacking velocity distribution of line 1262 as used for NMO correction and found by velocity analysis of every 100th CMP and of spatial and temporal variation every 10th CMP and every 0.002 seconds; red area represents the water velocity of 1.5 km/s in shallow portions, and the first water-bottom multiple at depth; stacking velocity contours have intervals of 0.25 km/s

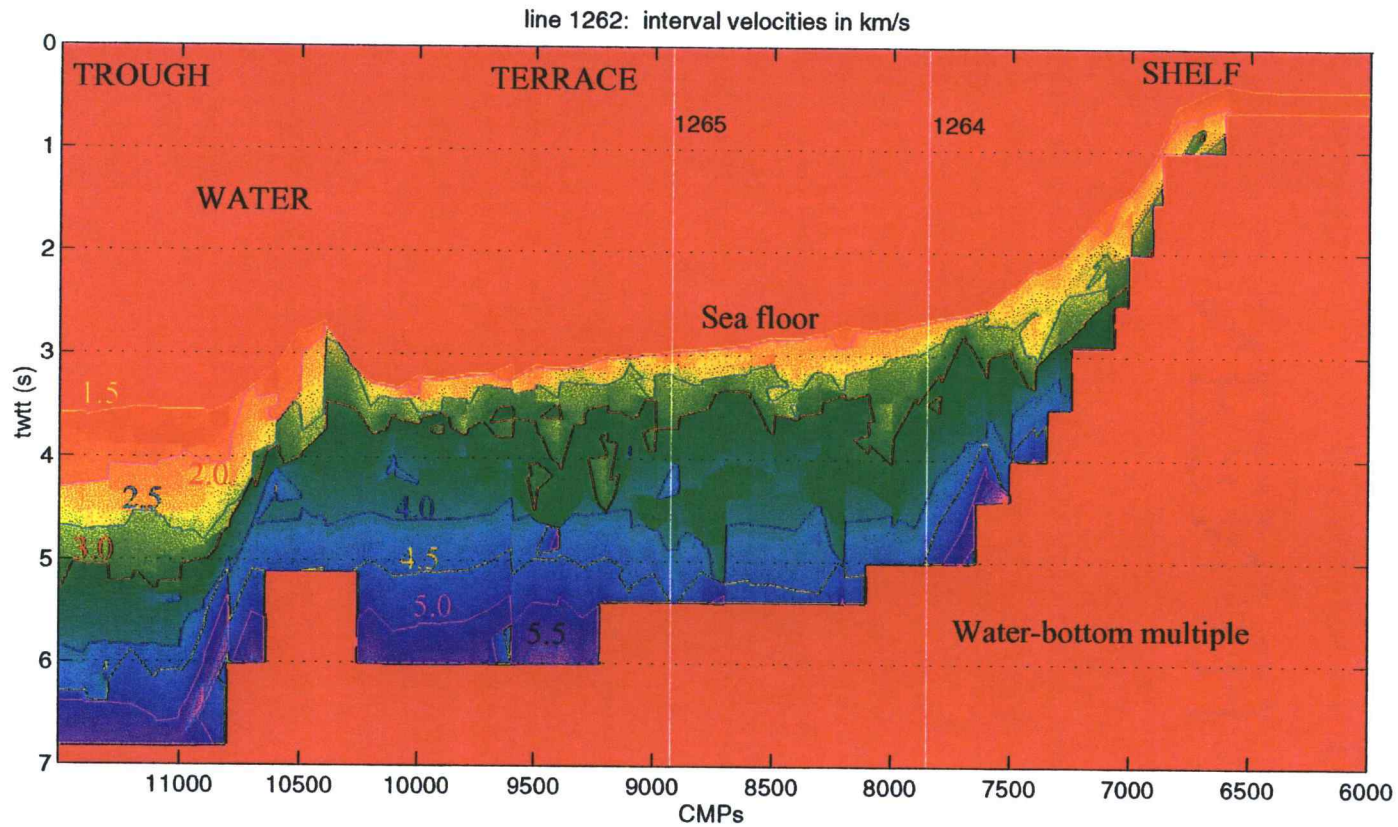
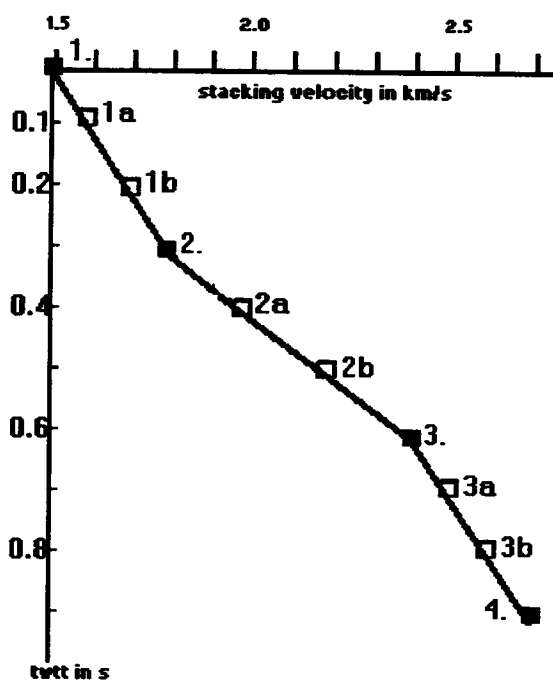


Figure 4.16 Two-dimensional interval velocity distribution of line 1262 found by applying the Dix formula to each column of the grid-file of stacking velocities of figure 4.15; its greater lateral and vertical variations and velocity reversals are partly artifacts produced by poorly constrained picks and their spatial and temporal variation

in figure 4.17 and table 4.6. Linear interpolation in the manner done to find the stacking velocity distribution was used to determine velocity-time pairs between control-points in the vertical direction. Slopes between control-points change abruptly. As seen in the table, interval velocities behave in a way that is less obvious. A linear increase in rms velocities means a linear increase in interval velocities, and slopes change accordingly. But only when rates stay at least constant, interval velocities increase monotonically. As soon as the second derivative of the stacking velocity function assumes a negative value (between control point 3 and 3b), interval velocity decreases to produce a low velocity zone. Spatial interpolation between picked velocity functions enhances the likelihood of such behavior, especially since intercepts at which interval velocities were calculated are very small (0.002 seconds). Small zones of low velocity or lateral variation might not be real, but artifacts of a few poorly constrained velocity picks and their spatial and temporal variation. This is why interval-velocity distributions obtained in this manner can only give an idea of trends and tendencies of actual velocities in rocks. To get a better picture of the layered velocity structure, one must pick stacking velocities along specific reflectors and compute interval velocities between them.

In figure 4.14 the first and second order multiples are very striking and strong features. Due to the increase in water depth they arrive at continuously later times from east to west along the profile. Velocity estimates were strongly influenced by the presence of these multiples. Along the terrace and trough, especially, no high amplitude semblance values could be found at times after sea floor multiple reflections had arrived. On the shelf, water depth is so shallow that high order multiples were attenuated already at a few seconds depth. Unfortunately, the deeper subsurface of the shelf shows little reflectivity, and no continuous events are observable. Generally, velocity functions were linearly extrapolated when reasonable velocity picks were not possible because multiple reflection energy overprinted faint genuine reflections at depth or semblance peaks were simply nonexistent. That is why the area covered by first and higher order multiples were not included in the velocity distribution color schemes of figure 4.15 and 4.16.

Table 4.6 Data values corresponding to graph shown in figure 4.17



	rms velocity in km/s	twtt in s	interval velocity
1.	1.5	0	
			1.6
1a	1.6	0.1	
			1.794
1b	1.7	0.2	
			1.985
2.	1.8	0.3	
			2.506
2a	2.0	0.4	
			2.864
2b	2.2	0.5	
			3.219
3	2.4	0.6	
			3.214
3a	2.5	0.7	
			3.396
3b	2.6	0.8	
			3.396
4.	2.7	0.9	

Figure 4.17 Simple velocity function of four velocity-time pairs; numbers correspond to control points, letters to linearly interpolated values; velocity values are in km/s; first derivative of the stacking velocity relative to time is always positive but its second derivative assumes negative values at control points 3 and 3a; a low velocity zone is present between 3 and 3b.

A constant velocity analysis was carried out at various CMPs (10800, 10900, 11000, 11100, 11200, 11300, and 11500) west of the ridge. Figure 4.18 shows the stacked section from CMP 10700 through 11500 and includes stacking velocities from the same reflectors at CMP 10800, 10900, 11000 and 11300. Between CMPs 11000 and 10800, velocities at comparable depths increase significantly towards the topographic structure, where flat lying marine sediments in the trough to the west seem to be disrupted by a fault. Using these velocities, interval velocities were calculated and presented in figure 4.19 a) (dashed lines for CMPs 10800 and 10900). Interval velocities and thicknesses for the same layers of rock appear to increase toward the ridge. The lateral variation becomes more pronounced at depth and is as high as 2 km/s in places.

Two possible explanations can be found for this phenomenon. First, layers are squeezed, compressed and thickened towards the ridge. This would increase their velocity. It is questionable whether compression that generates an increase in velocity of 2 km/s is likely to occur over a short distance of 200 CDPs ( $\approx 2.5$  km). Also, if the interval velocity had increased, then  $\Delta t$  for that layer should have decreased, which was not the case. The second explanation is lateral heterogeneity. Velocities beneath the ridge and terrace are generally greater than those to the west, as can be seen on the distribution of stacking velocities. Raypaths of seismic waves that were recorded at traces associated with CMPs 10800 and 10900 must have partly traveled through this high velocity medium. The ridge will skew stacking velocities to greater values. Half the spread length ( $2800 \text{ m} / 2 = 1400 \text{ m} = 112 \text{ CMPs}$ ) could be an estimation for how far west from the ridge velocities will be affected. Raypath bending due to higher velocities might further increase this estimate. Adding 120 CMPs to the extent of the ridge at CMP 10800 yields CMP 10920, which is close to CMP 11000, where velocities seem to be "normal" again. This explanation is consistent also with the fact that the closer to the ridge and the deeper the reflector, the greater the deviation from the "normal" velocity function, since waves must have traveled through a larger portion

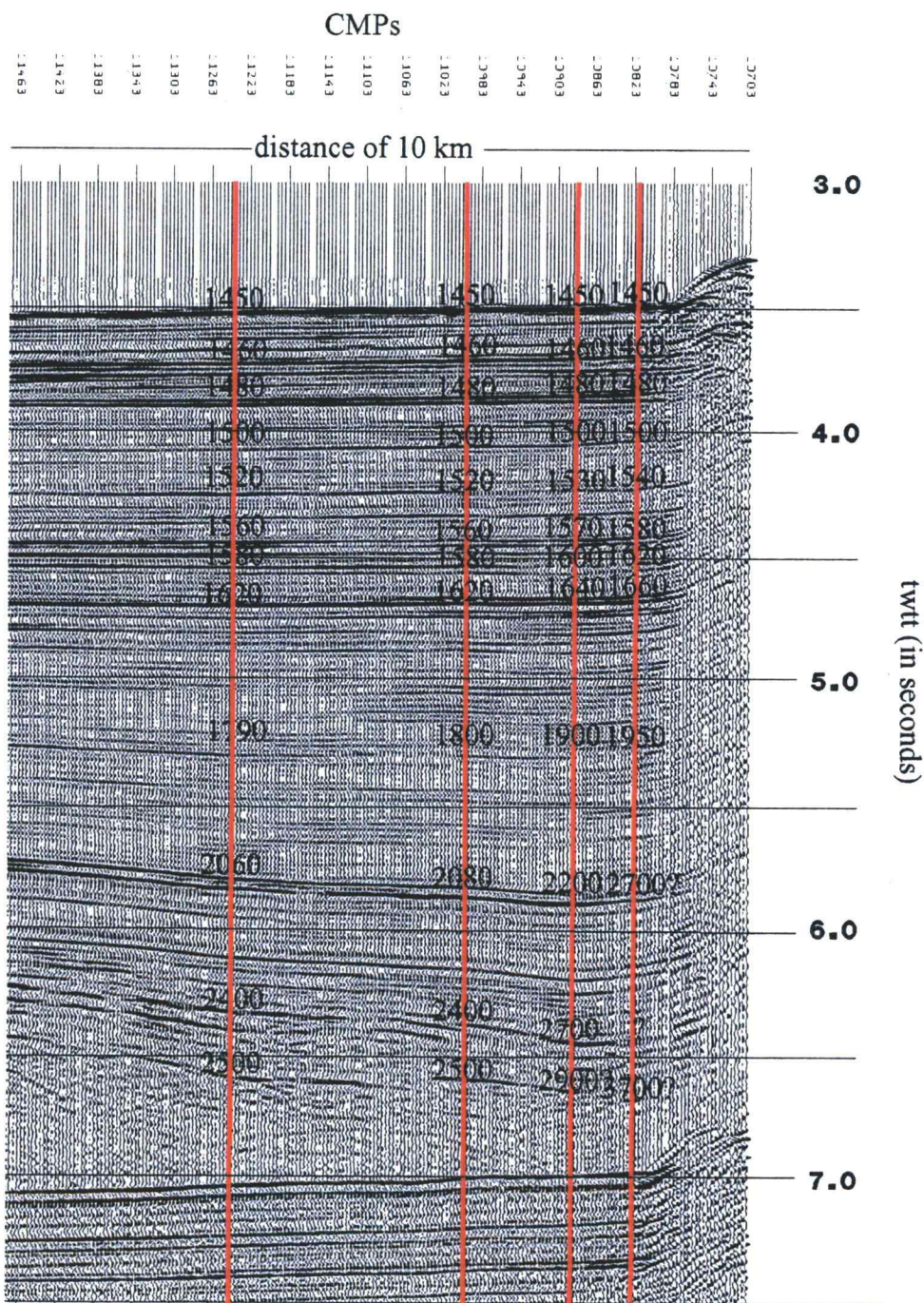


Figure 4.18 Stack of the trough portion of line 1262 from CMP 10700 through 11500; stacking velocities found by a detailed constant velocity analysis for various reflectors are marked and show an increase toward the ridge between CMP 11000 and 10800

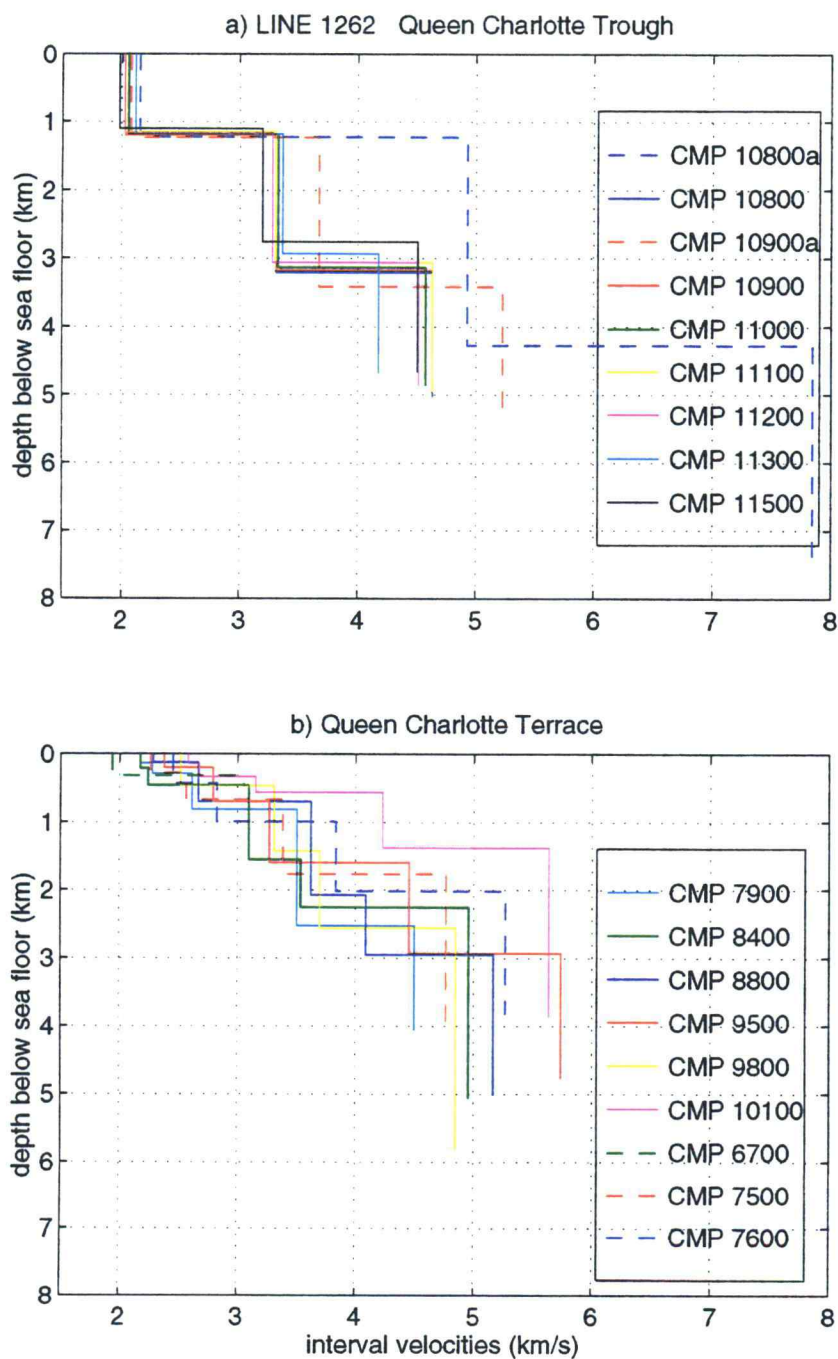


Figure 4.19 Curves of depth below sea floor (in km) versus interval velocities (in km/s) of the a) Queen Charlotte Trough portion and the b) terrace segment of line 1262; interval velocities and thicknesses for the same layers appear to increase for CMPs 10800 and 10900 (dashed), this becomes more pronounced with depth; solid curves for CMPs 10800 and 10900 were calculated by using the same interval velocities as for CMPs further west (11000-11500)

of the higher velocity medium. The second explanation seems to be the more plausible one and assuming its correctness, interval velocities in the vicinity of the ridge were changed to values found further to the west. Looking at figure 4.19 again, the graphs of CMP 10800 and 10900 (solid) perfectly resemble interval velocities and thicknesses of CMPs at greater distance from the ridge. Interval velocity-depth functions (hung from the water bottom) within the Queen Charlotte Trough and Terrace (figure 4.19) display a noticeable difference in their slopes. Interval velocity increases more rapidly in the terrace. An interpretation will follow in subsequent chapters.

#### **4.5.4 CMP Stacking**

The stacking velocity distribution of figure 4.15 including extrapolations to 8 seconds depth finally served as input for normal moveout correction and stacking (figure 4.14).

#### **4.5.5 Post-stack Processes**

Post-stack processing was for the most part concerned with the improvement of display. A linear prediction deconvolution was applied to the shelf area of line 1262 to reduce the periodic reoccurrence of the water-bottom multiple, which reappears at an interval of 0.34 seconds twtt. This time delay of the event to be removed was input as the prediction distance. An autocorrelation of the design window was taken and an inverse filter was designed so that the autocorrelation of the same window after deconvolution resulted in a spike followed by zeros.

For plotting purposes four adjacent traces (50 m) were mixed (added), which for one reduced the profile length and for the other increased genuine continuous reflectors and further attenuated random noise. The mixing of traces, however, is only an advantage if reflector dips over the range of mixed traces are small enough to not

produce smearing or broadening of the reflector, which is the case for most portions of the ACCRETE data.

All stacked sections were displayed by using a mild AGC with a time window of 1 second and the same constant scalar of  $1.5E-07$  to preserve amplitude relationships between traces. The horizontal scale is fixed at 130 mixed traces per inch and the vertical scale set to 0.5 inches per second leading to a vertical exaggeration of 2.19.

The following sections will show stacking and interval velocity distributions as well as the final stacks of lines 1250, 1264 and 1265. Processing for these profiles closely resembled the sequence presented in the flowchart of section 4.4.

#### **4.6 LINE 1250**

Line 1250 comprises the first 85 km of the ACCRETE ship cruise track (figure 3.1) and crosses the Queen Charlotte Trough, the terrace, the shelf break and a small part of the shelf just 30 km south of line 1262. Its westernmost portion bends southward and thereby crosses line 1263 and S.P. Lee 3 (figure 2.2). No major changes in the processing procedure were required for this line, except for CMPs 550-750, where a prestack convolutional zero phase bandpass filter (filter length 156 ms) with a low cut of 20 Hz instead of 10 Hz was chosen, due to the increased low frequency noise in this area. The stacked section is shown in figure 4.20, and its stacking and interval velocity distributions are given in figures 4.21 and 4.22, respectively.

#### **4.7 LINES 1264 AND 1265**

Line 1264 parallels the shelf break at a distance of approximately 15 km. From south to north it ties to line S.P. Lee 3, 1250, S.P. Lee 5, and line 1262. Line 1265 is

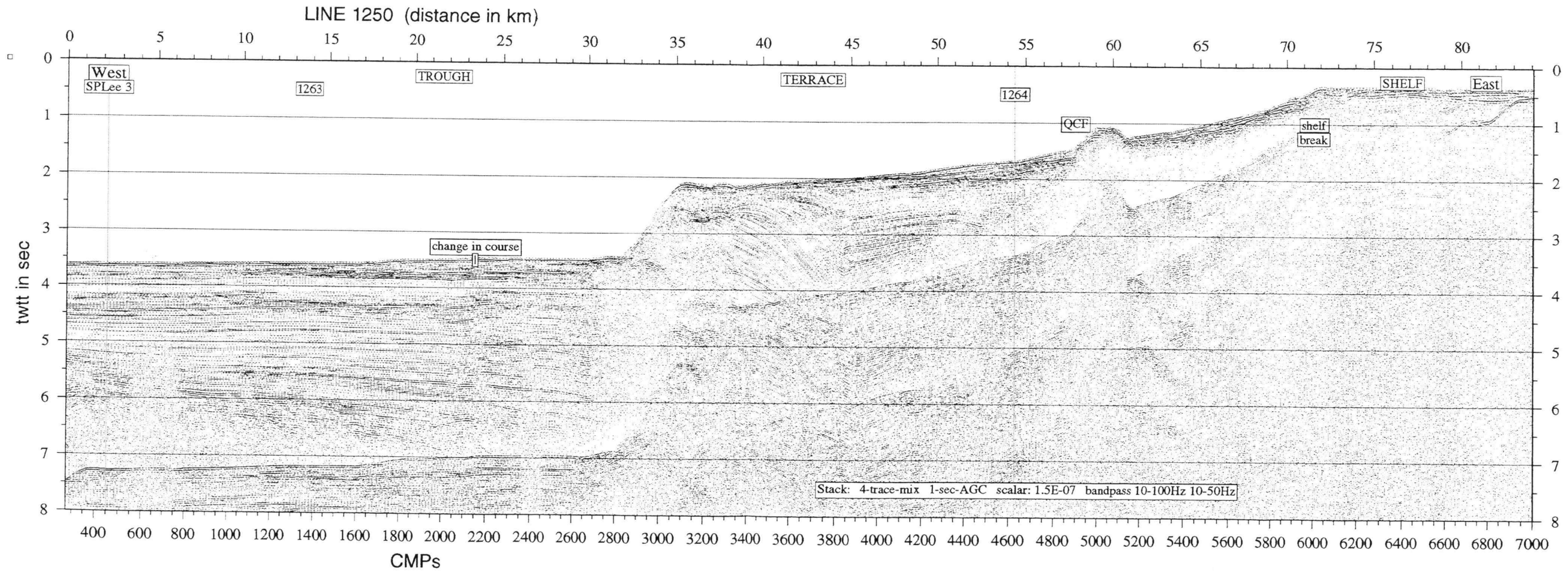


Figure 4.20 Final stacked section of profile 1250, using the stacking velocities as displayed in figure 4.21; marked are the three structural domains, the Queen Charlotte Trough, the Queen Charlotte Terrace, and the continental shelf, as well as the location of the Queen Charlotte Fault zone; the data are displayed after application of a 4-trace-mix, a prestack time-variant bandpass filter (passband 10-100 Hz above and 10-50 Hz below the first water-bottom multiple), and a 1-second AGC; vertical exaggeration: 2.19

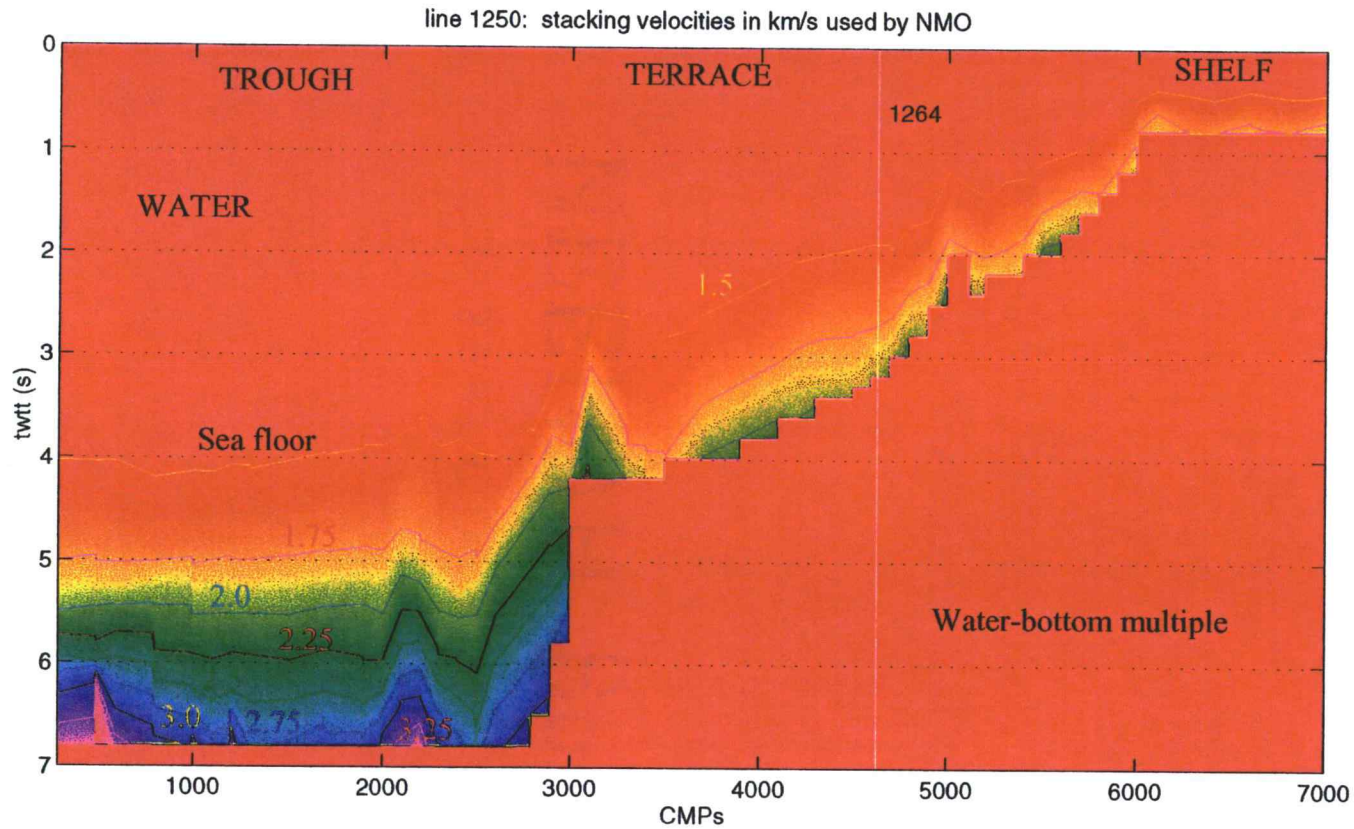


Figure 4.21 Final two-dimensional stacking velocity distribution of line 1250 as used for NMO correction and found by velocity analysis of every 100th CMP and of spatial and temporal variation every 10th CMP and every 0.002 seconds; red area represents the water velocity of 1.5 km/s in shallow portions, and the first water-bottom multiple at depth; stacking velocity contours have intervals of 0.25 km/s

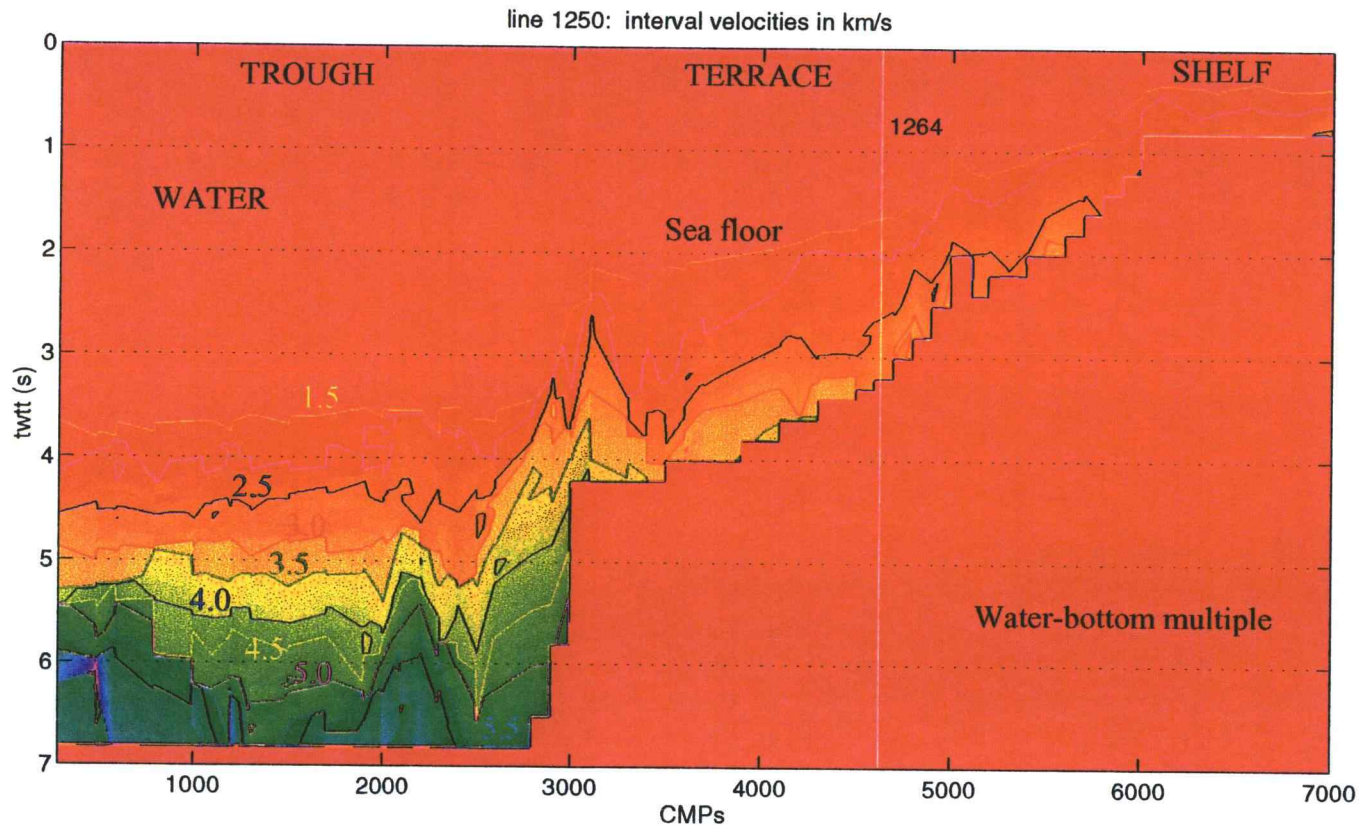


Figure 4.22 Two-dimensional interval velocity distribution of line 1250 found by applying the Dix formula to each column of the grid-file of stacking velocities of figure 4.21; its greater lateral and vertical variations and velocity reversals are partly artifacts produced by poorly constrained picks and their spatial and temporal variation

located entirely on the terrace and forms the last profile that could be recorded within the time limits of the cruise. It is the extension of line 1264 but oriented in a northwest southeast direction crossing lines 1262 and S.P. Lee 5. Unfortunately, the line stops just before the interesting area of transition between trough and terrace is reached. Increased low frequency noise in portions of these profiles required the low cut of the prestack convolutional zero phase bandpass filter to be raised to 17 Hz for CMPs 5000-5195 of line 1264 and for CMPs 275-560 and 901-1160 of line 1265. The following six figures (figures 4.23 - 4.28) demonstrate again the stacked sections and their stacking and interval velocity distributions.

#### **4.8 MIGRATION**

Following stacking, migration is the last principal step of seismic data processing. Reflections in the stacked sections of lines 1250, 1262, 1264 and 1265, especially at regions with structural dip, have a complex appearance. Diffraction hyperbolas are associated with faulting, due to the sharp discontinuities at both ends of the reflector. Irregular water-bottom topography can consist of point sources that produce diffractions as well. Bowtie-like features occur at synclinal structures, whereas anticlines look much broader than they really are.

The main goal of migration is to transform these undesired features of the stack into a display that more accurately reflects subsurface geology. Although a geologic cross section's vertical axis should be depth, migrated data is mostly presented in two-way travel time. One advantage is that computing a time migrated section is much less time consuming; another is that it permits comparison of stacked and migrated sections to evaluate their validity. This is an important part of the interpretation process. To obtain a depth migrated section one needs a much more accurate estimate of velocity. If this is not available, time migration may be preferable to depth migration.

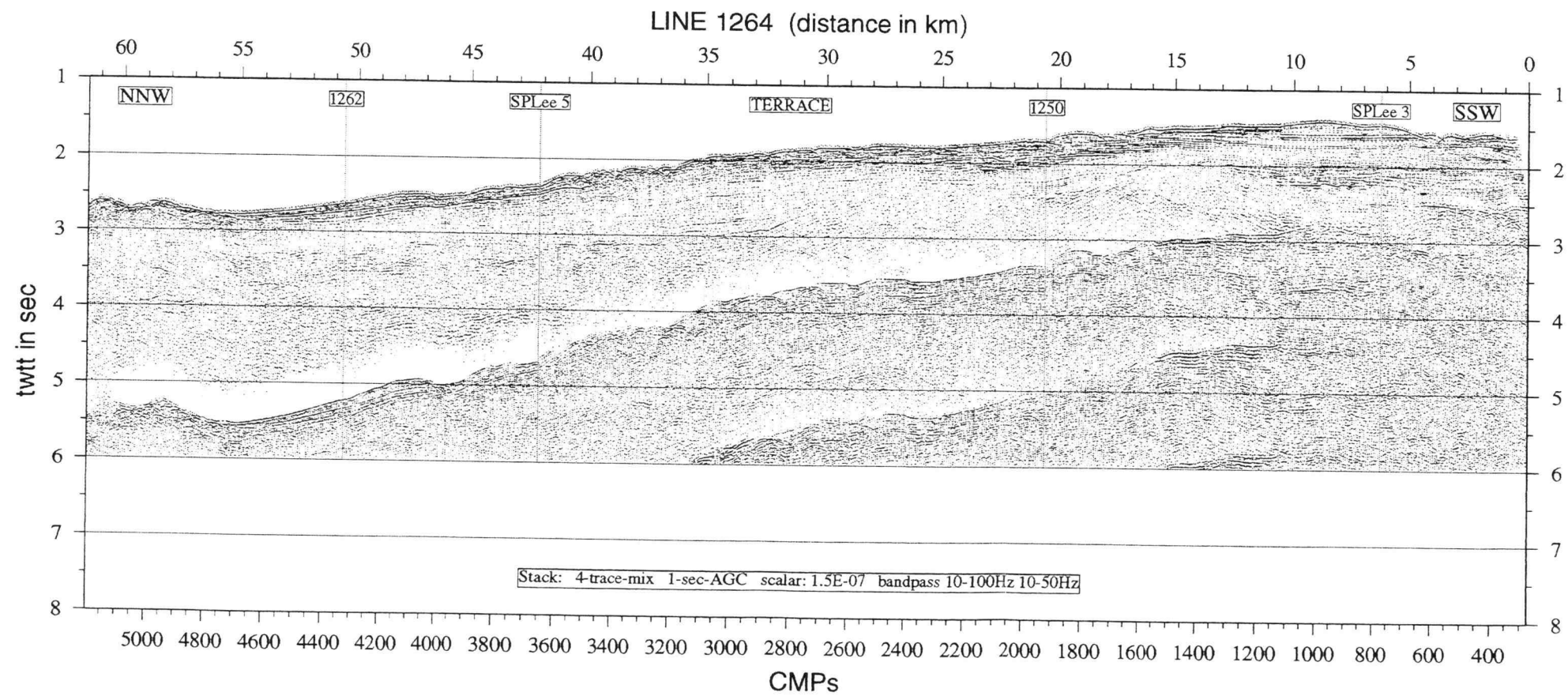


Figure 4.23 Final stacked section of profile 1264, using the stacking velocities as displayed in figure 4.24; the data are displayed after application of a 4-trace-mix, a prestack time-variant bandpass filter (passband 10-100 Hz above and 10-50 Hz below the first water-bottom multiple), and a 1-second AGC; vertical exaggeration: 2.19

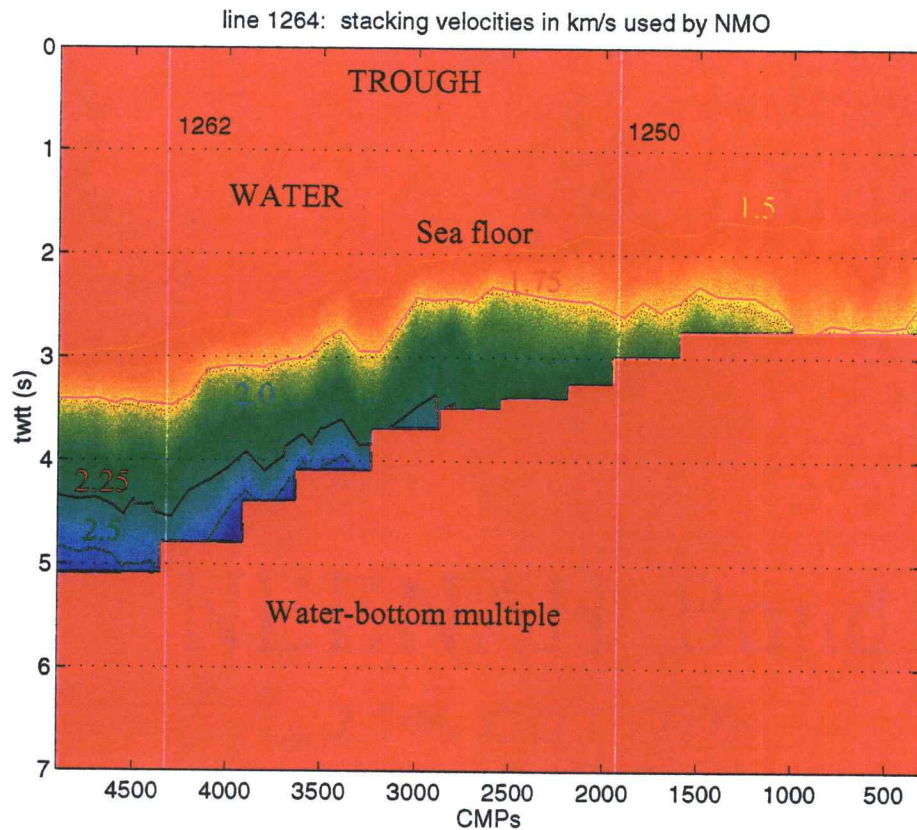


Figure 4.24 Final two-dimensional stacking velocity distribution of line 1264 as used for NMO correction and found by velocity analysis of every 100th CMP and of spatial and temporal variation every 10th CMP and every 0.002 seconds; red area represents the water velocity of 1.5 km/s in shallow portions, and the first water-bottom multiple at depth; stacking velocity contours have intervals of 0.25 km/s

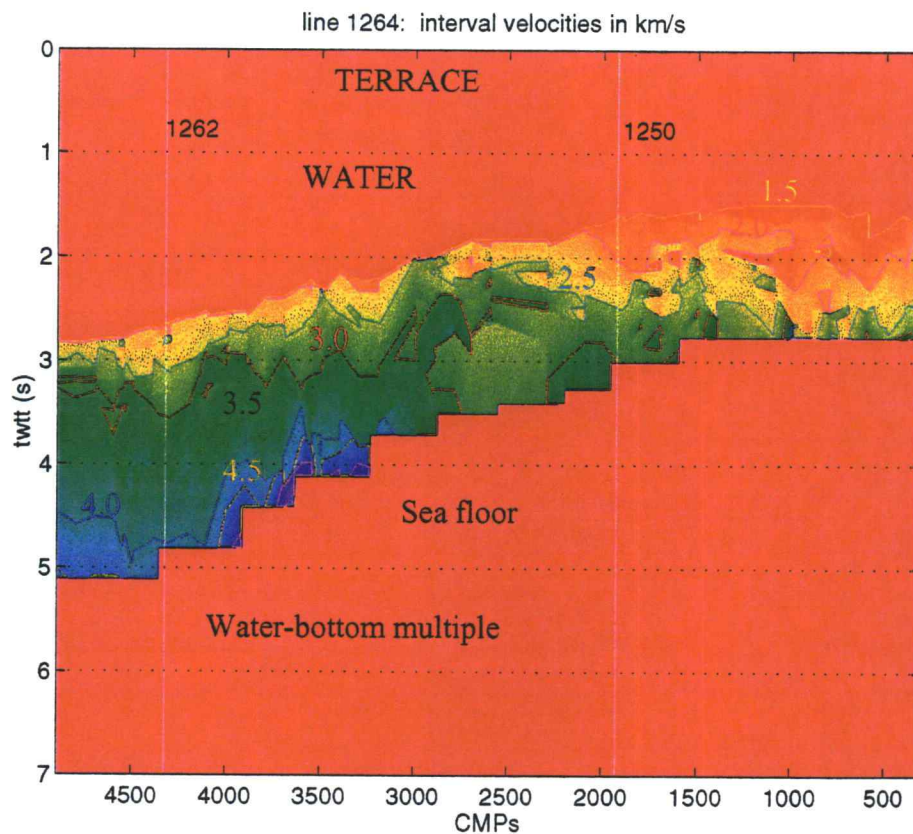


Figure 4.25 Two-dimensional interval velocity distribution of line 1264 found by applying the Dix formula to each column of the grid-file of stacking velocities of figure 4.24; its greater lateral and vertical variations and velocity reversals are partly artifacts produced by poorly constrained picks and their spatial and temporal variation

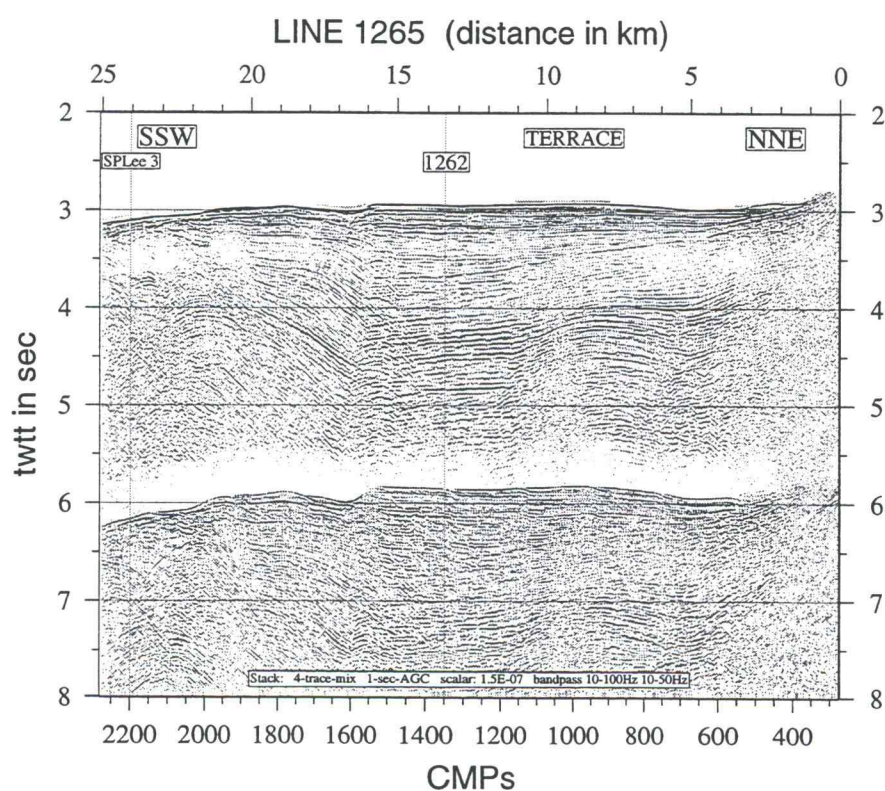


Figure 4.26 Final stacked section of profile 1265, using the stacking velocities as displayed in figure 4.27; the data are displayed after application of a 4-trace-mix, a prestack time-variant bandpass filter (passband 10-100 Hz above and 10-50 Hz below the first water-bottom multiple), and a 1-second AGC; vertical exaggeration: 2.19

line 1265: stacking velocities in km/s used by NMO

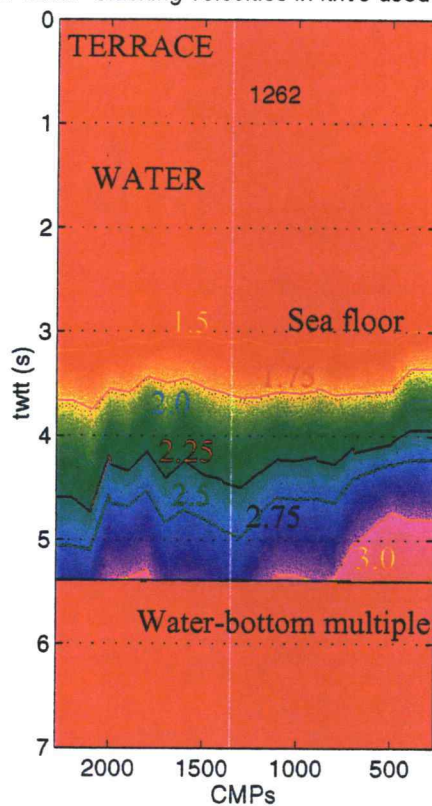


Figure 4.27 Final two-dimensional stacking velocity distribution of line 1265 as used for NMO correction and found by velocity analysis of every 100th CMP and of spatial and temporal variation every 10th CMP and every 0.002 seconds; red area represents the water velocity of 1.5 km/s in shallow portions, and the first water-bottom multiple at depth; stacking velocity contours have intervals of 0.25 km/s

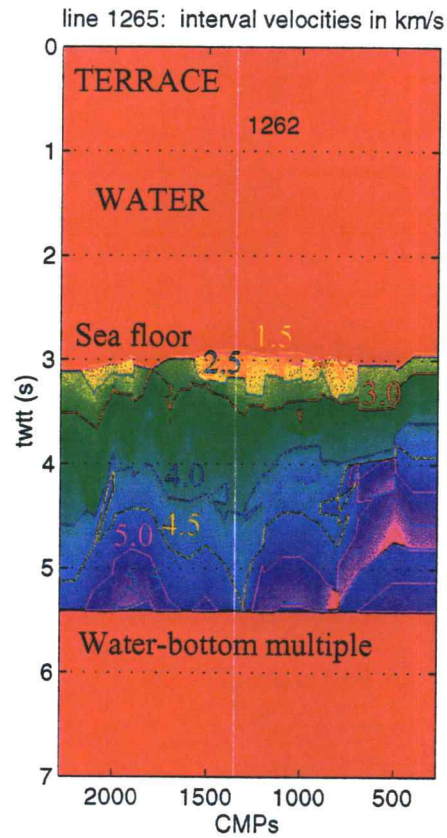


Figure 4.28 Two-dimensional interval velocity distribution of line 1265 found by applying the Dix formula to each column of the grid-file of stacking velocities of figure 4.27; its greater lateral and vertical variations and velocity reversals are partly artifacts produced by poorly constrained picks and their spatial and temporal variation

Generally, migration collapses diffractions and shortens, steepens and moves reflectors in the updip direction to place them at their true subsurface position. Spatial resolution is improved by delineating detailed subsurface features, making it easier for the interpreter to detect faults and derive a structure map, which will be of major concern in the next chapter.

Several migration algorithms exist, but none of these algorithms explicitly models multiple reflections, surface waves or noise. Such energy is treated the same as primary reflections. That is why ease of interpretation of a migrated section depends mainly on the quality of the stacked section from which it is derived. The different migration algorithms and their advantages and disadvantages are briefly discussed in Appendix C.

The 45-degree-finite-difference algorithm is implemented in SIOSEIS and was used to migrate the ACCRETE profiles. This method is capable of handling dips only up to angles of 45-degrees with sufficient accuracy. On the other hand, it has fewer problems dealing with lateral velocity variations unless they are abrupt. This was considered to be more significant for the ACCRETE data, for the stacking velocity distributions presented in the previous sections contain lateral variation. In addition, strongly dipping reflectors are only significant at the ridge-like structure which forms the westward boundary of the terrace in line 1262, and at the more steeply sloping portion of the terrace close to the shelf break. Application of prestack depth migration to these regions would be useful.

One important parameter of finite-difference migration is the depth-step size. For time migration this step size ( $\Delta\tau$ ) will be in seconds. Small step sizes improve the migration result, but too small a step size requires large amounts of computer time. Here, a step size of 50 ms was chosen.

The abrupt edges of the seismic section, where the profile terminates, require a pad zone to prevent data that should migrate past these edges from being reflected back in. The pad zone contains traces of zero amplitude to allow dipping events to be

moved into this area. The different sections of the ACCRETE profiles were padded with 200 traces on each side.

The finite-difference migrated profiles 1262, 1250, 1263, 1264 and 1265 are presented in chapter 5 along with their structural interpretation. A  $t^2$ -gain correction was applied premigration, and energy below the first water-bottom multiple was muted before migration to prevent multiples from being migrated into the section. Some overmigration smiles or smearing are still visible in the deeper parts of the terrace in lines 1262 and 1265. This could be due to bursts of amplitude in the input section, which were migrated into smiles. Smearing occurs preferentially at the bottom and side boundaries of the section. The S/N ratio is lower at the side boundaries because of the decreasing fold and the faintness of genuine events relative to a stable noise level. At depth, velocities are high and more difficult to pick, resulting in greater uncertainty.

Overall, the finite-difference migration produced satisfactory results, except at the location of the ridge in profile 1262. Special treatment of strong dips before stacking is necessary there to properly image this region and to extract all possible structural information from the data.

The following chapter will deal with the geologic interpretation of all four lines presented here, as well as of line 1263, which was partly processed by Kristin M. M. Rohr, Geological Survey of Canada. Three different types of data display will be used for this purpose. The stacked section is of great importance to help the interpreter evaluate the quality of the time migrated sections. To get an image of orientation and dip of the structure, a time-to-depth conversion was conducted along vertical raypaths, using the same stacking velocity distribution as was used for the stack and migration process. This method is strictly valid only for velocity that varies solely with depth and can not handle structural dip. However, small and smooth velocity variations produce reasonable depth conversions. For a complete display of processing results, figure 4.29 presents profile 1262 as an example of a time-to-depth converted section. The data were plotted at a horizontal scale of 130 mixed traces per inch and a vertical scale of 0.5 km/ inch; the vertical exaggeration is 3.29. Although a depth section is the

preferred result of a geologic interpretation, only time-migrated sections were used here. After dominant reflectors were traced and marked on the migrated profiles, results at certain CMPs were converted to depth to be used as constraints on gravity forward modeling in chapter 6.

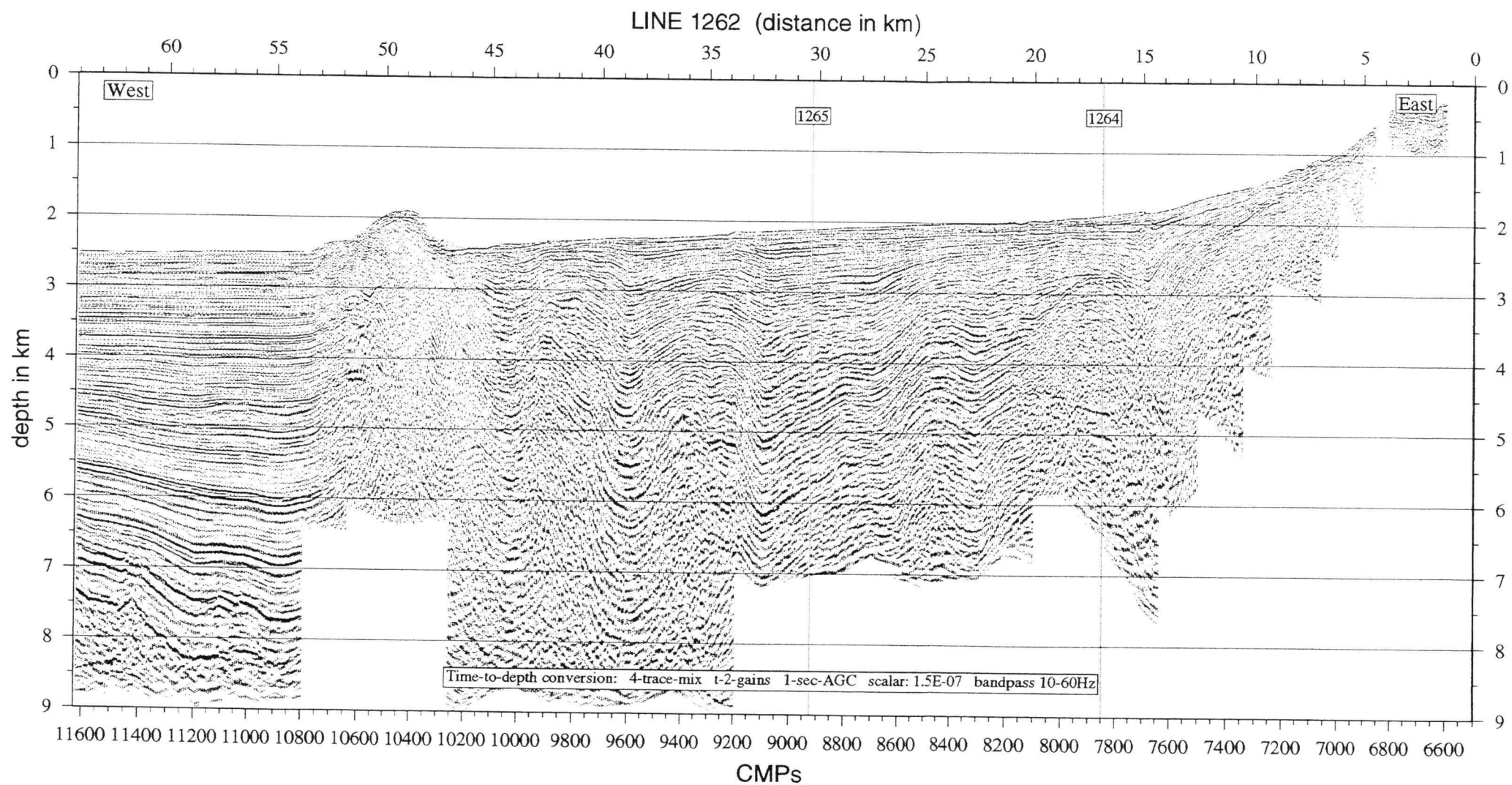


Figure 4.29 Time-to-depth conversion of the migrated section of line 1262 by using the stacking velocity distribution of figure 4.15; this method is strictly valid for velocity that varies with depth only; vertical exaggeration: 3.29

## **5. GEOLOGIC INTERPRETATION AND DISCUSSION OF SEISMIC DATA**

Seismic data are very useful in revealing features of sedimentary basins and deeper structure. The tectonic setting can govern the type of structures that are present in an area and how structural features relate to each other. In this thesis, structural information was obtained on the Queen Charlotte Fault in the region offshore Dixon Entrance. The ACCRETE profiles, which were shot in different directions to obtain three-dimensional information, were used:

- (1) to map faults, channels, and folds (structural analysis);
- (2) to delineate seismic sequences bound by unconformities, which represent different time-depositional units, and to recognize seismic facies from seismic reflection characteristics, which might suggest the depositional environment (stratigraphic interpretation);
- (3) to construct a cross section of each profile, that contains information from (1) and (2);
- (4) to correlate features across profiles to obtain a three-dimensional image;
- (5) to use the above results as input to forward gravity modeling of two profiles across the plate boundary
- (6) to deduce information on the geologic and tectonic history of the area.

The final interpretation must be consistent with all the seismic data that is available (location of ACCRETE profiles and other seismic lines shown in figure 2.2). It should also be consistent with other geological and geophysical information about this area, including gravity and magnetic data, heat flow, well logs, surface morphology and geology. Unfortunately, no well data were available to relate actual geology to the ACCRETE seismic data set in Dixon Entrance. However, a gravity model will be constructed from the seismic structural interpretation (chapter 6). Also, the location of the Queen Charlotte Fault trace from GLORIA sidescan data will be integrated into the interpretation.

## **5.1 GEOPHYSICAL ASSUMPTIONS AND DEFINITION OF UNITS**

The following fundamental assumptions (Sheriff and Geldart, 1987) were implicit in all subsequent interpretations. Acoustic-impedance contrasts in the Earth reflect energy. These contrasts are aligned along deposition and erosional time lines, which are surfaces that at one time have been the surface of the earth. The thickness of consecutive surfaces is much smaller than seismic data can resolve, but due to their parallelism, constructive interference over a widespread area with slow lateral changes produces coherent line-ups of reflection events. Sets of subparallel events are subdivided into units, which have angular relations to each other. Adjacent units represent periods of sediment deposition in different environments or tectonic regimes. Their boundaries, referred to as unconformities, generally indicate a gap in geologic time, during which sediments were tectonically tilted, not deposited, or eroded away (hiatus). Unconformities are often the more prominent reflectors because the nature of the sediments changed across them to form a large acoustic-impedance contrast. By tracing these prominent events, which bound whole depositional sequences or facies, across all the profiles a map can be constructed which represents the geologic structure of unit surfaces.

## **5.2 STRUCTURAL FEATURES**

The type of tectonic setting influences strongly what structural features are dominant and how they relate to each other. The Queen Charlotte Transform Fault Zone in the region off Dixon Entrance is predominantly a strike slip fault with a small component of convergence. The stress produced by plate movement of this kind is typically confined to a relatively narrow linear zone along the principal strike-slip direction and is relieved mainly through structural features concentrated on a single master fault or distributed over a set of parallel faults (Harding and Lowell, 1979).

Secondary stresses account for secondary structural features, these in turn produce tertiary features, and so forth.

Basement-involved wrench-faulting is typical for transform plate boundaries and varies between pure strike-slip, convergent, or divergent wrenching depending on the orientation of the plate boundary relative to regional plate motion (Harding and Lowell, 1979). The primary wrench fault is commonly accompanied by secondary features that are oriented en echelon at angles of about  $30^\circ$  (thrusts or folds) or  $60^\circ$  (normal faults) to it (Figure 5.1) (Christie-Blick and Biddle, 1985). These structures are consistently overlapping, aligned parallel with each other but oblique to the zone of deformation, and tend to steepen with depth. Also observed in model studies involving clay or unconsolidated sand are synthetic strike-slip faults or conjugate Riedel (R') shears, secondary synthetic faults or P-shears, or faults parallel to the principal displacement zone (Christie-Blick and Biddle, 1985). Because rocks are heterogeneous, and because early-formed structures rotate during continuing deformation, geological examples tend to be more complicated, and observed arrangements of structures do not necessarily conform to those predicted by models. A component of convergence along the transform boundary promotes the occurrence of upward-spreading fault zones over a high-angle fault stem, called flower-structures, whose elements have reverse separation. Flower structures are very distinctive in seismic data, much more so than pure strike slip faults, which do not possess a vertical throw. The following detailed interpretation of the seismic sections revealed the presence of such structural features.

### **5.3 PROCEDURE**

To facilitate the interpretation process the region of the Queen Charlotte Fault zone was subdivided into its three structural segments: the continental shelf and shelf break, bounded by the Queen Charlotte Fault to the west; the Queen Charlotte Terrace or continental slope; and the Queen Charlotte Trough. Supplementing the ACCRETE

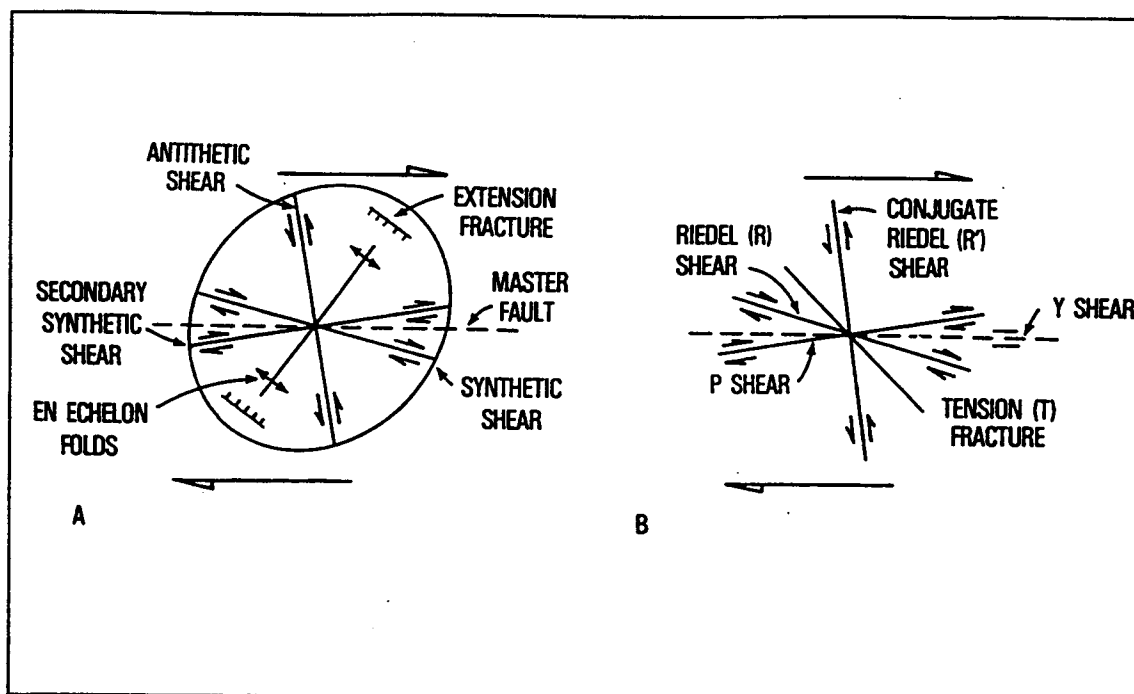


Figure 5.1 The angular relations between structures that tend to form in right-lateral simple shear under ideal conditions, compiled from clay-cake models and from geological examples; (A) Terminology superimposed on a strain ellipse (from Wilcox et al., 1973); (B) Riedel shear terminology, faults with reverse separation tend to develop parallel to the orientation of the fold in A (from Christie-Blick and Biddle, 1985)

profiles is a set of four 24-fold multichannel seismic reflection lines that were collected in 1977 by the US Geological Survey and the Geological Survey of Canada on the research vessel S.P. Lee (Rohr et al., 1992). Their locations, as well as the three structural segments, are shown in figure 5.2.

Processing of the S.P. Lee data included a spherical spreading correction, velocity analysis, band-pass filtering and stacking (Rohr et al., 1992). Snively et al. (1981) interpreted the northernmost of these lines which lies about 10 km south of line 1262. Although the quality of the S.P. Lee stacks is inferior to the ACCRETE profiles, an interpretation of all four lines was undertaken to constrain a more complete tectonic model.

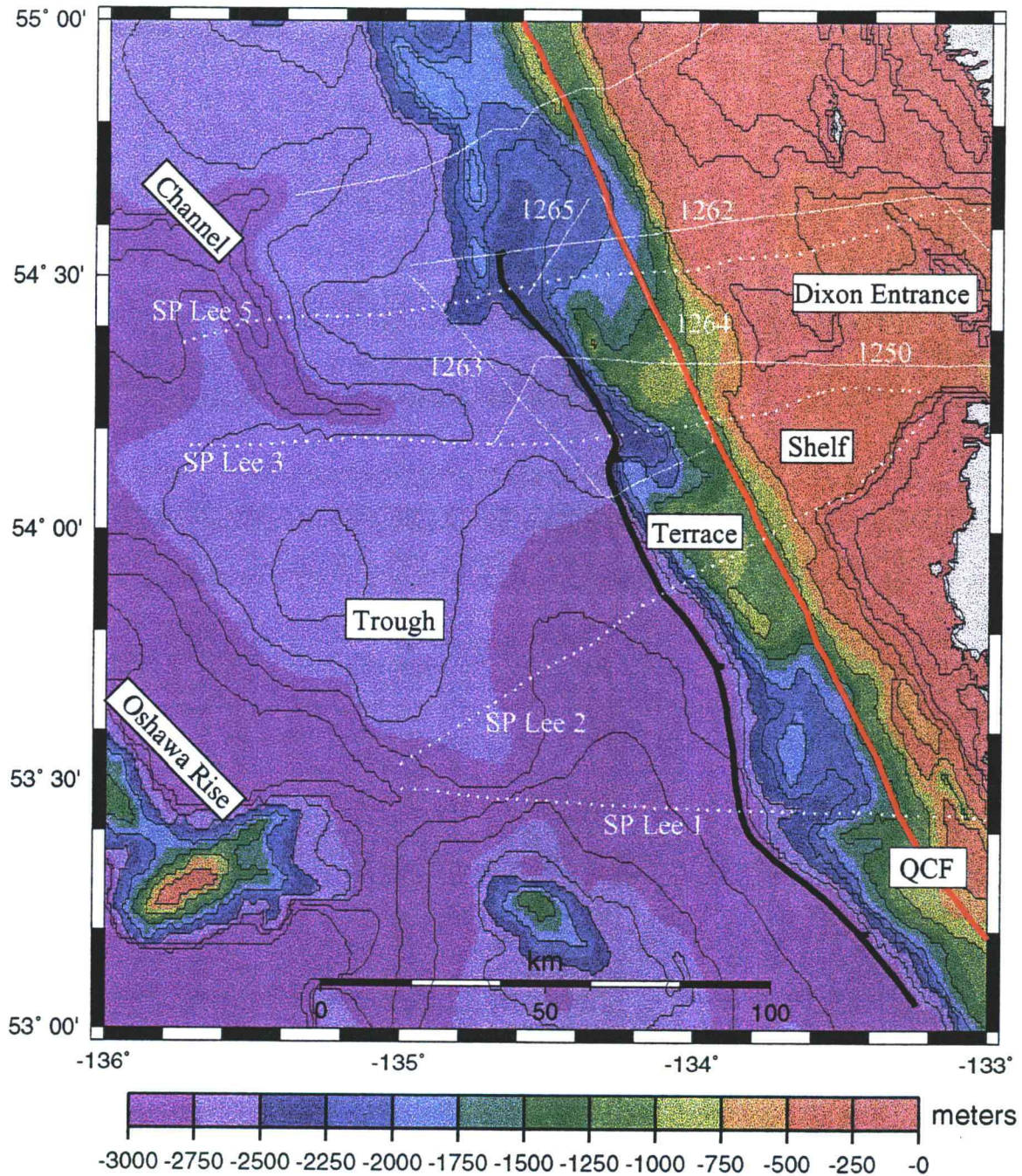


Figure 5.2 Location map of all interpreted profiles of this study overlain on bathymetry (in meters); shown also are the three structural segments, the Queen Charlotte Trough, the Queen Charlotte Terrace, and the continental shelf off Dixon Entrance; the western terrace boundary is marked by a significant step in bathymetry (black line), its eastern boundary by the Queen Charlotte Fault (QCF)

For the ACCRETE profiles, interpretations were based on migrated sections, but features are compared to unmigrated stacks to be aware of possible migration errors. During structural analysis, events were followed throughout each seismic section, and faults identified where reflections are displaced. Ideally, reflections terminate abruptly on each side of the fault. Diffractions, however, if not removed by migration, make the fault plane less clearly visible.

Since the attitude of seismic reflections follows that of depositional time lines, rather than facies changes, a seismic-sequence analysis was carried out by identifying time-depositional units. A unit is confined by unconformities, which are easy to recognize in seismic data if they are angular. Angular unconformities were then mapped through regions where such angularities ceased to exist. Reflections of unit boundaries were then checked for consistency on the stacked sections at CMPs of intersecting lines and the same horizons and faults were correlated between profiles. Results were displayed in geologic cross sections and maps of unit thickness or structural features to obtain a three-dimensional image.

In the next step, it is attempted to tie the structural information to geologic history by determining relative ages of different horizons. Absolute age correlation with the geologic time scale was difficult, due to the lack of well data. Finally, the interpreted profiles are converted to depth and used as input for gravity modeling.

#### **5.4 THE QUEEN CHARLOTTE TROUGH REGION**

Profiles that supply information on the Queen Charlotte Trough are lines 1262 (figure 5.3), S.P. Lee 5 (figure 5.4), 1250 (figure 5.5), S.P. Lee 3 (figure 5.6) and 1263 (figure 5.7). As described in chapter 4, lines 1262 and 1250 cross the Queen Charlotte Fault, the terrace and a small portion of the trough, from west to east. S.P. Lee lines 5 and 3 also cross these features and continue an additional distance of almost 70 km westward toward the Oshawa Rise (figure 2.2). Line 1263 is oriented in a northwest-southeast fashion, to tie all above lines together. S.P. Lee 1 (figure 5.8) and 2 (figure

5.9) show the structure further south, west of the northern Queen Charlotte Islands (see figure 2.2 or figure 5.2 for location).

#### 5.4.1 Basement

Oceanic basement can be identified over the entire trough region on all profiles (blue line on interpreted sections) by the change in reflectivity from flat-lying, continuous reflectors to a rougher reflection pattern. This acoustic basement is considered the top of the oceanic crust. On the S.P. Lee stacked sections the interface shows many strong hyperbolae, indicating a rough surface, whereas on the migrated ACCRETE lines the interface is resolved by migration into a hummocky and partly disrupted strong reflector. Line 1263 (figure 5.7) exemplifies the change in appearance from a continuous acoustic basement between CMPs 275 and 2000 to broken-up pieces of it, visible as discontinuous events from CMP 2000 to CMP 4400, where it becomes more coherent again. This is an interesting observation as it coincides with the location between two nearly vertical disruptions of the sediments and possible basement involvement at CMP 2300 and CMP 4320 (called N-S fault and S-fault in figure 5.7). Faulting will be discussed in more detail below.

On lines 1262 and 1250 (figures 4.16 and 4.19), interval velocities within the top layers of the basement fall in the range of 5-5.5 km/s ( $\pm 0.5$  km/s). This value is not very well constrained and was obtained by only one additional velocity pick below the assumed sediment-basement interface (see figure 4.12). Nevertheless, this velocity corresponds well with velocities obtained from refraction work west of the southern Queen Charlotte Islands and Moresby Island in comparable oceanic crust. Horn et. al. (1984, figure 2.7) found velocities of 3.8-5.2 km/s for a layer interpreted as "slightly sheared pillow basalts and spilites" within the upper oceanic crust. Dehler and Clowes (1988, figure 2.11) associated a velocity of 5.0 km/s with tholeiitic basalts and defined the top of the oceanic crust as composed of a 3.8 km/s-section of basaltic pillow lavas

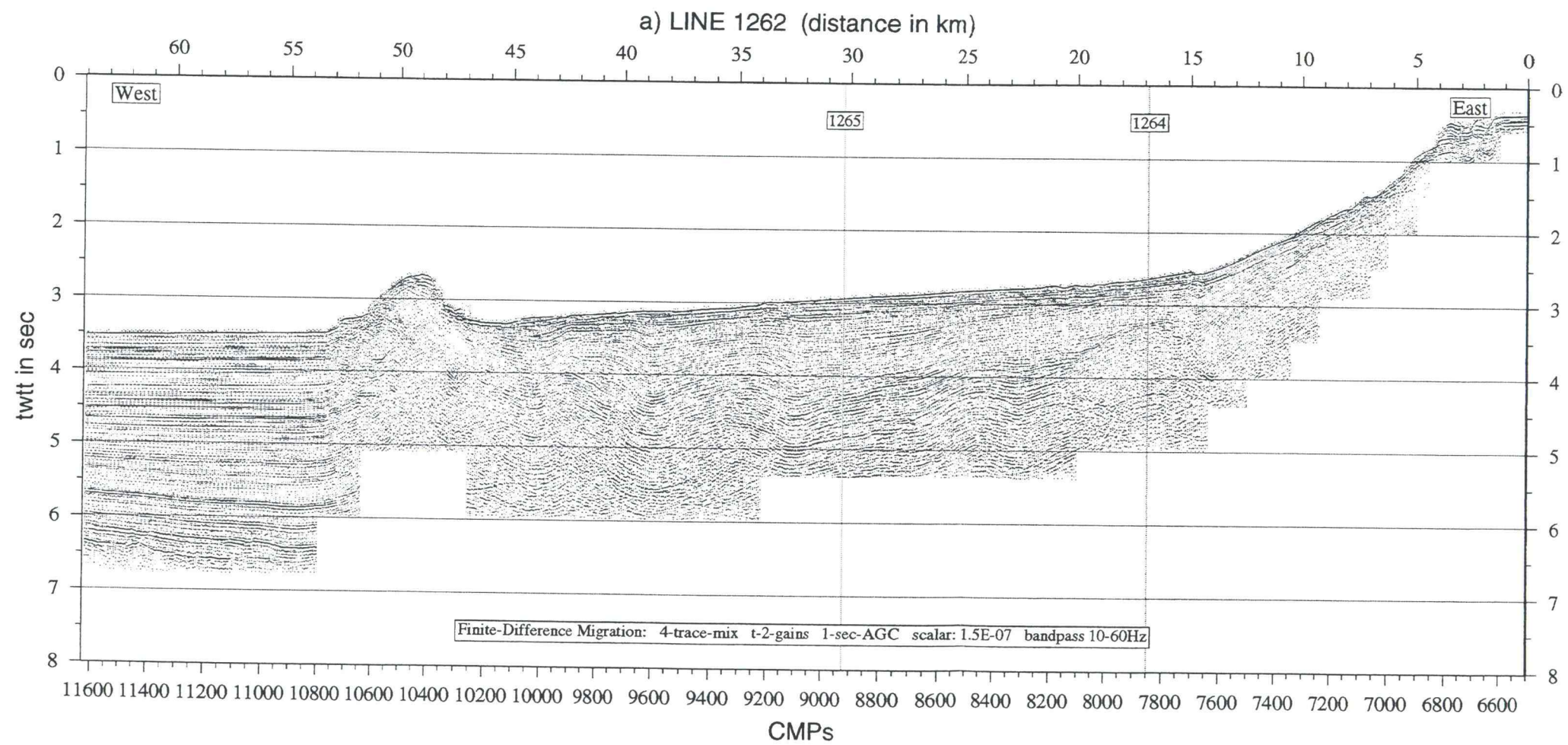


Figure 5.3 a) Finite-Difference Migration of line 1262; intersections with other lines, and some brief processing parameters are marked on the plot; vertical exaggeration: 2.19

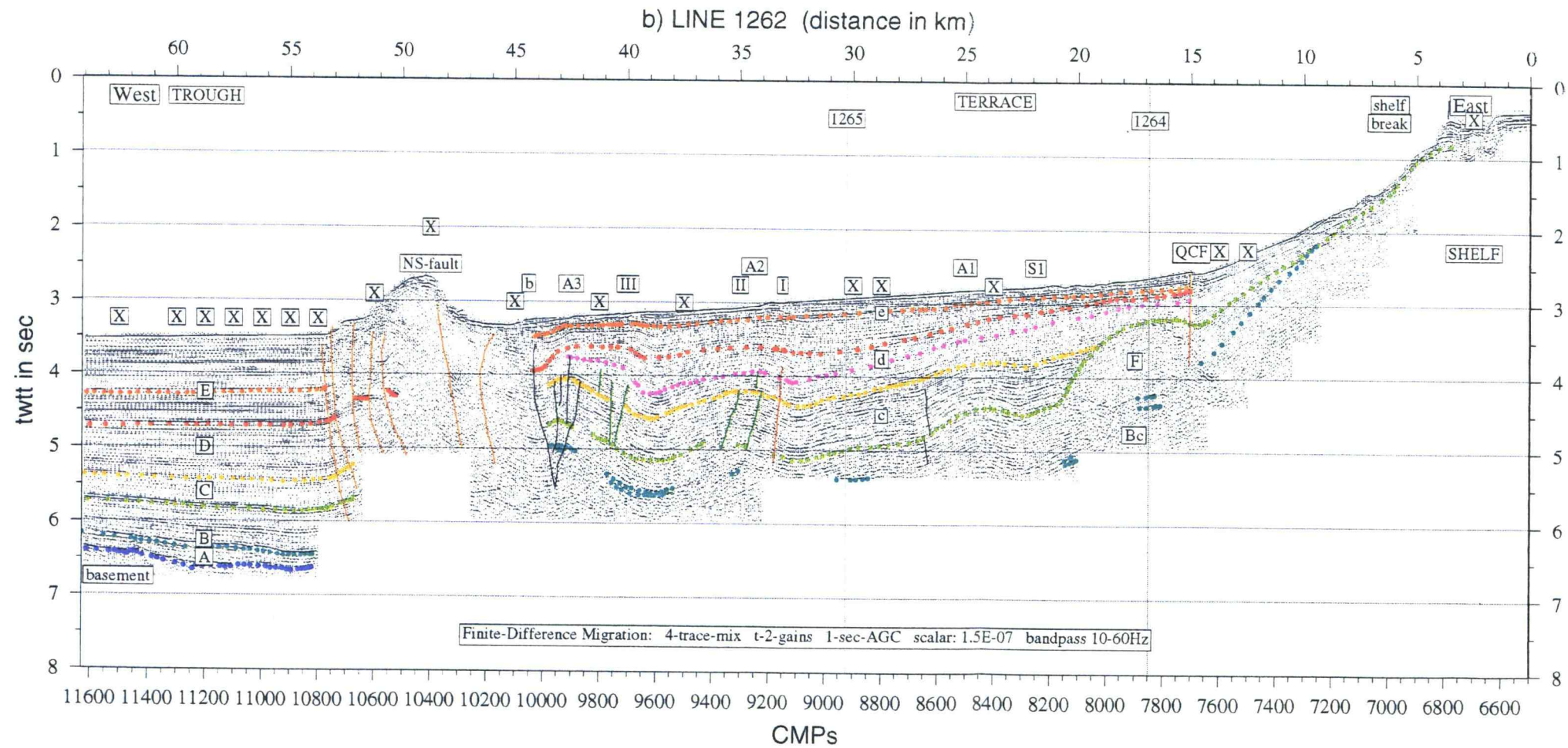


Figure 5.3 b) Structural interpretation of line 1262, showing depositional units E, D, C, B, and A in the trough and units e, d, c, F, and Bc (Basement Complex) in the terrace; units within the terrace could not be correlated with units in the trough, but coloring represents estimated timing of deposition; X = locations of constant velocity analysis; b = trough-terrace boundary, A1-3 = anticlines, S1 and S2 are synclines; I,II, and III refer to faults I,II, and III shown in the same colors on figure 5.21; vertical exaggeration: 2.19

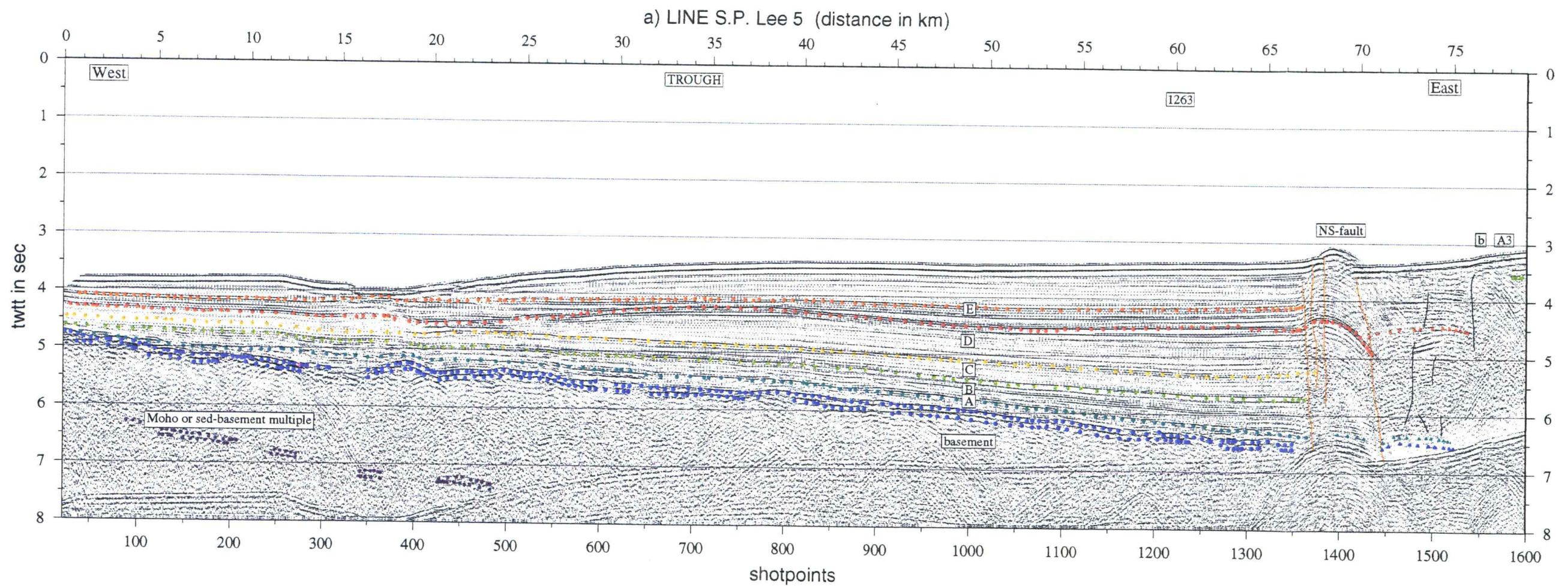


Figure 5.4 a) Stack of the trough portion of line S.P. Lee 5; water-bottom-multiple obscures data below 7 seconds; structural interpretation shows depositional units E, D, C, B, and A; location of the possible Moho reflector is marked; vertical exaggeration: 2.08

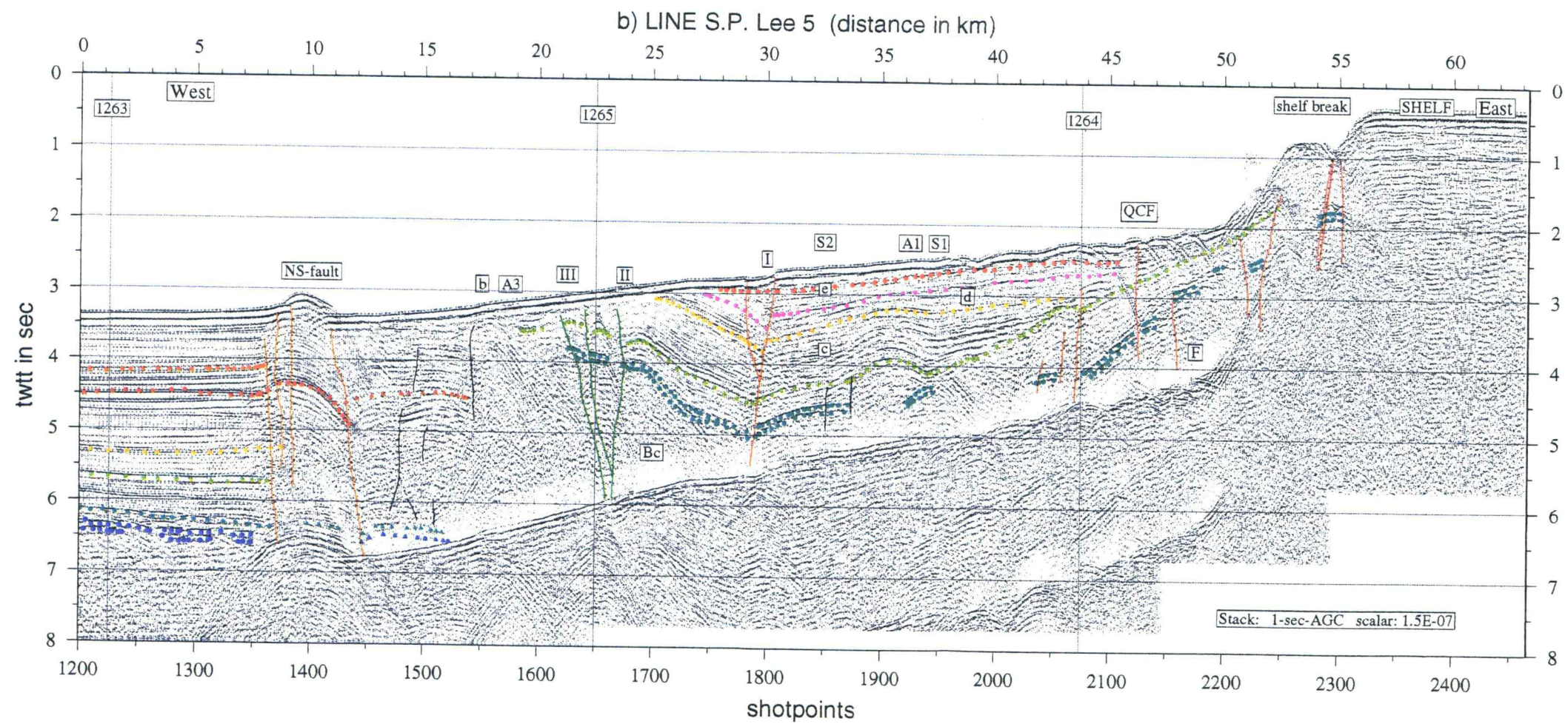


Figure 5.4 b) Stack of the terrace portion of line S.P Lee 5; water-bottom-multiple obscures data at depth; structural interpretation shows depositional units e, d, c, F, and Bc (Basement Complex); units within the terrace could not be correlated with units in the trough, but coloring represents estimated timing of deposition; horizons marked by triangles denote the possible extension of the basement reflector and the shallow unconformity across the NS-fault; b = trough-terrace boundary, A1-3 = anticlines, S1 and S2 are synclines; I,II, and III refer to faults I,II, and III shown in the same colors

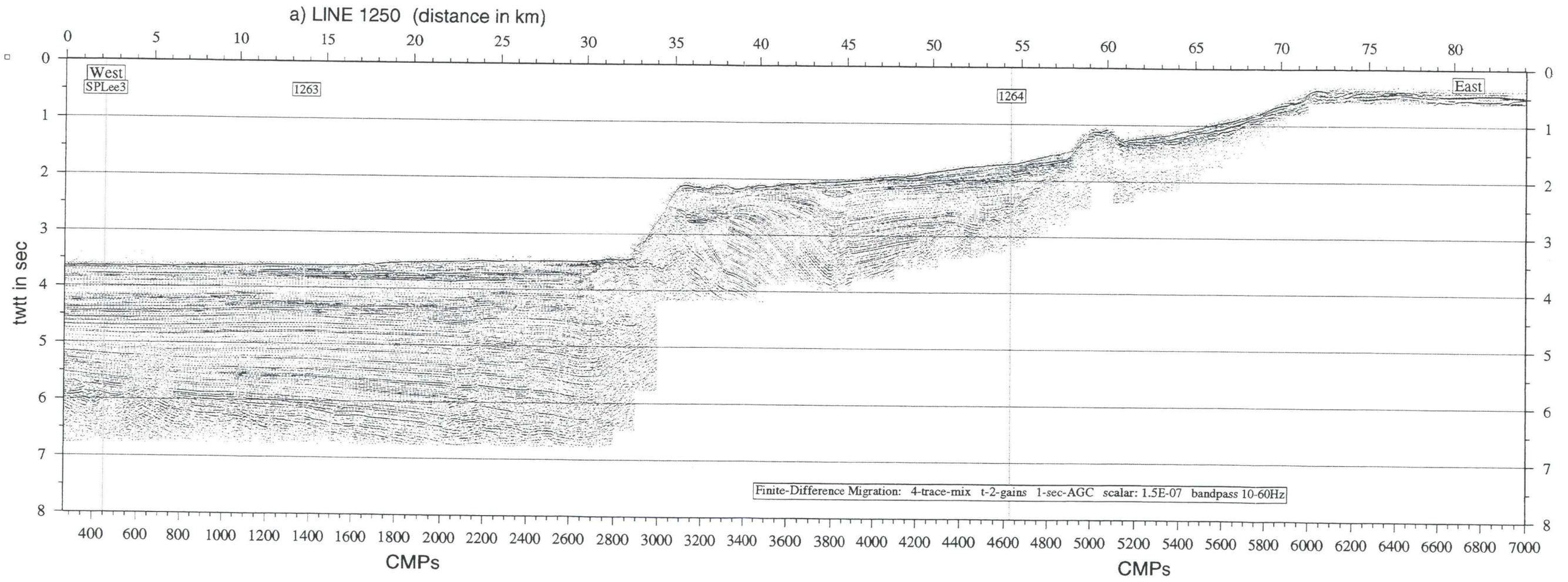


Figure 5.5 a) Finite-Difference Migration of line 1250; intersections with other lines, and some brief processing parameters are marked on the plot; vertical exaggeration: 2.19

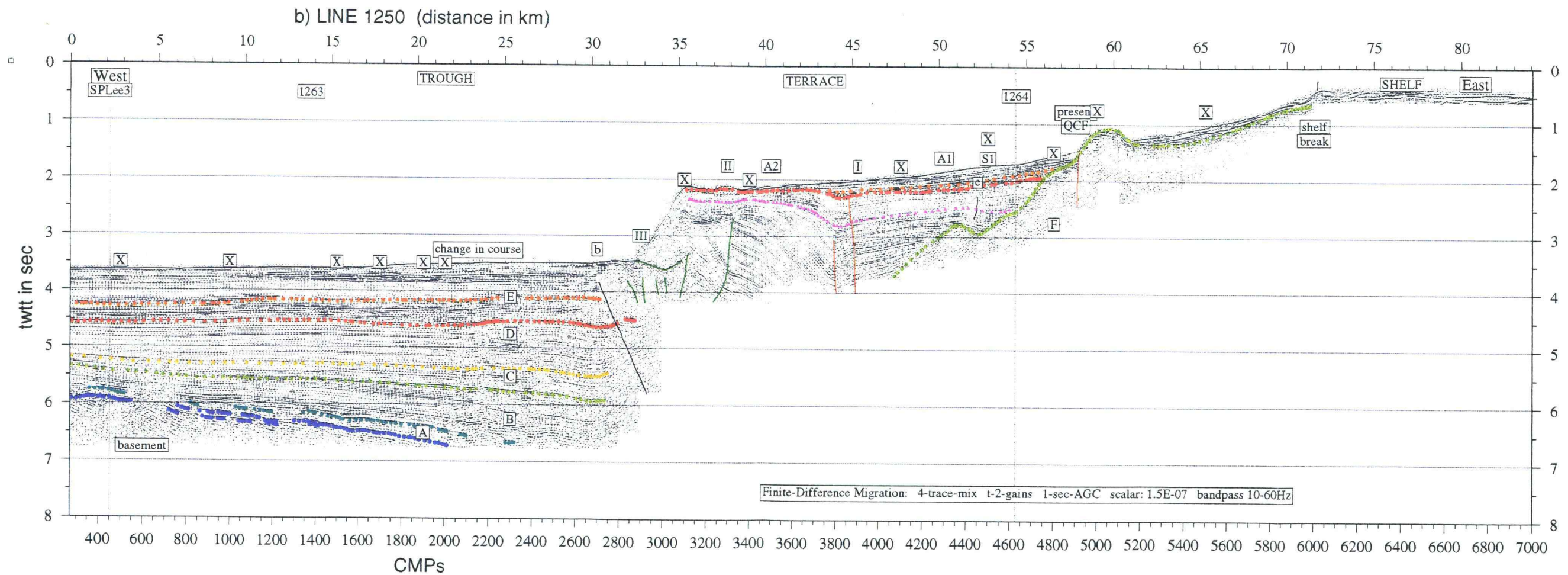


Figure 5.5 b) Structural interpretation of line 1250, showing depositional units E, D, C, B and A within the trough and units e and F within the terrace; units within terrace could not be correlated with units in the trough, but coloring represents estimated timing of deposition; b = trough-terrace boundary, A1-3 = anticlines, S1 and S2 are synclines X = location of constant velocity analysis; I,II, and III refer to faults I,II, and III shown in the same colors on figure 5.21; vertical exaggeration: 2.19

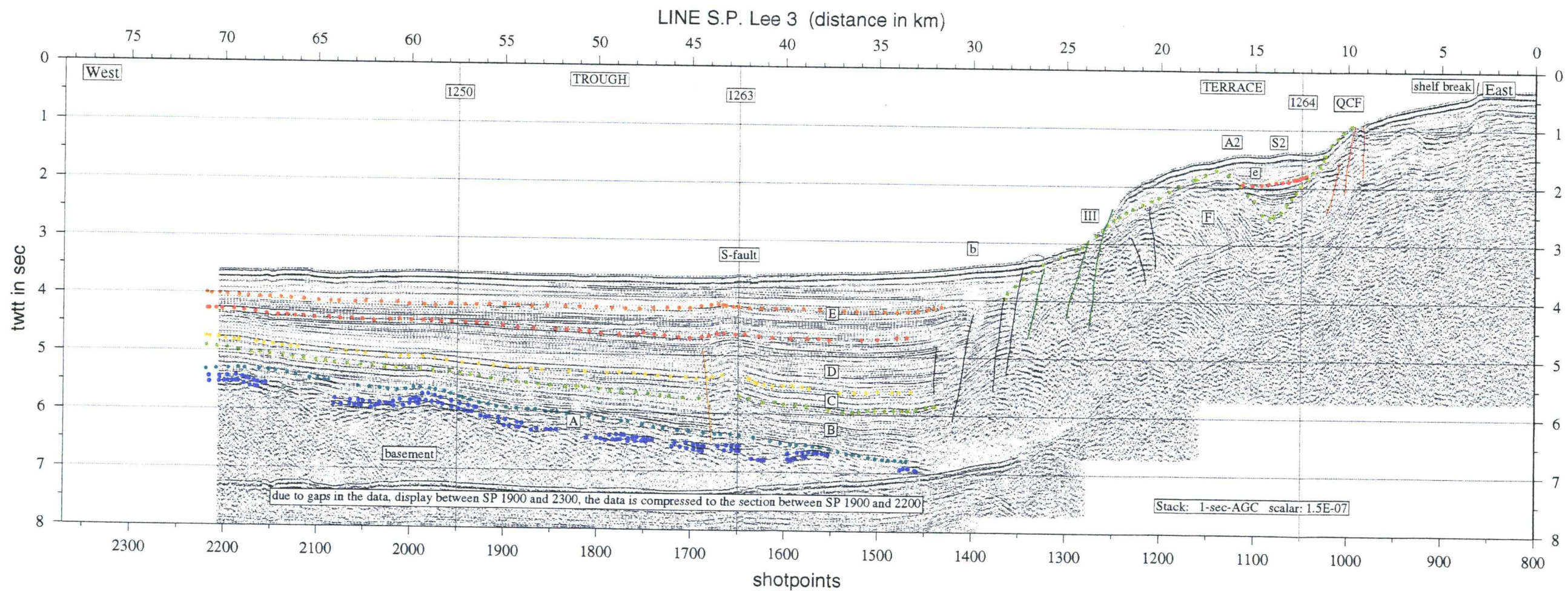


Figure 5.6 Stack of line S.P. Lee 3; water-bottom-multiple obscures data below 7 seconds in the trough and at lower twtts in the terrace; structural interpretation shows depositional units E, D, C, B, A, and F within the trough and e and F within the terrace; units within terrace could not be correlated with units in the trough, but coloring represents estimated timing of deposition; b = trough-terrace boundary, A1-3 = anticlines, S1 and S2 are synclines; III refers to fault III shown in the same color on figure 5.21; vertical exaggeration: 2.08

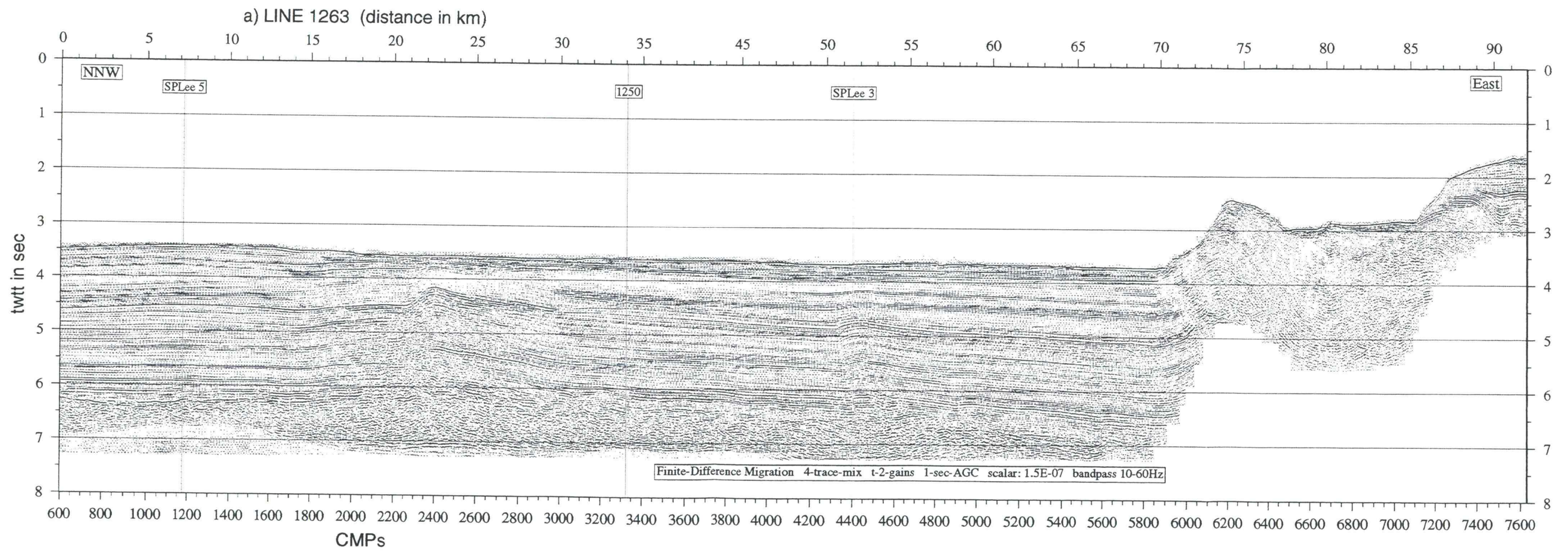


Figure 5.7 a) Finite-Difference Migration of line 1263; intersections with other lines, and some brief processing parameters are marked on the plot; vertical exaggeration: 2.19

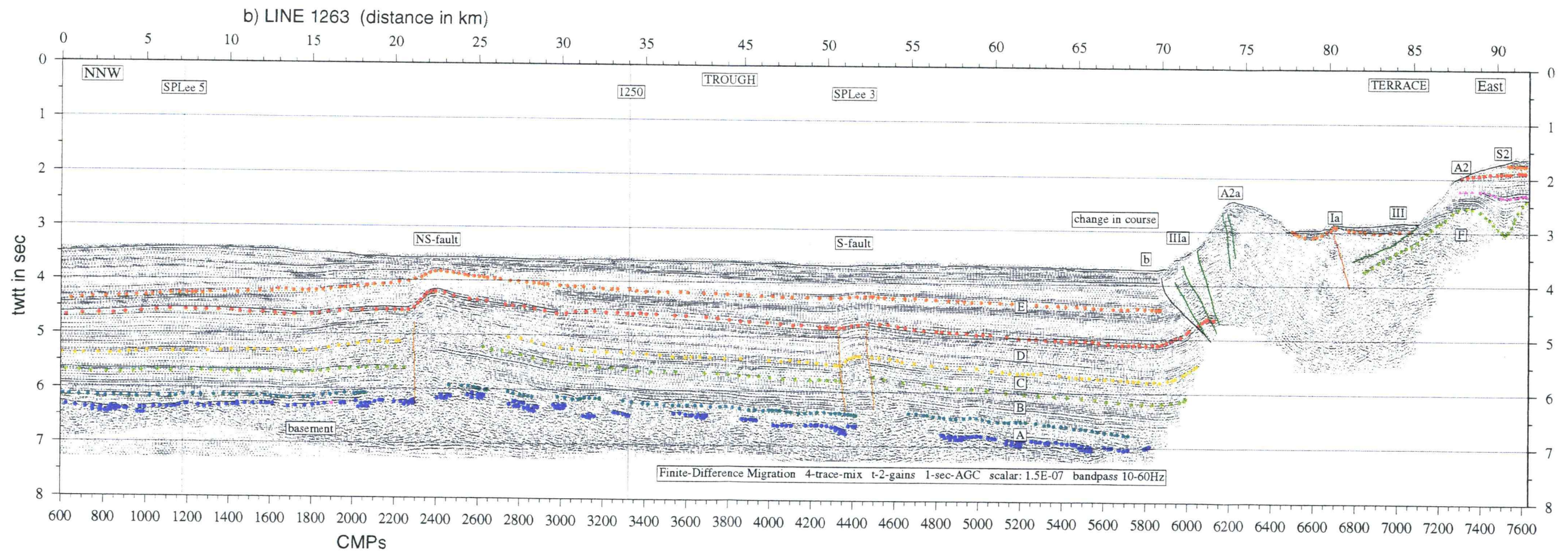


Figure 5.7 b) Structural interpretation of line 1263, showing depositional units E, D, C, B, and A within the trough, and F within the terrace; units within the terrace could not be correlated with units in the trough, but coloring represents estimated timing of deposition; b = trough-terrace boundary, A2 and A2a are anticlines, S2 = syncline; Ia, III, and IIIa refer to faults Ia, III, and IIIa shown in the same colors on figure 5.21; vertical exaggeration: 2.19

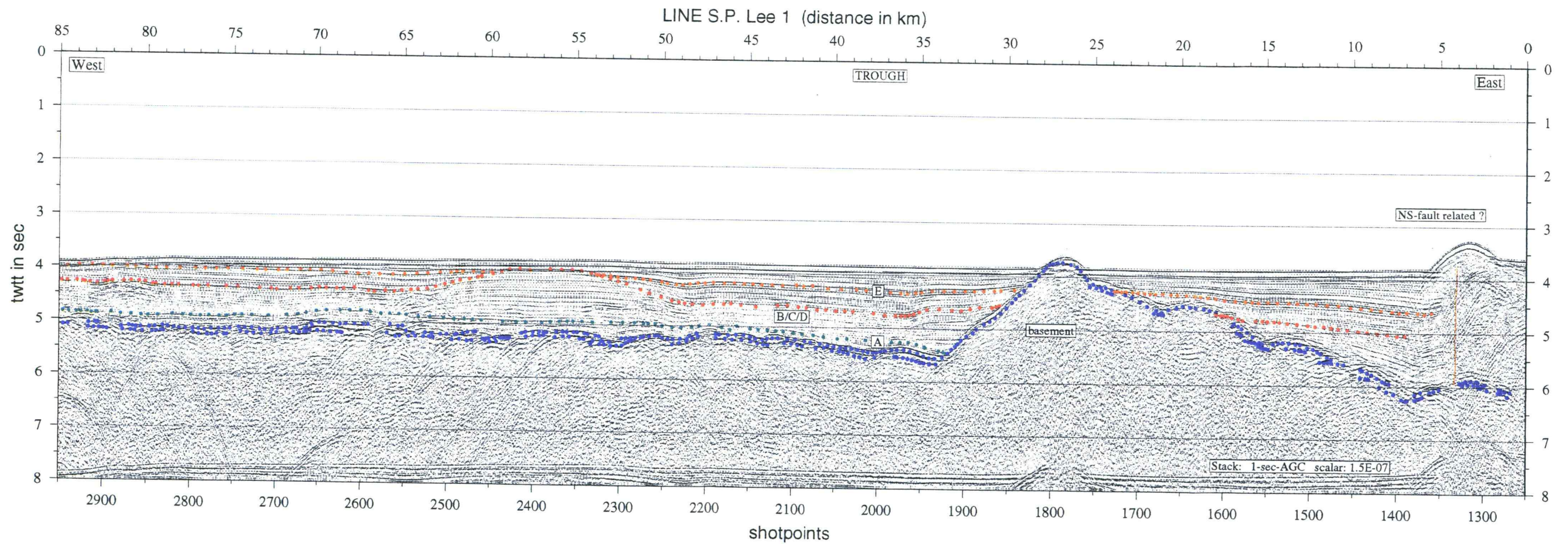


Figure 5.8 Stack of the trough portion of line S.P. Lee 1; water-bottom-multiple starts to obscure data at 7.75 seconds; structural interpretation shows depositional units E, D, C, B, and A; a fault is visible at the easternmost portion of the section, which resembles the NS-fault on line 1262 and S.P.Lee 5; here, the basement reflector can be traced below the terrace, supporting the assumption of a similarly throughgoing basement reflector farther north; vertical exaggeration: 2.08

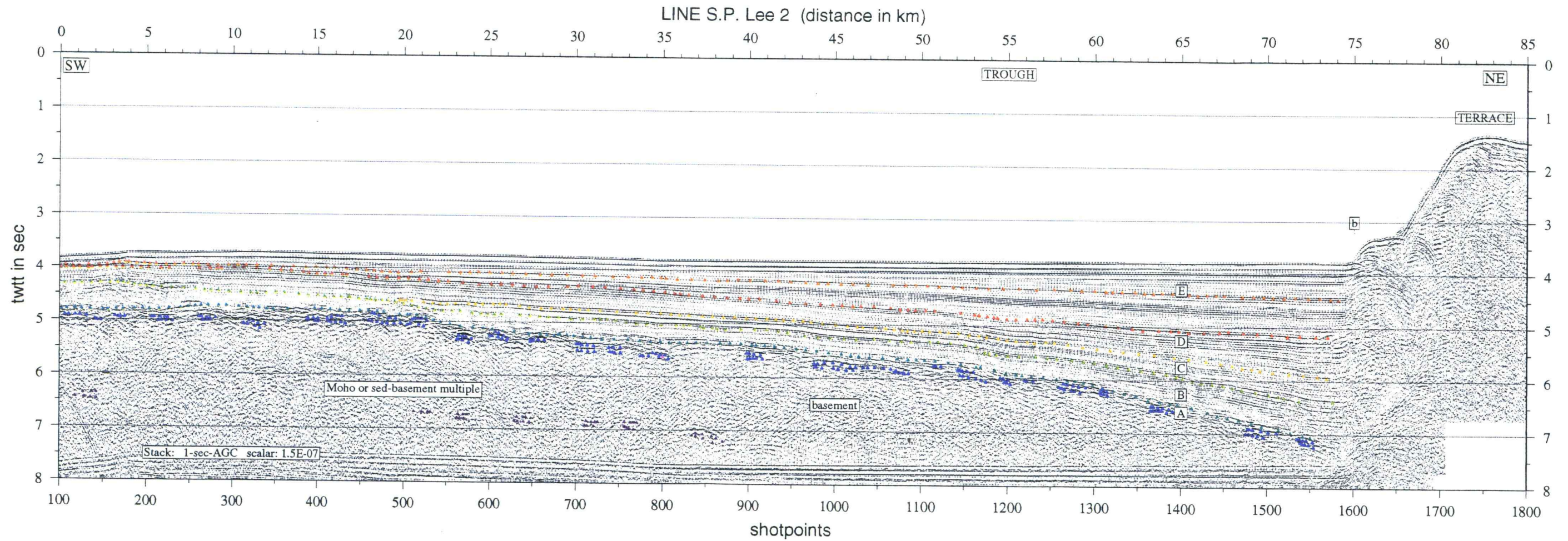


Figure 5.9 Stack of the trough portion of line S.P. Lee 2; water-bottom-multiple starts to obscure data at 7.75 seconds; structural interpretation shows depositional units E, D, C, B, A, and the possible location of a Moho reflector, b = trough-terrace boundary; vertical exaggeration: 2.08

and sheet flows underlain by a 6.7 km/s-layer of interlayered gabbro and peridotites. Measurements of velocity in different rock types (Sheriff and Geldart, 1987, p. 2) confirm as well that velocities between 5-6 km/s for basaltic rocks are generally expected.

Less than half a second above the sediment-basement reflector there is a reflector with a reflectivity similar to basement, but which is more coherent (unit A in interpreted sections). The velocity of this layer (5 km/s) approaches values as earlier assigned to basement rock, probably forming a transition composed of pillow basalt with interbedded breccia or sedimentary rocks. For two reasons, it is possible that the bottom reflector of this layer is an interbed multiple. One is the extreme parallelism of the unit boundaries, the second that a unit of pillow basalt with interbedded sediments on top of basalt would not produce a strong reflector as was observed at the bottom of unit A.

Deep within the basement at the western ends of S.P. Lee 5 and 2 (figures 5.4 and 5.9) from just below 6 s a reflector dips eastward till it disappears into the multiple at SP 500 (S.P. Lee 5) and between SP 900 and 1000 (S.P. Lee 2), at about 7.5 and 7.3 seconds two-way traveltimes, respectively. It could be the Moho discontinuity, which is typically found about 2 seconds below the acoustical basement reflector in oceanic crust. An argument against this would be the apparent eastward thickening of the crust. Assuming a crustal velocity of 6 km/s, the crust would be anomalously thin at the western ends of the profiles ( $\approx 4$  km) and thickens to a normal thickness of about 6 km to the east. No other indication or reason for a significant change in crustal thickness can be found in this data or in other work done in the area; e.g. a refraction line shot near S.P. Lee 5 (Shor, 1962) resolved a normal oceanic crust with its Moho at a depth between 9 and 9.8 km. Thus, this reflector is most likely a peg-leg multiple traveling between the sea floor and basement.

### 5.4.2 Sediments

To convert two-way traveltime to depth, figure 5.10 a) shows depth below sea floor versus two-way traveltime in the trough portion of line 1262, obtained by using the same interval velocities as in figure 4.19. Assuming that this curve is applicable throughout the trough region off Dixon Entrance and the velocity gradient is uniform over distances of 70 and 90 km along lines S.P. Lee 5 and 3, respectively, sediment thickness varies from about 5 km at its easternmost end to only 1.5 km in the west. The water depth varies from 2990 m in a deep-sea channel (S.P. Lee 5, SP 360) and 2850 m approaching the Oshawa Rise to between 2500 or 2600 m at the base of the continental slope (figure 5.2). The combination of a generally shallowing sediment-water interface and an eastward dipping basement creates a wedge of sediments that thickens toward the terrace segment (see also Snavely, 1981). By accounting for water depth variation, the average eastward dip of the oceanic crust can be estimated as approximately 3°.

A stratigraphic interpretation of sediment units was only possible in the northern portion of the trough segment, where seismic profiles are tied to each other, and this only in a relative sense, since no rock samples from drill cores with absolute ages were available in this area. Correlation with seismic sections S.P. Lee 1 and 2 was only speculative.

The sedimentary sequence is characterized by many continuous, parallel reflectors forming several principal units that are separated by angular unconformities and onlap patterns. Five units are distinguished, and are correlated between all northern sections, three of the units conform with those interpreted from line S.P. Lee 5 by Snavely et al. (1981).

**Unit A** has already been described above as a possible layer of pillow basalts with interbedded sedimentary rocks.

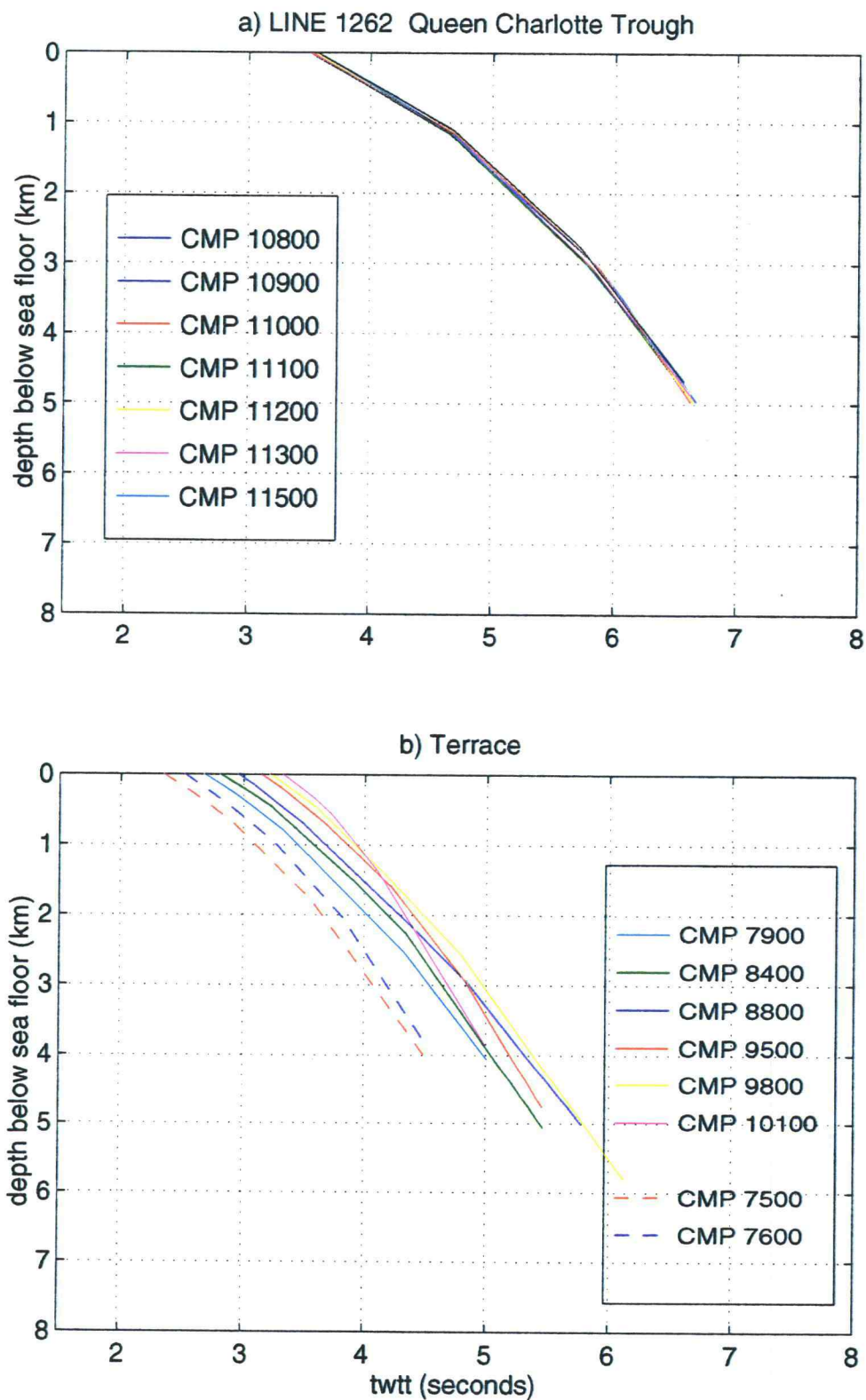


Figure 5.10 Graph showing twtt (in seconds) versus depth (in km) below the sea floor for line 1262 in the Queen Charlotte Trough (a) and in the terrace segment (b)

**Unit B:** This unit is characterized by its subparallel orientation to the basement reflector. It mimics the acoustical roughness of basement, e.g. at SP 2950 on line S.P. Lee 3 and 390 on S.P. Lee 5, making it a little less coherent than all overlying younger units. Using the interval velocity-depth curves of figures 4.19 (line 1262) and 5.11 (line 1250) a unit velocity of about  $4.6 \text{ km/s} \pm 0.3 \text{ km/s}$  is found; this is slightly higher than that (3.7-4.4 km/s) suggested by Snavely et al. (1981) on the basis of sonobuoy measurements, and a little lower than the 4.71 km/s-block from the refraction line of Shor et al. (1962), but satisfies both estimates within its errors. At the base of the slope (near CMPs 10800 of line 1262, and 1300 of S.P. Lee 5) Unit B thus is approximately 1.5 km thick and thins progressively to the west to a thickness of 600 m.

**Unit C:** Unit C lies conformably on unit B and increases its thickness from about 300 to 800 m from west to east.

**Unit D:** An unconformity between unit C and D can only clearly be recognized on section 1250 and possibly on line 1263, at its intersection with 1250. It is striking that unit D thickens tremendously toward the east. The paleo-surface of unit D displays a number of erosional features and is clearly unconformable to the overlying unit E. Centered around SP 470 (S.P. Lee 5), for instance, an ancient submarine channel is found, whose axis has shifted westward to SP 370 at present. A high east of the ancient channel could either be a levee or a high between two sea channels (Snavely et al., 1981). In any case, erosion or non-deposition took place along this paleo-surface.

Figure 5.12, obtained by measuring the two-way-travel time in seconds from the sea floor to the unconformity, demonstrates the uneven surface structure of unit D. Absolute depth to this interface can only be directly related to twtt if the velocity of the sediment and water layers above stay constant. This is not always the case, but since lateral variations are small, figure 5.12 still gives a good idea of locations of the ancient channel and of other irregularities of the top of unit D. Features on this surface closely match trends of bathymetry contours (figure 5.12). Notable is the 100 m-westward

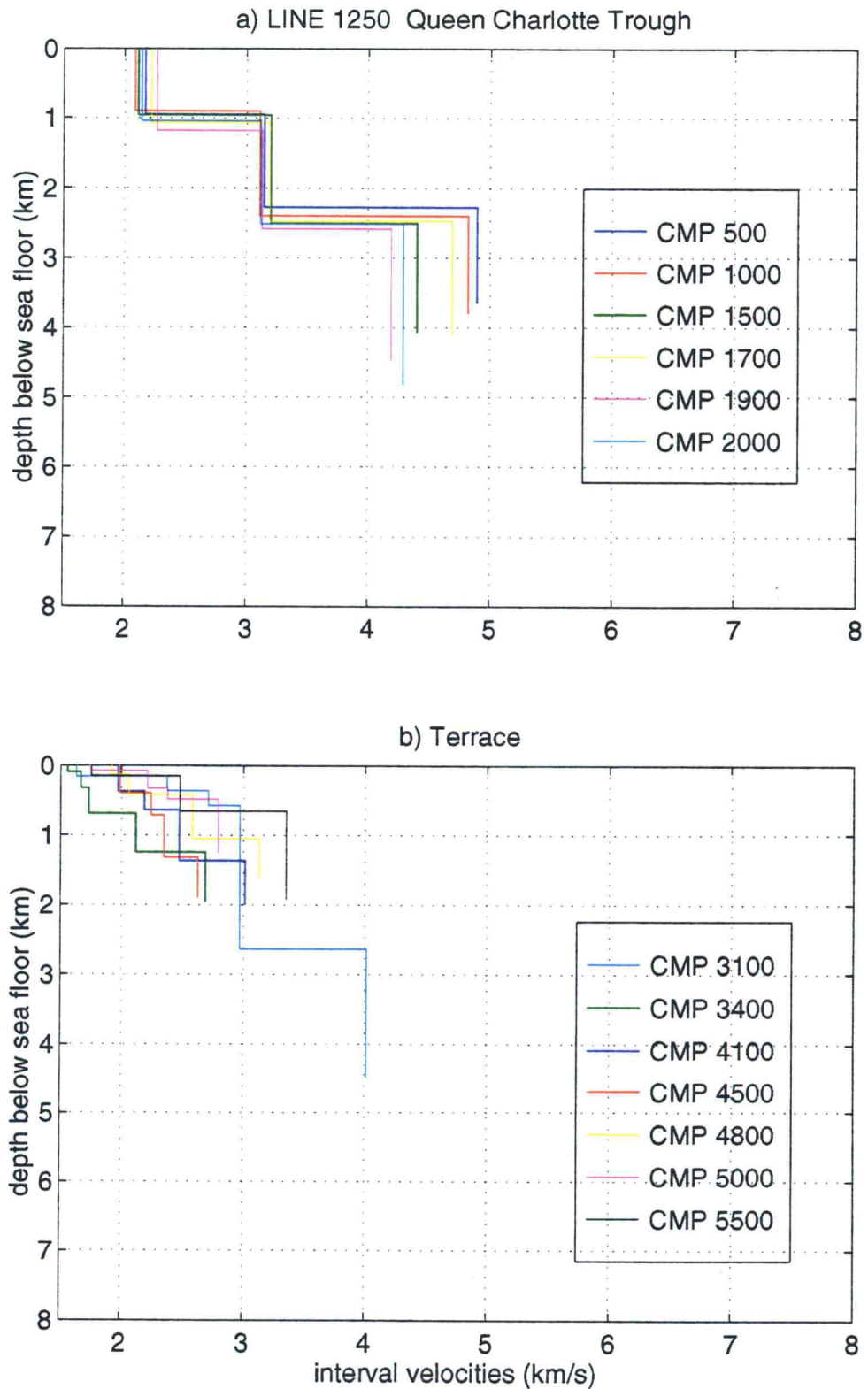


Figure 5.11 Graphs showing interval velocity (in km/s) versus depth (in km) below the sea floor for line 1250 a) in the Queen Charlotte Trough and b) in the terrace segment

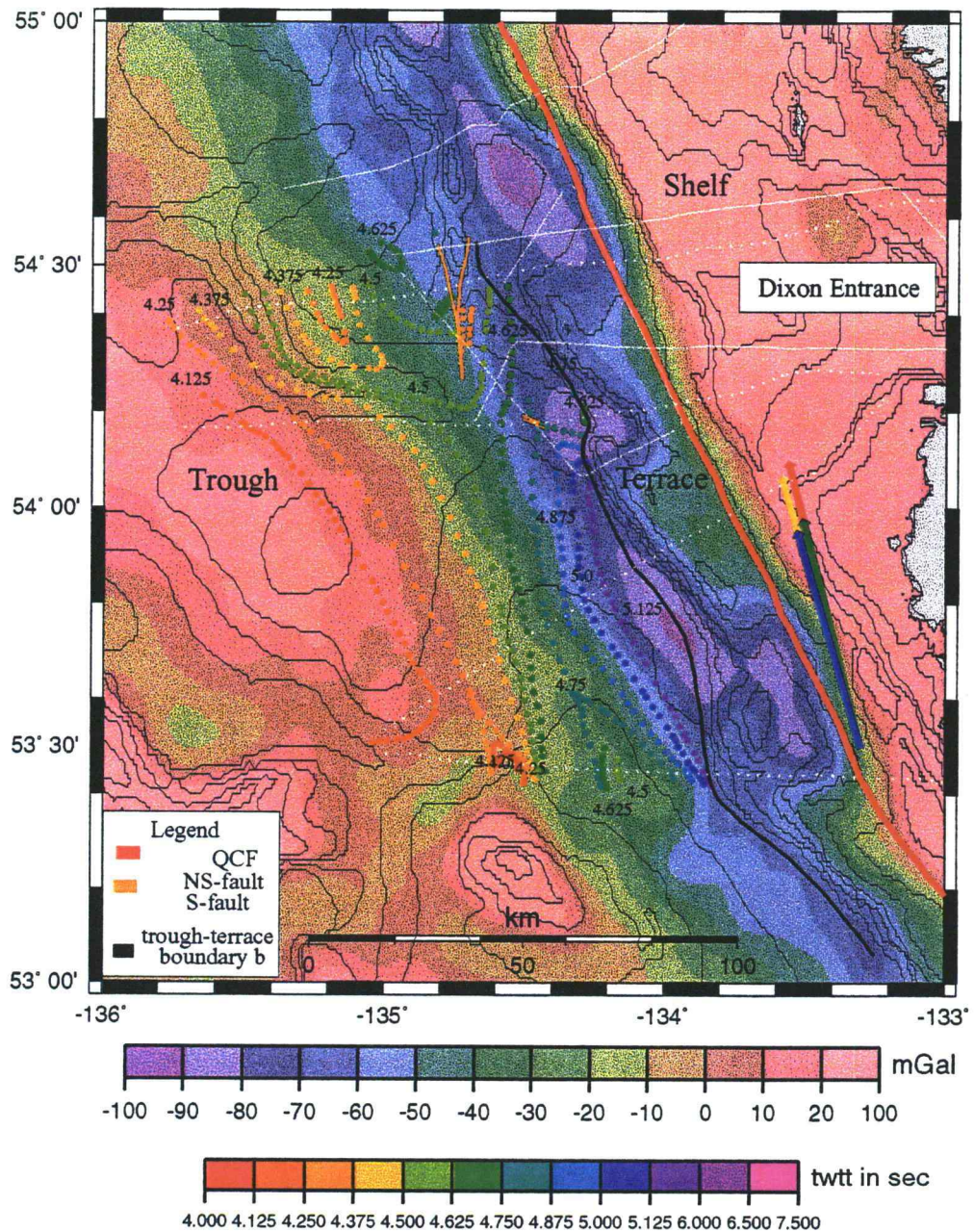


Figure 5.12 Map of contours of twtt (in seconds) to the unconformity between units D and E interpolated between all seismic lines and superimposed on regional free-air gravity data (in mGal) and bathymetry contours; segment boundary between Queen Charlotte Trough and Terrace (in black); location of Queen Charlotte Fault trace (red), N-S, and S-fault (orange); relative plate motion vector (from table 2.1): red and yellow (maximum and minimum angle and distance 5 Ma), green and blue (maximum and minimum angle and distance 4 Ma)

shift of the deep sea channel over a time interval between completion of deposition of unit D and E. The present channel still follows roughly the path of its ancient precursor. Figure 5.13 is a plot of two-way travelttime-contours of the unconformity that separates units C and D. No similarity with morphology is recognizable and no evidence for a submarine channel that might have existed at that time is observable.

For their velocities, units C and D are regarded as one unit and figures 4.17 and 5.11 show an interval velocity of approximately  $3.2 \text{ km/s} \pm 0.2 \text{ km/s}$ , which corresponds exactly to the value Snavely et. al (1981) found for S.P. Lee 5. The combined unit thickness varies from about 2 km at SP 1350 of line S.P. Lee 5 to only 600 m between SP 500 and the western end of the section. Thus, comparing the change in thickness from west to east with that of unit B, an estimate of vertical movement due to flexure and sediment loading during deposition of units C and D lies in the range of 500 m. Because of compaction through subsequent sediment loading non-uniformly distributed over the trough region, the original sediment volume was probably greater than now measured. This amount is, therefore, a minimum value.

**Unit E:** Similar to units C and D, E (between sea floor and red horizon in interpreted sections) shows very continuous reflectors that extend over almost the whole length of the imaged trough. First, sediments cover the erosional surface of unit D by onlapping its slopes and overtopping its highs. Following this phase of complete infilling of topographic lows, such as the ancient sea channel (SP 390, SP 500, line S.P. Lee 5) and the trough, more sediments were deposited near the continent (above orange horizon in interpreted sections), resulting in an eastward thickening of unit E.

Simultaneously, a new channel carved itself into the young sediment layer centered around SP 370 west of the ancient channel. Figures 4.17 and 5.11, again, give similar interval velocities for unit E, ranging between  $2.0\text{-}2.2 \text{ km/s} \pm 0.1 \text{ km/s}$ , and resulting in a maximum thickness of about 1.2 km in the east and 500 m in the west. Conclusions about the vertical movement in the trough during deposition of unit E are difficult, since the depositional environment might have changed significantly in the Quaternary.

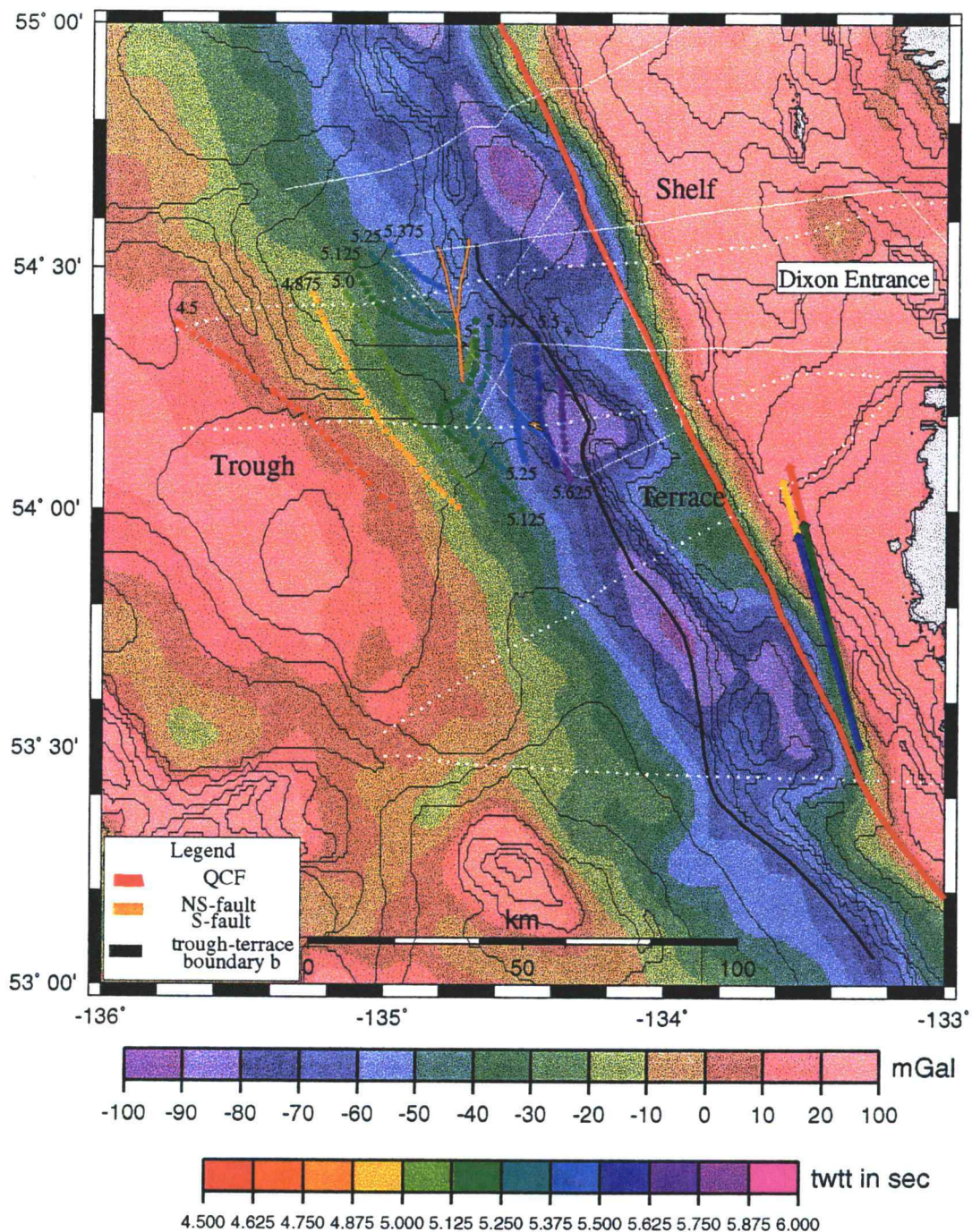


Figure 5.13 Map of contours of twtt (in seconds) to the unconformity between units C and D interpolated between all seismic lines and superimposed on regional free-air gravity data (in mGal) and bathymetry contours; segment boundary between Queen Charlotte Trough and Terrace (in black); location of Queen Charlotte Fault trace (red), N-S, and S-fault (orange); relative plate motion vector (from table 2.1): red and yellow (maximum and minimum angle and distance 5 Ma), green and blue (maximum and minimum angle and distance 4 Ma)

**Age:** The maximum age of sediments is constrained by the age of the basement, which is known from the identification of magnetic anomalies. Figure 2.3 showed their present distribution within the northeastern Pacific plate. As described in the geologic history of the region in chapter 2.2, age of the oceanic plate increases with distance from the continent, due to subduction of the Farallon/Pacific Spreading Ridge. The western ends of profiles S.P. Lee 5 and 3 correspond to the negative magnetic anomaly between chrons 5D and 5C (18-17 Ma) (Atwater, 1989), whereas the eastern portion images basement about 15 Ma old. The age of the oceanic layer is therefore early to middle Miocene. S.P. Lee 1 and 2 a little further south cross chrons 5B to 5 (15-10 Ma) and 5B to 5A (15-12 Ma) from west to east, respectively. Within the Queen Charlotte Trough, sediments of any of the seismic lines therefore cannot be older than 18 Ma.

Unfortunately, little is known about sedimentation rates and deposition, but an increase in material coming through the channels of Dixon Entrance during and after the last ice age (0-2 Ma) is expected, creating a different environment than to the south, where the Queen Charlotte Islands form a barrier to sediment influx. This is reflected in the total sediment thickness overlying the basement rocks of the Pacific plate: Horn et al. (1984) and Dehler and Clowes (1988) state an average of 1-km of sediments west of Moresby Island, while a maximum total thickness of 5 km is commonly found in the trough off Dixon Entrance. Looking at the seismic reflection profile from Davis and Seemann (1981) in figure 2.4, the Queen Charlotte Trough in the south is not completely filled with sediments, whereas lines S.P. Lee 3 and 5 show no actual depression of the sea floor. The trough off Dixon Entrance simply has been filled completely due to higher sedimentation rates, while west of the islands part of the trough still remains to be filled.

The following age estimates are made in correlation with those interpreted for the same units in Snavelly et al (1981), but it is possible that all imaged sediments are very young (Pleistocene), since Miocene faulting and subsidence formed many

extensional basins, which probably trapped most of the sediments from the eroding Coast Mountains.

The age of unit B can only be assumed, as its uppermost portion must be younger than the youngest basement (15 Ma) rock it covers. Following suggestions from Snavely et al. (1981), it could be assumed to range in age between 18 Ma to the end of the Miocene (about 7 Ma). This would place the complete deposition of unit B before the onset of transpression. If the shift in relative plate motion from purely strike-slip to oblique convergent between 6-5 Ma (Cox and Engebretson, 1985, Riddihough and Hyndman, 1991) occurred during or towards the end of deposition of Unit C, then this could explain the unconformity between unit C and D. The beginning of transpression and shortening would have caused flexure of the oceanic lithosphere, which moved towards and collided with the continental lithosphere of North America. Units A and B covered the oceanic crust while there was only a slight bend of the oceanic lithosphere. The decrease in unit thickness to the west could be an effect of the increase in distance from continental shelf sediment sources. When the tectonic regime changed and transpression was initiated during deposition of unit C (5-7 Ma), flexure of the lithosphere produced a trough, which continuously traps more sediments at its eastern end. This may be why unit B and C seem to belong to the same depositional environment, which was subjected to a major change before deposition of unit D.

The phase of erosion that carved the ancient sea channel into the paleo surface of unit D could coincide with the beginning of the Pleistocene ice age about 2 Ma ago. Unit E is the most recent depositional unit and probably of Quaternary age.

As mentioned earlier, unit ages in this study can only be determined relative to other available information, such as the age of the basement, a change in tectonic environment and correlation with well data far away in the Queen Charlotte Basin. There, 5-6 Ma ago, an unconformity is found between upper Miocene syn- and Pliocene post-rift sediments (Rohr and Dietrich, 1992). Syn-rift faulting in the basin is associated with middle to late Miocene transtension, that ended in a phase of local uplift and erosion of the syn-rift sections. During the initiation of Pliocene

transpression, post-rift strata formed in broad relatively shallow depocenters and pinches out on the eastern side of the basin and towards Dixon Entrance, where uplift occurs at the northern end of the basin. Rohr and Dietrich (1992) considered large inversion structures (compression) and uplift that affected both syn-rift and post-rift strata as evidence for intensified transpressional tectonism in the late Pliocene. This conclusion matches well with the ages inferred for the sections offshore Dixon Entrance. Intensified compression would have resulted in a greater amount of flexure of the oceanic lithosphere as indicated by the increased thickening of unit D. Quaternary strata were interpreted to unconformably overly Tertiary beds within extensional grabens and half-grabens in Dixon Entrance, as shown in the three single-channel reflection lines interpreted by Rohr and Dietrich (1992, figure 5.14). Presumably, some of the material eroded from the continent during the Pleistocene and Holocene was trapped in these topographic lows. The remains were transported through the channels of Dixon Entrance toward the continental slope to be deposited as unit E in the Queen Charlotte Trough. The horizontal orientation of the orange surface within this unit suggests that, at imaged locations, no more flexure of the oceanic lithosphere took place in the trough region during the Holocene and that through the increased terrigenous influx these youngest sediments downlap onto it (SPs 400-600, S. P. Lee 5).

### **5.4.3 Faults**

The trough region was defined as that portion of the seismic sections that for the most part contains undeformed, flat-lying sediments over oceanic basement. The trough-terrace boundary is marked in figure 5.2 (black line).

But one major fault is observable within this otherwise undeformed segment. Unlike in the interpretation of Snavely et al. (1981), who proposed another en echelon linear ridge that resulted from wrench tectonics, it is considered different in nature and

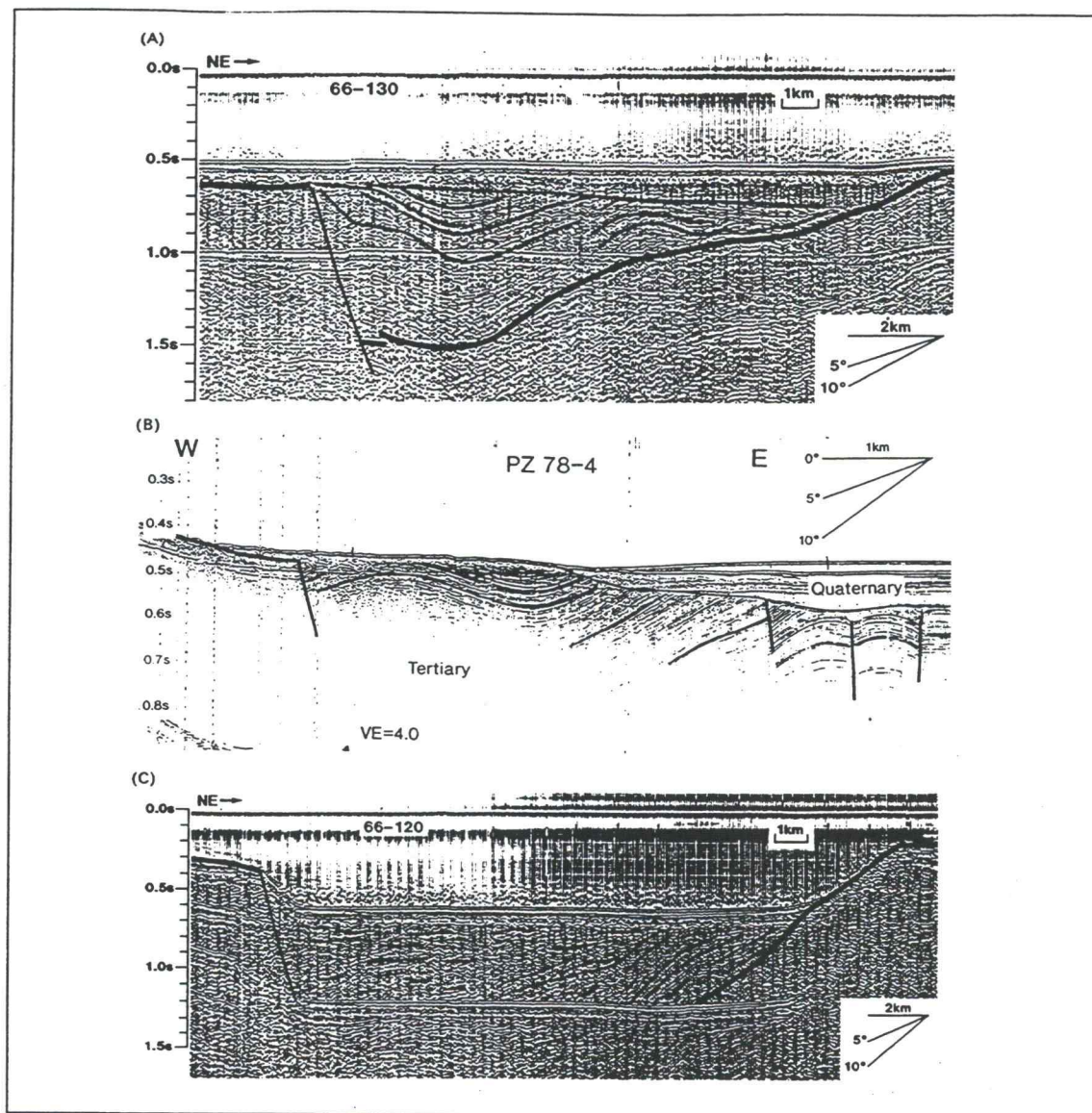


Figure 5.14 East-west trending single-channel reflection data in Dixon Entrance; (A) shows a characteristic half-graben shape with an extensional fault on the west side; basement is evident as overlapping diffractions underlain by incoherent energy; sedimentary rocks consist of subparallel beds that have been folded; an extensional fault is interpreted to exist at the abrupt near vertical contact between basement and sedimentary rocks more than 0.5 s deep; on the eastern side of the basin, however, basement shallows gradually from 1.0 s to 0.5 s over 9 km; (B) this line shows folding and faulting adjacent to Principe-Laredo Fault in northern Dixon Entrance; folds and faults have deformed the lower stratified section which is interpreted to be Miocene or Pliocene; the section above is Quaternary; (C) this line shows an angular unconformity west of Learmonth Bank, a basement high that outcrops at the seafloor; tilted and partially truncated sedimentary rocks are overlain by flat-lying strata (from Rohr and Dietrich, 1992)

origin from faults found within the terrace (next section). This fault is trending approximately north-south (N-S fault) (figures 5.3 b), 5.4 a) and 5.7). The N-S fault shows no topographic expression on line 1263 (CMP 2300) and seems to be inactive there at present. In contrast, on lines S.P. Lee 5 (CMPs 1370-1440) and line 1262 (CMPs 10780-10300) the fault splays into two (S.P. Lee 5) or more faults, bounding a pressure-ridge like structure with an increase in topographic expression to the north. These faults are probably active near-vertical faults that might merge into one vertical stem, as is found in positive flower structures typical for convergent wrenching (figure 5.15, Wilcox et al., 1973; Harding and Lowell, 1979; Harding, 1985). Due to the presence of water-bottom multiples it is difficult to determine whether basement is involved in the faulting process, and east of the ridges the basement reflector most likely disappears under the multiple. On line S. P. Lee 5 just east of the ridge (SP 1450-1530, dashed line) basement might be visible, but correlation of any other unit interfaces across the ridge is obscured by diffractions from the sea floor topography.

On line 1263, the fault clearly ceased to displace reflectors before the end of deposition of unit D, for its top reflectors drape over the discontinuity. Subsequent movement along the fault occurred during deposition of lower unit E (Pleistocene), but ceased thereafter. The basement, here observable on both sides of the fault, seems to be uplifted to its east. By checking for the presence of a possible velocity-pull-up, the time-to-depth-conversion of this section (figure 5.16) still shows a small step-up to the east, and the adjacent basement reflector appears even more disrupted than in the time-migrated section. Hence, basement could be involved as well in the faulting process further north.

It is difficult to correlate unit interfaces across the N-S fault on line 1263, that are deeper than the horizon between units D and E. Units east of the fault were identified using information from all intersecting sections, where unconformities are more visible (e.g. interface between unit C and D on line 1250), and by comparing units' reflectivity characteristics. Since 1263 represents the tie between all lines, the N-S fault becomes a gap in correlation and units A, B, C, and D are not linked directly to

each other. Unit thicknesses seem to vary, and it was often impossible to identify a sequence of identical looking reflectors within the same unit from one side of the fault to the other. Obviously, a significant change occurs from west to east that affects the sedimentary sequence, and this might be the reason for the altered appearance of the basement reflector. This could be a possible indication of strike-slip movement and juxtaposition of different sedimentary sections.

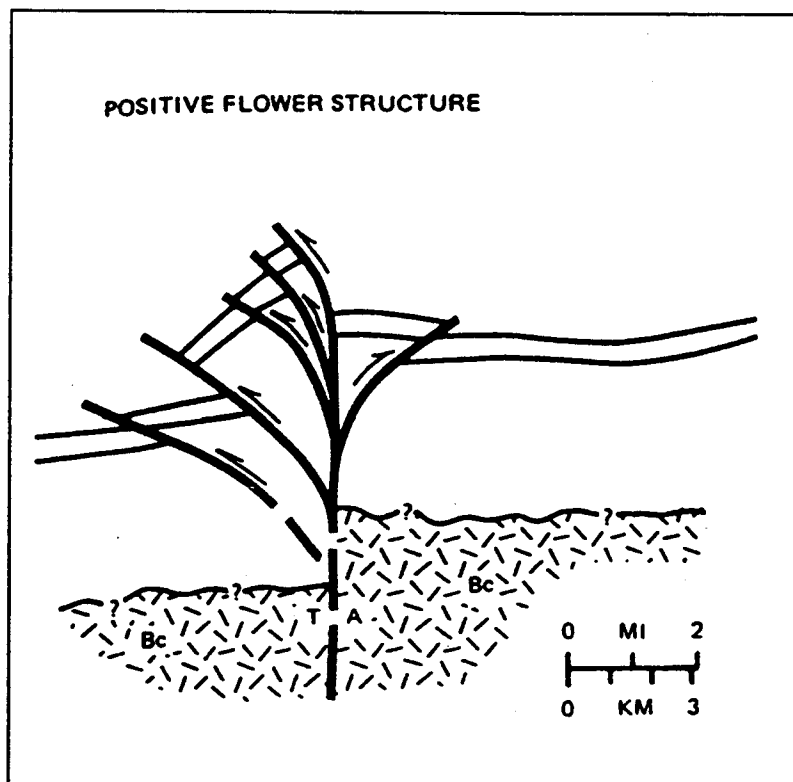


Figure 5.15 Schematics of a positive flower structure; T: displacement toward viewer; A: away from viewer; Bc: basement complex (after Harding, 1985)

Another fault is detected on line 1263 (CMP 4440) and S.P. Lee 3 (SP 1650), where both lines intersect, which unfortunately, makes a determination of its strike time

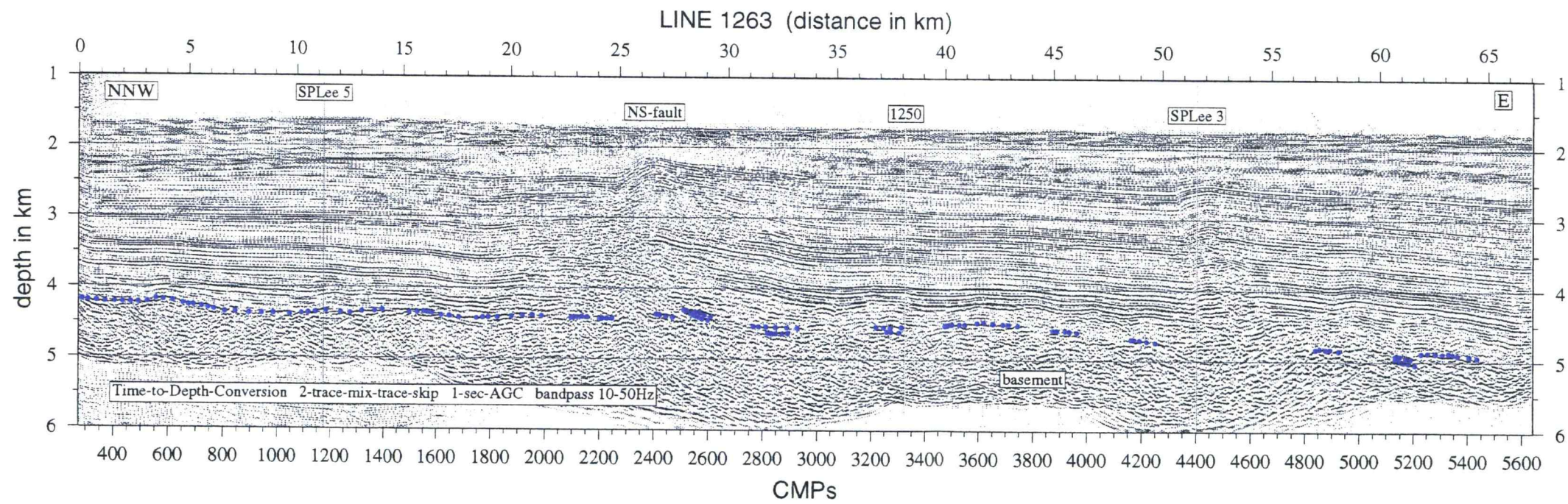


Figure 5.16 Time-to-depth conversion of the western portion of line 1263 demonstrates a real small step down to the west of the oceanic basement (processed by K.M.M. Rohr) vertical exaggeration: 3.29

nearly impossible. This fault (S-fault in interpreted sections) has been active at the same nearly impossible. This fault (S-fault in interpreted sections) has been active at the same as the N-S fault of line 1263, although with much less vertical displacement, and a possible correlation of units across it.

A contour plot of the twtt-to-basement on regional free-air-gravity is shown in figure 5.17. Although velocity functions change laterally from east to west (with lower velocity gradients to the east, since layers are generally much thicker there), it can be assumed that their variation is little along lines of equal two-way traveltime. This validates the contouring procedure, and allows a qualitative determination of trends. The connection of points of similar two-way traveltime-values across seismic sections was guided by the orientation of gravity anomaly contours.

As expected, contours of equal basement depth align with contours of equal free-air gravity, which are believed to roughly image the sediment-oceanic crust interface, provided water depth is not changing significantly. As the N-S fault offsets basement contours, it produces a signature in the regional gravity field (figure 2.5). West of the fault, gravity and basement contours parallel the Queen Charlotte Fault, while east of the fault their trends bend toward it. Since detailed bathymetry and gravity data are only available up to 55°N, the continuation of this pattern is uncertain.

Although no twtt-to-basement values could be obtained east of the pressure-ridge on lines 1262 and S.P. Lee 5, contours were extended following the trends of gravity. An increase in contour offset across the fault seems to occur toward the north, where the surface expression of the pressure ridge becomes more pronounced as well. Although it is dangerous to deduce too much detail from twtt-contours, the analysis of basement contours (figure 5.17) favors an increase in compression to the north.

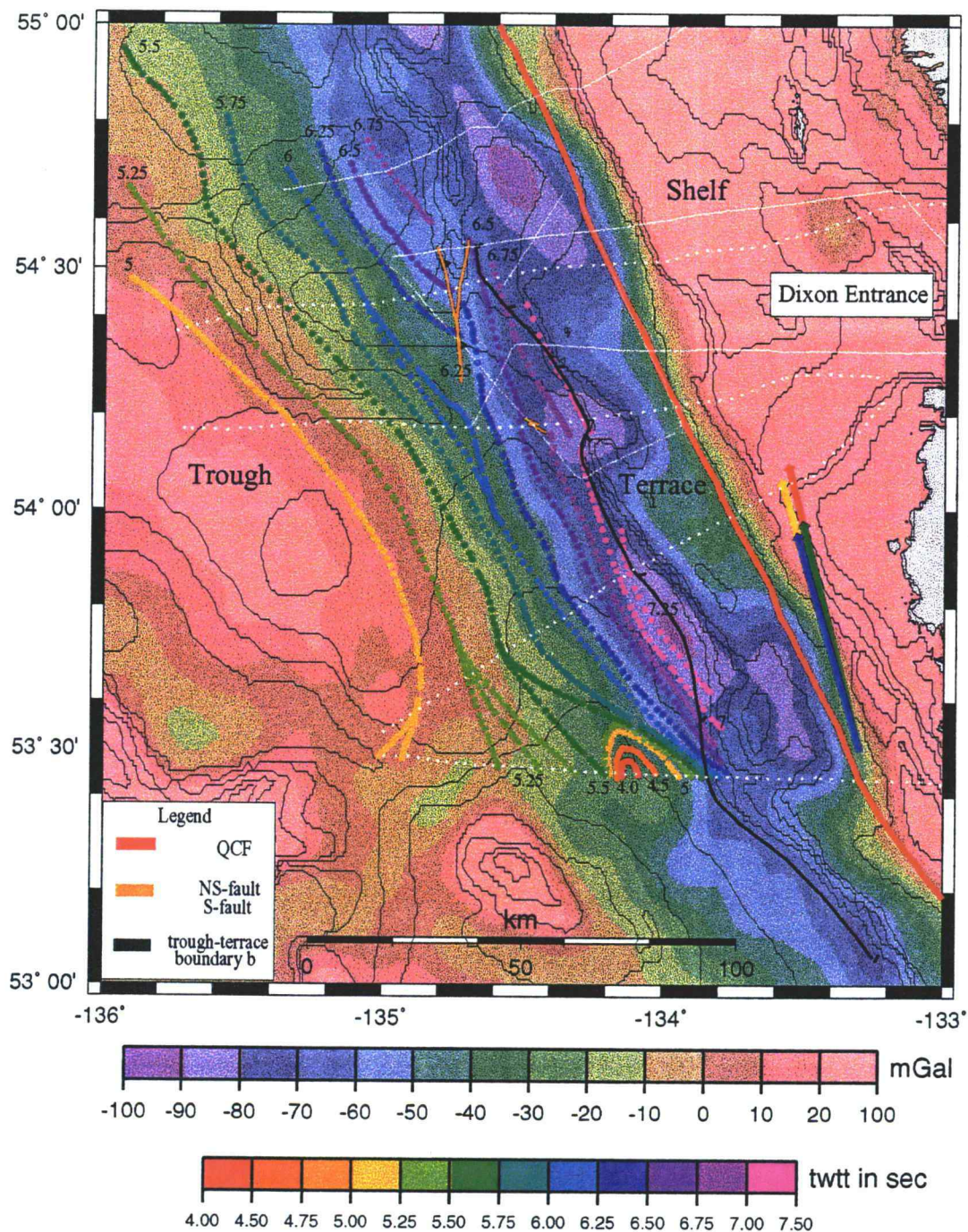


Figure 5.17 Map of contours of twtt (in seconds) to the top of the basement interpolated between all seismic lines, and superimposed on regional free-air gravity (in mGal); segment boundary between Queen Charlotte Trough and Terrace (in black); location of Queen Charlotte Fault trace (red), N-S, and S-fault (orange); relative plate motion vector (from table 2.1): red and yellow (maximum and minimum angle and distance 5 Ma), green and blue (maximum and minimum angle and distance 4 Ma)

## 5.5 THE QUEEN CHARLOTTE TERRACE

Two additional seismic sections provide information on the structure of the Queen Charlotte Terrace. Line 1264 (figure 5.18) parallels the shelf break and is located as close as 2 km west of what is thought to be the active trace of the Queen Charlotte Fault (QCF) (see location map of figure 5.2). It ties all other lines that cross the QCF. Line 1265 (figure 5.19) is the extension of line 1264 and intersects lines 1262 and S. P. Lee 5. Generally, the terrace includes a great structural variability, as was indicated by bathymetry (figure 2.6) and gravity (2.5) data.

To study this more complex terrace structure of the northern region off Dixon Entrance, analysis of the reflection profiles was divided into two parts, one covering more recent deposits due to high sediment influx and the other covering the underlying structure.

### 5.5.1 Structure at Depth

No Moho or oceanic basement similar to that characteristic of the trough region was observable anywhere in the deeper sections of the terrace, because the strong WBM-reflection obscures faint events at depth. However, some possible deeper reflections were examined but these were concluded to have arisen from side-swipe energy. A unit of material, especially well exposed on line 1250 (marked "F" in figure 5.5 b), is clearly distinctive by its seismic facies. It is separated by an unconformity from flat-lying continuous reflections of younger sediments. This unit rises to the sea floor at CMP 5100, where it forms a ridge. Its appearance is characterized by chaotic reflectivity, and low energy similar to that of basement rock. The interval-velocity distribution above the WBM of line 1250 (figure 4.19), however, indicates a velocity ranging between 2.5-3.0 km/s  $\pm$  0.5 km/s, with even lower velocities, where this unit is exposed at the sea floor. Although interval velocity estimates within this chaotic unit F

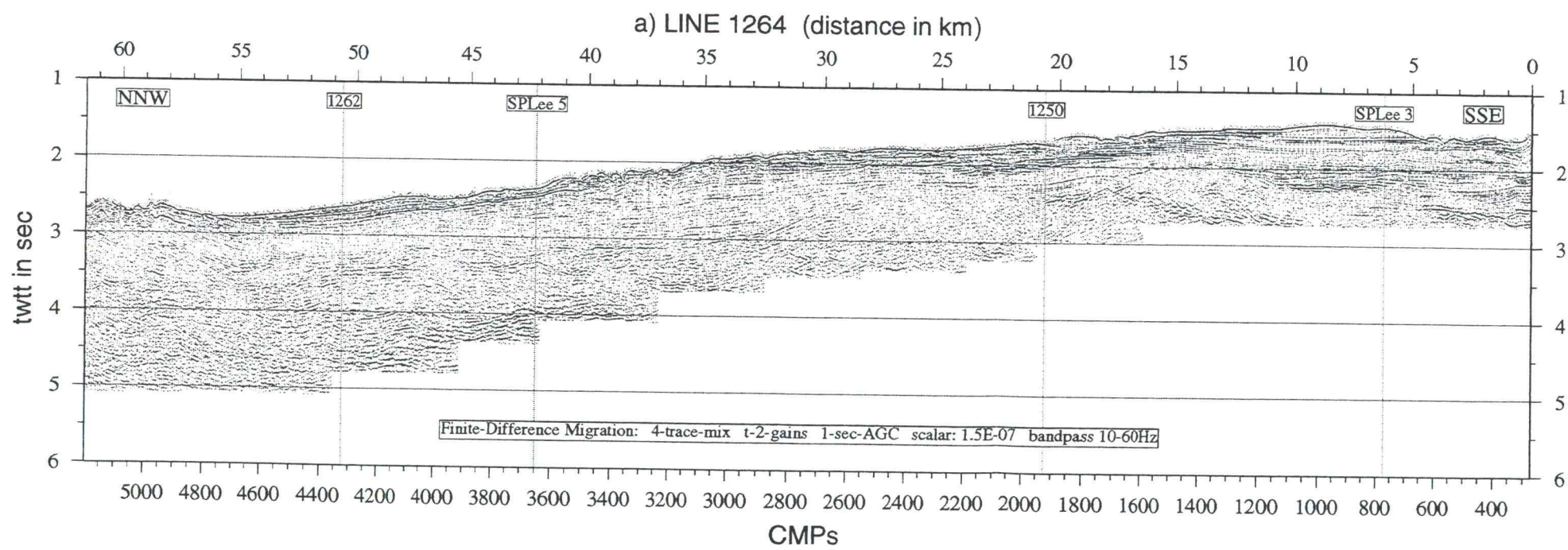


Figure 5.18 a) Finite-Difference Migration of line 1264; intersections with other lines, and some brief processing parameters are marked on the plot; vertical exaggeration: 2.67

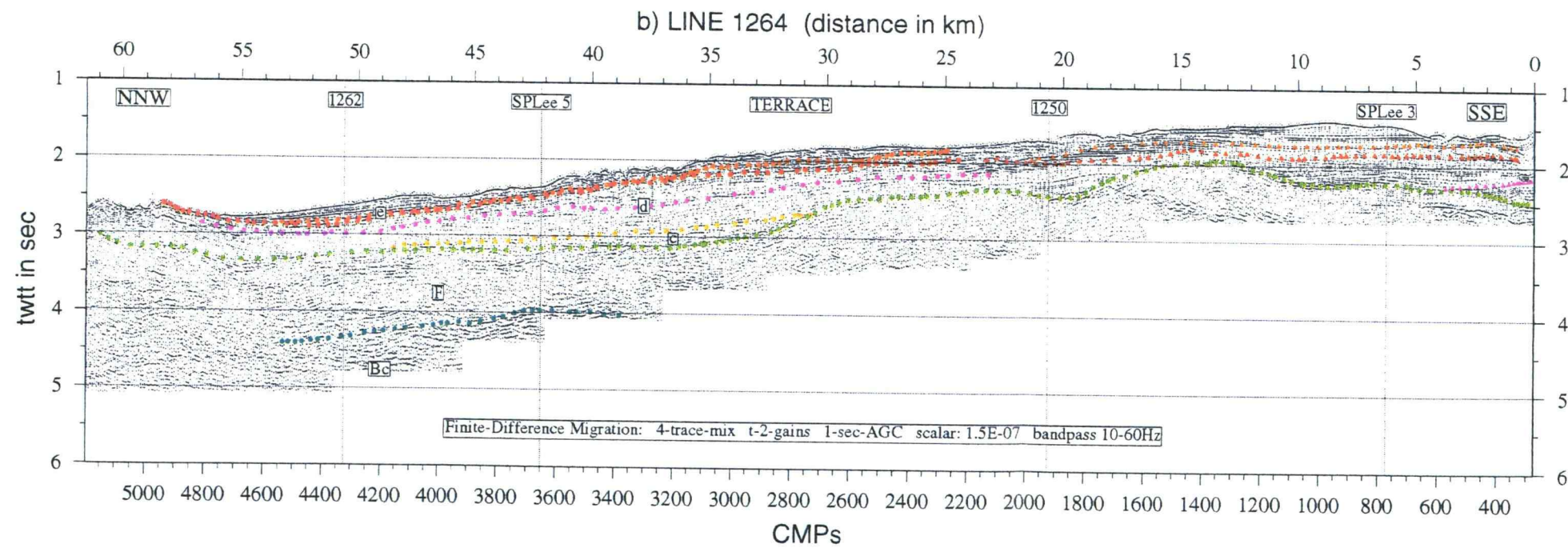


Figure 5.18 b) Structural interpretation of line 1264, showing depositional units e, d, c, and F; Bc = (Basement Complex); the change to triangles denotes the change in sediment properties described in the text; vertical exaggeration: 2.19

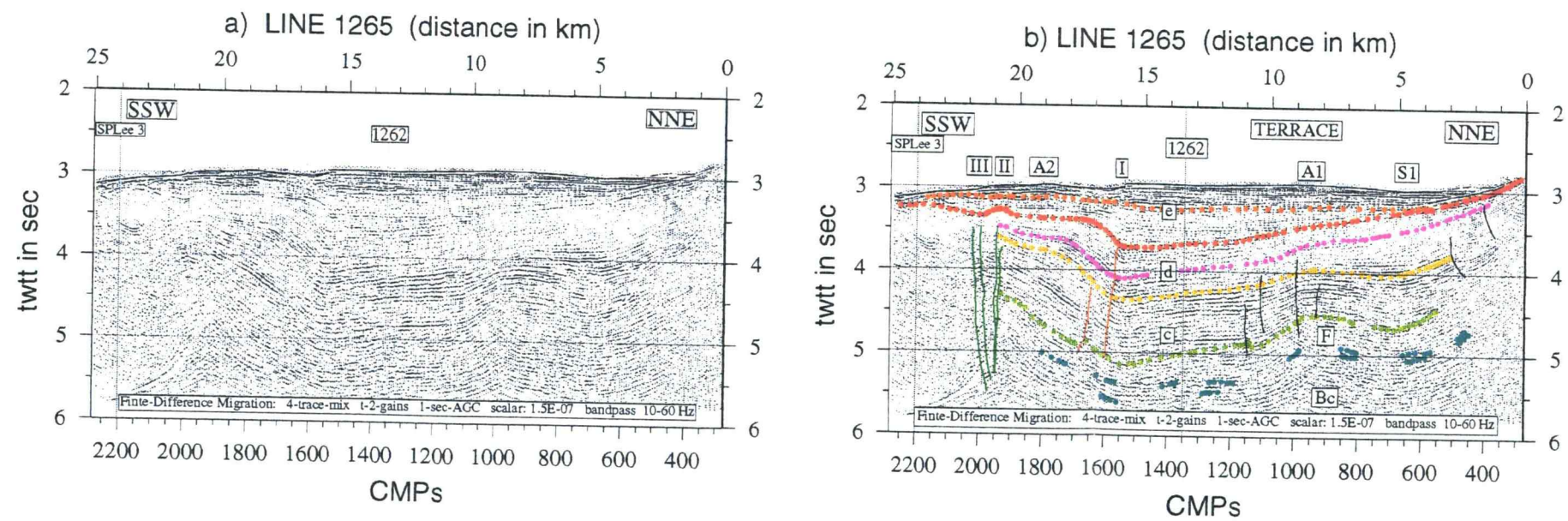


Figure 5.19 Line 1265 a) without and b) with structural interpretation, showing depositional units e, d, c, and F within the terrace; Bc = (Basement Complex), A1 and A2 are anticlines, S1 = syncline; I,II, and III refer to faults I,II, and III shown in the same colors on figure 5.21; vertical exaggeration: 2.19

are based on few imprecise velocity picks a correlation with uplifted oceanic basement is considered unlikely. The extent and structure of unit F below 4 seconds depth is not known.

Unit F was identified on line 1264 and correlated with all other lines. The interface (green horizon in interpreted sections) between unit F and overlying sediments is very distinct in areas where it forms an angular unconformity with the overlying sediments, such as between CMP 1100 and 2900 on line 1264 and CMP 7700 and 8200 on line 1262. In other places, identification is more problematic. Interval velocities tend to be as low as  $2\text{--}2.5 \text{ km/s} \pm 0.5 \text{ km/s}$  at depths shallower than 2.5 seconds and range between  $3\text{--}4.5 \text{ km/s} \pm 0.5 \text{ km/s}$  at 3.5-5 seconds depth (figures 4.14, 4.20, 4.29). Unit F may consist of consolidated and deformed sedimentary rocks that were tectonically uplifted and are now capped by younger sedimentary layers.

Results are again compiled in a twtt-contour plot (figure 5.20), which attempts to image the orientation of the top of unit F in map-view. Due to the sparseness of data points, there is not always a unique solution to connecting identical twtt-values across different sections, and the real surface could be far more complex. Nevertheless, this interpretation is believed to represent general trends and structures. Plotting the contours on top of free-air gravity illustrates the close relation between the depth to the consolidated sediments, which are of a greater average velocity and density than the unconsolidated sediments and observed gravity. F occurs at shallow depth where the tip of the triangular terrace block merges with the QCF, and seems to be tilted down to the north-west. The surface of unit F shows anticlinal and synclinal features (marked A1, A2, A3, and S1 and S2, respectively in figure 5.20 and in seismic sections), oriented in a northwest-southeast direction and forming an angle of about  $20^\circ$  with the trend of the Queen Charlotte Fault. This trend approximates that of the curved outer scarp, which defines the western boundary of the terrace.

On profiles S.P. Lee 5, 1262 and 1264, another discontinuous but prominent reflector about 0.5 seconds below the top of unit F (Bc in interpreted sections) is

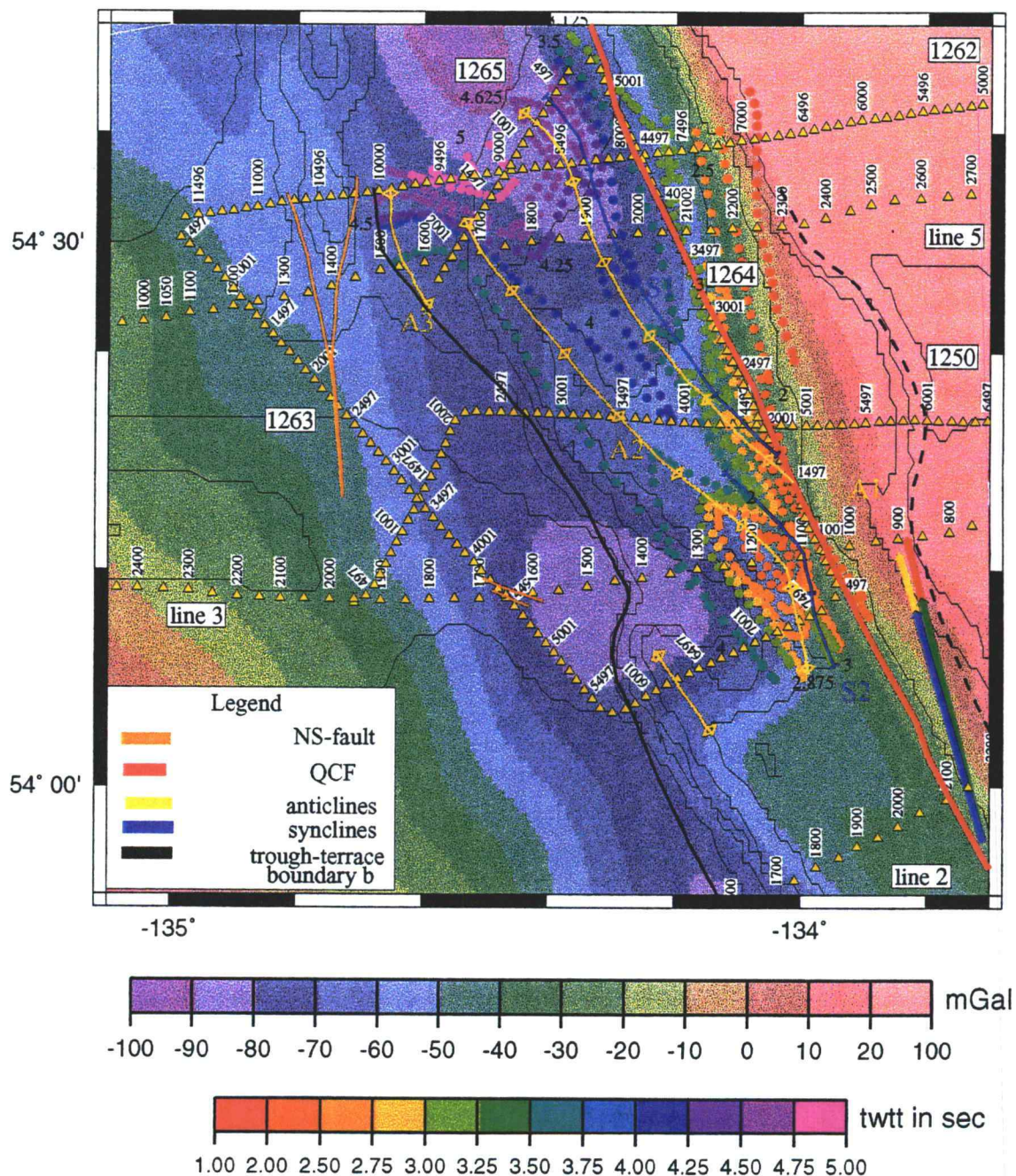


Figure 5.20 Map of contours of twtt (in seconds) to the top of unit F within the terrace interpolated between all seismic lines and superimposed on regional free-air gravity (in mGal) and bathymetry contours; segment boundary between Queen Charlotte Trough and Terrace (black); shelf break (dashed); location of the present and old Queen Charlotte Fault traces (red); N-S, and S-fault (orange); anticlines (A) and synclines (S) (yellow and blue); relative plate motion vector (from table 2.1): red and yellow (maximum and minimum angle and distance 5 Ma), green and blue (maximum and minimum angle and distance 4 Ma)

striking within the otherwise chaotic reflection pattern. Especially clear is a change to greater reflectivity at about 4 seconds between CMP 3300 and 4300 of line 1264. Interval velocities increase to approximately 4-5 km/s (figure 4.29, 4.14) just below this interface, reaching values close to those found for the top of the oceanic basement. Rocks could be either very consolidated and compressed sediments or a melange of highly fractured oceanic basement and sedimentary rocks. Horn et al. (1984) distinguished two velocity units below pelagic and turbiditic sediments of the terrace segment (figure 2.7). The shallower unit 6 is thought to be highly compressed sediments with a possible base of sheared basalts and velocities between 3.3-4.6 km/s, while those of unit 7 range from 5.5-7.4 km/s and are interpreted as sheared basalts and gabbros. Dehler and Clowes (1988, figure 2.11) also found similar velocities. The terrace seems to be underlain by units with velocities ranging between values typical for the stratified sedimentary section and oceanic crust. The interface between units F and Bc (Basement complex) is not believed to be the simple equivalent to the basement interface observed in the Queen Charlotte Trough, but rather a complexly fractured and interbedded surface.

While in the trough region gravity was influenced mainly by the dipping oceanic basement-sediment interface, the triangular gravity highs on the terrace seem to be the direct result of accumulations of consolidated, deformed and sheared, denser material below units of stratified much less consolidated sediments.

### **5.5.2 Stratified Units**

The young sedimentary section, which is draped over preexisting topography of units F and Bc and found on the different seismic profiles imaging the terrace, is characterized by a great variability over short distances within one triangular block from north to south.

As mentioned above it was very difficult to correlate sedimentary units across the pressure-ridge of lines 1262 (figure 5.3 b) and S.P. Lee 5 (figure 5.7 b), although

line 1263 demonstrates that oceanic crust and sediment stratigraphy continues to exist east of the N-S fault. For this reason, the N-S fault is not considered a part of the terrace segment, but an independent structure of the trough. Hence, the boundary between terrace and trough segments (b) further south is drawn as interpreted from lines 1263, S.P. Lee 3 and 1250 to coincide with the termination of flat-lying undisturbed sediment reflections and a significant step up in bathymetry (figure 5.21). Further north, this boundary, though not explicitly visible in either the seismic or bathymetry data, is interpolated to almost coincide with the broadening surface expression of the N-S fault. On line S.P. Lee 5, the trough-terrace boundary is assumed to be located at SP 1540 and at CMP 10000 on line 1262 (fault b on interpreted sections). The base of unit E might be identifiable east of the ridge on S.P. Lee 5 at a depth of 4.5 seconds. As indicated by the truncation of reflectors (e.g. at 5.3 seconds, S.P. Lee 5), the short distance between the ridge of the N-S fault and the trough-terrace boundary underwent at least minor compression and fracturing as if it was squeezed between these two main structures.

In any case, sediments found east of the trough-terrace boundary cannot be directly related to units in the trough segment. Conditions under which deposition occurred on the terrace might have been quite different. Unit boundaries interpreted on the terrace are based on changes in reflectivity characteristics and onlap patterns of angular unconformities. To help get a feel for probable ages of units in the terrace their interfaces are colored similarly to deposition periods found in the trough. This estimate is based on a comparison of unit velocities found in the trough with interval velocity distributions of lines 1262, 1264, and 1250 (figures 4.14, 4.17, 4.20, 4.23, and 5.13) in the terrace. Differences in the velocity distribution exist between the terrace and trough segment as well as a gradual change from north to south within the terrace:

LINE 1262:

- An equivalent to the Holocene portion of unit E in the trough region is almost absent on line 1262; lowest velocities at the seafloor start at 2 km/s



- and increase more rapidly with depth (as seen in figure 4.17); already at 500 m velocities are characteristic of unit D (3.2 km/s) suggesting erosion of upper Quaternary strata and compression of remaining sediments.
- Units c and d, with an average velocity of 3.2 km/s, were found to overlay unit F and maintain the same thickness as their equivalents in the trough; they have been deformed into folds and faults with decreasing magnitude toward the surface; the interface between units c and d is speculative, although, supported by a change in reflectivity.
- Velocities of unit B (4.5 km/s) correspond to those of unit F in the terrace; the time of deposition of unit C was thought to coincide with the onset of transpression (end of Miocene, beginning of Pliocene); if deposition of unit F occurred simultaneously with that of unit B, then fracturing and folding of unit F could be due to the transpressional regime.

#### LINE 1264:

- a radical change in the velocity gradient and reflectivity pattern appears to occur just north (CMP 2400), where this line intersects 1250; velocities are generally much lower to the south in the uplifted portion of the terrace triangle where a thick layer of unconsolidated sediments covers unit F; there is no indication whether units d and c can be correlated in any way across the area, where the top of unit F forms two ridges centered at CMP 2400 and CMP 1500 (figure 5.18)
- complicated erosional paleo-surfaces and unconformities are visible around CMP 1880; further south some reflectors (2 seconds) show a wiggly appearance, transmitted to deeper reflectors which might be flat. A change in depositional environment for this region could be related to its location within the axis of a channel running through Dixon Entrance to the shelf break

- velocities above the WBM south of CMP 2000 are very low and range from 1.5 to 2.5 km/s and, thereby, image only the upper 1.5 km
- an angular unconformity (purple triangles in interpreted section) is traced over lines 1263 and 1250
- the sea floor rises about 750 m between intersections with line 1262 and 1250

#### LINE 1250:

- the upper layers of sediments have very low velocities, between 1.5-3 km/s above the WBM (2 km), which is not compatible with the velocity structure and units recognized on line 1262
- velocities seem to decrease further west of fault I at CMP 3900, where immense uplift during deposition produced patterns of onlap

### 5.5.3 Faults

Despite the obvious change of the depositional environment, faults and structural features can be correlated between lines 1262, 1265, 1250, S.P. Lee 3 and 1263 (figure 5.21). Fault I is the fault that separates gently-dipping strata to the east from steeply inclined reflections that culminate in the anticline A2, to the west. This fault consists of 2 branches. This and the juxtaposition of dipping reflectors on its western side with nearly flat-lying strata on the other, suggests a component of shear. The sense of lateral motion is very likely to be synthetic with the motion on the Queen Charlotte Fault, thus transporting material to the northwest. Fault I appears in a similar fashion on line S.P. Lee 5, splaying into two faults, between which, relative displacement forms a small graben-like structure on the seafloor. Sediments on both sides dip towards the disruption.

Another fault (II) is located at the western flank of anticline A2, probably combining a thrust component with dextral slip. Anticline A2 corresponds to a northwest-southeast trending fold, which is well resolved in bathymetry just north of

line 1250 (between CMP 3000 and 3500) and south of S.P. Lee 5, where the surface expression is eroded away. Anticline A2 and fault II seem to merge with fault I on line 1262. Fault III corresponds to the outermost fault, which uplifted the terrace segment and roughly delineates the abrupt change in topographic relief, which defines the northwest-southeast trending ridge. It has an arcuate appearance and curves towards the main Queen Charlotte Fault (figure 5.21).

Line 1263 and S.P. Lee 2 give an idea of the structure within another triangular terrace block just to the south. 1263 traverses the tip of a ridge that looks like the counterpart to the one forming the westward edge of the terrace block to the north. It is thus very likely that their structure and origin is the same. To be consistent with the labeling of faults and anticlines, names in the interpreted sections carry the extension (a) to distinguish their affiliation with a different terrace segment. Anticline A2a is probably active at present as seen in recent uplift indicated by the lack of flat-lying sediments, topping the folded ones. The seaward edge of this terrace segment forms a wedge that is bounded by splays of faults resembling a positive flower structure or a thrust fault with multiple branches (IIIa). The easternmost portion of line 1263 traverses the southern end of the northern terrace block, including fault III at CMP 7100. Between the anticline A2 and fault III, a fault (Ia) cuts the seafloor at CMP 6700, which could be the equivalent of fault I. However, this fault shows vertical displacement, which resulted in the formation of a wedge of sediments trapped between this fault and a normal fault (III) to the east. Sediments have been deposited while sliding down one flank of the graben. Whether this normal fault is the inverted extension of the thrust fault III is not clear. Also uncertain is the location of fault Ia at depth. Ongoing movement on this fault forms the two grabens to its west and east, which are being filled with very young sediments.

On lines S.P. Lee 5 and 1262, another anticline (A3) occurs between fault III and the proposed trough-terrace boundary, where structures of the terrace meet the N-S fault. This adds to the features that indicate intense compression in this region. Anticline A3 (S.P. Lee 5, SP 1560) forms the seaward edge of the terrace segment.

While the trough-terrace boundary (b) corresponds to fault III and IIIa on lines 1250 and 1263, they are separated by about 5 km on lines 1262, S.P. Lee 5 and S.P. Lee 3. This is an interesting observation, since the trough-terrace boundary is an active feature on the former two profiles. Anticlines A3 and A2 show no surface expression on lines 1262 and S.P. Lee 5, and are truncated by erosion. S.P. Lee 3 gives an age constraint on the time when the trough-terrace boundary became inactive. The amount of trough sediments that cover thrust faults of the trough-terrace boundary suggest that since the end of the Pliocene active faulting moved either inward to fault III or ceased completely. Inactivity on line S.P. Lee 3 seems to occur because compression was taken up by fault IIIa imaged in 1263.

## 5.6 THE CONTINENTAL SHELF REGION

One very important aspect to being able to divide the whole region into different segments is to know the location of the active Queen Charlotte Transform Fault, that forms the present and most recent boundary between continental North America and the oceanic Pacific plate. GLORIA sidescan data (reference) highlight a linear feature parallel to and a little west of the shelf break. The location of this feature coincides exactly with a vertical fault (CMP 7700) that is found on line 1262 at the low end of the steep sloping flank between shelf and terrace. Assuming this is the active fault trace of the Queen Charlotte Fault, its location from the sidescan map is superimposed on all intersecting seismic lines and illustrated in figure 5.21. A disruption of reflectors on line 1262 is clearly observable, but a correlation becomes difficult on line S.P. Lee 5 just 10 km south. The GLORIA data place the fault trace at SP 2125. Since only the stacked section of line S.P. Lee 5 is available, diffraction hyperbolas obscure the seafloor and hinder identification of a real disruption. Pure strike slip-faults are structures that are not easy to trace. But a fault and disruption of unit F and the deeper structure seems present at SP 2070 and another one at SP 2160. On line 1250, the surface fault trace coincides with the western flank of the

outcropping unit F at the seafloor, but due to the chaotic character of reflections no distinct fault is noticeable. It is problematic to localize the Queen Charlotte Fault in the seismic data, but referring to the results of the GLORIA sidescan the actual rupture occurs on one big fault.

The shelf break is defined to be where water depth increases to more than 300 m (0.4 seconds) and is marked as a black dashed line in figure 5.21. Distances between the shelf break and the Queen Charlotte Fault trace are quite variable. The small topographic relief visible at the sea floor (1262, figure 5.3 b, S.P. Lee 5, figure 5.4 b), and the great lateral variability in topography from north to south along the assumed present trace suggest that the current location is not very old. West of the present Queen Charlotte Fault trace on figure 5.20, contours show a slope of what is interpreted to be the top of unit F toward the shelf break. An older Queen Charlotte Fault could have been located somewhere further to the east and closer to the shelf break. The material within the wedge between the present and old Queen Charlotte Faults would then be of oceanic origin, now accreted to the continent.

East of the old Queen Charlotte Fault, basement rock is thought to be continental crust. In contrast to the nearly absent continental shelf west of the Queen Charlotte Islands, the shelf along Dixon Entrance is broad and nearly horizontal (Snaveley et al., 1981). A few half-grabens bound by east-side down normal faults are present in the stacked section of line 1262 and on the eastern portions of lines S.P. Lee 5 and 3. These grabens trend predominantly NNW-SSE and were interpreted to contain folded Tertiary and flat-lying undeformed Quaternary strata (Rohr and Dietrich, 1992, figure 5.14). The basement crops out at the seafloor at various locations and no indication of sediments younger than the beginning of the Pliocene is found on the basement platforms between half-grabens (Rohr and Dietrich, 1992). This could be an indication of recent uplift of this region of the continental crust or little extensional subsidence due to lateral heat loss.

## 5.7 SUMMARY

A compilation of results obtained in this chapter forms the basis for the tectonic model presented in the next chapters.

Table 5.1 summarizes all units and horizons interpreted in the Queen Charlotte Trough. Only two faults are observed in this segment, a north-south trending fault (the NS-fault) and a second fault of indeterminate strike and extent (the S-fault). Both seem to disrupt basement, with a step down to the west for the N-S fault. The N-S fault is inactive in the south, but shows progressively increasing surface expression to the north, where it develops into a pressure ridge.

The terrace is characterized by a repetitive pattern of triangular blocks arranged in an en echelon fashion and exhibiting a pressure ridge or anticline at their outer edge. Activity varies along the trough-terrace boundary. It seems to be inactive where the oceanic plate is sheltered by a ridge that is forming seawards, and building the tip of the adjacent triangular segment to the south. Pelagic and turbiditic sediments that cover the terrace show great variability. A correlation of sedimentary units was neither possible within the terrace from north to south, nor between the trough and the terrace segments. Faults and structures within the terrace are roughly oriented in a northwest-southeast direction, parallel to the ridge on the western boundary of the terrace. This ridge is probably a flower structure formed by combination of thrusting and dextral slip at an angle of about  $20^\circ$  with the Queen Charlotte Fault. This implies a direction of maximum compressive stress oriented northeast-southwest at about  $70^\circ$  to the fault and is consistent with the stress field caused by right-lateral shear.

The terrace is thought to be underlain by very consolidated sediments (unit F) and a melange of highly fractured oceanic basement and sedimentary rocks (Bc). This basement complex is tilted down to the northwest, forming a basin at the northern portion of the triangle. The depression has been filled with sediments, which underwent subsequent contraction. Erosion of the upper Quaternary strata in the basin east of the pressure ridge and the increase in magnitude of compression as the terrace block approaches the N-S fault suggest recent uplift of the northern portion and ongoing

complex deformation. The cause of the development and subsequent folding of units F and Bc, which are of assumed Miocene age, is thought to be related to an important change in the tectonic environment by the onset of transpression at the end of the Miocene or the beginning of Pliocene.

Table 5.1 Properties of units and horizons within the Queen Charlotte Trough segment; average velocities are determined from data of figures 4.17 and 5.13, see also tables 6.1 and 6.2

<b>unit or horizon</b>	<b>depth to horizon</b>	<b>average velocity</b>	<b>unit thickness at western end of profile</b>	<b>unit thickness at eastern end of profile</b>	<b>estimated relative age</b>	<b>composition</b>	<b>tectonic environment at the time of formation</b>
Moho	9-9.8 km (from Shor et al. 1962)						
top of basement		5-5.5 km/s	average dip: 3°		S.P. Lee 5/3: 15-17/18 Ma S.P. Lee 1/2 10/12-15 Ma	sheared pillow basalts, spilies and sheet flows	strike-slip of the QCF
total sediment thickness			1.5 km	5 km	0-18 Ma	sediments	

Table 5.1 (continued)

A		$\approx 5$ km/s			middle Miocene (10-18 Ma)	pillow basalt with interbedded sedimentary rocks	strike-slip of the QCF
B		$4.64 \pm 0.31$ km/s	0.6 km	1.5 km	upper Miocene (7-18 Ma)	sedimentary rock	strike-slip of the QCF
C and D		$3.23 \pm 0.09$ km/s	0.6 km	2 km	C: late Miocene (5-7 Ma) D: Pliocene (5-2 Ma)	sedimentary rocks	onset of transpression
E		$2.09 \pm 0.09$ km/s	0.5 km	1.2 km	Quaternary (0-2 Ma)	sediments	intensified compression in the late Pliocene (3-2 Ma); no ongoing flexure of oceanic lithosphere in the Holocene

## **6. GRAVITY MODELING**

Two-dimensional forward-gravity-modeling was carried out for lines 1262 and 1250 to place limits on the configuration of the Pacific-North American plate boundary using the new constraints on sediment velocity and density from the seismic reflection data. As was stated in chapter 2, gravity reflects the tectonic signature of an active plate boundary superposed on a simple edge-effect of a continent/ocean transition. The goal of this chapter is to determine this signature and deduce information about the nature of the terrace block and its configuration at depth, where constraints from seismic reflection images are not available.

### **6.1 CONSTRAINTS ON GRAVITY MODELING**

The GM-SYS gravity and magnetics software of Northwest Geophysical Associates (Corvallis, Or) was used to conduct the modeling. A summary of the mathematical techniques implemented in the software is described in Fleming (1996). Since the profiles are approximately perpendicular to the strike of the plate boundary and thereby to major tectonic features (trough and terrace), a two-dimensional interpretation was assumed valid. To traverse a larger portion across the plate boundary, gravity data were extended in east and westward directions to a total of 160 km by extracting corresponding values from the regional free-air gravity anomaly field of figure 2.5 (see also chapter 3). Edge-effects from the outer boundaries of the model were avoided by extending the model  $\pm 30000$  km to the west and east.

In a constant velocity analysis, reflectors that were thought to correspond to unit interfaces as interpreted in chapter 5 were picked at various CMPs of lines 1250 and 1262 (locations marked in figures 5.3 and 5.5). Tables 6.1 and 6.2 compile interval velocities, interface depths, and unit thicknesses at those CMPs.

Table 6.1 Compilation of interval velocities, unit thicknesses, and depths to interfaces between units at several selected CMPs (figure 5.3) within the Queen Charlotte Terrace and shelf transition, which is bounded by the shelf break and the QCF trace as determined by GLORIA sidescan data, and within the Terrace and Trough region of line 1262 (figure 4.17); units correspond to units in the interpretation of figure 5.3, and properties of units in the trough are comparable to those in table 5.1; velocity-density conversion was done with the aid of the dotted curve in figure 6.3, representing Gardener's rule  $p = aV^{1/4}$ ; WBM = Water Bottom Multiple

		Terrace/Shelf transition		QCF	Terrace				
	CMP	7500	7600		7900	8400	8800	9500	9800
	km along profile	88.75	90.0		93.7	100.0	105.0	113.75	117.5
<b>Unit e</b>	interval velocity in km/s	2.26	2.45		2.17	2.17	2.28	2.37	2.52
	average velocity/density	2.36 ± 0.13 km/s 2.15 g/cm <sup>3</sup>			2.3 ± 0.15 km/s 2.15 g/cm <sup>3</sup>				
	depth to interface D/E in km	1.9	2.0		2.2	2.7	3.1	3.2	3.0
	unit thickness in km	0.3	0.4		0.3	0.5	0.7	0.7	0.5
<b>Unit d</b>	interval velocity in km/s	2.98	3.33		2.45	2.67	2.99	3.03	3.5
	average velocity/density	3.16 ± 0.25 km/s 2.3 g/cm <sup>3</sup>			2.93 ± 0.4 km/s 2.3 g/cm <sup>3</sup>				
	depth to interface D/C in km	3.4	3.6		2.7	3.8	4.5	4.1	3.9
	unit thickness in km	1.5	1.6		0.5	1.1	1.4	0.9	0.9
<b>Unit c</b>	interval velocity in km/s	4.76	5.27		3.5	3.53	3.47	4.45	4.84
	average velocity/density	5.02 ± 0.36 km/s 2.6 g/cm <sup>3</sup>			3.96 ± 0.64 km/s 2.45 g/cm <sup>3</sup>				
	depth to interface C/F in km	5.6	5.4		4.4	4.5	5.4	5.4	5.1
	unit thickness in km	2.2 to WBM	1.8 to WBM		1.7	0.7	0.9	1.3	1.2
<b>Unit F</b>	interval velocity in km/s				4.49	4.95	4.39	5.74	4.84
	average velocity/density				4.88 ± 0.53 km/s 2.55 g/cm <sup>3</sup>				
	depth to interface F/Bc in km				6.0	7.3	7.4	7.3	8.3
	thickness to WBM in km				1.6	2.8	2.0	1.9	3.2

Table 6.1 (continued) Remarkable is the fact that average interval velocities for the trough units match perfectly the ones determined from sonobuoy data along profile S.P. Lee 5 as described in Snavelly et al. (1981); \* = not determined from velocity analysis since too close to pressure ridge or outside range of profile, instead, average interval velocity is used to obtain depths and thicknesses

		Trough							
	CMP	10800	10900	11000	11100	11200	11300	11500	interpolated from SPLee 5
	km along profile	130.0	131.25	132.5	133.75	135.0	136.25	138.75	195.0
<b>Unit E</b>	interval velocity in km/s	2.02	2.02	2.05	2.03	2.02	2.12	1.98	*
	average velocity/density	2.03 ± 0.04 km/s 2.1 g/cm <sup>3</sup>							
	depth to interface E/D in km	3.74	3.82	3.81	3.78	3.8	3.82	3.76	3.3
	unit thickness in km	1.15	1.2	1.18	1.15	1.16	1.18	1.11	0.5 (see table 5.1)
<b>Unit C and D</b>	interval velocity in km/s	3.31	3.31	3.32	3.31	3.28	3.36	3.19	*
	average velocity/density	3.30 ± 0.05 km/s 2.3 g/cm <sup>3</sup>							
	depth to interface C/B in km	5.8	5.8	5.77	5.69	5.71	5.57	5.41	3.9
	unit thickness in km	2.06	1.98	1.96	1.91	1.91	2.74	1.74	0.6 (see table 5.1)
<b>Unit A and B</b>	interval velocity in km/s	5.03	4.91	4.87	4.97	4.51	4.17	4.51	*
	average velocity in km/s	4.7 km/s ± 0.32 2.5 g/cm <sup>3</sup>							
	depth to basement in km	7.63	7.53	7.5	7.6	7.5	7.32	7.32	4.5
	unit thickness in km	1.83	1.73	1.73	1.91	1.79	1.75	1.91	0.6 (see table 5.1)

Table 6.2 Compilation of interval velocities, unit thicknesses and depths to interfaces between units at several selected CMPs (figure 5.5) within the Queen Charlotte Terrace and shelf transition, which is bounded by the shelf break and the QCF trace as determined by GLORIA sidescan data, and the Terrace and Trough region of line 1250 (figure 5.13); units correspond to units in the interpretation of figure 5.5 and properties of units in the trough are comparable to those in table 5.1; velocity-density conversion was done with the aid of the dotted curve in figure 6.3, representing Gardener's rule  $p = aV^{1/4}$ ; remarkable is the fact, that average velocities for the trough units match perfectly the ones determined from sonobuoy data along profile S.P. Lee 5 as described in Snaveley et al. (1981); ); WBM = Water Bottom Multiple; \* = not determined from velocity analysis since too close to pressure ridge or outside range of profile, instead, average velocity is used to obtain depths and thicknesses

	CMP	Trough interpolated from SPLee 5	500	1000	1500	1700	1900	2000	2600	2700	Fault III 2800
	km along profile	-80	8.25	14.5	20.75	23.25	25.75	27.0	34.5	35.75	37.0
	interval velocity in km/s	*	2.17	2.08	2.11	2.22	2.26	2.14	*	*	*
<b>Unit E</b>	average velocity/density (same as for line 1262)		2.16 ± 0.07 km/s 2.1 g/cm <sup>3</sup>								
	depth to interface D/E in km	3.3	3.69	3.62	3.66	3.73	3.83	3.68	3.58	3.6	3.73
	unit thickness in km	0.5	0.95	0.9	0.96	1.06	1.18	1.04	1.1	1.1	1.1
	interval velocity in km/s	*	3.14	3.10	3.20	3.19	3.13	3.12	*	*	*
<b>Unit C and D</b>	average velocity/density		3.15 ± 0.04 km/s 2.3 g/cm <sup>3</sup>								
	depth to interface B/C in km	3.9	5.02	5.12	5.2	5.14	5.24	5.15	5.68	5.7	5.83
	unit thickness in km	0.6	1.33	1.5	1.54	1.41	1.41	1.47	2.1	2.1	2.1
	interval velocity in km	*	4.89	4.82	4.41	4.70	4.19	4.29	*	*	*
<b>Unit A and B</b>	average velocity/density		4.55 ± 0.29 km/s 2.5 g/cm <sup>3</sup>								
	depth to basement in km	4.5	6.39	6.51	6.78	6.77	7.12	7.45	7.378	7.4	7.5285
	unit thickness in km	0.6	1.37	1.39	1.58	1.63	1.88	2.3	1.7	1.7	1.7

Table 6.2 (continued)

		Terrace		fault I	Terrace			Terrace/Shelf transition	
	CMP	3100	3400	3800	4100	4500	4800	5000	5500
	km along profile	40.75	44.5	49.5	53.25	58.25	62.0	64.5	70.75
Unit e	interval velocity in km/s	1.63	1.55		1.97	1.99	1.92	1.74	1.75
	average velocity/density	1.59 ± 0.06 km/s 2.0 g/cm <sup>3</sup>			1.96 ± 0.04 km/s 2.05 g/cm <sup>3</sup>			1.75 ± 0.01 km/s 2.0 g/cm <sup>3</sup>	
	depth to bottom of interface E in km	1.7	1.6		1.8	1.6	1.5	1.1	1.04
	unit thickness in km	0.2	0.1		0.4	0.4	0.4	0.1	0.1
unit down to F	interval velocity in km/s	2.37	1.7		2.33	2.29	2.58	2.46	2.92
	average velocity/density	2.37 km/s 2.15 g/cm <sup>3</sup>	1.7 k km/s 2.0 g/cm <sup>3</sup>		2.31 ± 0.028 km/s 2.1 g/cm <sup>3</sup>		2.58 km/s 2.2 g/cm <sup>3</sup>	2.46 km/s 2.2 g/cm <sup>3</sup>	2.92 km/s 2.25 g/cm <sup>3</sup>
	depth to top of unit F in km	1.9	2.2		2.8	2.5	2.2	2.3 to WBM	2.6 to WBM
	unit thickness in km	0.2	0.6		1.0	0.9	0.7	1.2 to WBM	1.8 to WBM
'top of unit F'	interval velocity in km/s	2.84	2.41		3.01	2.62	3.13		
	average velocity/density	2.84 km/s 2.25 g/cm <sup>3</sup>	2.41 km/s 2.15 g/cm <sup>3</sup>		3.01 km/s 2.3 g/cm <sup>3</sup>	2.62 km/s 2.2 g/cm <sup>3</sup>	3.13 km/s 2.3 g/cm <sup>3</sup>		
	depth to interface in km	4.1	2.7 to WBM		3.4 to WBM	3.1 to WBM	2.7 to WBM		
	thickness in km	2.2	0.5 to WBM		0.6 to WBM	0.6 to WBM	0.5 to WBM		

Table 6.2 (continued)

<b>'unit F'</b>	interval velocity in km/s	4.02							
	average velocity/density	4.02 km/s 2.45 g/cm <sup>3</sup>							
	depth to WBM in km	6.0							
	thickness to WBM in km	1.9							

In the trough segment, interval velocities correspond to unit velocities because picked reflectors are believed to be identical with unit boundaries, whereas in the terrace, especially for line 1250, this could not always be carried out, since reflectors here are hard to identify as unit interfaces or units could not be correlated between profiles. Thus, averages were calculated from interval velocities of different CMPs whenever they seemed to be within a close enough range. Finally, densities were determined from average interval velocities with the aid of the p-wave velocity-density relationship of figure 6.1.

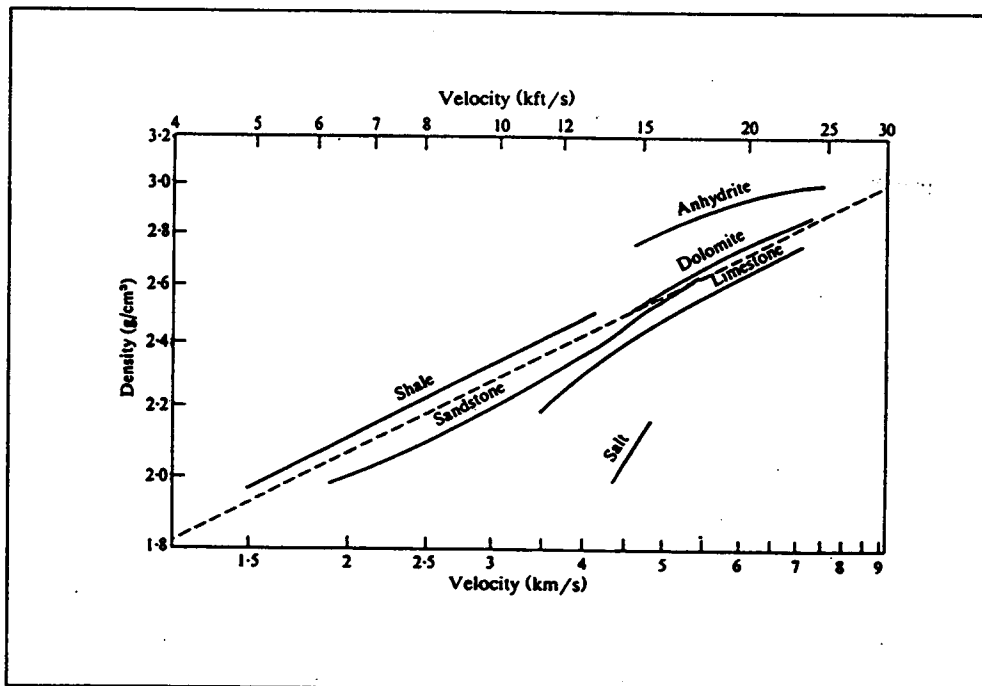


Figure 6.1 P-wave velocity-density relationships for different lithologies (log-log scale); the dotted line represents Gardener's rule:  $\rho = aV^{1/4}$  (from Telford et al., 1994)

Furthermore, water density was taken to be the typical value of salt water:  $1.024 \text{ g/cm}^3$ . Mantle, continental and oceanic crust are assigned densities of  $3.3 \text{ g/cm}^3$ ,  $2.8 \text{ g/cm}^3$ , and  $2.85 \text{ g/cm}^3$ , respectively, consistent with the gravity modeling of Horn

et al. (1984). The thickness of the oceanic crust was assumed to be 7 km. All constraints from seismic reflection data and the assumed normal oceanic crust were put into two starting models, one for line 1262 and one for line 1250. Model calculations reach down to 40 km, but only the upper 25 km are shown in the following figures.

## 6.2 RESULTS

The first important result of the gravity forward modeling procedure is the fact that continental crust has to be exceptionally thin north of the Queen Charlotte Islands off Dixon Entrance to match the observed gravity signature. An important aspect of the density model is the location of the Queen Charlotte Fault, or a fault zone within which the transition between continent, terrace block and oceanic crust occurs. A safe guess is to locate the leading edge of the continent at least as far west as the shelf break, because the bathymetry indicates a change in underlying structure, and the location of the shelf break lies in the vicinity of the zero-crossing of the gravity high/low pair, where the "edge" is expected. By positioning the plate boundary at the shelf break, assuming 7 km of oceanic crust ( $2.85 \text{ g/cm}^3$ ) to its west,  $2.8 \text{ g/cm}^3$  for continental crust, as well as sediment densities from tables 6.1 and 6.2, the crust/mantle interface below the continent can only be modeled at a depth of about 24 km for distances greater than 40 km east of the boundary, where it shallows to less than 20 km at the shelf break. A deeper Moho would produce too low a level of gravity, while a shallower Moho would have the opposite effect. Of course, the depth of 24 km would change slightly with a more detailed resolution of the crustal density structure in the continent. The only density contrast in this model that is resolvable from the seismic data is the sediment-basement interface between continental basement rocks ( $2.85 \text{ g/cm}^3$ ) and sedimentary rocks that fill the array of half-grabens in Dixon Entrance. Since the sediment fill within these basins, and sediments covering the basement highs, were interpreted to be predominantly Tertiary in age (Rohr and Dietrich, 1992), the

density of this unit was chosen equivalent to the upper Tertiary section found in the Queen Charlotte Trough, with a density of  $2.3 \text{ g/cm}^3$ .

To illustrate non-uniqueness of gravity modeling, and to get insight into the range of allowable models for line 1262, four different models that fit the data will be discussed. For all those models, units constrained by the reflection data are dashed. The location of the plate boundary and the best-fitting continental thickness of 24 km were held fixed. For model 6.2 a), the assumption was made that the oceanic crust extends beneath the terrace at the same dip as is observed in the trough segment. The two blocks (I and II) mark the remaining parts where parameter values can be modified to attain the best fit given the assumptions. The boundary between block II and the material above was drawn where the water bottom multiple limits the constrained area. Modeling was not very sensitive at the steeply sloping gravity curve above block I, and best fitting values were reached for densities ranging between  $2.6\text{-}2.9 \text{ g/cm}^3$ . Block II required a density as low as  $2.2 \text{ g/cm}^3$ , which is equivalent to sediments found in the undeformed unit E of the trough segment. Such low density is unlikely at this depth of more than 7 km. Even sedimentary material underthrust and carried along with the descending oceanic crust would be expected to be of greater density, and similar to that of unit A/B ( $2.5 \text{ g/cm}^3$ ) observed in the trough region. Besides, density of sediments tends to increase through lithification and compaction through higher confining pressures at greater depths. To demonstrate the magnitude of impact this low density block has on the total calculated gravity curve, block II was set to a density of  $2.55 \text{ g/cm}^3$ , which is equivalent to that of the overlying strata. The resulting dashed curve displays a difference of up to 25 mGal to the best fit.

Figure 6.2 b) on the other hand, fixes block II at a density of  $2.55 \text{ g/cm}^3$  and keeps block I unchanged, while the dip of the oceanic crust was increased until a best fit was reached. As a result, the oceanic Moho seems to just merge with the mantle/crust interface of North America. Higher densities of block II would require an even steeper dip of the oceanic Moho beneath the terrace, while as was seen in figure 6.2 a), lower densities go with a flatter orientation of the crust/mantle boundary. For

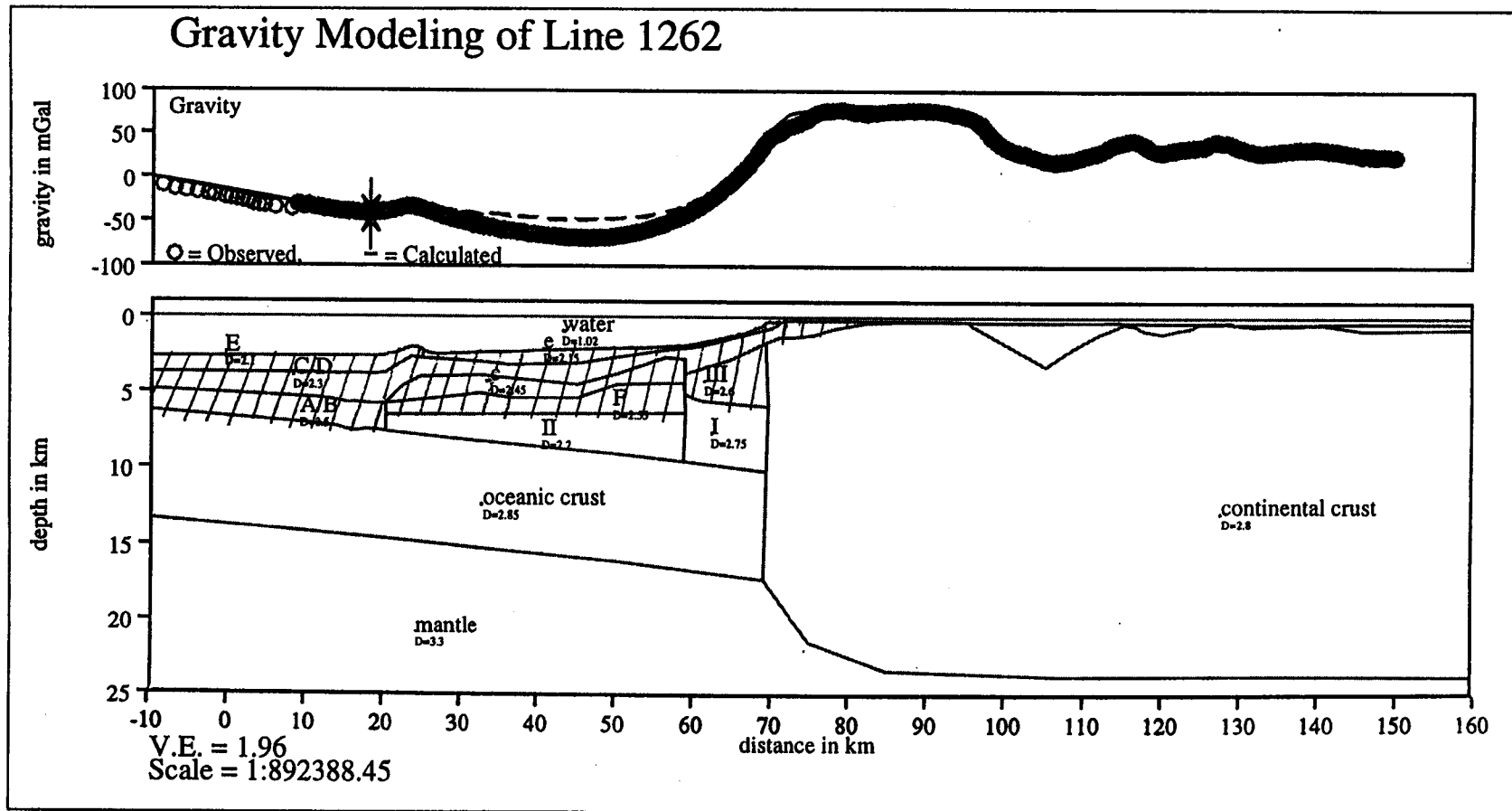


Figure 6.2 a) Gravity forward model of line 1262; dashed areas are constrained by seismic reflection data, oceanic crust is assumed to be “normal” with a thickness of 7 km and a constant dip extending beneath the terrace, continental crust and mantle are held fixed; blocks I and II are modeled for; a best fit is obtained with a density ranging between 2.6-2.9 g/cm<sup>3</sup> for block I, and of 2.2 g/cm<sup>3</sup> for block II, while the dashed gravity curve demonstrates its impact, by setting the density of block II to 2.55 g/cm<sup>3</sup>

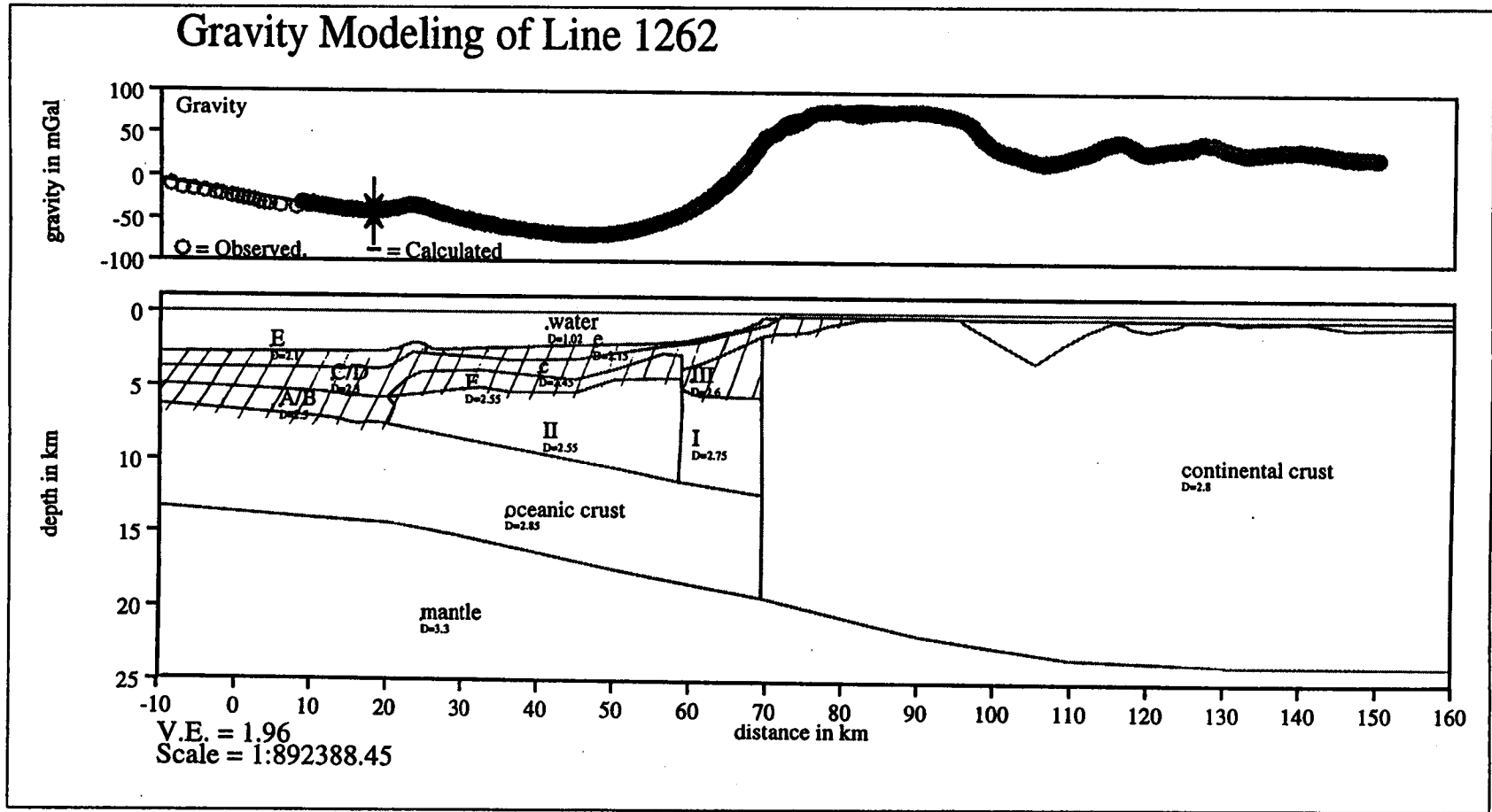


Figure 6.2 b) Gravity forward model of line 1262; dashed areas are constrained by seismic reflection data, oceanic crust is assumed to be "normal" with a thickness of 7 km; continental crust and mantle are held fixed; blocks I and II are set to  $2.75 \text{ g/cm}^3$  and  $2.55 \text{ g/cm}^3$ , respectively; the dip of the oceanic Moho is increased, till a best fit is reached

this density of block II, the oceanic Moho dip beneath the terrace obtained from figure 6.2 b) is about  $6^\circ$ , considerably less than the  $19^\circ$  suggested by Dehler and Clowes (1988) for their profile west of Moresby Island. However, the depth at which the Moho is located beneath the inner edge of the terrace is the same, at about 20 km, while the Moho depth at the outer edge is only 12 km west of Moresby Island but 15 km at line 1262. This combined with the increasing width of the terrace from 25 km to almost 50 km from south to north, makes the change in Moho dip beneath the terrace seem plausible. A greater oceanic Moho dip beneath the terrace with a plate boundary of this configuration is mechanically not logical: oceanic Moho located at deeper than the adjacent continental Moho would result in underthrusting of oceanic crust beneath the continent as subjected to compression by convergence.

Figure 6.2 c) simply extends the oceanic crust of figure 6.2 b) beneath the continent, while in figure 6.2 d), the oceanic Moho dip beneath the terrace was set to a steeper value of  $19^\circ$  as was proposed by Dehler and Clowes' (1988) refraction model west of the Queen Charlotte Islands. For this case, a good fit could only be reached for very high densities between 2.9 and 3.1  $\text{g/cm}^3$  for blocks I and II (figure 6.2 d), and a continental crust that thins to 17 km close to the plate boundary, which is required due to the existence of subducted lower density oceanic crust at mantle depths. Such high densities that exceed those of average oceanic crustal material in the lower terrace are unlikely. Hence, an extension of the oceanic crust beneath the North American continent is only possible if the Moho of the slab does not descend deeper than the 24 km of crust/mantle transition that was previously modeled. The density contrast between oceanic and continental crust of only 0.05  $\text{g/cm}^3$  is too small to produce a resolvable gravity signature. Thus, the case of a continental and oceanic crust welded together by very shallow subduction is indistinguishable by gravity data from that of a simple juxtaposition of continental and oceanic crust at the plate boundary. Nevertheless, inferences about the dip of the oceanic Moho beneath the terrace as well as about the allowable density of the material just above the oceanic crust can be made.

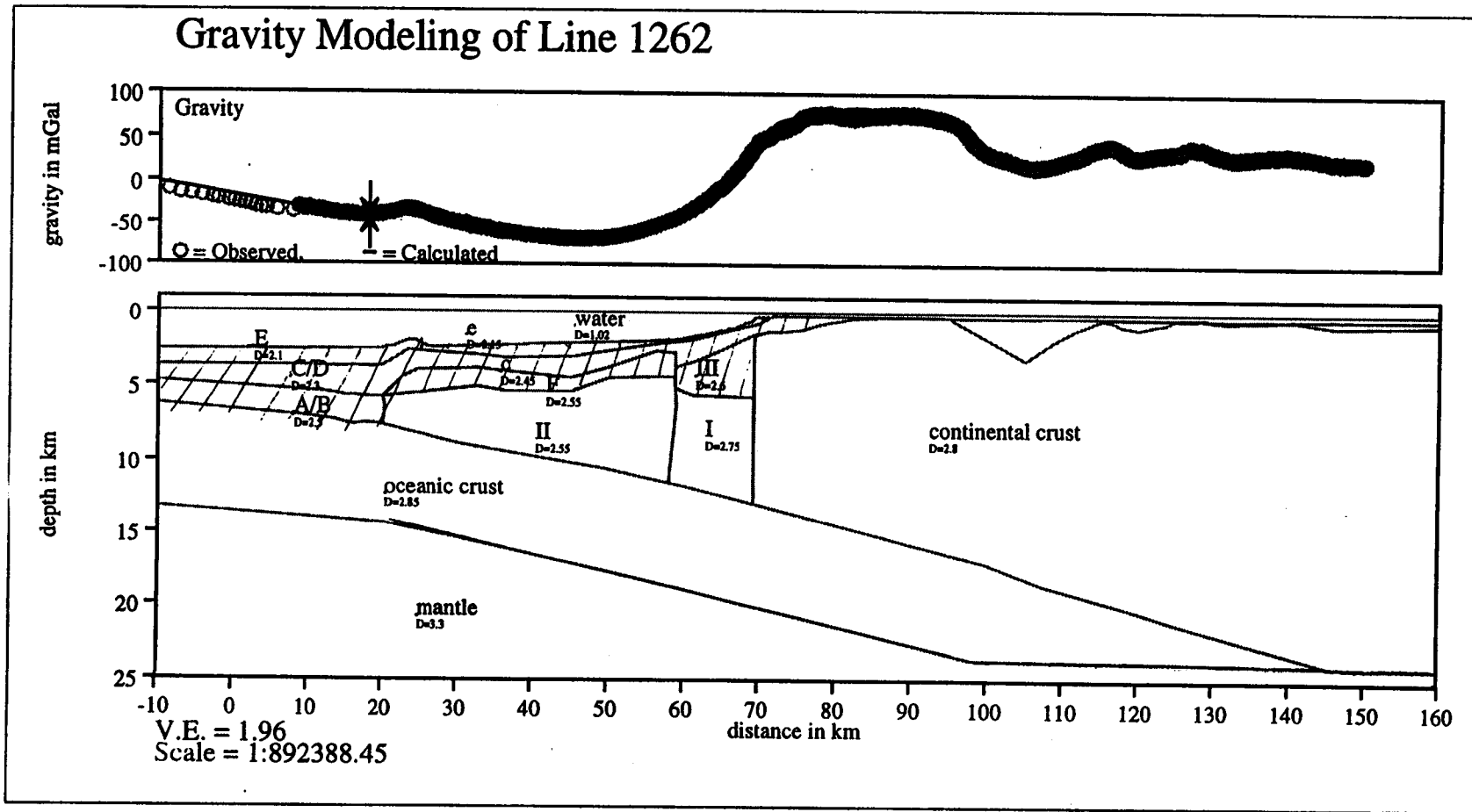


Figure 6.2 c) Gravity forward model of line 1262; dashed areas are constrained by seismic reflection data, oceanic crust is assumed to be “normal” with a thickness of 7 km; continental crust and mantle are held fixed; blocks I and II are set to 2.75 g/cm<sup>3</sup> and 2.55 g/cm<sup>3</sup>, respectively; the oceanic crust is extended beneath the continent

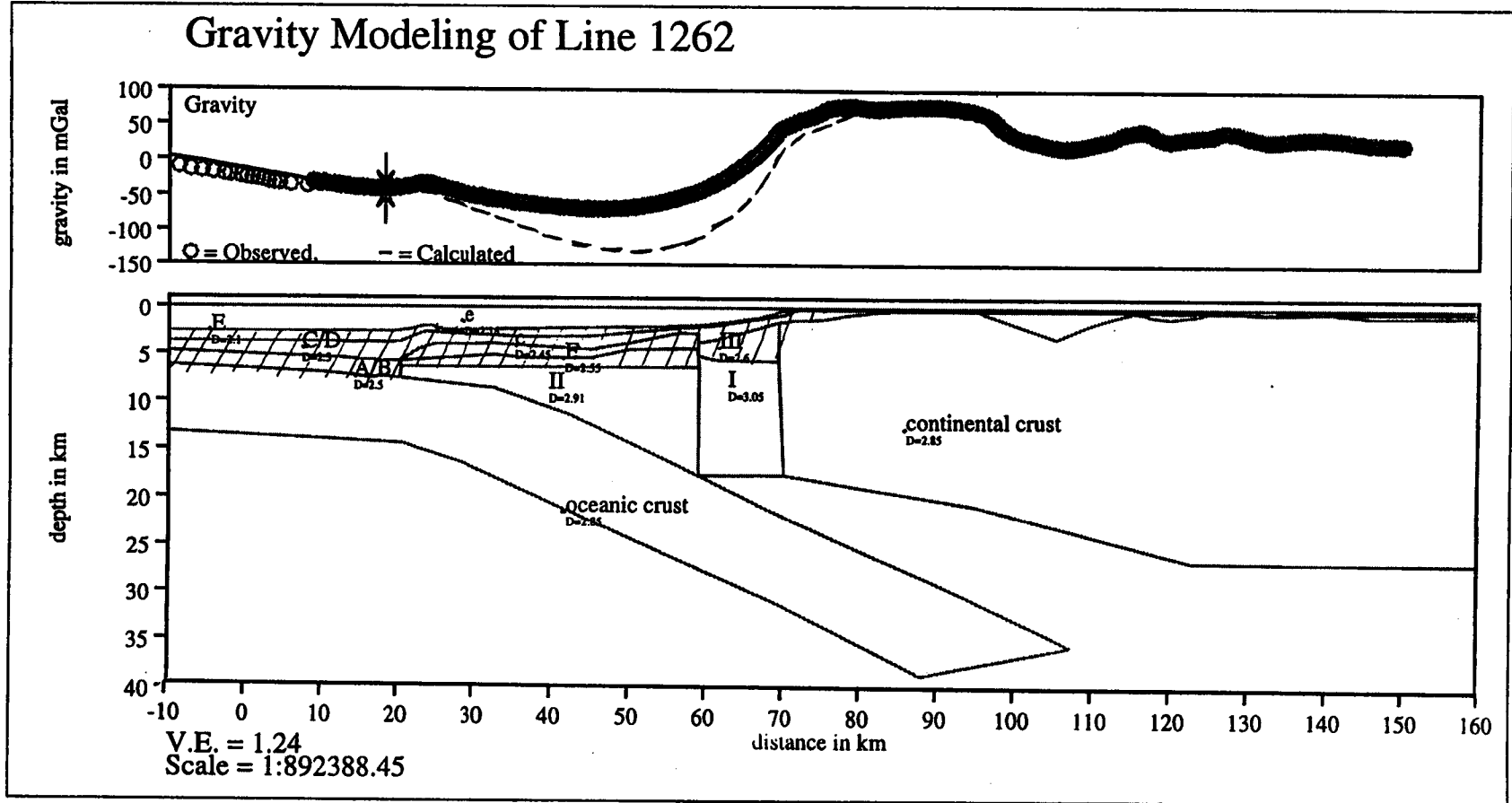


Figure 6.2 d) Gravity forward model of line 1262; dashed areas are constrained by seismic reflection data, oceanic crust is assumed to be “normal” with a thickness of 7 km; the oceanic Moho dip beneath the terrace is set to 19°; inversion for blocks I and II results in densities ranging between 2.9 and 3.1 g/cm<sup>3</sup> and a continental crust as thin as 17 km; the dashed curve demonstrates the effect if lower terrace densities are only 2.55 g/cm<sup>3</sup> and 2.75 g/cm<sup>3</sup> for blocks II and I, respectively

The main conclusion is that the Queen Charlotte Terrace seems to be underthrust by oceanic crust. Although the oceanic crustal block could be modeled as continent with a density of  $2.8 \text{ g/cm}^3$  as well, it makes no sense to introduce a 7 km thick slab of continental crust below the thick wedge of sedimentary rocks. This would mean the actual plate boundary is located close to the NS-fault, which was interpreted to be a structure, originating in the trough as dipping oceanic basement was found east of it further south of line 1262. An oceanic crust with increasing dip beneath the terrace is the preferred model.

As discussed in chapter 5, the unit of density  $2.55 \text{ g/cm}^3$  (F/Bc) within the terrace could be a melange of compressed and very consolidated sediments and fractured upper oceanic basement. Units above this block are thought to be of pure sedimentary origin. Sedimentary units are slightly higher in density than neighboring units in the trough, probably, due to compression.

Blocks are split 10 km west of the shelf break based on the location of the QCF from sidescan data. The density of block III is weakly constrained by interval velocities obtained from reflection data and indicates an increase in densities across the fault. Block I is modeled to have a density of  $2.75 \text{ g/cm}^3$  to fit the gravity. There seems to be a transition zone between the present Queen Charlotte Fault and the shelf break east of which continental crust is assumed to exist. If the Queen Charlotte Fault has jumped westward from the shelf break to its new location, then the origin of block I should be oceanic. If the QCF has not jumped and blocks I and III are sheared continental crust, then the current shelf break has probably been eroded back from the plate boundary.

Figures 6.3a) through c) demonstrate the same modeling procedure for line 1250, where the terrace is narrower. Again, a low density block is required just above the descending oceanic basement beneath the terrace if oceanic Moho is assumed to have a shallow dip. If the dip of the oceanic Moho is increased to meet the crust/mantle interface at about 23 km depth beneath the shelf (b) a density of  $2.67 \text{ g/cm}^3$  for block II is allowed. Figure 6.3 c) shows again, how underthrusting of the oceanic crust beneath the continent would not change the gravity signature.

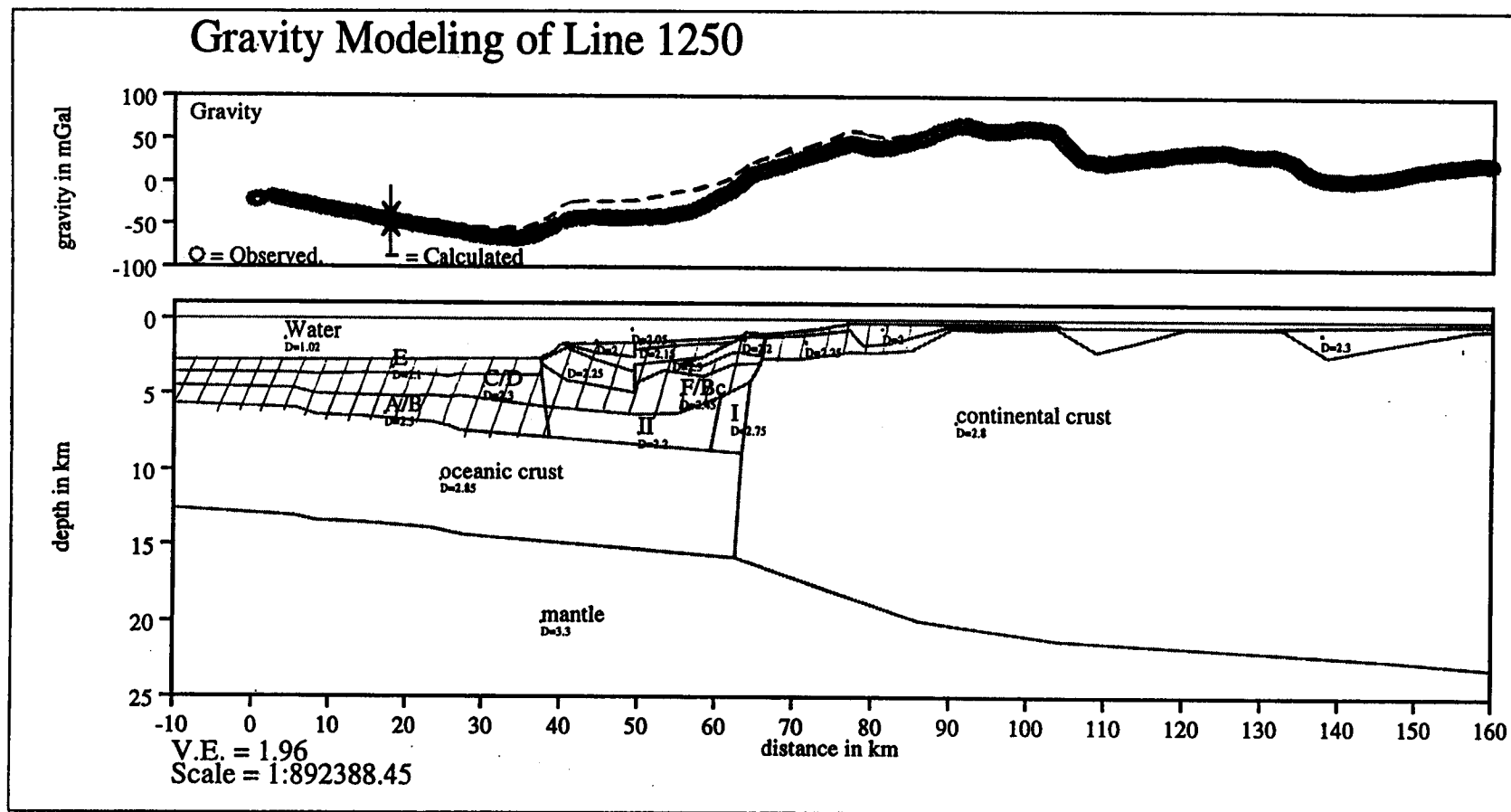


Figure 6.3 a) Gravity forward model of line 1250; dashed areas are constrained by seismic reflection data, oceanic crust is assumed to be “normal” with a thickness of 7 km and a constant dip extending beneath the terrace, continental crust and mantle were held fixed; blocks I and II are modeled for; a best fit is obtained with a density ranging between 2.6-2.9 g/cm<sup>3</sup> for block I, and of 2.2 g/cm<sup>3</sup> for block II, while the dashed gravity curve demonstrates its impact, by setting the density of block II to 2.67 g/cm<sup>3</sup>

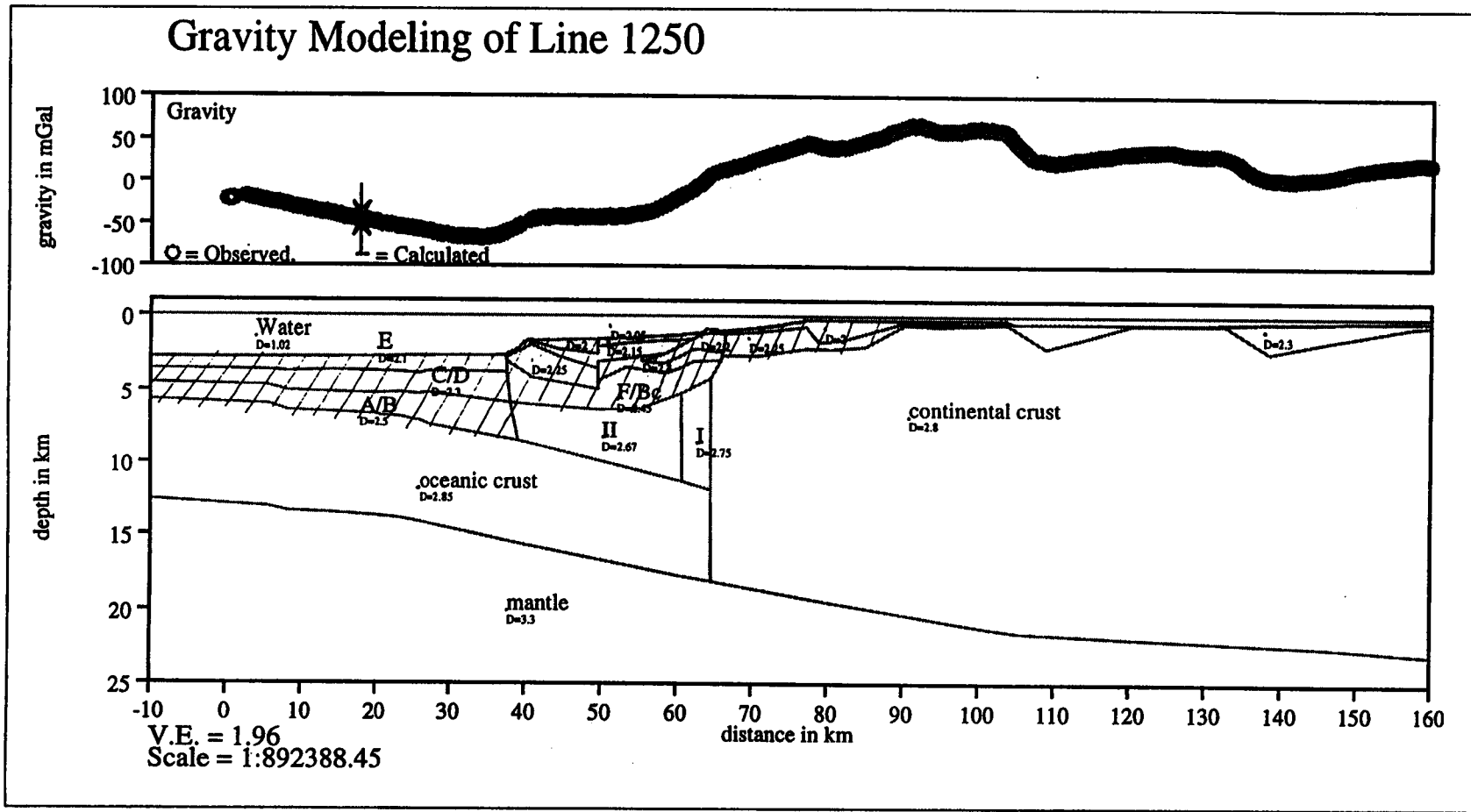


Figure 6.3 b) Gravity forward model of line 1250; dashed areas are constrained by seismic reflection data, oceanic crust is assumed to be “normal” with a thickness of 7 km; continental crust and mantle are held fixed; blocks I and II are set to 2.75 g/cm<sup>3</sup> and 2.67 g/cm<sup>3</sup>, respectively. the dip of the oceanic Moho is increased, till a best fit is reached

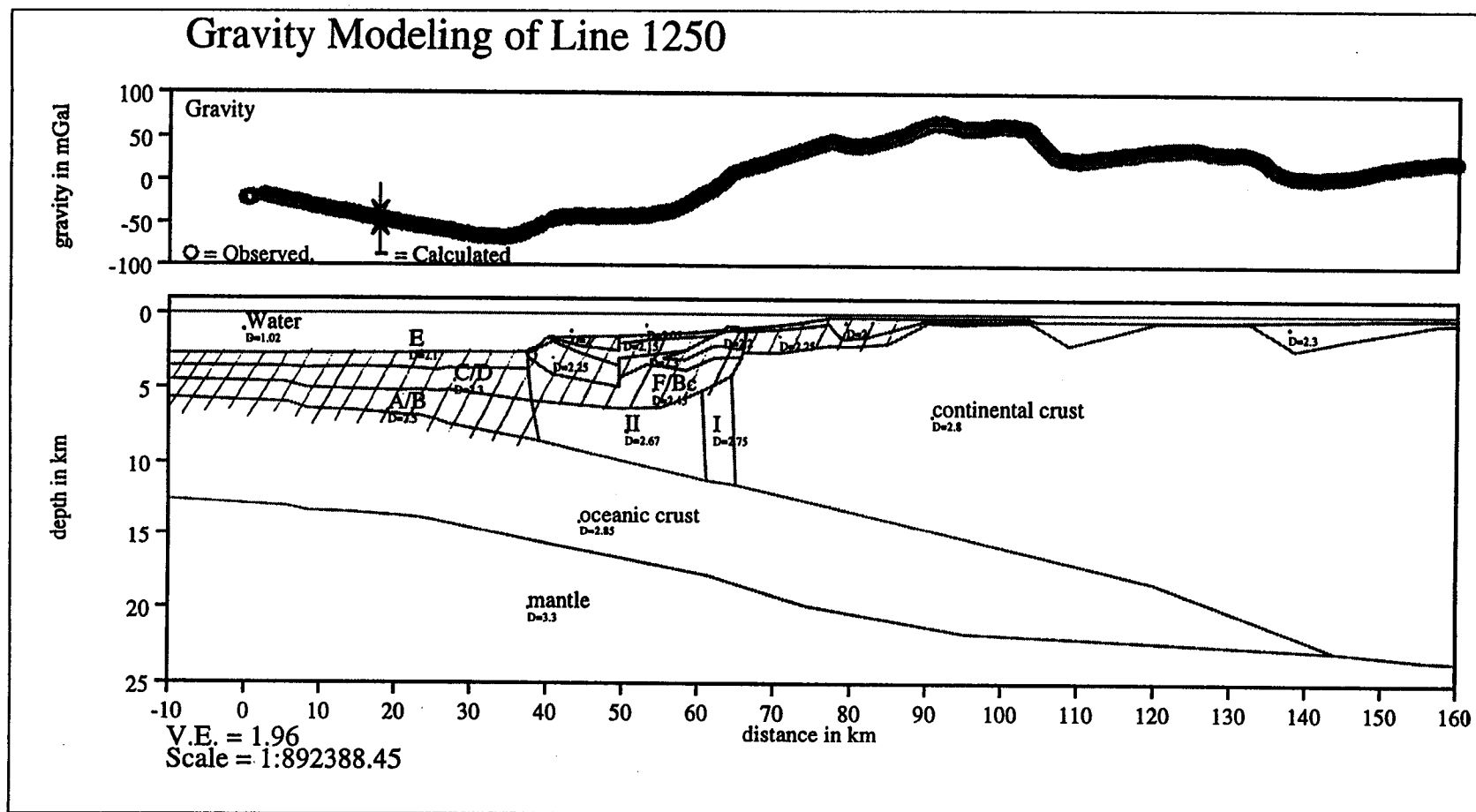


Figure 6.3 c) Gravity forward model of line 1250; dashed areas were constrained by seismic reflection data, oceanic crust was assumed to be “normal” with a thickness of 7 km; continental crust and mantle were held fixed; blocks I and II were set to 2.75 g/cm<sup>3</sup> and 2.67 g/cm<sup>3</sup>, respectively; the oceanic crust was extended beneath the continent

The overall appearance of the observed gravity along line 1250 is different from that along line 1262. The lowest gravity values are not centered over the terrace segment, but are at the terrace/trough boundary (compare with figure 2.5). From there, gravity increases continuously with a more moderate gradient to a gravity high some 40 km inland of the present Queen Charlotte Fault. This phenomenon can be explained either by a shallower dip of the oceanic Moho beneath the terrace or by the existence of a block of denser material as was done in figure 6.3 b). Since line 1250 traverses one of the triangular terrace slivers, which is characterized by elevated bathymetry and a higher gravity anomaly superimposed on the edge effect of the plate boundary, the emplacement of a higher density block beneath the terrace seems reasonable. The leading edge of the continent is assumed to extend just east of the location where unit F outcrops at the seafloor (60 km). As it was for line 1262, this corresponds to the site of the zero-crossing of gravity values on regional gravity.

Gravity forward modeling with the available seismic constraints cannot resolve whether oceanic crust is actually underthrusting the continent. If underthrusting occurs, it must be very shallow and oceanic crust must be welded to the anomalously thin continental crust. The dip of the oceanic Moho increases beneath the terrace and a block of high density material ( $2.55\text{-}2.67\text{ g/cm}^3$ ) is found below the up to 3 km thick section of sedimentary rocks covering the terrace. This high density block corresponds to units F/Bc, which are interpreted as consisting of a melange of fractured oceanic basement rock and highly consolidated sediments overlying the oceanic crust.

Whether or not the region across the Queen Charlotte Fault is in local isostatic equilibrium is an interesting question. If underthrusting occurs, lithosphere is flexed (model 6.2 c) and local isostatic equilibrium would not be expected. In the case of simple juxtaposition of oceanic and continental lithosphere along a vertical boundary (model 6.2 a), the area would be assumed to be in local equilibrium. Table 6.3 shows the calculation of isostasy to a depth of 40 km at 20 km intervals along profile 1262. The deviation in percent from km 0 (continent) was compared to values that result from flexure of the lithosphere at the Hawaiian Islands (Watts and Brink, 1989). There,

the deviation between mass of a column at the flexural bulge and of a column of unflexed lithosphere is approximately 1.5 %. Deviations across the Queen Charlotte terrace are of the same magnitude suggesting that flexure is important in this area and that it is out of local isostatic equilibrium. The mass anomaly matches the free-air gravity anomaly (figure 6.2), with a high/low pair over the edge of the continent. This indicates that the gravitational signature of flexure is part of the measured gravity anomaly, this observation is thus supportive of the models presented in figures 6.2 b) and c). These two models both include flexure of the oceanic lithosphere.

Table 6.3 Calculation of isostasy at various sites along the profile 1262; isostasy is obtained by adding the product of densities and heights distributed within a column of unit area and 40 km depth and the gravitational acceleration ( $\rho g h$ )

km along the profile	pressure of unit column in $10^6 \text{ Pa}$	deviation in % from value at km 0
0	1166.998	
20	1172.197	+0.4
40	1169.254	+0.2
60	1182.694	+1.3
80	1187.697	+1.7
90	1158.561	-0.7
100	1148.751	-1.6
120	1159.052	-0.7
140	1159.542	-0.6
160	1170.137	+0.3

## **7. TECTONIC MODEL AND CONCLUSION**

### **7.1 PRESENTATION OF A TECTONIC MODEL**

New images of structures within the terrace segment off Dixon Entrance as deduced from the multichannel seismic reflection profiles, and gravity modeling, provide insights into the processes of terrace formation and development and the tectonic evolution of this plate boundary. Two previously published end-member models, neither of which satisfies all observations, were introduced in chapter 2 to explain the tectonics of the Queen Charlotte Fault region. Up to 100 km of shortening (table 2.1) west of the Queen Charlotte Islands, or up to 55 km off Dixon Entrance for the past 5 Ma must have been accommodated somehow.

One model (figure 2.10 b) juxtaposes continental and oceanic crust along a vertical boundary, with convergence taken up by internal deformation of the Pacific plate. Thickening of the oceanic crust beneath the terrace segment or visible deformation of the oceanic plate further offshore are predicted. However, oceanic crust west of the terrace shows little deformation. Placing the required thickening of oceanic crust within the 30-km-wide terrace implies a 20-30 km thick layer with velocity and density characteristic of oceanic crust. The volume of the terrace segment, estimated by the gravity models obtained in chapter 6, is not sufficient to store all this material. Transportation of basement rock along the plate margin at a faster rate than the parallel component of plate motion would be necessary. However, a mechanism for decoupling slices that rapidly migrate northward along the margin to make room for incoming new crust is difficult to visualize in this compressive configuration. Also, ongoing thickening of the terrace section would quickly result in a terrace block that is thicker than the adjacent continental crust. Moreover, transmission of compressive stresses across the plate boundary would result in thickening of the continental crust. Neither thickening of

the continent or a terrace underlain mostly by high oceanic crustal velocities is observed.

In contrast, a wide range of data support an underthrust or at least a partially underthrust Pacific plate. An underthrust plate is allowed, but not required, by the gravity models of chapter 6. The top layers of the Queen Charlotte Terrace seem to be composed mainly of young and unconsolidated sedimentary rock (units above unit F in profiles of chapter 5), underlain by a melange of very consolidated sediments (unit F) and possible fractured oceanic basement (unit Bc), forming a wedge between underlying oceanic and continental crust to the east. The existence of the Queen Charlotte Trough and a characteristic offshore bathymetric high about 100 km seaward suggest flexure of the Pacific plate. The characteristic parallel bands of very low and high gravity over the trough and the west coast of the islands and Dixon Entrance are not just results of a simple edge-effect but are amplified by a flexed oceanic crust topped by low density sediments and water, and a possibly uplifted and eroded (Sutherland Brown, 1968) thin continental crust. The heat flow pattern across the margin (Hyndman et al., 1982) corresponds to that predicted for subducting young oceanic crust - high offshore and low on the terrace and margin due to a thick layers of sediment. The lack of arc volcanism, which is normally found about 200 km inland of the trench, can be explained by the relatively recent initiation of underthrusting. This distance would have not been reached within 5-6 Ma.

Flexure modeling by Prims et al. (1997) suggested underthrusting of the oceanic crust of 10-15 km west of the Queen Charlotte Islands, which accounts only for a small portion (10-15 %) of the shortening that has been taken place in this region. Whether or not flexure modeling in absence of compressional stresses can be representative of the real amount of underthrusting is not discussed here, although it is important. The same modeling procedure finds arguments against the subduction hypothesis proposed by Yorath and Hyndman (1983). In this hypothesis the Queen Charlotte Fault cuts through the descending slab to produce faults that migrate downward with it to allow for partitioned strike-slip movement and thrust events. The

resolution of depth and location and the amount of earthquake data to date are not good enough to sufficiently constrain the fault plane of the Queen Charlotte Fault or its maximum depth. A more complete and detailed analysis is required to detect possible thrust events occurring on the suture between oceanic and continental plates and within the terrace.

Both models discussed above are two-dimensional and steady state. Because the study region is just north of a bend in the plate boundary, where the maximum convergence angle changes from  $26^\circ$  to  $13^\circ$  (table 2.1), the key to understanding structures that are currently present in the terrace segment off Dixon Entrance is to understand terrace formation further south west of the Queen Charlotte Islands. As was mentioned before, north and south of the bend in strike of the Queen Charlotte Fault, the appearance of the terrace changes drastically. While the area off Dixon Entrance is characterized by its repetitive pattern of triangular shaped blocks, and a rather wide (45 km) and irregular terrace segment, it becomes narrower and very linear west of the islands. These observations indicate that a 4-dimensional model of plate boundary evolution in time and space is needed.

Although, the details of a transition from a strike-slip boundary to a component of steady-state underthrusting of the oceanic lithosphere are undoubtedly complex, figure 7.1 shows a simplified schematic illustration of this process that combines parts of the two end-member models. At 5-6 Ma, before the onset of transpression and the beginning of flexure of the oceanic plate, it is assumed to be horizontal (7.1 a). After initiation of the transpressional regime, the juxtaposition of the thicker continental crust and the thin oceanic crust will hinder immediate underthrusting. Steady state underthrusting will not occur until the leading edge of the oceanic crust reaches the base of the continental crust. During this phase, stresses build up across the fault zone and when it is locked, result in distributed shear. Figure 7.2 demonstrates the expected orientation of fractures and folds in such a transpressional environment. Sanderson and Marchini (1984) showed, in their study of transpression, that the  $45^\circ$  obliquity of

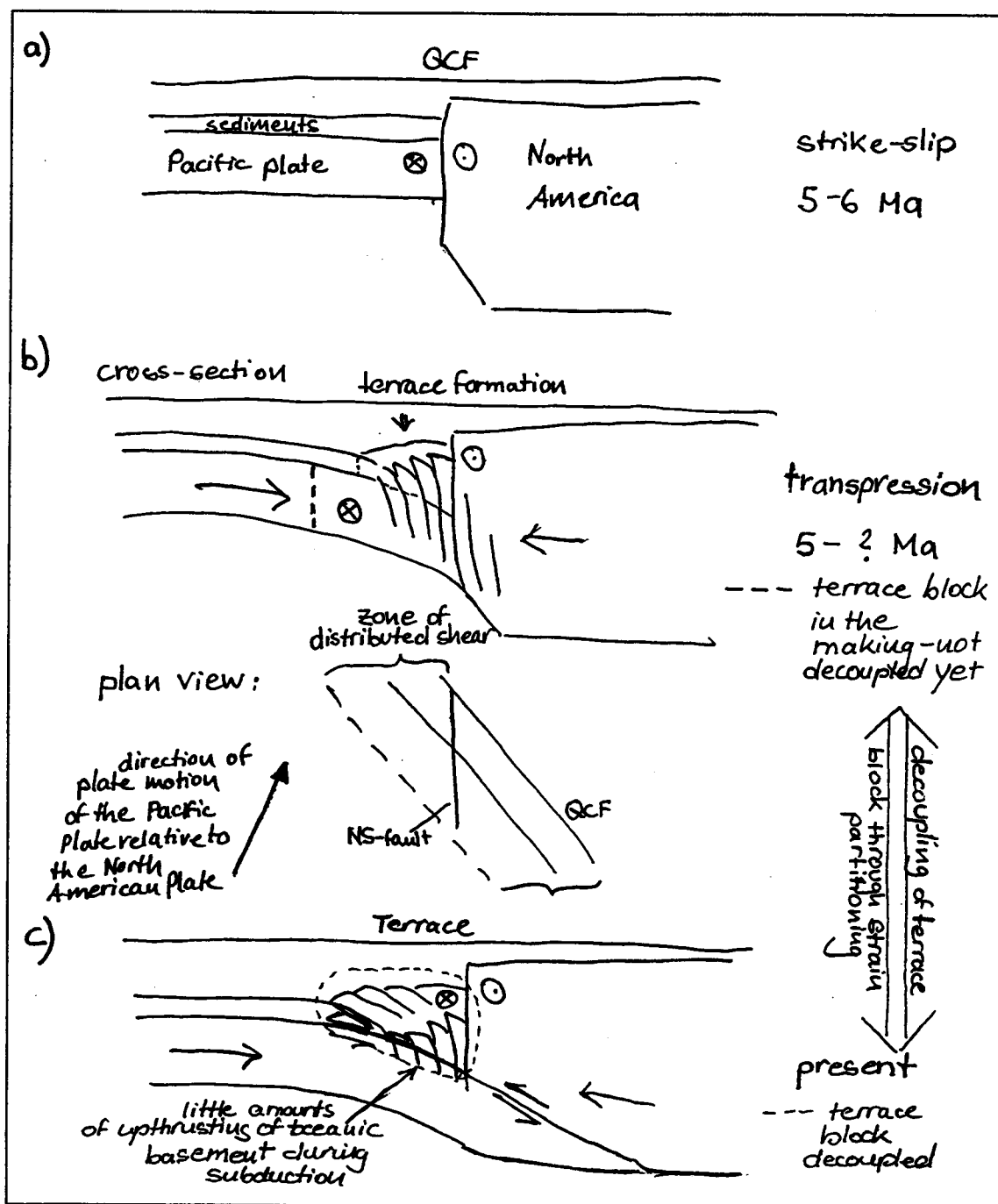


Figure 7.1 Block diagrams showing the beginning a) and development of the transpressional regime west of the Queen Charlotte Islands; b) demonstrates the flexure of the oceanic crust and its upthrusting at the plate boundary, while shear strain is distributed in periods when the Queen Charlotte Fault is locked; c) steady state configuration of underthrusting after the top of the leading edge of the oceanic lithosphere has reached the bottom of the continental crust, only little amounts of upthrusting of the oceanic basement, for plan view see figure 2.2

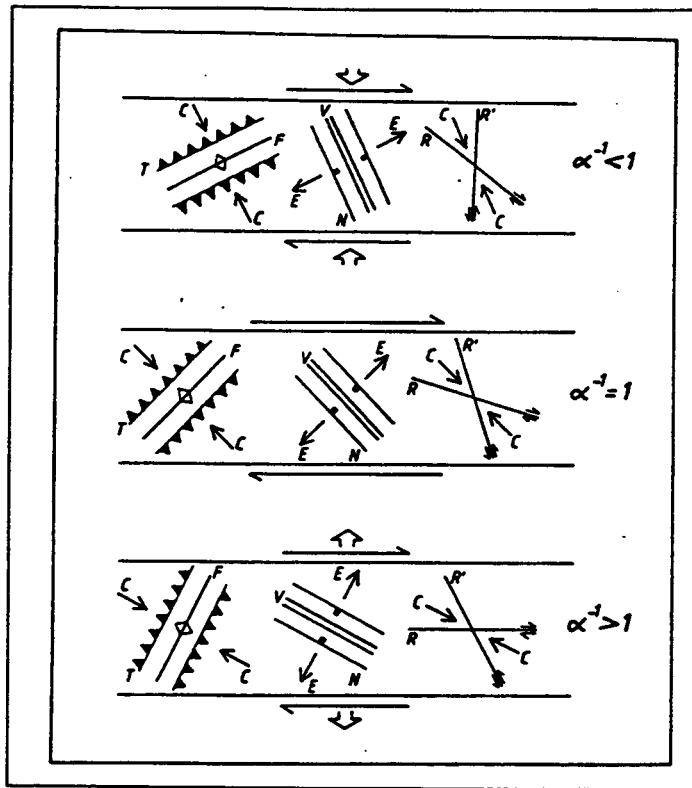


Figure 7.2 Diagrams show orientations of fractures in a) a transpressional regime, b) a simple shear environment or the classic wrench tectonic model for comparison, and c) a transtensional regime; C = compression axis ( $\sigma_1$ ), E = extension axis ( $\sigma_3$ ), N = normal faults, T = thrust faults, R, R' = Riedel shears or wrench faults, V = veins, dykes or extension fractures, F = fold axes (adapted from Sanderson and Marchini, 1984)

structures in simple shear zones (7.2 b) is modified. The vertical stretch is described by  $\alpha$ , and the horizontal shortening across the zone is described by  $\alpha^{-1}$ , while  $\gamma$  is the shear strain parallel to it. The case of simple shear is specified by  $\alpha = 1$  and  $\gamma = 0$  specifies pure shear. For  $\alpha^{-1} < 1$  (transpression), folds and thrusts initiate at a much lower angle to the zone, whereas extensional features initiate at higher angles (7.2 a). The opposite applies for  $\alpha^{-1} > 1$  (transtension) as seen in figure 7.2 c). For simple shear, the first Riedel shears or synthetic shears develop at an average angle of  $17^\circ$  as studied in sandbox models by Naylor and Mandl (1986). Antithetic Riedel shears strike at  $72^\circ$  to

the basement fault, with an opposite sense of shear to the Riedels (figure 7.2 b). Under transpression both of these angles are increased (figure 7.2 a).

Although, it might be dangerous to apply results of small scale sandbox or clay models to large scale motions of crustal blocks, similar structures might develop during a phase of early distributed transpression across the Queen Charlotte Fault. The orientation of the NS-fault at about  $25^\circ$  to the Queen Charlotte Fault corresponds to the expected orientation of Riedel shears in a transpressional environment. In addition, to that, the trend of the N-S fault lines up with the north-south-direction of magnetic sea floor spreading anomalies, as were presented in figure 2.3. Zones of weakness commonly occur parallel to the spreading axis at which oceanic crust was formed. Thus, Riedel shears are even more likely to develop along such preexisting zones of weakness and to remain within this orientation. During this phase until a steady-state subduction configuration is reached, oceanic crust could possibly be deformed as a cause of distributed shear. The result would be wrench-faulting along the Queen Charlotte Fault Zone and the development of Riedel shears in a north-south direction. According to this hypothesis, the displacement on the NS-fault is right-lateral. It might be noted that in support of this theory, some distributed shear is interpreted to occur in the continental plate within the Queen Charlotte Basin (Rohr and Dietrich, 1992)

Figure 7.1 b) demonstrates this phase of transition, where oceanic crust flexes downward. Whenever no movement takes place on the Queen Charlotte Fault plate boundary itself, distributed shear might form folds and faults according to figure 7.2 a) in shallower sedimentary sections within a zone that develops into the Queen Charlotte Terrace. The tremendous amount of shortening that has to be accommodated over time will result in basement-involved upthrusting of the oceanic crust at the continent/ocean transition until a stable steady-state configuration of underthrusting is reached. How exactly this upthrusting and faulting takes place is not known. It is believed, that it results in the development of a terrace, which is decoupled from both the continent and the Pacific plate as an effect of strain partitioning (figure 2.12). Due to the previously upthrusting basement rocks, the decoupled terrace block contains high densities and

high velocities at its bottom, which are interpreted as very consolidated sediments and a melange of those with basement rock, consistent with refraction results of Dehler and Clowes (1988), Horn et al. (1984), and interpretations in chapter 5 and 6. Although structures probably formed under the influence of a shear zone of the kind in figure 7.2 a), their orientations are believed to change with time and to approach parallelism with the plate boundary. This is supported by the fact that their orientations already are at lower angles to the main basement fault than would be expected without a component of convergence. The longer shear and compression are distributed over the area, and the more the terrace block is decoupled from the two plates, the more obliquity within it will disappear. The result will be a linear feature that parallels the Queen Charlotte Fault, as now observed west of the Queen Charlotte Islands.

The idea of a decoupled terrace block is adapted from a model Fitch (1972) presented first for western Sunda, where horizontal shear and underthrusting occur, concurrently, on the Semangko fault and along the inner wall of the Java trench, respectively. This is explained by convergence in which slip that is oblique to the plate margin is at least partially decoupled between parallel zones of transcurrent faulting and underthrusting. The mechanism of decoupling oblique slip in the manner proposed by Fitch (1972) is favored because a nearly vertical surface concentrates horizontal shear more effectively than an inclined surface of equal or greater strength. The configuration of this model applied to the Queen Charlotte Fault region is shown simplified in figure 2.12 and 7.1 c) and corresponds to the gravity model presented for line 1262 in figure 6.4 c). The Queen Charlotte Fault accommodates the shear component of plate motion down to a depth of at least 12 km (figure 6.4 c) off Dixon Entrance, and deeper if the fault is found to cut through the subducting slab. This is left to future studies of earthquake mechanisms in this region. The component of convergence is taken up by the underthrusting of the Pacific plate beneath North America in a manner that might be aseismic, since to date, no thrust events are correlated with the descending slab. The terrace block itself thus moves northward with respect to the continent, while it

overrides the oceanic crust perpendicularly (figure 2.12) to produce a wedge of sedimentary rock that stores the compressed material.

The terrace block is not only thought to be composed of sedimentary rock, but of having a base that is partly due to the upthrusting that occurred at terrace formation and the involvement of basement in the subduction process at subsequent stages. At depths greater than 10-15 km (Robert Lillie, personal communication), basement tends to be incorporated in the process of underthrusting as sediments become more lithified and strong and the contrast between their strength and that of the upper basement decreases. This base of the terrace builds the foundation for the zone of uplift and deformation, and the seaward limit forms a barrier that develops into the outer scarp of the terrace, which bounds the undeformed trough region. In the south, west of the Queen Charlotte Islands, this barrier is linear and parallel to the plate boundary; farther north however, it is discontinuous, as marked (b) in interpreted sections of chapter 5.

It was noted that the orientation of faults interpreted to bound these terrace slivers off Dixon Entrance (fault III) and other structures as well (as faults II,I, and anticlines A1-A3) are parallel to the plate boundary west of the Queen Charlotte Islands, but are oblique to the plate boundary north of the eastward bend. Figures 7.3 a)-c) try to demonstrate an explanation for such coincident directions. As described above, the terrace segment west of the Queen Charlotte Islands is thought to have developed through a combination of upthrusting and subsequent underthrusting and decoupling into a wedge of off-scraped consolidated and deformed sediments with a foundation of fractured basement. This terrace block migrates northward along the margin and with it plate boundary sub-parallel faults and fractures of this foundation. The terrace is still undergoing deformation and is involved in the underthrusting process through its close location to the Pacific plate/ terrace suture (figures 7.3 a). Along the plate margin the terrace is subjected to different sedimentation environments. Basement fractured material and consolidated deformed sediments are covered with younger material at varying and generally increasing rates to the north. The amount of

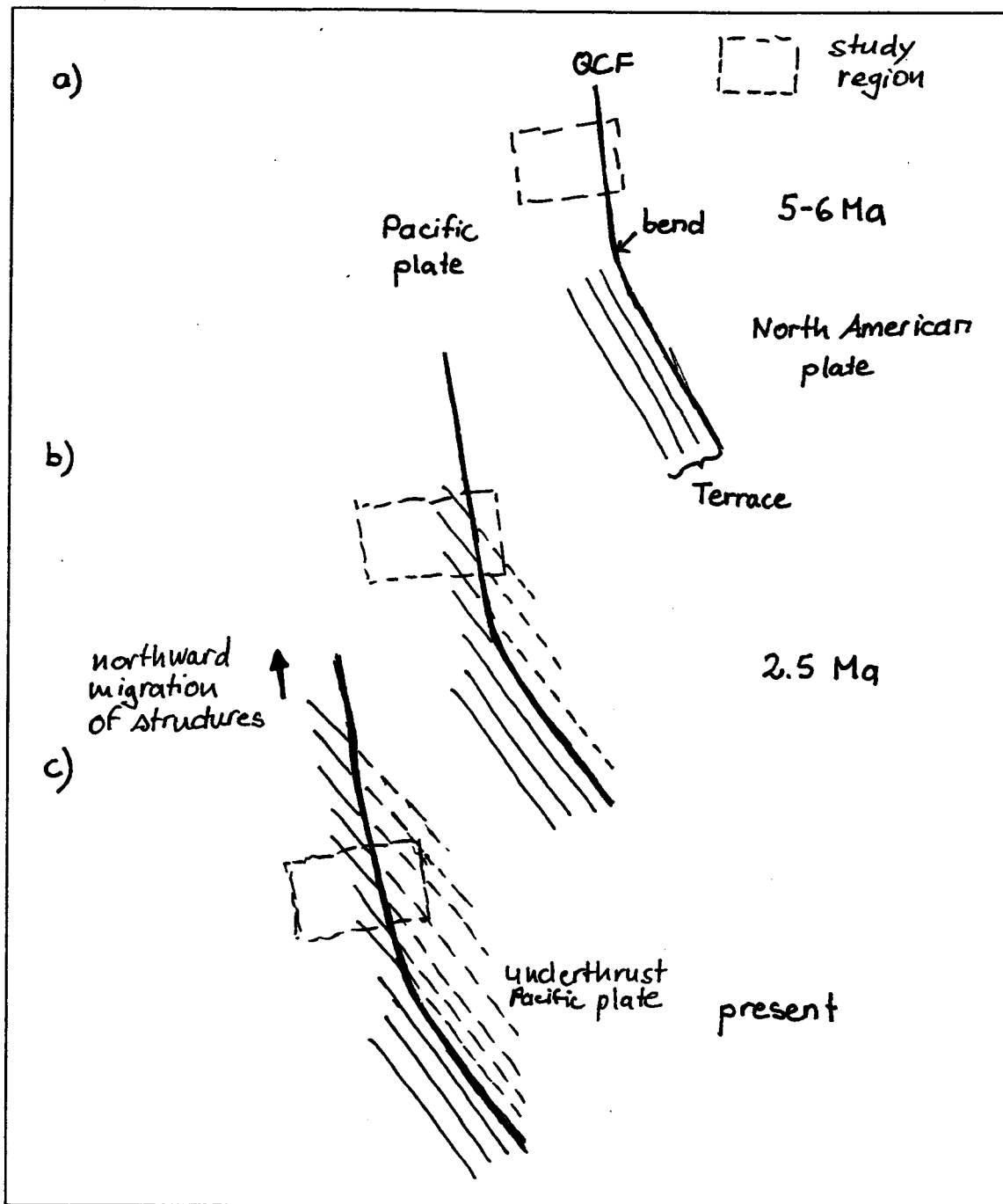


Figure 7.3 Cartoon demonstrating the migration of plate boundary parallel fractures and thrusts of the base formation of the terrace west of the Queen Charlotte Islands, which control the oblique appearance of the terrace boundary north of the eastward bend of the Queen Charlotte Fault; a) 5-6 Ma ago; b) 2.5 Ma ago; c) present

sediment scraped off from the Pacific plate will logically increase to the north as the infill of the trough increases from a thickness of 1 to 5 km as well, to produce a higher amount of uplift of the terrace off Dixon Entrance. As the terrace reaches the eastward bend of the Queen Charlotte Fault, underthrusting and faulting north of it will occur along preexisting fractures within the terrace foundation. Then the whole terrace block will rotate around the corner to parallel the more northward orientation of the fault (figure 7.3 b). The outer edge of the terrace is now discontinuous, but the fractures are still parallel to the plate boundary west of the Queen Charlotte Islands. The angle (about  $20^\circ$ ) formed between fault III (see figure 5.21) and the Queen Charlotte Fault is similar to that observed between folds and thrust faults in a transpressional regime (figure 7.2 a), structures which are promoted by a component of convergence. It is proposed here that the development of the basic shape of the terrace off Dixon Entrance is guided by the existence of older material at the bottom of the terrace block. Further deformation and compression is confined along faults III, II, and I and the production of anticlinal and synclinal structures between them. High sediment influx in this area is trapped within these faults to form ridges (A2 and A2a) with onlap patterns (as was seen nicely in anticline A2 of profile 1250) due to simultaneous deposition and deformation. Anticlines A2 and A2a are thus thought to be structures resulting from the same tectonic processes as at the outer edges of the terrace segment. The outer structural zone that was interpreted on line 951 of Bruns and Carlson (1987, figure 2.8), a little bit farther north, may also, result from a similar process. This shows, that active tectonism has a strong influence on sediment dispersal, and that the seaward boundary of the terrace is not simply a relict trench, but an active feature with ongoing uplift, deformation, and deposition (see A2a on line 1263 and A2 and fault III on line 1250). Shear within the terrace block might be taken up such that material within the terrace moves southeast relative to material in the trough. This results in an uplift of the triangular block where it merges with the Queen Charlotte Fault and explains the high bathymetry and gravity observed there. Supporting this is the tilting down to the northwest of the terrace base formation and older sediments as was suggested in the

discussion of figure 5.20's contours of the top of unit F. Figure 7.3 c) shows the northernmost position that fractures might have reached after initiation somewhere in the terrace west of the Queen Charlotte Islands when transpression started 5 Ma ago.

The seaward boundary of the triangular terrace block that is traversed by lines 1262 and 1250 was marked b in figure 5.21. All structures east of this limit are interpreted to be caused by the process of underthrusting and shear within this wedge of material and to build a trap for young incoming sediments. The NS-fault, as explained above, is thought to be of different origin. Its trend corresponds to the magnetic anomaly pattern in this region and to the orientation of synthetic shear of the transpressional strain ellipse at the time of the beginning of this tectonic environment. In chapter 5, it was suggested that movement on this fault ceased at the end of the Tertiary, where line 1263 intersects it, while it is an active structure at present further north. Coincidentally, in the north, this fault seems to collide with the terrace segment and its structures, suggesting its reactivation due to recent compression. Assuming movement along the NS-fault is right-lateral then the underthrusting trough portion east of it rotates counterclockwise, producing a component of up-to-the-east compression (figure 7.4). This process results in rotation of contours of equal basement depth in the opposite direction (clockwise) as was noted in the discussion of figure 5.18 and a basement step down to the west. The S-fault, although not clear in its orientation, is very likely to be a structure that was caused by the termination of the rotated trough portion to the south, taking up resulting compression or tension.

In summary, the tectonic model suggested here can explain structures and faults identified in the seismic reflection data and is consistent with the gravity forward modeling and other previous data sets of the region.

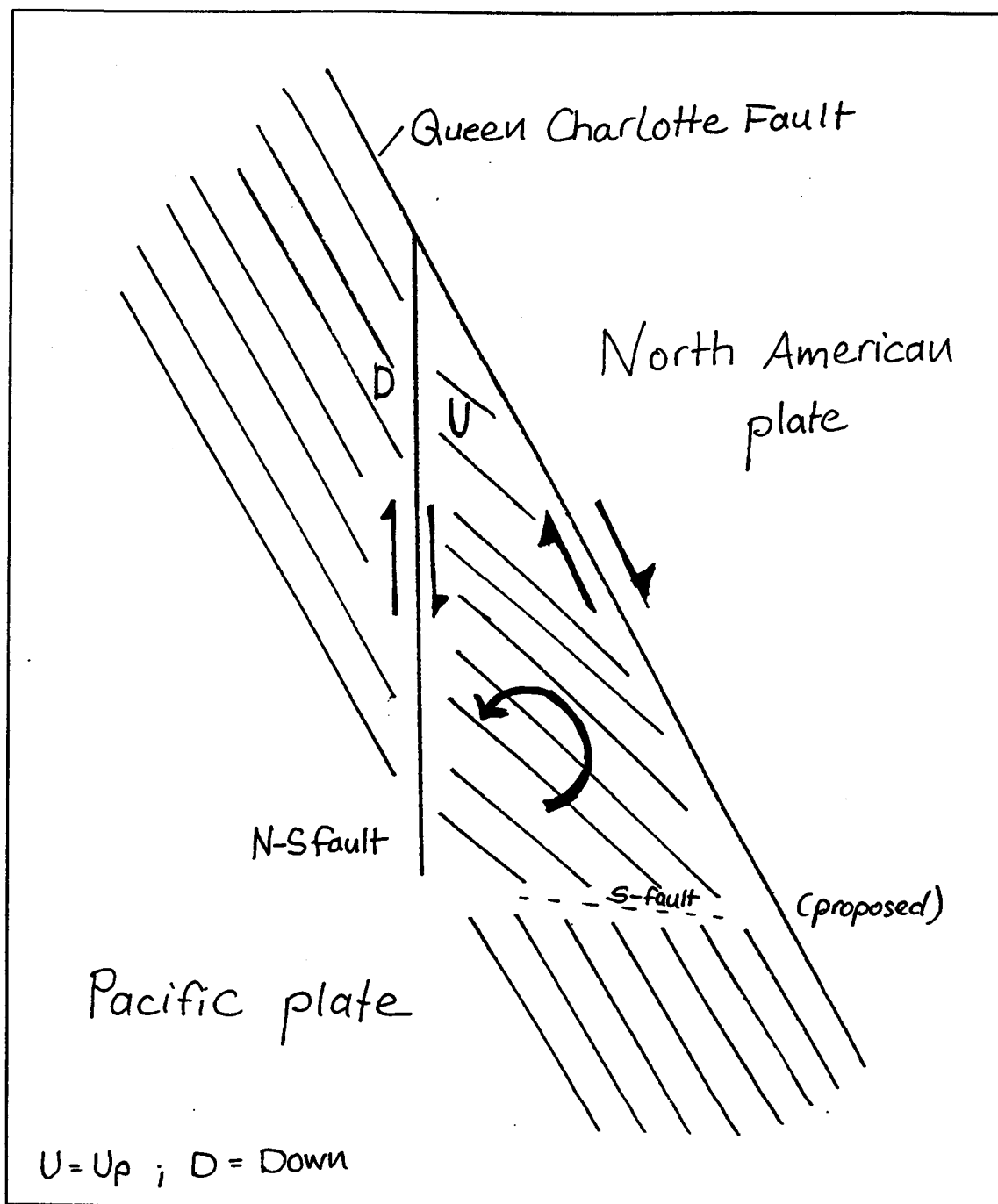


Figure 7.4 Block diagram to illustrate relative movements on the NS-fault, and the Queen Charlotte Fault; the result is a counterclockwise rotation of the trough portion east of the NS-fault and west of the terrace boundary to produce compression and a basement step up to the east across it; black lines prior to rotation refer to contours of equal distance from the plate boundary

## 7.2 CONCLUSIONS

To explain the morphology of the Queen Charlotte Terrace, from a narrow linear feature west of the Queen Charlotte Islands to a broader zone of discontinuous blocks off Dixon Entrance, a model of an underthrusting Pacific plate beneath the continent is considered more appropriate than a model of pure upthrusting and translation of pieces of material along the margin. About 5-6 Ma ago, transpression initiated and oceanic lithosphere was flexed and upthrust at the plate boundary eventually reaching a steady state configuration of a subducting slab. Fractured basement rock and highly consolidated sediments at depth of the accretionary complex form the foundation of the terrace segment. The terrace is decoupled from the North American plate as it moves both along and perpendicular to the underthrusting Pacific plate. As the terrace migrates along the margin and reaches the location of the eastward bend of the Queen Charlotte Fault west of Graham Island, underthrusting north of this bend occurs obliquely to the new orientation of the fault, and follows preexisting fractures and thrusts within the base of the terrace. A repetitive pattern of broken up terrace slivers results, and the outer edge of the terrace forms an angle with the Queen Charlotte Fault of about  $30^\circ$ , an orientation promoted by the transpressional strain ellipse for compressional structures. Faults and folds within these slivers trend northwest-southeast. Compression and shear along them controls more recent sediment dispersal as seen in ridges found at the outer edges of the terrace blocks. Ridges show patterns of onlap from simultaneous deformation and deposition. The NS-trending fault is thought to be of different origin than structures within the terrace. It corresponds to the direction of magnetic sea floor spreading anomalies and to the predicted orientation of synthetic strike-slip faults. Faults might have been initiated along these zones of weakness in an environment of distributed shear. Reactivation of such preexisting faults could be caused by their collision with the terrace complex as the oceanic plate is being underthrust. As a result, the trough portion west of the terrace boundary and east of

the NS-fault would rotate counterclockwise to produce compression and right-lateral shear on this fault and a basement step down to the east.

### **7.3 SUGGESTED FUTURE INVESTIGATIONS**

In spite of being only a piggy-back pilot survey, intended to provide a basis for proposing a more complete survey, this study has brought significant insight into the nature and variety of structures occurring on this transform plate boundary. Various additional data sets could complement the existing seismic reflection data. Drilling at at least three sites, one within the trough segment, and two on the terrace, would provide much needed temporal constraints. The trough hole would sample undeformed sediments and place constraints on sedimentation rates in the area. At least two terrace holes are needed to sample the older melange, where it is uplifted and one to sample a region of apparently rapid recent deposition. A refraction line paralleling the terrace would help establish a good velocity model, which is presently poorly constrained because of sparse ray coverage in refraction experiments crossing the plate boundary west of Moresby Island (Horn et al, 1984, and Dehler and Clowes, 1988). A refraction experiment across the plate boundary off Dixon Entrance could confirm the Moho dip beneath the terrace. Well-determined earthquake focal mechanism and depth constraints on events along the Queen Charlotte Fault plane and a determination of possible thrust events on the downgoing slab is essential to allow distinction between very different proposed configurations of the plate boundary. Finally, a more closely spaced and complete network of seismic reflection profiles, distributed over a wider area from south to north to cover the large variety of structures would be needed to develop a more accurate understanding on the complex four-dimensional tectonic activity of the Queen Charlotte Fault Zone.

## BIBLIOGRAPHY

- Abers, G., McCaffrey, R., 1988, Active deformation in the New Guinea fold-and-thrust belt: Seismological evidence for strike-slip faulting and basement-involved thrusting, *Journal of Geophysical Research*, v. 93, p. 13332-13354
- Atwater, T., 1989, Plate tectonic history of the northeast Pacific and western North America, in: Winterer E. L., Hussong, D. M., and Decker, R. W. (Eds.), *The Eastern Pacific Ocean and Hawaii*, The Geology of North America, Boulder, Colorado, *The Geological Society of America* N, p. 21-72
- Bérubé, J., Rogers, G. C., Ellis, R. M., and Hasselgren, E. O., 1989, A microseismicity study of the Queen Charlotte Island region, *Canadian Journal of Earth Sciences*, v. 26, p. 2556-2566
- Bruns, T. R., Carlson, P. R., 1987, Geology and petroleum potential of the southeast Alaska continental margin, *Earth Sciences Series*, v. 6, p. 269-282
- Bruns, T. R., Stevenson, A. J., Dobson, M. R., 1992, GLORIA investigation of the Exclusive Economic Zone in the Gulf of Alaska and off southeast Alaska: M/V Farnella Cruise F7-89-GA, June 14-July 13, 1989: *US Geological Survey*, Open File Report 92-317, 16 p.
- Chase, R. L., Tiffin, D. L., Murray, J. W., 1975, The western Canadian continental margin, in: Yorath, C. J., Parker, E. R., Glass, D. J. (Eds.), *Canada's continental margins and offshore petroleum exploration*, *Canadian Society of Petroleum Geologists*, Memoir 4, p. 701-721
- Christie-Blick, N., Biddle, K. T., 1985, Deformation and basin formation along strike-slip faults, Biddle, K. T., Christie-Blick, N., (Eds.), *Strike-slip deformation, basin formation and sedimentation*, Special Publications *Society of Economic Paleontologists and Mineralogists*, Tulsa, v. 37, p. 1-34
- Claerbout, J. F., Doherty, S. M., 1972, Downward continuation of moveout-corrected seismograms, *Geophysics*, v. 37, p. 741-768
- Cox, A., Engebretson, D., 1985, Change in motion of Pacific plate 5 Myr BP, *Nature*, v. 313, p. 472-474
- Currie, R. G., Cooper, R. V., Riddihough, R. P., Seemann, D. A., 1983, Multiparameter geophysical survey off the west coast of Canada, 1973-1982, Current Research, Part A, *Geological Survey of Canada*, Paper 83-1A, p. 207-212

- Davis, E. E., Seemann, D. A., 1981, A compilation of seismic reflection profiles across the continental margin of western Canada, *Geological Survey of Canada*, Open File Report 751
- Dehler, S. A., Clowes, R. M., 1988, The Queen Charlotte Islands refraction project. Part I. The Queen Charlotte Fault Zone, *Canadian Journal of Earth Science*, v. 25, p. 1857-1870
- DeMets, C., Gordon, R. G., Argus, D. F., Stein, S., 1990, Current plate motions, *Geophysical Journal International*, v. 101, p. 425-478
- Diebold, J., 1994, R/V EWING leg EW9412 -- "ACCRETE", 12 Sept. - 22 Sept. 1994 Prince Rupert B. C. - Prince Rupert, *Cruise Report*
- Fitch, T. J., 1972, Plate convergence, transcurrent faults and internal deformation adjacent to southeastern Asia and the western Pacific, *Journal of Geophysical Research*, v. 77, p. 4432-4460
- Fleming, S. W., 1996, Bulldozer blades and colliding submarine mountain chains: constraints on central Oregon convergent margin tectonics from magnetics and gravity, *M. Sc. Thesis*, Oregon State University, Corvallis, Oregon, 84 p.
- Harding, T. P., 1985, Seismic characteristics and identification of negative flower structures, positive flower structures, and positive structural inversion, *The American Association of Petroleum Geologists Bulletin*, v. 69, p. 582-600
- Harding, T. P., Lowell, J., 1979, Structural styles, their plate-tectonic habitats, and hydrocarbon traps in petroleum provinces, *The American Association of Petroleum Geologists Bulletin*, v. 63, no. 7, p. 1016-1058
- Horn, J. R., Clowes, R. M., Ellis, R. M., and Bird, D. N., 1984, The seismic structure across an active oceanic/continental transform fault zone, *Journal of Geophysical Research*, v. 89, p. 3107-3120
- Hyndman, R. D., Ellis, R. M., 1981, Queen Charlotte fault zone: microearthquakes from a temporary array of land stations and ocean bottom seismographs, *Canadian Journal of Earth Science*, v. 18, p. 776-788
- Hyndman, R. D., Hamilton, T. S., 1993, Queen Charlotte area Cenozoic tectonics and volcanism and their association with relative plate motions along the Northeastern Pacific margin, *Journal of Geophysical Research*, v. 98, p. 14257-14277
- Hyndman, R. D., Lewis, T. J., Wright, J. A., Burgess, M., Chapman, D. S., Yamano, M., 1982, Queen Charlotte fault zone: Heat flow measurements, *Canadian Journal of Earth Science*, v. 19, p. 1657-1669

- Mackie, D. J., Clowes, R. M., Dehler, S. A., Ellis, R. M., Morel-a-l'Huissier, P., 1989, The Queen Charlotte Islands refraction project. Part II. Structural model for transition from Pacific plate to North American plate, *Canadian Journal of Earth Sciences*, v. 26, p. 1713-1725
- Minster, J. B., and Jordan, T. H., 1978, Present day plate motions, *Journal of Geophysical Research*, v. 83, p. 5331-5354.
- Naylor, M. A., Mandl, G., Sijpesteijn, C. H. K., 1986, Fault geometries in basement-induced wrench faulting under different initial stress states, *Journal of Structural Geology*, v. 8, p. 737-752
- Nishenko, S. P., Jacob, K. H., 1990, Seismic Potential of the Queen Charlotte-Alaska-Aleutian Seismic Zone, *Journal of Geophysical Research*, v. 95, no. B3, p. 2511-2532
- Norton, I., 1995, Plate motions in the north Pacific: the 43 Ma nonevent, *Tectonics*, v. 14, p. 1080-1094
- Prims, J., Furlong, K. P., Rohr, K. M. M., Govers, R., 1997, Lithospheric structure along the Queen Charlotte margin in Western Canada: constraints from flexural modeling, *Geo-Marine Letters*, v. 17, p. 94-99
- Riddihough, R. P., 1982, Contemporary movements and tectonics on Canada's west coast, A discussion, *Tectonophysics*, v. 86, p. 319-314
- Riddihough, R. P., Hyndman, R. D., 1991, Modern plate tectonic regime of the continental margin of western Canada, Chapter 13, in: Gabrielse, H., Yorath, C. J., (Eds.), *Geology of the Cordilleran Orogen in Canada*, *Geological Survey of Canada*, Geology of Canada, no. 4, p. 435-455, (also Geological Society of America, *The Geology of North America* v. G-2)
- Rohr, K. M. M., Dietrich, J. R., 1992, Strike-slip tectonics and development of the Tertiary Queen Charlotte basin, offshore western Canada: evidence from seismic reflection data, *Basin Research*, v. 4, p. 1-19
- Rohr, K. M. M., Lowe, C., Snavely, P. D. Jr., 1992, Seismic reflection, magnetics, and gravity data across the Queen Charlotte fault and Dixon Entrance, *Geological Survey of Canada*, Open File Report 2615
- Sanderson, D. J., Marchini, W. R. D., 1984, Transpression, *Journal of Structural Geology*, v. 5, p. 449-458
- Sheriff, R. E., Geldart, L. P., 1985, Exploration seismology, Volume 1, History, theory, and data acquisition, *Cambridge University Press*, New York, 253 p.

- Sheriff, R. E., Geldart, L. P., 1987, Exploration seismology, Volume 2, Data-processing and interpretation, *Cambridge University Press*, New York, 221 p.
- Shor, G. G., 1962, Seismic refraction studies off the coast of Alaska, 1956-1957, *Bulletin of the Seismological Society of America*, v. 52, p. 37-57
- Smith, W. H. F., Sandwell, D. T., 1995, Marine gravity field from declassified GEOSAT and ERS-1 altimetry, *EOS Transactions, AGU*, 76(46), Fall Meeting
- Snaveley, P. D. Jr., Wagner, H. C., Tompkins, D. H., Tiffin, D. L., 1981, Preliminary geologic interpretation of a seismic reflection profile across the Queen Charlotte Island fault system off Dixon Entrance, Canada-United States, *Geological Survey Open-File Report 81-299*, 12 p.
- Spence, G., Asudeh, I., 1993, Seismic velocity structure of the Queen Charlotte Basin beneath Hecate Strait, *Canadian Journal of Earth Science*, v. 30, p. 757-805
- Stock, J. M., Molnar, P., 1988, Uncertainties and implications of the Late Cretaceous and Tertiary position of North America relative to the Farallon, Kula, and Pacific plates, *Tectonics*, v. 7, p. 1339-1384
- Sutherland Brown, A., 1968, Geology of the Queen Charlotte Islands, British Columbia, *Bulletin of British Columbia Department of Mines and Petroleum Research*, v. 54, 225 p.
- Sweeney, J. F., Seemann, D. A., 1991, Crustal density structure of Queen Charlotte Islands and Hecate Strait, British Columbia, Woodsworth, G. J., (Ed.), in: Evolution and hydrocarbon potential of Queen Charlotte Basin, British Columbia, *Geological Survey of Canada*, Paper 90-10, p. 89-96
- Taner, M. T., Koehler, F., 1969, Velocity spectra - digital computer derivation and applications of velocity functions, *Geophysics*, v. 32, p. 859-881
- Telford, W. M., Geldart, L. P., Sheriff, R. E., 1994, Applied Geophysics, Second Edition, Cambridge University Press, 770 p.
- Thompson, R. I., Thorkelson, D. J., 1989, Regional mapping update, central Queen Charlotte Islands, British Columbia, Current Research, Part H, *Geological Survey of Canada*, Paper 90-10
- Watts, A. B., Brink, U. S. T., 1989, Crustal structure, flexure, and subsidence history of the Hawaiian Islands, *Journal of Geophysical Research*, v. 94, p. 10473-10500
- Wilcox, R. E., Harding, T. P., Seely, D. R., 1973, Basic wrench tectonics, *The American Association of Petroleum Geologists Bulletin*, v. 57, p. 74-96

Yilmaz, Ö., Seismic data processing, Investigations in Geophysics, 1988, Doherty , S. M. (ed.), *Society of Exploration Geophysicists*, Tulsa, 526 p.

Yorath, C. J., Hyndman, R. D., 1983, Subsidence and thermal history of Queen Charlotte Basin, *Canadian Journal Earth Science* 20, p. 135-159

**APPENDICES**

## APPENDIX A: NORMAL MOVEOUT

For a single constant-velocity horizontal layer, the traveltime curve as a function of offset is a hyperbola. If  $x$  is the offset,  $t_0$  the two-way-traveltime along the vertical path and  $v$  the true velocity of the medium down to the reflector, the hyperbola is described by the equation

$$(I) \quad t^2(x) = t_0^2 + \frac{x^2}{v^2}.$$

Assuming the earth consists of several horizontal iso-velocity layers, the traveltime equation derived by Taner and Koehler (1969) then is

$$t^2(x) = C_0 + C_1x^2 + C_2x^4 + C_3x^6 + \dots,$$

where

$$C_0 = t_0^2,$$

$$C_1 = \frac{1}{v_{rms}^2},$$

and

$C_2, C_3, \dots$  are complicated functions that depend on layer thickness and interval velocity.

By making the small-spread approximation, that is assuming offsets are small compared to depth, this equation can be simplified to

$$(II) \quad t^2(x) = t_0^2 + \frac{x^2}{v_{rms}^2}.$$

The rms-velocity is defined by (Yilmaz, 1988)

$$(a) \quad v_{rms}^2 = \frac{1}{t_0} \sum_{i=1}^N v_i^2 \Delta t_i(0),$$

where  $v_i$  is the interval or average velocity of the  $i$ th layer, and  $\Delta t_i$  is the vertical two-way traveltime through the  $i$ th, and  $t_0$  through all layers down to the reflector. Layers are unfortunately not always oriented horizontally. Considering a single dipping layer in three dimensions the traveltime curve will depend on the apparent dip of the layer as well (Yilmaz, 1988).

$$(III) \quad t_0^2 = t_0^2 + \frac{x^2 \cos^2 \phi'}{v^2},$$

where  $\phi'$  is the angle between the surface and the intersection of the profile with the dipping plane (apparent velocity), and  $v$  is again the medium velocity. If only small spreads are considered, this expression approximates the hyperbola of equation II the gentler the dips are.

The time difference between traveltimes at a given offset and at zero offset is called normal moveout (NMO)

$$\Delta t_{NMO} = t(x) - t_0.$$

After making the small-spread and small-dip approximation, the traveltime curve is hyperbolic and given by

$$(V) \quad t^2(x) = t_0^2 + \frac{x^2}{v_{NMO}^2}.$$

This velocity is called normal moveout (NMO) velocity representing the medium velocity for a single horizontal layer, or the rms velocity for a multi-layered structure. The NMO velocity for dipping events is greater than the interval velocity above the reflector (equation III). Hence, a high velocity horizontal layer yields the same NMO as a dipping layer of low velocity. Dealing with dipping structure, though, requires special care. Fortunately, the change in velocity for dips not exceeding 15 degrees is insignificantly small and can be neglected (Yilmaz, 1988).

Normal moveout is estimated as

$$\Delta t_{NMO} = \sqrt{t_0^2 + \frac{x^2}{v_{NMO}^2}} - t_0.$$

This term quantifies the increase of NMO with offset and the decrease with depth ( $t_0$ )

$$\Delta t_{NMO} = \left\{ \left[ \frac{x^2}{v_{NMO}^2 t_0^2} \right]^{1/2} - 1 \right\}.$$

Once the NMO velocity is known, travel times can be corrected by shifting all parts of the gather by  $\Delta t_{\text{NMO}}(x, t_0)$ , to remove the influence of offset. An NMO-corrected gather then consists of flat lines for each genuine reflector, and over- or undercorrected hyperbolas for all others. Traces will be summed to obtain a single stacked trace at this CMP location.

In practice, normal moveout velocity should be distinguished from stacking velocity. Stacking velocity optimally stacks traces in a CMP gather. A hyperbola describes the shape of that curve as well, but is not necessarily the same small-spread hyperbola of equation (V). Equation (V) always matches the actual measured traveltime for very small spread lengths. The greater the offset the larger the discrepancy will be between actual and small-spread hyperbola. For a given maximum offset, which is defined by the recording geometry, a hyperbola can be found that best fits over this particular spread length. The corresponding velocity is called stacking velocity. However, to be able to estimate interval velocities, normal moveout (or  $v_{\text{rms}}$ ) and stacking velocities were assumed to be the same.

## APPENDIX B

### SEMBLANCE

The *velocity spectrum method* displays coherency of the signal along a hyperbolic trajectory over the entire spread length of a CMP gather. There are different measures of coherency (Yilmaz, 1988). The simplest utilizes the stacked amplitude

$$s_t = \sum_{i=1}^M f_{i,t(i)},$$

where  $f_{i,t(i)}$  is the amplitude value on the  $i$ th trace at two-way time  $t(i)$  and  $M$  is the fold of the CMP gather. The stacking amplitude is determined by stacking along the trajectory of the trial stacking hyperbola

$$t(i) = \sqrt{t_0^2 + \frac{x_i^2}{v_{stack}^2}}.$$

The velocity spectrum then shows the stacking amplitude at two-way zero-offset time on the vertical versus the different stacking velocities on the horizontal axis. This method of display provides a means to distinguish between primaries and multiple reflections. Multiples correspond to much lower stacking velocities than genuine reflections do at the same zero-offset time.

Stacking amplitude alone is not the best display quantity when signal-to-noise ratio is poor. Besides other possible measures, such as the normalized stacked amplitude, the unnormalized and normalized crosscorrelation, which calculates the crosscorrelation within a time gate that follows the path of the trial stacking hyperbola, semblance is the normalized output-to-input energy ratio, defined by

$$\text{sembl.} = \frac{1}{M} \frac{\sum_t s_t^2}{\sum_t \sum_{i=1}^M f_{i,t(i)}^2},$$

where  $\sum_i s_i^2$  is the energy of the stacked trace, and  $\sum_t \sum_{i=1}^M f_{i,t(i)}^2$  is the sum of the energy of all individual traces within a time gate  $t$  that is shifted along the trajectory of the trial hyperbola.

## INTERVAL VELOCITY

Interval velocities for horizontal constant velocity layering ( $v_{stack} \approx v_{rms}$ ) were found by using the definition of rms velocity (Telford et al., 1994)

$$v_{rms}^2 = \frac{1}{t_0} \sum_{i=1}^N v_i^2 \Delta t_i(0),$$

where  $t_0 = \sum_{i=1}^N t_i(0)$ . Thus, the rms velocity to reflector  $n$  is denoted by

$$v_L^2 = \frac{1}{\sum_{i=1}^N t_i(0)} \sum_{i=1}^N v_i^2 \Delta t_i(0)$$

or (a) 
$$v_L^2 \sum_{i=1}^N t_i(0) = \sum_{i=1}^N v_i^2 \Delta t_i(0),$$

whereas the rms velocity to reflector  $n-1$  is

$$v_U^2 = \frac{1}{\sum_{i=1}^{N-1} t_i(0)} \sum_{i=1}^{N-1} v_i^2 \Delta t_i(0)$$

or (b) 
$$v_U^2 \sum_{i=1}^{N-1} t_i(0) = \sum_{i=1}^{N-1} v_i^2 \Delta t_i(0).$$

The Dix formula describes the interval velocity by subtracting (b) from (a)

$$\sum_{i=1}^N v_i^2 \Delta t_i(0) - \sum_{i=1}^{N-1} v_i^2 \Delta t_i(0) = v_L^2 \sum_{i=1}^N t_i(0) - v_U^2 \sum_{i=1}^{N-1} t_i(0)$$

or 
$$v_n^2 = [v_L^2 \sum_{i=1}^N t_i(0) - v_U^2 \sum_{i=1}^{N-1} t_i(0)] / \Delta t_n(0).$$

## APPENDIX C: MIGRATION

The migration theory is based on data that was recorded with zero-offset, as if source and receiver were at coincident locations. The CMP recording geometry provides nonzero offset wave fields. After using the hyperbolic normal moveout correction, which assumes no strong lateral velocity variations, and structural dip, the data are stacked onto the midpoint time plane at zero offset. The more valid the normal moveout assumption is, the more the stacked resembles the desired zero-offset section. Not only can there be the problem of lateral velocity variation and dipping structure, but the stacked section can be contaminated as well by the presence of multiples with different stacking velocities or sideswipe energy that comes from outside the plane.

Kirchhoff migration collapses the diffraction hyperbola by summing its amplitudes and placing them at the apex in the migrated section. This migration algorithm works for all dips. Two other migration techniques are carried out in the frequency-wavenumber domain. The first, the Stolt-method requires a constant-velocity medium. Since this is normally not the case, the time axis is stretched to produce a constant-velocity section before applying the algorithm. This stretching is removed afterwards. The second is the phase-shift migration, which can only handle vertical velocity gradient. But both f-k-migration techniques are accurate for dips up to 90-degrees.

The 45-degree-finite-difference algorithm was developed by J. F. Claerbout (Claerbout, 1972) at Stanford University and is based on the parabolic approximation to the scalar wave equation. All three techniques have some advantages and some disadvantages. Compared to the Kirchhoff and f-k-migration algorithms, the finite-difference method is being capable of handling dips only up to angles of 45-degrees with sufficient accuracy. In contrast, it has less problems dealing with lateral velocity variation unless they are fast.

The finite-difference migration is based on downward continuation. The wavefield is recorded at  $z=0$ . Normally, the seismic sections are represented in the (x,

$t$ )-plane, whereas migrated sections will be represented by the  $(x, z)$ -plane. Principally, downward continuation means that the location of the receiver cable is moved down into the earth as if to record the same wave field as at the surface, thereby collapsing hyperbolas to their apex whenever  $t=0$ . This process is called the imaging principle and images at each depth step the shape of a wave field at observation time  $t=0$  as if generated by an exploding reflector at that depth. The migrated section is then constructed by the  $(x, z)$ -plane at  $t=0$ .